Localisation de la lumière dans des rugosités de taille nanométrique de surfaces métalliques traitée par les équations intégrales et les ondelettes

Camille Maxime

▶ **To cite this version:**

HAL Id: tel-00681803

https://theses.hal.science/tel-00681803

Submitted on 22 Mar 2012

THÈSE

Pour obtenir le grade de

DOCTEUR DE L'UNIVERSITÉ DE GRENOBLE

Spécialité : **Matière Condensée et Rayonnement**

Arrêté ministériel : 7 Août 2006

Présentée par
Camille MAXIME

Thèse dirigée par **Aude BARBARA**
et codirigée par **Pascal QUEMERAIS**

préparée au sein de l'**Institut Néel, CNRS-UJF**
et de l'**École Doctorale de Physique de Grenoble**

Light localization within nano-scale roughness of metallic surfaces treated by surface integrals and wavelets

Thèse soutenue publiquement le **27 Janvier 2012**,
devant le jury composé de :

Eric Bonnetier
Laboratoire Jean Kuntzmann, UJF (Grenoble), Président
Brahim Guizal
Laboratoire Charles Coulomb, CNRS-UM2 (Montpellier), Rapporteur
Brian Stout
Institut Fresnel, CNRS-AMU (Marseille), Rapporteur
Lukas Eng
Institut für Angewandte Photophysik, TUD (Dresden), Examinateur
Aude Barbara
Institut Néel, CNRS-UJF (Grenoble), Directeur de thèse
Pascal Quémerais
Institut Néel, CNRS-UJF (Grenoble), Co-Directeur de thèse

Contents

Acknowledgments

x

Notations

Mathematics notations

$\Re(A)$ the real part of A

$\Im(A)$ the imaginary part of A

$\lceil x \rceil$ the ceiling function: the smallest integer not less than x

$\mathscr{C}^{(2)}$ the space of functions which have continuous derivatives up to the second order

$H_0^{(1)}$ the modified Hankel function of the first kind

J_n the Bessel functions of the first kind

Y_n or N_n the Bessel functions of the second kind

$\delta_{n,m}$ the Kronecker symbol is equal to one if n=m and is equal to zero otherwise

A^T the transpose of A

Abbreviations

AOA   Abnormal Optical Absorption

CM   Cavity Mode

DWT   Discrete Wavelet Transform

EF   Enhancement Factor

EM   Electromagnetic

FWT   Fast Wavelet Transform

IR   Infra Red

MRA   Multi Resolution Analysis

RAM   Random Access Memory

SERS   Surface Enhanced Raman Scattering

SIE   Surface Integral Equation

SM   Surface Mode

SPP   Surface Plasmon Polariton

General Introduction

Plasmonics is a new field of science and technology that offers new ways to concentrate and manipulate light. The ability of Surface Plasmon Polaritons (SPP) to confine electromagnetic (EM) fields in a sub-wavelength volume is responsible for unique optical properties of metallic surfaces.

Metallic surfaces are very good reflectors in the visible and infra-red (IR) spectral range. A dip in the reflectivity, which is normally close to one for good conductors, may indicate the existence of an electromagnetic resonance at the metallic surface. At the beginning of the 20th century, Wood did not expect to find narrow bright and dark bands in the reflection spectrum of metallic grating [1]. These bands appeared at specific frequencies and angles, and some also depended on the polarization. As they were not understood at that time, they were named Wood anomalies. Some of the anomalies, at equally spaced frequencies, were found to coincide with the emergence of a diffraction order in 1907 by Rayleigh [2]. However no rigorous explanation was given for the remaining ones.

Fano is the first to introduce a lossy permittivity in its modeling of a metallic grating excited by a plane wave, thus enabling the existence of polarized quasi-stationary waves bound at the interface of the metal and the dielectric [3]. These waves are a superposition of Transverse-Magnetic (TM) polarized EM waves localized at the interface and propagating along the surface which would be later called a Surface Plasmon Polariton (SPP). As Fano acknowledged, Sommerfeld had already mathematically described such EM waves impinging at grazing incidence on a dielectric surface to describe radio waves propagating on the sea. The reflection being on a dielectric, Sommerfeld thus did not foresee the rich physics associated with metallic surfaces. Fano made a parallel between the quasi-stationary waves on the metallic gratings surface with Sommerfeld's wave reflecting on a conducting surface (i.e., when there is a total reflection of the wave impinging on the surface).

The EM description of the SPP was, however, not done as such since the plasmon has not yet been introduced and thus the electronic nature of the wave had not been identified. A few years later, Pines explained the energy losses which are observed experimentally when fast electrons go through metals as the excitation of the collective motion of the free electrons in the bulk metal [4, 5]. He named the quantum of an elementary excitation, a plasmon, whose energy is $\hbar\omega_p$ and whose frequency is the plasma frequency of the electrons in the metal ω_p. A few years later, Ritchies showed that surface plasmons could be excited by accelerated electrons at a smaller frequency ω than the plasma frequency ω_p of

1

oscillation of the plasmons [6]. The Wood anomalies were finally interpreted by Ritchies as the coupling between a surface-plasmon and photons, a SPP, the coupling being made possible by a grating [7].

Under the right excitation, free electrons of a conductor may oscillate collectively at the surface. This phenomenon can be equally described as an EM wave which propagates along the interface between a dielectric and a metal and is evanescent in the direction perpendicular to the metallic surface. The collective electrons' excitation and the propagation of photons are two aspects of one phenomena: the SPP. The EM field of the SPP is trapped at the surface without being diffracted. This confinement of the SPP at the surface is an attractive property which leads to unprecedented applications ranging from biology to circuitry.

In order to excite an SPP optically, the wavevector of the incident EM wave has to match the one of the SPP. The SPPs are not radiative since the wavevector of the SPP in the direction of propagation is greater than the one of light. In 1968, Otto, Kretschmann and Raether proposed two experimental techniques [8, 9] to excite SPPs using a prism to match the momentum of light to the one of the SPPs, opening the way to the field of Plasmonics. Nowadays, the number of available experimental techniques has been widened and a description of the main ones may be found in [10]. Along with the experimental study of SPPs, there is a need for the modeling and simulation of plasmonics systems. This thesis is a contribution to the numerical simulation of EM problems aimed at the understanding of the physics of metallic surfaces.

The optical properties of metallic surfaces may drastically change when the roughness of the surface goes from smooth variations of a few nanometers, to very abrupt variations of about 10 to 20 nanometers. A surface corresponding to the latter characteristics will be called a nano-scaled rough surface. Such surfaces may exhibit a strong absorption in the visible spectral range. This observation is strongly puzzling, as defects whose dimensions are much smaller than the incident wavelength do not usually interact with a plane wave.

Another one of the most puzzling optical phenomena discovered around nano-scaled rough metallic surfaces in the 20th century is probably the Surface Enhanced Raman Scattering (SERS): the enhancement of the Raman scattering of molecules when they are close to such surfaces. The underlying phenomena behind these two changes in a metallic surface's optical behavior is the existence at the metallic surface of highly localized, strong electric fields, called hot-spots. The existence of hot-spots on these particular surfaces is believed to be triggered by SPPs. Similar optical properties were observed on nano-structured surfaces, i.e. surfaces with a nanoscale roughness, usually periodic, fabricated by standard lithography techniques.

In this thesis, we address the question of the origin and the condition of existence of these hot-spots. To do so, we investigate the excitation by a plane wave of metallic surfaces with defects, ridges or grooves whose sizes are much smaller than the length of the surface and also much smaller than the wavelength of the incident plane wave. Within this framework, the study of the EM near-field, which is the EM field standing in the region where the distance to the metallic surface is less than the wavelength, as well as the reflectivity, may

offer a way to understand the processes involved in the creation of hot-spots.

The study of the optical properties of metallic nano-structured gratings is an important topic of research in our group. A simple way to model rough surfaces is to consider rectangular groove metallic gratings. It is a pertinent choice for three reasons. The first one is that the rectangular grooves grating may be efficiently modeled with a modal method that gives a direct link to the physics of the optical properties. The second one is that they can be made experimentally and enable confrontation of the calculated and experimental optical properties. Lastly, their study shows that they can reproduce some of the observations made for rough surfaces.

As first described by Hessel and Oliner, there may exists waveguide modes in the deep and sub-wavelength rectangular grooves of a grating [11]. These modes, which we call *cavity mode*, can enter in a forced resonance at specific wavelengths, sometimes refered to in the literature as *shape resonances*. These resonances are Fabry-Perot like resonances of a guided EM wave, where the groove acts as a resonator. This EM wave is made of two out-of-phase coupled SPP propagating along each vertical wall of the groove. These resonances play an important role in the localization of the EM field in rectangular grooves gratings. The localization effects were extensively studied both theoretically and experimentally among our team [12, 13, 14, 15, 16, 17].

Attention was paid to tiny grooves of metallic gratings whose size matches realistically the one of rough surfaces. It was shown that tiny grooves of width w =5 nm and depth h =15 nm may support a cavity mode resonance in the visible spectral range for a wavelength $\lambda \sim 500nm >> h$. The resonance of such grooves gives rise to an electric field with an enhancement high enough to cause the SERS effect and is associated with a dip in the reflectivity which goes down to almost zero [18, 17]. These ground-breaking results for the understanding of the optical properties of rough surfaces were made possible by the development of the exact modal method. The modal method is, however, limited to grooves with a rectangular profile.

In order to investigate these optical phenomena further, the main goal of this thesis is to be able to calculate the electromagnetic field accurately around very small defects, whose characteristic size h is of a few nanometers, on very wide metallic surfaces in the visible range. The main difficulty in doing so is the discrepancy of the problem dimensions: the incident field wavelength λ and the length d of the surface are much bigger than the height h of the groove (λ >> h and d >> h).

To generalize some of these results to more general profiles and in view of a future study of the localization effects on rough surfaces, we have decided to use the surface integral equations (SIE) method since the surface under scrutiny may be of arbitrary shape. The SIE method is especially appropriate for plasmonic problems as the EM problem in TM polarization to solve (the Maxwell equations and the boundary conditions), is reduced to two equations for the magnetic field only at the surface.

The numerical resolution of the integrals requires solving a linear set of equations for the magnetic field values at equally spaced points on the surface. In spite of the reduction of

the problem to a one-dimensional problem, the step has to be small, sometimes of the order of magnitude of the angström, and the number of unknowns increases quickly with the length of the profile. In order to solve the dense matrix which results from this system, the time and memory space requirement issues have to be tackled. It is otherwise impossible to study larger profiles than surfaces whose length is a few hundred nanometers.

The large required number of unknowns is due to the fact that the description of the sharper variations of the magnetic field has to be done at the scale of the angström although the dimensions of the problem are otherwise a few hundred nanometer. There co-exist simultaneously, at the surface, EM waves whose wavelength is of the order of magnitude of the incident one and much more localized ones similar to the ones of the hot-spots.

In order to improve the performances of the original method, we have investigated a way to treat separately the different scales of the problem and to describe it efficiently so that the number of unknowns, and accordingly the memory space, are reduced. The wavelets draw our attention since they are a mathematical tool dedicated to the study of functions as a function of their level of details. Indeed, the wavelet basis divides the space of functions in subspaces which have different resolutions. The EM waves at the surface whose modulation is smooth are described accurately within a subspace whose resolution is low, with a few points distributed over the whole surface. On the contrary, the hot-spots need to be described within a subspace whose resolution is high, but only locally, with a few points drawn closer at that precise spot. We may make use of this property to adapt the expansion of the magnetic field as a function of its location on the surface and increase the accuracy of the description where it is needed, in the deep grooves at the surface. By doing so, the number of terms needed to represent the magnetic field at the surface in the wavelet basis is reduced compared to the number of points discretizing the surface in the SIE method. That is why the wavelets seems appropriate to help solve our problem whose dimensions have different scales.

Additionally, the transformation of the initial dense matrix in a wavelet basis yields a sparse matrix to solve. The gain in memory space may be made the most of, in order to treat a larger system. However, the application of wavelets is not direct and the right method has to be chosen in order to really improve the performances of the SIE method. Two different applications, one using the wavelet transform and the other one using a specific wavelet (Coiflets) as an expansion and test basis functions, were considered, the latter only theoretically. The potential of the use of wavelets with the SIE is illustrated in this thesis.

The work presented in this manuscript is the modeling and numerical simulation of the EM phenomena on rough surfaces by the resolution of the SIE. A new approach to the resolution, which uses wavelets, aims at studying larger nano-scale rough surfaces. The manuscript is organized in five chapters, described hereafter:

- The first chapter presents the motivations for studying nano-scale rough surfaces, an overview of the physics of the SPP and some related results obtained previously with rectangular groove metallic gratings in our group.

- The second chapter presents a review of the modeling of metallic surfaces, describes the surface integral equations method and details the numerical implementation and the validation of the method.

- The third chapter gives a few examples of the application of the SIE to nano-scale rough surfaces in the form of the study of the EM resonances of Gaussian-shaped-groove gratings.

- The fourth chapter presents the basic principles of the wavelet theory.

- The fifth chapter comments on the most efficient way to apply wavelets to the SIE and is an illustration of the possibilities of this new approach.

Chapter 1

Introduction to the surface plasmon excitation at rough or nano-structured metallic surfaces

The broad context of this PhD thesis, the optical properties of metallic surfaces, is presented in this first chapter. We introduce our motivations for studying nano-scaled rough surfaces in the first section 1.1, putting a particular emphasis on coldly evaporated films. The following section 1.2 gives a quick overview of the surface plasmon polaritons, an EM wave which propagates along metallic surfaces. Lastly, the optical properties of a model rough surface, the rectangular groove metallic grating, are presented in section 1.3.

1.1 Motivation and Interests
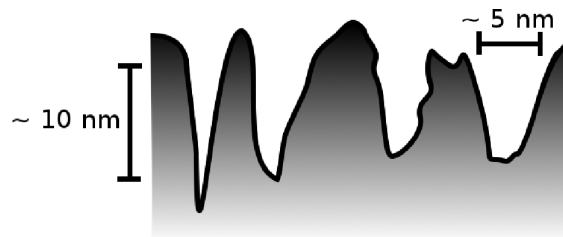
Figure 1.1: *Sketch of a nano-scaled rough surface.*

The metallic surfaces we focus on are nano-scaled rough surfaces similar to the one sketched in figure 1.1. Their profile has very stiff slopes although the variations amplitude is between 5 and 30 nm. The ability of nano-scaled rough surfaces to enhance the Raman emission of molecules deposited on the latter was first observed by Fleischmann who did

not realize the importance of this discovery [19]. He was studying the Raman signal of pyridine molecules deposited on a rough silver electrode and recorded an enhancement of the signal. His initial motivation was to roughen the silver electrode to increase the total effective surface on which the molecules were adsorbed in order to enhance the Raman signal. He has thus analyzed his observation as coming from this effect. However, it quickly appeared that the observed enhancement of the Raman scattering could not be accounted for only by this fact. In this section, we describe the basics of SERS theory, we give an insight on the experimental characterization of coldly evaporated films and finally we relate these phenomena with the hot-spots and the localization of the EM waves at very small scales.

1.1.1 Surface Enhanced Raman Scattering

Although SERS was first observed by Fleischmann [19], the effect was actually discovered by Van Duyne and Jeanmaire [20] who were the first to point out the active implication of the rough metallic surface in the Raman enhancement and proposed to explain it by an electromagnetic effect. Albrecht and Creighton proposed in the same year an explanation which relied on a chemical effect [21]. The possible effect of Surface Plasmon Polaritons to convert the ordinary Raman effect into a much stronger resonant one was raised two years before by Philpott [22] and important research followed to relate SERS and plasmonic effects. Twenty years later, the SERS effect led to the detection of the Raman scattering of a single molecule reported by two independent groups [23, 24] which requires enhancement factors of the electric field as high as 10^{14}. We describe briefly the mechanism of SERS [25, 26].

The Raman scattering results from the interaction of light with, in most cases, the vibrational modes of a molecule. In a classical description, one can say that a photon of frequency ν_L can be scattered inelastically by a molecule. During the inelastic scattering, the photon can either acquire the energy $h\nu_M$ of a phonon of the molecule which will be annihilated (anti-Stokes process) or lose the energy $h\nu_M$ necessary to excite the phonon (Stokes process). The Raman spectra thus consists in two peaks on each side of the excitation energy $h\nu_L$ of the incident photon, attesting to the photon being scattered at an energy $h\nu_S = h\nu_L - h\nu_M$ and $h\nu_{aS} = h\nu_L + h\nu_M$. Figure 1.2 shows a sketch of this mechanism via the energy levels of the molecule. During the Stokes process, the absorption of the incident photon excites the molecule initially in its ground state $h\nu_0$ to a virtual level $h\nu_0 + h\nu_L$. The molecule relaxes in its excited vibrational state $h\nu_0 + h\nu_M$. The relaxation of the molecule is accompanied by the emission of a photon $h\nu_S = h\nu_L - h\nu_M$ and the creation of a phonon of frequency ν_M. In this description, the phonon is described by the transition of the molecule from its excited vibrational state $h\nu_0 + h\nu_M$ to its ground state $h\nu_0$. During the anti-Stokes process, the incident photon excites the molecule when it is in its excited vibrational state $h\nu_0 + h\nu_M$. The molecule is thus excited to a higher virtual level $h\nu_0 + h\nu_M + h\nu_L$ and relaxes into its ground state $h\nu_0$ by emitting a photon $h\nu_{aS} = h\nu_L + h\nu_M$. In the process, the initial phonon of frequency ν_M is de-excited.
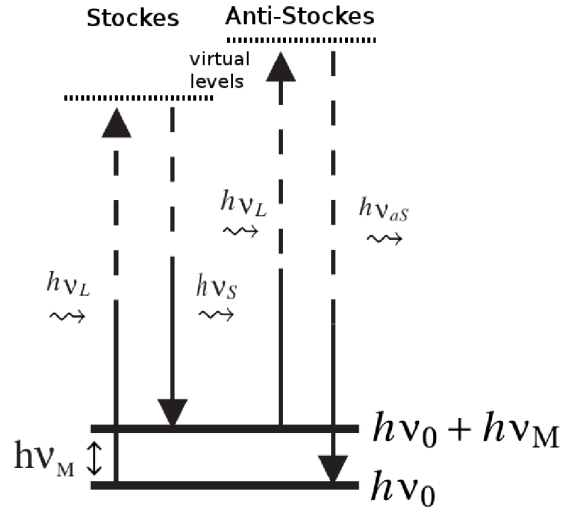
Figure 1.2: *Sketch, modified from [27], of the energy levels of the molecule, as well as the transition $\pm v_M$ due to a photon absorption v_L which yield in a Stokes v_S or anti-Stokes v_{aS} emission.*

The Raman spectra is thus characteristic of a molecule and is an essential tool for materials characterization. The Raman scattering is however very weak since its scattering cross section σ_{RS} is of the order of $10^{-30} cm^2$/molecule. The scattering cross section of fluorescence for instance is 10 orders of magnitude higher. The Raman scattering is a spontaneous event and therefore the power of the Raman beam is linearly proportional to the intensity of the exciting beam I

$$P \propto \sigma_{RS} I \quad .$$

The Surface Enhanced Raman Scattering (SERS) effect is the enhancement of the Raman scattering of the molecules due to their proximity to a metallic object. The SERS effect is mainly due to a resonant enhancement of the local exciting field $E_{exc} = E(v_L)$ as well as the local emitted field $E_{em} = E(v_{S/aS})$. Its nature may also be a chemical one, the bounds of the metallic surface with the molecule being responsible for an increase in the Raman cross section σ_{SERS}. The maximum of this enhancement is however estimated to be only of the order of 10^2 and is still under debate. The enhancement factor (EF) of the SERS effect is defined as the enhancement of the intensity of the Raman beam and is estimated by [28]

$$EF = \frac{P_{SERS}}{P} = \left| \frac{E_{exc}}{E_0} \right|^2 \left| \frac{E_{em}}{E_0} \right|^2 \frac{\sigma_{SERS} I}{\sigma_{RS} I} \quad .$$

where E_0 is the incident electric field.

The chemical EF is $\frac{\sigma_{SERS}}{\sigma_{RS}}$ while the electromagnetic EF is $\left| \frac{E_{exc}}{E_0} \right|^2 \left| \frac{E_{em}}{E_0} \right|^2$ and can experimentally reach a value up to 10^{12} [23].

The mechanisms which are responsible for the increase of the electric field are still not completely well understood even if we know that the surface plasmons as well as the lightning rod effect are two important electromagnetic phenomena which take place. For instance, in the case of molecules in a solution with silver colloids (dispersed nanoscale objects), this enhancement is due to the localized surface plasmon resonances of small metallic particles which creates an enhanced near field at the surface of the particle. There are one or several plasmonic effects for each kind of metallic structure involved in the SERS and therefore they must be considered individually.

For all these structures, however, either due to the broad peak of the resonance or to a broad distribution of the sizes of the features, there is a wide repartition of resonance energies leading to a high electric field. The resonance energy is thus generally broader than the Stokes or Anti-Stokes energy shift ($\nu_M \approx 0.05$ eV [29]) and the local field enhancement can be considered to be the same for the excited and the emitted fields. Hence, the EF can be defined by only considering the exciting field and is approximated by $\left|\frac{E_{exc}}{E_0}\right|^4$ with respect to the incident field E_0 [29]. To obtain EF of the order of 10^{12}, the near-field has to be enhanced by three orders of magnitude. This is a value encountered in the case of the single molecule detection. In more general experiments on rough metallic surfaces, the SERS EF is usually lower, of the order of 10^6 to 10^{10}, as it is an average over the different spots where the electric field is high, called the active sites. The active sites for the SERS effect are the hot-spots. It is difficult to estimate experimentally as well as theoretically a SERS EF as it depends on the number of molecules as well as on their spatial repartition on the surface or near the colloids. For this reason, only the order of magnitude of the SERS EF is given.

1.1.2 The coldly evaporated surfaces: SERS, Anomalous Optical Absorption (AOA) and topography

In this thesis, as already mentioned, we focus on a specific type of SERS surfaces namely, the *coldly evaporated* ones, or cold films, which played an important role in the study of SERS. Their capacity to exhibit SERS was discovered together with another phenomenon, the Anomalous Optical Absorption (AOA). From the beginning, the very small size of the abrupt roughness of these films at low temperature was spotted as a key parameter. When metallic surfaces are grown at low temperature (100 K < T < 250 K), their surfaces have a particular roughness and they exhibit specific physical properties which disappear as they are warmed up to room temperature and as their roughness also disappears. The optical properties of the cold films depend strongly on the way they are fabricated ie on the deposited silver thickness and the temperature of deposition [30]. This points out the importance of the geometry as well as the scale of the roughness and experimental results on the surface structure of cold films, and is therefore summarized below.

The characterization of the surfaces of the coldly evaporated silver films is a tough task. Gimzewski *et al.* studied them by Scanning Tunneling Microscopy (STM) in the most
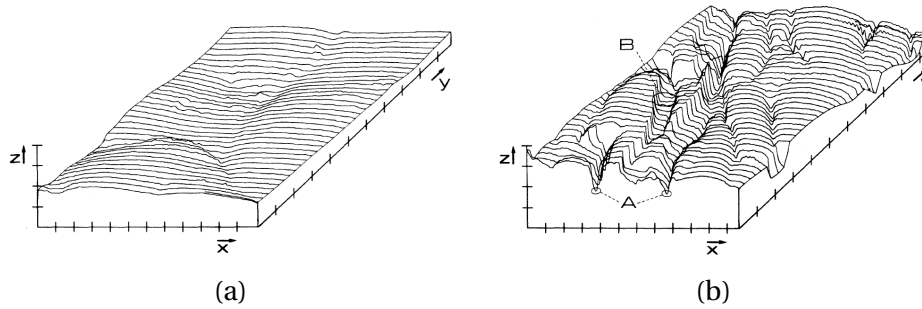
Figure 1.3: *Figures taken from [31]. (a) Scanning tunneling microscopy picture of a warm-condensed silver surface and (b) of a coldly evaporated one. Example of V-shaped sites where the tip size limits the topographic precision are indicated by the letter A while U-shaped sites measured accurately are indicated by the letter B. Division on the axis correspond to 5 nm.*

accurate way up to now. They compared warm-condensed films with cold-condensed films whose respective topographies are shown in figure 1.3. They showed that warm-condensed films are flat and very smooth whereas the cold-condensed films have additional "trenches <1-3 nm in width, 3- (>4.5 nm) in depth, and separated by 5-15 nm"[31]. However, we must note that the cold films could not be imaged in situ and had to be brought back to air and ambient temperature to be transfered into the STM chamber. Therefore a thick layer of pyridine molecules was deposited before the transfer at room temperature in order to maintain the structure of the cold film. The original structure probably changed a little prior to the STM measurement. During the process, the spatial repartition of the trenches was very likely not modified but the sizes of the cavities might have been reduced with respect to the ones existing before the warm up.

The spatial lateral resolution is very accurate as it was limited by the tip size estimated to be less than 1 nm. The authors explained that the experimental apparent depth, however, can underestimate the real one. Indeed, if the tip is able to reach the bottom of the U-shaped trenches whose width is greater than the tip width (indicated by the letter B in figure 1.3), it is not the case for the V-shaped grooves, whose width is less than the tip width (indicated by the letter A). In that case, the real height of the groove cannot be measured. What we know is thus that cold films have flat surfaces interrupted by grooves of width up to 5 nm, which are at least 4.5 nm deep and separated by 5 to 15 nm.

Douketis *et al.* did a similar experiment in 1995 to acquire *in situ* images of the surface topography of coldly evaporated silver surfaces [32, 33]. They found the surfaces to be self-affine surfaces. The self-affine surfaces resemble the fractal surfaces but only for a limited range of scales. The geometry was qualified to be "cauliflower-like" and the dimensions observed at the top of the surface are of the order of 5-15 nm at 130 K to 30-50 nm at 250 K due to the melting of the deposited silver atoms. They admitted that the scan of the depth of the roughness was out of reach. The trenches observed by Gimzewski correspond probably to the gaps between the cauliflower-like branches of Douketis.

These observations are consistent with what is known on the formation of the evap-orated films. The coldly-evaporated surfaces at low temperature grow as micro-crystalline films. The films therefore consists in an assembly of pillars of silver with grain boundaries a few nanometer wide and whose depth can be of the order of the thickness of the film [34]. Most of the experimental work thus indicates that the defects on the surface resemble grooves separated by 5 to 30 nm and whose width is less than 5 nm.

One of the optical properties of the coldly evaporated films is their wide absorption in the visible spectral range. This phenomenon is known as the Abnormal Optical Absorption (AOA) because metallic surfaces are good reflectors at room temperature and are expected to have a low absorption as is the case for a flat silver surface. The absorption of a coldly evaporated silver film on sapphire surface at 140 K was measured by Hunderi *et al.* [35], shown by white dots in figure 1.4. The same surface was warmed up at room temperature and the absorption is shown in the same figure (crosses) for comparison. A large abnormal absorption band of 2 eV width appears at 2.5 eV for the cold film and disappear after the warming up of the film.
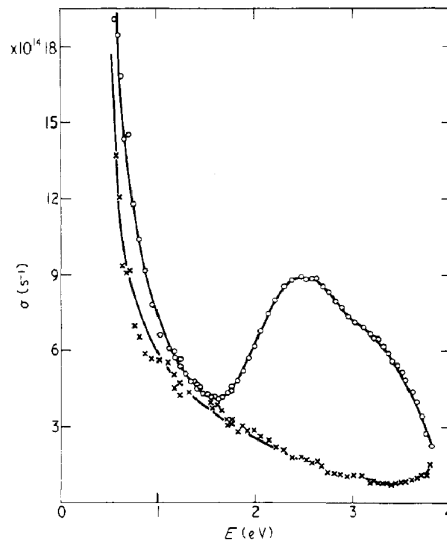
Figure 1.4: *Absorption for coldly evaporated rough silver surface (white dots) at 140 K and for the same surface flatten after being warmed up at room temperature (crosses) and published in [35].*

Other similar studies were made in order to further investigate the AOA on silver by varying the temperature and thermal history of the films. The abnormal absorption band disappears progressively when the cold-film is warmed up at room temperature [36]. If the roughness of the film is maintained by evaporating an additional 5 Ålayer of aluminum be-fore the warming of the film, the abnormal absorption does not disappear when measured close to room temperature [37] which proves that the roughness is indeed at the center of the phenomena.

We have seen that the cold films present an Abnormal Optical Absorption (AOA) and we know that they are good SERS substrates. Several evidences led to relate the two phenomena with the nano-scaled roughness of the cold films and therefore its role will be discussed in the next paragraph.

1.1.3 Notion of active sites: the Hot Spots

A possible explanation to the AOA is to look for in the trapping of the EM incident wave in the tiny cavities of the rough surface of cold films. Those regions where the EM field is localized and strongly enhanced, called hot-spots, would be good candidates to explain at the same time the electromagnetic enhancement factor of SERS and the AOA. The experimental evidence of such *active sites* on the surface of cold films and the understanding of their physical origin has been a long journey. We present the main steps here.

An important experiment for the understanding of these points was that of Albano *et al.* who proposed that the deep crevices in between the pillars of silver which grow at low temperature are active sites of SERS [38]. He showed it experimentally by comparing the Raman scattering of pyridine molecules deposited on silver in three different cases.
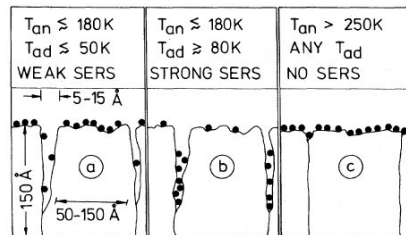
Figure 1.5: *Sketch of pyridine molecules on coldly evaporated silver surfaces in three cases from [38].*

The case of a flat surface, at room temperature when the crevices are joined, in figure 1.5(c) shows no SERS effect. In the two other cases, the surface of coldly evaporated silver is believed to have deep crevices. If the pyridine molecules are simply deposited at the surface, in figure 1.5(a), a weak SERS exists. However, if they are thermally diffused into the crevices, in figure 1.5(b), a strong SERS is observed. They conclude that the two requirements to observe a strong SERS are a rough metallic surface and pyridine molecules situated at the bottom of the deep crevices. From this experiment, one may indeed deduce that a high EM field is localized into the narrow and deep crevices and responsible for a strong SERS. They report an increase of the Raman cross section of 10^4-10^5 at the bottom of the groove compared to the one at the surface.

Seki *et al.* discussed this interpretation in light of several experimental evidences obtained on cold films. They concluded that the active sites are atomic scale cavity sites rather than adatoms on the surface [30]. They also emphasized that only films with a thickness

greater than 15 nm exhibit SERS and that films whose thickness is above 100 nm have the stronger SERS. On the contrary, the films where adatoms are deposited show a weak SERS.
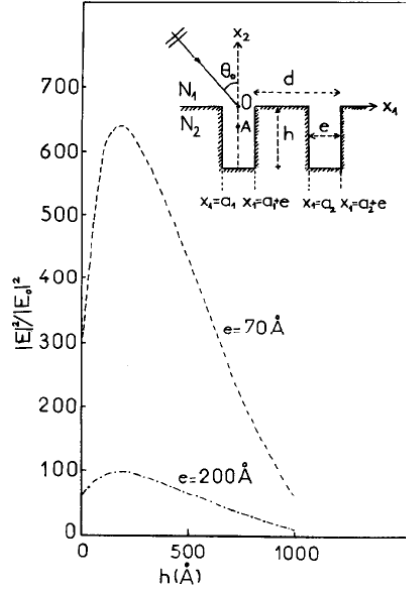
Figure 1.6: *Sketch from [39] of the rectangular groove gratings (inset) and electric field enhancement as a function of the depth of the channel h at point A for two channel width e=7 nm and e=20 nm for a silver grating of period d=100 nm and at normal incidence. The wavelength of the incident light is $\lambda = 514.5$ nm.*

Several groups attempted to explain the physical phenomena responsible for the active sites in the general SERS phenomenon [40, 41, 42, 43]. Wirgin and Lopez-Rios were the first to model the surface of cold films by a metallic grating with rectangular grooves [39, 44] similar to the one sketched in figure 1.6. They proposed a scenario for the light-trapping by crevices: a guided mode in the deep and narrow rectangular grooves could undergo a Fabry-Perot like resonance leading to a stationary wave into the cavity (thus localized). Their model showed that grooves of width equal to 7 and 20 nm have an EM resonance in the visible for a depth equal to 100 nm and can exhibit an EF up to 10^5. However, in this model, the resonant phenomena no longer exists for a groove depth equal to 20 nm which is the realistic size for the cavities existing on cold films. The size difference of one order of magnitude between the experiments and theory was not understood until very recently [17].

In 2008, Le Perchec *et al.* showed that the approximations used by Wirgin and Lopez-Rios were not valid when studying the resonances of rectanguler grooves in the visible range and this was the reason for the wrong order of magnitude in the height of the cavities with respect to the real height of the roughness. An exact modal method had to be applied to explain why grooves a few nanometers deep and wide may give rise to strong electromagnetic EF equivalent to the ones in SERS and also strongly absorb visible light as in the AOA effect

[17]. More details will be given later in section 1.3. Recently, the SERS and AOA effect for a gold grating with very tiny grooves has been evidenced experimentally by Deng *et al.* [45], confirming the theoretical predictions of [17]. A dip in the reflectivity of visble light exciting a gold grating with trenches of width w=18 nm and height h=30 nm was measured by Polyakov *et al.* [46] demonstrating experimentally the resonance of such grooves.

We have seen that nano-scaled rough metallic surfaces such as cold films play an active role in enhancing, up to 10^5 orders of magnitude, the Raman signal of molecules close to such surfaces and in absorbing the visible light strongly. The two phenomena are believed to exist because of plasmonic resonances in small (height ~ 15 nm) and narrow (width ~ 5 nm) cavities at the surface. The existence of EM resonances in rectangular grooves of similar dimensions was demonstrated theoretically and evidenced experimentally. One of the goals of this thesis is to verify that the results obtained on rectangular groove gratings may be generalized to arbitrarily-shaped cavities and more complex arrangements of the latter to better take into account the complex topography of rough surfaces.

1.2 Surface Plasmon Polaritons of a flat metal-dielectric interface

1.2.1 The electromagnetic problem of a metal dielectric interface
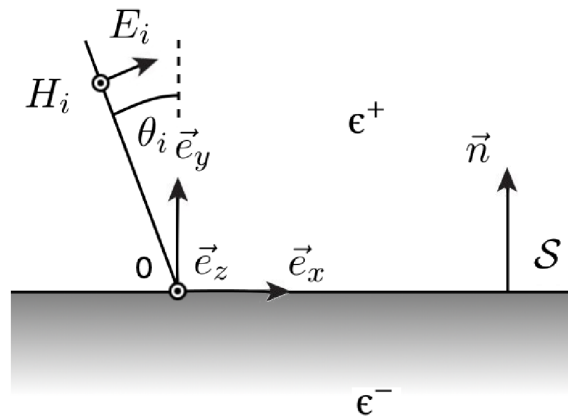
Figure 1.7: *Sketch of a dielectric (ϵ^+) / metal (ϵ^-) flat interface S of normal vector $\vec{n}$ illuminated by a TM-polarized plane EM wave with an incidence angle θ_i.*

To introduce the field of plasmonics, we start by considering the propagation of an EM wave at a plane interface S between two media, a metal and a dielectric. We study the EM solutions existing at the plane interface, in the particular case of harmonic EM fields impinging on the surface which is invariant in the direction perpendicular to the incidence plane [47]. The chosen coordinates are shown in figure 1.7. The direction perpendicular to

15

the surface is the y direction. We define the xOy plane as the incidence plane or the plane of propagation of the EM field and the z direction as its perpendicular axis along which the problem is invariant. We will only address the problem of the Transverse Magnetic (TM) polarization: the electric field is in the xOy plane while the magnetic field is in z direction. This geometry will be used throughout the whole thesis.

Let us recall the general Maxwell equations for the electric field $\vec{E}$ and the magnetic field $\vec{H}$ in a media of relative permittivity ϵ and relative permeability $\mu = 1$ in SI-units [48]

$$\text{div}\left(\vec{E}\right) = \frac{\rho}{\epsilon\epsilon_0} \quad , \qquad\qquad \vec{\nabla} \wedge \vec{E} = -\mu_0\frac{\partial\vec{H}}{\partial t} \quad ,$$

$$\text{div}\left(\vec{H}\right) = 0 \quad , \qquad\qquad \vec{\nabla} \wedge \vec{H} = \vec{j} + \epsilon\epsilon_0\frac{\partial\vec{E}}{\partial t} \quad ,$$

where ρ is the charge, $\vec{j}$ is the current and ϵ_0 and μ_0 are respectively the permittivity and permeability of vacuum.

In a media free of charges and currents, and expressing the harmonicity of the field in the form $e^{-i\omega t}$, ω being the angular frequency of the wave, these equations are written as:

$$\text{div}\left(\vec{E}\right) = 0 \quad , \qquad\qquad \vec{\nabla} \wedge \vec{E} = i\omega\mu_0\vec{H} \quad , \tag{1.1}$$

$$\text{div}\left(\vec{H}\right) = 0 \quad , \qquad\qquad \vec{\nabla} \wedge \vec{H} = -i\omega\epsilon\epsilon_0\vec{E} \quad . \tag{1.2}$$

Taking $\vec{\nabla}$ of the equation 1.2 and substituting the equation 1.1 leads to the wave equation for $\vec{H}$. Since $\vec{H}(x, y, t) = H_z(x, y, t)\vec{e}_z$ and due to the invariance along the z direction, all the terms in $\partial/\partial z$ are null and one obtains the Helmholtz equation

$$\frac{\partial^2 H_z}{\partial x^2} + \frac{\partial^2 H_z}{\partial y^2} + \mu_0\epsilon_0\epsilon\omega^2 H_z = 0 \quad . \tag{1.3}$$

The equation 1.2 projected on the directions x and y gives the expression of the electric field:

$$E_x = \frac{i}{\omega\epsilon\epsilon_0}\frac{\partial H_z}{\partial y} \quad , \tag{1.4}$$

$$E_y = -\frac{i}{\omega\epsilon\epsilon_0}\frac{\partial H_z}{\partial x} \tag{1.5}$$

as a function of the derivatives of H_z. The determination of the magnetic field H_z is thus enough to solve the EM problem.

To look for the solutions to the problem, the Helmholtz equation is written in the upper (+) and the lower (-) media. To relate the fields in both media separated by the interface S with a normal vector $\vec{n} = \vec{e}_y$, we also write the boundary conditions:

$$\vec{n} \wedge (\vec{E}^+ - \vec{E}^-) = 0 \quad , \tag{1.6}$$

$$\vec{n}.(\vec{D}^+ - \vec{D}^-) = \rho_s \quad , \tag{1.7}$$

$$\vec{n}.(\vec{B}^+ - \vec{B}^-) = 0 \quad , \tag{1.8}$$

$$\vec{n} \wedge (\vec{H}^+ - \vec{H}^-) = \vec{j}_s \quad , \tag{1.9}$$

where $\vec{D}^{\pm} = \epsilon^{\pm}\vec{E}^{\pm}$ is the electric displacement field and $\vec{B}^{\pm} = \mu\vec{H}^{\pm}$ is the magnetic field ($\mu = 1$), in the upper (+) and lower (-) medium respectively. ρ_s is the surfacic charge density and $\vec{j}_s$ is the surfacic current.

The equations 1.6 and 1.8 assure the continuity of the tangential electric field E_x and E_z as well as the one of the normal component of the magnetic field H_y. Without any external sources, the two other relations (1.7 and 1.9) become

$$\epsilon^+ E_y^+ = \epsilon^- E_y^- \quad , \tag{1.10}$$

$$\begin{cases} H_x^+ = H_x^- \quad , \\ H_z^+ = H_z^- \quad . \end{cases} \tag{1.11}$$

The boundary conditions in the TM polarization thus are:

$$H_z^+ = H_z^- \quad , \tag{1.12}$$

$$E_x^+ = E_x^- \quad \Leftrightarrow \quad \frac{1}{\epsilon^+}\frac{\partial H_z^+}{\partial y} = \frac{1}{\epsilon^-}\frac{\partial H_z^-}{\partial y} \quad . \tag{1.13}$$

We assume a solution of the form $H_z^{\pm}(x,y,t) = A^{\pm}e^{ik_x^{\pm}x+ik_y^{\pm}y}e^{-i\omega t}$ in the upper and lower media. In order to fulfill the boundary condition, equations 1.13 and 1.12, the solution must satisfy:

$$\frac{1}{\epsilon^+}k_y^+ = \frac{1}{\epsilon^-}k_y^- \quad . \tag{1.14}$$

The Helmholtz equation must also be satisfied in each media thus:

$$k_x^{\pm 2} + k_y^{\pm 2} = \epsilon^{\pm}k_0^2 = \epsilon^{\pm}\left(\frac{\omega}{c}\right)^2 \tag{1.15}$$

where $k_0 = \omega/c = 2\pi/\lambda$ is the wavevector and λ the wavelength of light in vacuum. The conservation of momentum parallel to the interface gives $k_x^+ = k_x^-$ and together with the relations 1.14 and 1.15, we have:

$$\epsilon^+ k_0^2 - k_x^{+2} = \left(\frac{\epsilon^+}{\epsilon^-}\right)^2\left(\epsilon^- k_0^2 - k_x^{+2}\right)$$

$$\left(\left(\frac{\epsilon^+}{\epsilon^-}\right)^2 - 1\right)k_x^{+2} = \left(\frac{\epsilon^{+2}}{\epsilon^-} - \epsilon^+\right)k_0^2$$

In the TM polarization, there is a solution for the EM field at an interface when the relation

$$k_x = k_0\sqrt{\frac{\epsilon^+\epsilon^-}{\epsilon^+ + \epsilon^-}} \tag{1.16}$$

is fulfilled. A similar demonstration in the TE case leads to no solution.

The solution is a propagative one if the real part of k_x is much greater than its complex part. Considering two non-lossy media where the values of the permittivity are real, k_x is real

if $\epsilon_+ > 0$ and $\epsilon_- > 0$ or if $\epsilon^+\epsilon^- < 0$ and $\epsilon^+ + \epsilon^- < 0$. To take into account the dependence of ϵ^- on ω, we introduce the Drude model for the permittivity of the metal $\epsilon^- = 1 - (\omega/\omega_p)^2$ where ω_p is the plasma frequency [49]. We also consider that the permittivity of the dielectric is not dispersive. The wavevector of an EM field which follows the dispersion equation 1.16, in this particular case, is real for two ranges of pulsation

$$\begin{cases} \omega > \omega_p & , \quad \epsilon^- > 0 \quad \text{and} \quad \epsilon^+ > 0 \\ \omega < \frac{\omega_p}{\sqrt{1+\epsilon^+}} & , \quad \epsilon^- < 0 \quad \text{and} \quad |\epsilon^-| > \epsilon^+ \end{cases}$$

which are represented in figure 1.8. The first condition (upper branch in figure 1.8) corresponds to the dispersion of the EM wave in the metal [49] whereas the second condition (lower branch) corresponds to the Surface Plasmon Polariton (SPP). From now on, we will focus on the latter.
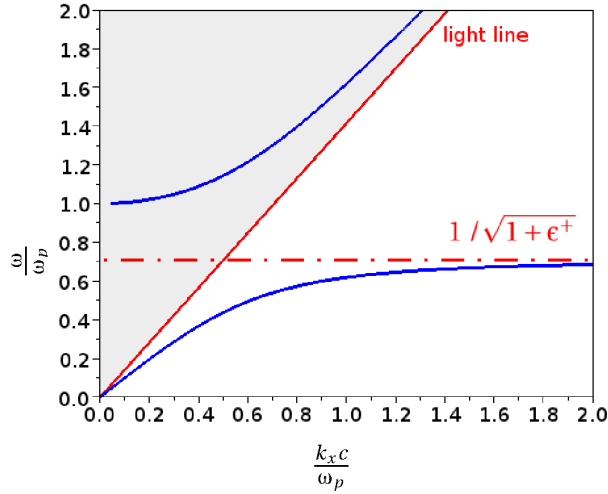
Figure 1.8: *Dispersion of the SPP: the wave angular frequency ω normalized by ω_p as a function of the wavevector k_x normalized by $\frac{\omega_p}{c}$, equation 1.16, considering a dielectric permittivity $\epsilon^+ = 1$ and a metallic permittivity $\epsilon^- = 1 - (\omega/\omega_p)^2$ (blue line). The light line (red line) and the asymptotic value $\omega = \omega_p/\sqrt{1+\epsilon^+}$ (red dashed line) are also given.*

1.2.2   The main characteristics of SPPs

We will now see the physics associated with the lower branch of the EM field dispersion at a metal/dielectric interface, represented in figure 1.8. This branch is under the light line, meaning that we have:

$$k_x^{\text{SPP}} > \sqrt{\epsilon^+}k_0 \quad \Rightarrow \left(k_y^{\text{SPP}}\right)^2 = \epsilon^+ k_0^2 - \left(k_x^{\text{SPP}}\right)^2 < 0 \quad .$$

Two important consequences can be seen from these relations. On the one hand, the SPP is not radiative and it thus cannot be excited by a propagating light (it is impossible to match

the momentum $\hbar k_x^{\text{SPP}}$ with the smaller one of the light $\hbar k_0$). On the other hand, this EM wave propagates along the interface (in the x direction) and is evanescent in the perpendicular direction (the y direction). Both facts are related as the more the SPP wavevector extends in the direction along the interface, the more it decays exponentially with distance away from it. The natural question that arises is what are the characteristic lengths of this wave bound to the interface? Including little losses in the model of the metallic surface i.e. describing the metallic permittivity with a real $\epsilon^{-'}$ and imaginary part $\epsilon^{-''}$ with $|\epsilon^{-''}| << |\epsilon^{-'}|$, the real part $k_x^{'}$ and the imaginary part $k_x^{''}$ of the SPP wavevector [50] read

$$k_x^{'} = k_0 \sqrt{\frac{\epsilon^+ \epsilon^{-'}}{\epsilon^+ + \epsilon^{-'}}} \quad , \qquad k_x^{''} = k_0 \frac{\epsilon^{-''}}{2(\epsilon^{-'})^2} \left(\frac{\epsilon^+ \epsilon^{-'}}{\epsilon^+ + \epsilon^{-'}} \right)^{\frac{3}{2}} \quad .$$

The SPP propagates along the interface with a propagation constant $k_x^{'}$ while $k_x^{''}$ is responsible for the damping of the SPP along its propagation. Its decay length $\delta_{\text{SPP}} = \frac{1}{k_x^{''}}$ is defined as being the distance traveled by the SPP when its intensity has decreased of a factor e. The decay lengths of the SPP perpendicular to the interface, in the metal and in the dielectric, are given by the value of $k_y^{\pm}$ such that

$$\delta^+ = \frac{1}{k_y^+} = \frac{1}{k_0} \left| \frac{\epsilon^+ + \epsilon^{-'}}{\epsilon^{+2}} \right|^{\frac{1}{2}} \quad , \qquad \delta^- = \frac{1}{k_y^-} = \frac{1}{k_0} \left| \frac{\epsilon^+ + \epsilon^{-'}}{\epsilon^{-'2}} \right|^{\frac{1}{2}} \quad .$$

For a semi-infinite metal and in the IR and visible spectral range, δ^-, the penetration depth of the SPP in the metal, follows the skin depth of the metal and δ^+, the characteristic decreasing length of the near field in the dielectric, follows the wavelength λ. The two lengths are illustrated in (b) in figure 1.9. A gold/air interface can typically support a SPP at $\lambda = 500$ nm with the characteristics $\lambda_{\text{SPP}} = 497$ nm, $\delta_{\text{SPP}} = 1\,\mu$m, $\delta^+ = 200$ nm and $\delta^- = 30$ nm. As we have seen, the SPP is a TM polarized EM wave bound to the interface, propagating along it and exponentially decreasing in its perpendicular direction.
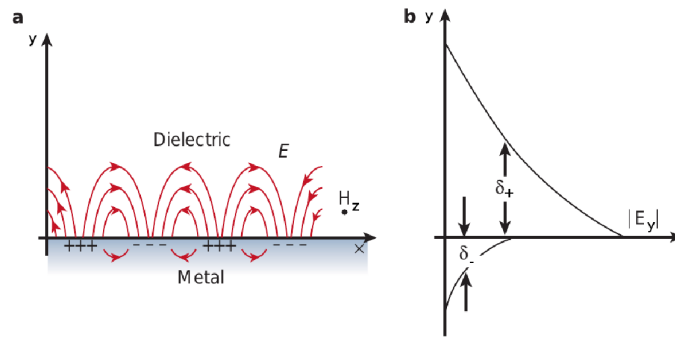
Figure 1.9: *Figure modified from [51]. (a) Electric field lines and charges associated with the SPP. (b) Representation of the penetration depth in the metal δ^- and in the dieletric δ^+ of the electric field E_y.*

19

This EM wave at the interface is associated with a collective oscillation of the free electrons at the surface of the metal as is represented in (a) in figure 1.9. Consequently, the Surface Plasmon Polariton is a hybrid mode between an EM propagative wave in the dielectric (a photon) and the collective oscillation of the free electrons in the metal (a plasmon). Hence the polaritonic nature of the mode results, by definition, from the coupling of a photon with a quasiparticule, here the plasmon. Depending on the angular frequency range (or equivalently the wavelength range), the nature of the mode is closer to one or the other component of the mode (photon/plasmon). The two competing behaviors are enlightened by the two red asymptotes of the SPP branch shown in figure 1.8. At low frequencies $\omega << \omega_p$, the SPP is more "light-like" ie the SPP dispersion is close to the light line (red line in figure 1.8). It corresponds to an optic behavior of the SPP where the retardation effects play a significant role. In this optical regime, the magnetic and electric field normalized by the incident field are comparable $|E/E_0| \sim |H/H_0|$ and the penetration depth of the SPP in the metal is of the order of magnitude of the skin depth of an EM wave at the same energy $\delta_- \sim \delta_s$. At higher frequencies, when the angular frequency ω reaches the asymptotic value of $\omega = \omega_p/\sqrt{1+\epsilon^+}$ (red dashed line in figure 1.8), the SPP wavevector k_x increases strongly. The SPP thus behaves in an electrostatic way where the group velocity of the electrons tends to zero and the retardation effects are negligible. The SPP is then more "electron wave like". In that case, the normalized electric field is much stronger than the normalized magnetic field $|E/E_0| >> |H/H_0|$ and the penetration depth in the metal is much smaller than the skin depth of an EM wave at the same energy $\delta_- << \delta_s$.

1.2.3   The optical excitation of SPP and the importance of gratings

In this section, we address the question of the excitation of a SPP, which is a non radiative wave as described in the previous section, by a plane wave. A plane wave which impinges on the interface with an angle of incidence θ can only excite a mode whose wavevector along the x direction matches $k_0 \sin\theta$. All the possible conditions of excitation of the system by a plane wave form the light cone (grey area in figure 1.8) and ranges from 0 to k_0 as θ ranges from 0 to 90°. As the wavevector of the SPP is greater than the one of light (white area in figure 1.8), the SPP dispersion is outside of this light cone and the plane wave cannot excite an SPP directly.

Otto was the first to propose an experimental set-up using a prism to couple light and SPPs [8]. His idea was to create an evanescent wave of wavevector k=n$k_0 \sin\theta$ at the back of a prism of refractive index n> 1, by the total reflection of the incoming light with an incident angle θ as shown in figure 1.10(a). The wavevector of the evanescent wave is increased compared to the initial plane wave one and enables one to excite a SPP on a metallic surface facing the prism at a distance less than the wavelength, i.e. at a distance smaller than the decay of the evanescent wave. The control of the relative positions of the prism and the metallic surface to create a gap of air was however difficult. Kretschmann proposed a more convenient set-up [9] which is however only suitable for thin films. The metallic thin film

is pressed against one side of the prism or is evaporated directly on the prism. The SPP is then excited on the side of the film which is not in contact with the prism as shown in figure 1.10(b), if the film is thin enough, typically of the order of magnitude of the skin depth. In both the Otto and the Kretschmann configurations, the matching condition for the excitation of SPPs is obtained when $k_x^{\text{SPP}} = k_0 n \sin\theta$.
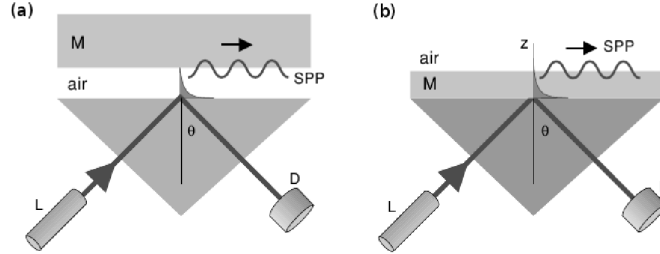
Figure 1.10: *Figures taken from [52]. Experimental set-up to excite SPPs in (a) the Otto configuration and in (b) the Kretschmann configuration. L is a laser and D a detector.*

Another way to increase the wavevector of the incident light is to use metallic gratings [50] whose periodicity d induces a pseudo momentum $\frac{2\pi}{d}m$ parallel to the interface, with m an integer as shown in figure 1.11(a). The momentum of light $k_0 \sin\theta$ (red arrow) adds up to the momentum of the grating $\frac{2\pi}{d}$ (blue arrow) to equal the momentum of the SPPs. More generally, each time the condition

$$k_x^{\text{SPP}} = \pm k_0 \sin\theta + \frac{2\pi}{d}m \qquad (1.17)$$

is satisfied, the incoming light excites a SPP mode. The dispersion branch of the SPP k_x^{SPP} (blue line in figure 1.11(a)) or $-k_x^{\text{SPP}}$ (green) translated by the momentum of the grating $\pm\frac{2\pi}{d}m$ forms a new branch of SPP modes. Each value of the integer m thus forms a different branch of the SPP modes represented by green and blue lines in figure 1.11(b). It is possible to excite the SPP modes whose dispersion branch is within the light cone. The modes which wavevector can, respectively cannot, be matched are represented in solid, respectively dashed, lines. The SPP modes which are excited by a plane wave impinging with a fixed angle of incidence θ, correspond to the intersection of the dispersion branch of the light and the one of the SPP mode, shown as dots in figure 1.11(b). These modes are called the mth order's surface mode $\text{SM}^{(\pm m)}$.

A particular emphasis must be put on the signature of the excitation of SPP modes by the incident EM wave in the reflectivity. When the incident plane wave impinges on the grating under the right conditions, it excites plasmonic resonances. The plasmonic mode propagates along the metallic surface which causes an energy loss in the metal. The stronger the field intensity is, the stronger the energy loss in the metal is. The loss of energy in the near-field due to a plasmonic mode excitation, is lacking in the far-field. Due to the excitation of a SPP mode, a dip appears in the reflectivity at the frequency of the SPP.

(a)

(b)
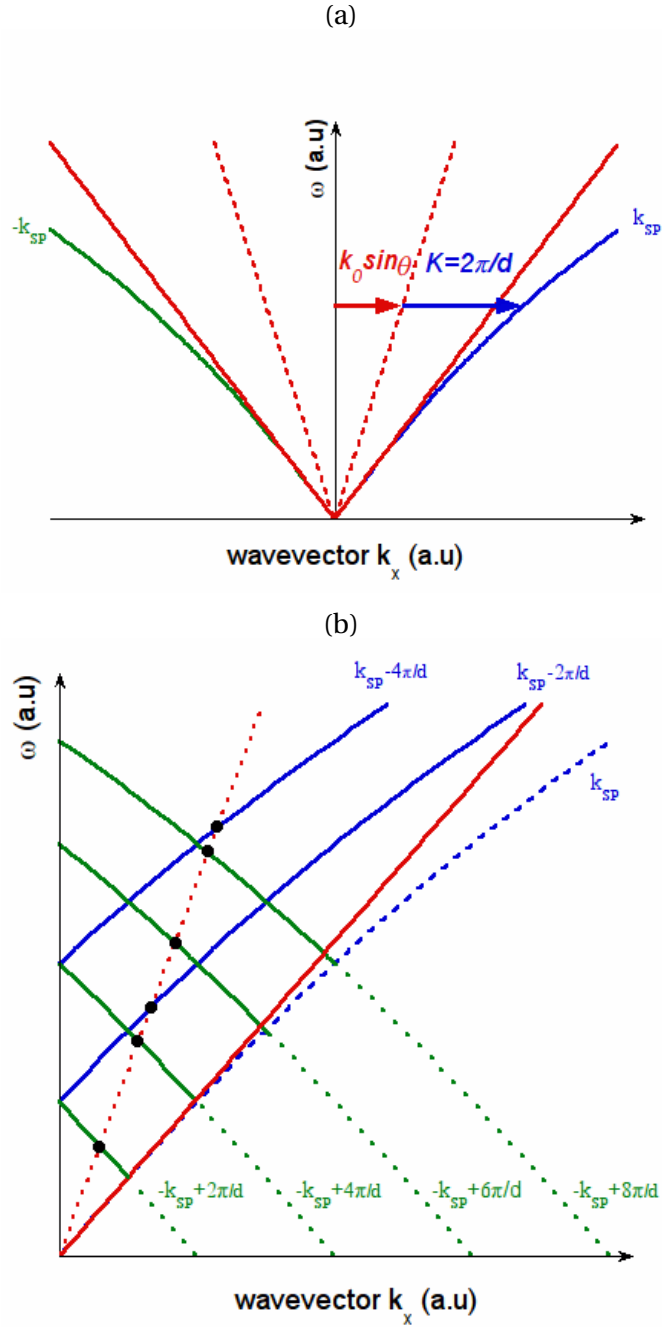
Figure 1.11: *(a) Dispersion curve, energy as a function of the wavevector parallel to the surface, of a non radiative SPP on a flat surface (blue and green lines). (a) and (b) The red curves represent the light line (solid line) and the dispersion curve of a plane wave impinging with an angle θ of pulsation ω (dashed line). (b) Dispersion curve of the SPP surface modes of a grating (blue and green lines). Modes which can be excited by TM polarized light are in solid lines whereas the modes which cannot are in dashed lines. The modes excited by a plane wave impinging with an angle θ of pulsation ω are indicated by black dots.*

We have seen in that section a key ingredient to the understanding of the enhancement of the Raman scattering of molecules close to a metallic surface: the surface plasmon polariton, an EM wave which is highly localized and propagates along the interface between a metal and a dielectric. We have presented different ways of exciting SPPs using a prism or periodic gratings. Other natural set-ups to excite SPPs, are metallic rough surfaces. Indeed, sub-wavelength defects scatter the incident light into evanescent waves with wavevectors larger than the one of light which are able to excite SPPs. However, the plasmonic modes on nano-scaled rough surfaces are in greater number than those excited on flat interfaces. We therefore take an interest in the rectangular groove gratings because they give an insight into the physics of rough surfaces while having resonances that can be studied and characterized in an easier way.

1.3 Optical properties of rectangular groove gratings as a model of rough surface

We have seen that metallic gratings, usually formed by grooves periodically spaced, are a kind of rough surface that can couple directly an incident plane wave and plasmonic surface modes. When the amplitude of the groove is of the order of magnitude of the wavelength of the incident EM field, an additional resonance appears which leads to the localization of the EM wave *inside* the groove itself. We will now focus on these resonances and investigate the specific conditions for which the grooves are able to localize EM waves . This is of particular interest as the ability of localizing the EM field into the rectangular groove grating can be a model explaining the hot-spots of SERS surfaces. We will address the question of the mechanisms which lead to the localization of the EM fields inside the groove.

Hessel and Oliner were the first to theoretically investigate EM resonances in such structures [11] and to predict that deep grooves gratings may support additional modes to the surface ones [1]. Their new modes consist in a Fabry-Perot-like resonance of a propagative EM wave guided in the groove. This resonance results in a stationary wave localized inside the groove which creates the enhancement of the EM field inside the grooves. Moreover, a dip in the reflectivity at the wavelength of the resonance is the signature of the EM mode in the far field [2]. In 1984, T. Lopez-Rios and A. Wirgin asked *Can surface-enhanced raman scattering be caused by waveguide resonances?* [39, 44] i.e. they discussed whether these modes in rectangular grooves could play a role in the SERS phenomena. Their proposition was that the rectangular grooves, with a width w < λ, may play the role of the crevices of the cold films. Other studies, among it the one by our team, followed [17, 18, 16]. Their principal results will be described in the rest of the chapter.

---

[1]The additional modes are TM and TE polarized if the width of the groove w> λ whereas they only exist in TM polarization if w< λ.

[2]These modes were first experimentally observed in 1998 [53]

Because of the specific geometry of the rectangular groove, we chose to calculate the optical response of the grating using the modal method. At the core of the modal method is the search of the eigenmodes of the grating and the expression of the magnetic field as a function of these eigenmodes. This method has been described in the thesis by the previous PhD student of our group [18]. We will give briefly in the next section a summary of the method as well as the obtained results on the optical properties of the sub-wavelength rectangular groove gratings.

1.3.1   The EM problem

To discuss the optical properties of the considered metallic gratings (figure 1.12), we focus on the following physical quantities: the reflectivity, the maps of intensity field and the enhancement factor of the fields. The reflectivity, which is an easily measurable quantity, enables to find the wavelength of resonance of the modes, at the location of the dip, and to compare the numerical calculation to the experimental data. The maps of intensity field allow us to identify the nature of the mode and the EF of the fields which gives an idea of the electromagnetic EF of possible SERS.
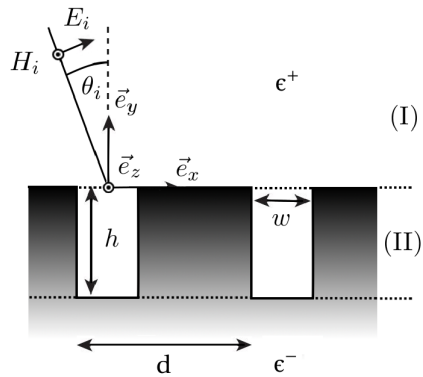
Figure 1.12: *Sketch of a grating of period d composed of rectangular grooves of width w and of height h. A TM polarized wave is incident on the grating with an angle* θ_i.

In TM polarization, the determination of the magnetic field H_z alone is enough, to obtain all these quantities, as the electric fields E_x and E_y are deduced from it with the Maxwell equations and the reflectivity is obtained from its far-field. To start with, we introduce the system under consideration: a grating of rectangular grooves of width w, height h and periodicity d, see figure 1.12, is excited by a TM polarized wave of wavelength λ impinging the surface at an incidence angle θ_i. We divide the space in three regions: the first one above the grating is the region (I), the second one in between the top and the bottom of the grooves is the region (II) and the last region, beneath the bottom of the groove, is not under scrutiny. In the region two, the system consist of alternative slices of metal and dielectric, in the x-

direction. The permittivity in the region (II) is therefore described as:

$$x \in \left[-\frac{w}{2}, \frac{w}{2} \right] \qquad\qquad\qquad \epsilon^{(II)} = \epsilon^+ \quad,$$

$$x \in \left[-\frac{d}{2}, -\frac{w}{2} \right[\cup \left] \frac{w}{2}, \frac{d}{2} \right] \qquad\qquad \epsilon^{(II)} = \epsilon^- \quad.$$

Now that the system has been presented, we are going to apply the modal method. First we express the fields as a sum of expansion functions which are different for each region. In the region (I), we use a Rayleigh expansion. In the region (II), the expansion functions for $H_z^{(II)}$ are chosen to be the eigenmodes of the groove. We then apply the continuity equations at the horizontal boundary between the region (I) and (II). The continuity equations are written as a function of the expanded fields in both region and are then projected on the expansion functions in order to obtain a set of equations. The numerical resolution of the system gives the magnetic field H_z in the whole space.

Let us give the general expression of the fields in the regions (I) and (II). In the region (I) defined as being the region above the grating, the field is expressed as a Rayleigh expansion

$$H_z^{(I)}(x, y) = e^{i k_0 (\gamma_0 x - \beta_0 y)} + \sum_{n=-\infty}^{+\infty} R_n e^{i k_0 (\gamma_n x + \beta_n y)} \tag{1.18}$$

with $\gamma_n = \sqrt{\epsilon^+} \left(sin(\theta_i) + n \frac{\lambda}{d} \right)$, $\beta_n^2 = \epsilon^+ - \gamma_n^2$ and R_n the amplitude of the plane wave in the direction $(k_0 \gamma_n, k_0 \beta_n)$.

Inside the grating (II), the field is first written as a modal expansion in each slice of media

$$x \in \left[-\frac{w}{2}, \frac{w}{2} \right] \qquad\qquad H_z^{(II)}(x, y) = \sum_{l=0}^{+\infty} F_l^+(x, y) \quad,$$

$$x \in \left[-\frac{d}{2}, -\frac{w}{2} \right[\cup \left] \frac{w}{2}, \frac{d}{2} \right] \qquad H_z^{(II)}(x, y) = \sum_{l=0}^{+\infty} F_l^-(x, y)$$

where $F_l^\pm(x, y)$ is the basis functions of the eigenmodes in the media of permittivity $\epsilon^\pm$. Without loss of generality, we suppose that there exists an infinity of modes and we index them with the integer l. Each media is contained in a rectangular shape and the basis function $F_l^\pm(x, y)$ can therefore be looked for using the separation of variables as $F_l^\pm(x, y) = X_l^\pm(x) Y_l^\pm(y)$. The mode fulfills the Helmholtz equation and thus $X_l^\pm$ and $Y_l^\pm$ relates in the same equation

$$Y_l^\pm(y) \frac{\partial^2 X_l^\pm}{\partial x^2}(x) + X_l^\pm(x) \frac{\partial^2 Y_l^\pm}{\partial y^2}(y) + \epsilon^\pm k_0^2 X_l^\pm(x) Y_l^\pm(y) = 0 \quad.$$

Hence,

$$\frac{1}{X_l^\pm(x)} \frac{\partial^2 X_l^\pm}{\partial x^2}(x) + \epsilon^\pm k_0^2 = -\frac{1}{Y_l^\pm(y)} \frac{\partial^2 Y_l^\pm}{\partial y^2}(y) \quad.$$

25

As x and y are independent variables, each side of the equality is a constant for the other. This constant will be called Λ_l^2 and the equations become

$$\begin{cases} -\frac{1}{Y_l(y)}\frac{\partial^2 Y_l}{\partial y^2}(y) = \Lambda_l^2 \quad , \\ \frac{1}{X_l^{\pm}(x)}\frac{\partial^2 X_l^{\pm}}{\partial x^2}(x) + \epsilon^{\pm}k_0^2 = \Lambda_l^2 \quad . \end{cases}$$

whose solutions are

$$Y_l(y) = A_l e^{i\Lambda_l y} + B_l e^{-i\Lambda_l y} \quad ,$$

$$x \in \left[-\frac{w}{2}, \frac{w}{2}\right] \qquad\qquad X_l^{+}(x) = C_l^{+} e^{ik_{l,x}^{+}x} + D_l^{+} e^{-ik_{l,x}^{+}x} \quad ,$$

$$x \in \left[-\frac{d}{2}, -\frac{w}{2}\right[\cup \left]\frac{w}{2}, \frac{d}{2}\right] \qquad X_l^{-}(x) = C_l^{-} e^{ik_{l,x}^{-}x} + D_l^{-} e^{-ik_{l,x}^{-}x} \quad .$$

with $k_{l,x}^{\pm}{}^2 + \Lambda_l^2 = \epsilon^{\pm}k_0^2$ and where A_l, B_l, $C_l^{\pm}$ and $D_l^{\pm}$ are complex constants for the determination of the amplitudes of the mode. The continuity equations are responsible for the continuity of the parallel wavevector Λ_l at the crossing of the horizontal boundaries x=± w/2 in the region (II). The magnetic field in the region (II) can thus be developed in each media of permittivity $\epsilon^{\pm}$ in the general form:

$$H_z^{(II)}(x, y) = \sum_{l=0}^{+\infty} X_l^{\pm}(x)\left(A_l e^{i\Lambda_l y} + B_l e^{-i\Lambda_l y}\right) \quad , \tag{1.19}$$

$$X_l^{\pm}(x) = C_l^{\pm} e^{ik_{l,x}^{\pm}x} + D_l^{\pm} e^{-ik_{l,x}^{\pm}x} \tag{1.20}$$

where $k_{l,x}^{\pm} = \sqrt{\epsilon^{\pm}k_0^2 - \Lambda_l^2}$.

The next step consists in finding the basis functions $X_l^{\pm}$ and the wavevectors Λ_l through the continuity equations of the magnetic field and its derivative. The continuity equations at $x = \pm w/2$ gives a set of complex non linear equations for Λ_l. In the visible spectral range, a study of the optical properties of the sub-wavelength groove gratings is reliable if the equations on Λ_l are solved in an exact way. This is a difficult task as it requires finding the wavevectors Λ_l which are the complex roots of complex non linear equations. In the IR spectral range, however, considering the vertical walls of the grating as being a perfect metal enables the simplification of the research of the eigenmodes. The approximation of surface impedance may also be applied for the horizontal metallic surfaces without compromising on the validity of the result. To begin with, we will describe this approximated modal method briefly and we will describe the exact modal method in the next section.

1.3.2 The approximated modal method

Here, we will first present the basics of the approximated modal method and then describe the EM resonances of metallic gratings excited in the IR spectral range.

1.3.2.1 Theory of the approximated modal method

In the infra-red, the metals are very good conductors i.e. the real part of the permittivity $\epsilon^{-'}$ is highly negative and the imaginary part $\epsilon^{-''}$ is negligible i.e. $\epsilon' << -1$ and $|\epsilon''| << |\epsilon'|$. In such good conductors, the magnetic field is almost zero ie $H_z^- \approx 0$. In accordance with the approximated continuity equations which will be given latter, the magnetic field H_z^+ in the dielectric may be solved without looking for the magnetic field H_z^- in the metal.

The first approximation of a good conductor is the approximation of surface impedance whose description is given in appendix in the section A.1. This approximation of surface impedance may be written as a condition of continuity at the boundaries for the fields in the dielectric, valid only for a point $\vec{r}$ which belongs to the interface S as:

$$\frac{\partial H_z^+}{\partial \vec{n}}(\vec{r}) - i\sqrt{\epsilon^+}k_0\xi H_z^+(\vec{r}) = 0 \tag{1.21}$$

where $\xi = \sqrt{\frac{\epsilon^+}{\epsilon^-}}$ and $\vec{n}$ is the vector normal to the surface. We will note $k^\pm = \sqrt{\epsilon^\pm}k_0$.

A second approximation of a good conductor is the perfect metal. The perfect metal is the limit of a very good conductor: it is supposed to have no losses, $\epsilon'' = 0$, and its permittivity tends to be a highly negative value, $\epsilon' = -\infty$. Substituting the permittivity of the perfect metal by $\epsilon^- = -\infty$ in the previous continuity equation ($\xi = 0$ in the equation 1.21) yields the continuity equation of the perfect metal

$$\forall \vec{r} \in S \qquad \frac{\partial H_z^+}{\partial \vec{n}}(\vec{r}) = 0 \quad . \tag{1.22}$$

The next step of the resolution is to determine the function basis of the eigenmodes of $H_z^{(II)}$. The vertical metallic walls are considered as being a perfect metal and the response of the horizontal metallic wall at the bottom of the groove is modeled by the surface impedance approximation. Due to this choice of boundaries for the dielectric slice in the region (II), there is no need to consider the magnetic field in the metal and we look for $H_z^{(II)}$ in the dielectric only. These approximations were proven experimentally to be valid in the infra-red spectral range [16, 54]. By applying the equation 1.22 at the vertical walls x=±w/2, we obtain

$$\forall y \in [-h,0] \qquad \left(\frac{\partial H_z^{II}}{\partial y}\right)_{x=\pm\frac{w}{2}} = 0$$

which gives

$$X_l^+(x) = \cos\left(\frac{l\pi}{w}\left(\frac{w}{2}+x\right)\right)$$

and $k_{l,x}^+ = \frac{l\pi}{w}$.

The approximation of surface impedance, equation 1.21, will be applied at the bottom of the groove such that the horizontal boundary condition becomes

$$\forall x \in \left[-\frac{w}{2},\frac{w}{2}\right] \qquad \left(\frac{\partial H_z^{II}}{\partial y}\right)(x,-h) = ik^+\xi H_z^+(x,-h)$$

and gives

$$B_l = r_l A_l \qquad \text{where} \qquad r_l = \frac{\Lambda_l + k^+ \xi}{\Lambda_l - k^+ \xi} e^{-2i\Lambda_l h} \quad .$$

The lth eigenmodes of the cavity is thus described by its function basis :

$$\cos\left(\frac{l\pi}{w}\left(\frac{w}{2} + x\right)\right)\left(e^{i\Lambda_l y} + r_l e^{-i\Lambda_l y}\right)$$

where Λ_l is its wavevector along the y axis and satisfies $\Lambda_l^2 + \left(\frac{l\pi}{w}\right)^2 = \epsilon^+ k_0^2$. The magnetic field in the dielectric cavity in the region (II) is then

$$x \in \left[-\frac{w}{2}, \frac{w}{2}\right] \qquad H_z^{II}(x,y) = \sum_{l=0}^{\infty} A_l \cos\left(\frac{l\pi}{w}\left(\frac{w}{2} + x\right)\right)\left(e^{i\Lambda_l y} + r_l e^{-i\Lambda_l y}\right) \qquad (1.23)$$

where A_l is the complex amplitude of the lth mode.

Now that H_z has been expressed in both region, we must apply the conditions of its continuity at the interface between the two media. At the top of the groove where there is no change of media, there is a simple continuity of the field and of its derivative. Therefore we get:

$$\forall x \in \left[-\frac{w}{2}; \frac{w}{2}\right] \qquad\qquad\qquad\qquad H_z^{(I)}(x,0) = H_z^{(II)}(x,0) \quad , \qquad (1.24)$$

$$\forall x \in \left[-\frac{w}{2}; \frac{w}{2}\right] \qquad \frac{\partial H_z^{(I)}}{\partial y}(x,0) - i k^+ \xi H_z^{(I)}(x,0) = \frac{\partial H_z^{(II)}}{\partial y}(x,0) - i k^+ \xi H_z^{(II)}(x,0) \quad . \qquad (1.25)$$

Outside of these points, there is a metal/dielectric interface and the continuity equations with the surface impedance approximation are applied:

$$\forall x \in \left[-\frac{d}{2}, -\frac{w}{2}\right[\cup \left]\frac{w}{2}, \frac{d}{2}\right] \qquad \frac{\partial H_z^{(I)}}{\partial y}(x,0) - i k^+ \xi H_z^{(I)}(x,0) = 0 \quad . \qquad (1.26)$$

This set of equations projected on the basis functions of (I) and (II) leads to a matrix system whose resolution permits us to calculate the A_l and R_n terms [18]. With those quantities, both the near and the far field can be deduced and the problem is solved. The numerical implementation is described in the section A.2.

The $m^t h$ order of the reflectivity is directly deduced to be $\frac{\beta_m}{\beta_0}|R_m|^2$ when β_m is real. The magnetic and electric fields have to be recomposed by summing all the function bases in the region (I) or all the modes in the region (II). In the groove, the determination of the fundamental mode, whose amplitude is A_0, gives already a good approximation of the total field since it is the only propagating wave when $w < \lambda$. The study of the eigenmodes calculated by the approximated modal method show the existence of EM resonances in the grooves, which we will call cavity mode, additionally to the surface ones.

1.3.2.2 Electromagnetic resonances of the gratings

We will focus our attention on the cavity modes of the gratings as they are the ones which localize the EM fields in a sub-wavelength volume and are pertinent in our search of a better understanding of SERS. In TM polarization and for sub-wavelength grooves ($w < \lambda$), it is only possible to excite one guided mode in the grooves in the direction $\vec{e}_y$ with a wavevector Λ_0 for which $\Lambda_0^2 > 0$. This unique guided mode is the fundamental mode and the higher order modes are evanescent $\Lambda_{l>0}^2 < 0$. Due to the evanescence of the higher order modes, the field in the groove is very well approximated by considering only the unique guided mode Λ_0. This is the unimodal approximation. In the perfect metal case and for an isolated groove ($w << d < \lambda$) it is easy to show that the amplitude of the fundamental mode A_0 is inversely proportional to $\cot(k_0\sqrt{\epsilon^+}h)$ ie that it diverges for $k_0\sqrt{\epsilon^+}h = (2m-1)\pi/2$ [13, 55]. The fundamental mode thus has the same resonance condition as a Fabry-Perot resonance

$$\frac{1}{\lambda} = \frac{2m-1}{4h\sqrt{\epsilon^+}} \qquad \forall m \in \mathbb{N} \tag{1.27}$$

where λ is the wavelength of the incident plane wave. These modes will be called the mth order's SPP cavity mode, noted $CM^{(m)}$, to differentiate them from the SPP mode at the surface of the grating, noted $SM^{(\pm m)}$. The finite height groove acts as a Fabry Perot resonator for the EM guided wave in the groove and a stationary wave is thus established when the equation 1.27 is satisfied. One very important point is the fact that the wavelength of the incident wave λ at the resonance is of the order of 4h. The other important point is that the cavity mode resonance does not depend on the angle of incidence and is non-dispersive.

In order to go deeper into the understanding of these modes, we will now investigate the example of a gold grating of period d=1.75 µm with rectangular grooves of width w=0.75 µm and height h=1.11 µm illuminated by a TM polarized plane wave impinging with an angle $\theta_i = 20°$. In the spectral range considered, the light wavelength ranges from 1 to 9 µm, which is larger than the width of the groove (0.75 µm) and of the order of magnitude of the height (1.11 µm). A more complete study of the EM resonances of this grating is presented in [12]. In the considered spectral range, three modes appear in the theoretical reflectivity spectra calculated by the approximated modal method (red line) whereas only two are visible in the experimental specular reflectivity (blue line) as shown in figure 1.13.

First of all, a first cavity mode $CM^{(1)}$ is expected at $4h \sim 4.4\mu$ m ~ 2300cm^{-1}, which corresponds to m=1 in the equation 1.27 and is observed as a dip at 2030cm^{-1} in figure 1.13. The calculated EM field modulus maps at this resonance frequency are shown in the left column in figure 1.14. The magnetic field modulus map, figure 1.14(a), is consistent with a Fabry Perot mode since the field is localized in the sub-wavelength groove. The magnetic field is maximum at the bottom of the groove whereas the electric field $|E_x|$, figure 1.14(c), is maximum at the top of the groove. The electric field $|E_y|$, figure 1.14(e), is negligible inside the groove as the magnetic field is invariant in the x direction. The dip in the calculated reflectivity associated with the cavity mode is underestimated in the approximated modal
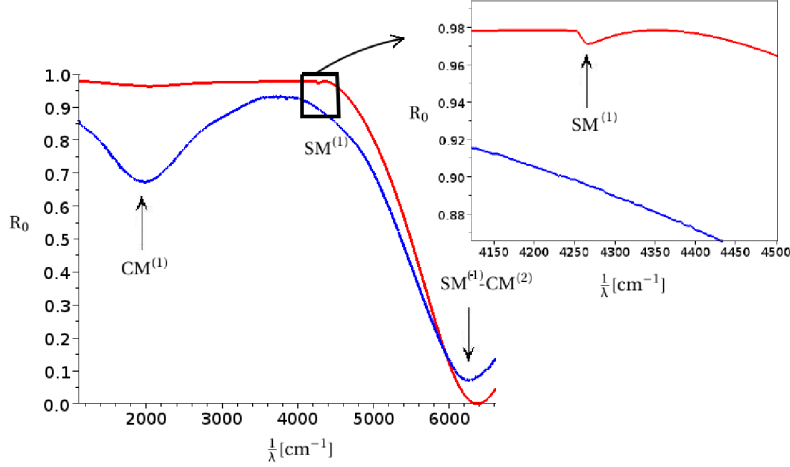
Figure 1.13: *The specular reflectivity measured on a gold grating of period d=1.75 μm with rectangular grooves of width w=0.75 μm and height h=1.11 μm excited by a TM polarized wave impinging at an incident angle $\theta_i = 20°$ (blue) and theoretical spectra calculated by the approximated modal method (red). Experimental example taken from [12]. The inset shows a zoom at 4250 to 4500 cm^{-1}.*

method with respect to the experimental one since no damping of the EM guided mode is taken into account along the metallic vertical walls considered as perfect, only the damping at the bottom of the groove is.

A surface mode $SM^{(1)}$ is expected at $d(1-\sin(20°)) \sim 2.35\mu$ m $\sim 4255cm^{-1}$ which corresponds to m=1 in the equation 1.17. The dip in the reflectivity is too small to be measured experimentally although it can be seen in the theoretical one at $4255cm^{-1}$. The calculated EM field modulus maps at this resonance frequency are shown in the right column in figure 1.14. The magnetic field, shown in figure 1.14(b), is bound to the surface where it shows oscillations.

Eventually a third mode is seen at 6250 cm^{-1} whose resonance is close to the second order cavity mode CM^2, its energy being three times the one of the first cavity mode ($6900cm^{-1}$ with m=1 in the equation 1.27). The EM field maps of the mode show, however, that the mode is a hybrid mode between the second cavity mode and a surfacic one $SM^{(-1)}$.

Gratings with sub-wavelength aperture rectangular groove show EM guided mode resonances for grooves sufficiently deep ($\lambda \sim 4h$). These cavity modes are able to localize the EM field in a sub-wavelength sized groove. This is why such gratings are a first step in the modeling of SERS surfaces. However there are still unresolved questions when we compare these EM resonances with the observations made on cold films. For instance, the calculated enhancement of the electric field in the grooves is too weak to explain the SERS electromagnetic EF and the height of the groove is of the order of magnitude of the resonance wavelength when the scaling relation 1.27 is fulfilled, i.e. a few hundreds of nanometers in the
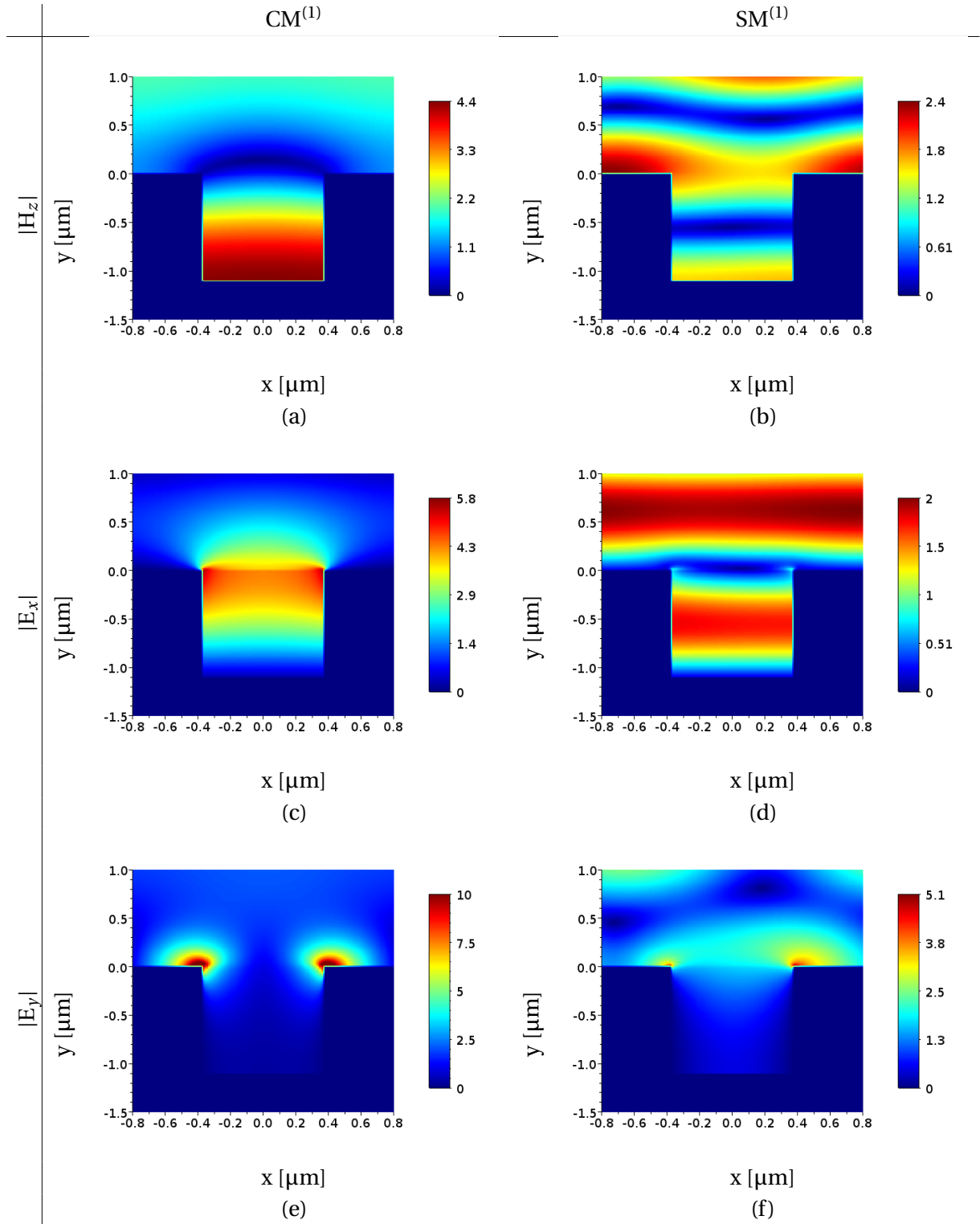
Figure 1.14: *Calculated EM field modulus maps of the first cavity mode CM*$^{(1)}$ *(left column) and the surface mode SM*$^{(1)}$ *(right column) for a gold grating of period d=1.75 µm with rectangular grooves of width w=0.75 µm and height h=1.11 µm illuminated by a TM polarized plane wave with an incident angle* $\theta_i = 20°$. *|H$_z$| is (a) and (b), |E$_x$z| is (c) and (d) and |E$_y$| is (e) and (f).*

visible, which is much bigger than the scale of the roughness of the coldly evaporated films.

1.3.3 The exact modal method

As mentioned previously, the cold films have an abnormal optical absorption in the visible. Therefore the study of the sub-wavelength groove gratings is widened in that particular spectral range, the visible. The metals are good reflectors in the IR spectral range but their behavior in the visible spectral range changes drastically because of the existence of interband electron transitions (in the band diagram of the energy density of states of the electrons). In the higher energies of the visible spectral range, the conductivity of the metal is lower and it can be accompanied by a very strong damping (p.293 [56]). In the visible, the real part of the metal permittivity $\epsilon^{-'}$ ranges between -30 and -5 and the ratio with its imaginary part $|\epsilon^{-''}/\epsilon^{-'}|$ increases when the wavelength decreases, especially for gold. Due to the good conductivity of metals in the IR, the sub-wavelength groove gratings have been studied with approximated boundary conditions which were justified. These approximations are not valid in the visible spectral range anymore. In the visible, an exact modal method must therefore be used which makes the calculations much more difficult to handle. In particular, the determination of the wavevectors Λ_l, the complex roots of a non-linear complex equation have to be supervised manually and the function basis $X_l^{\pm}$ in the expression pf $H_z^{(II)}$, equation 1.20, are non orthogonals. The theoretical study of the modal method applied to metallic gratings has been performed by the groups of Sheng [57], Botten, Craig, McPhedran, Adams, and Andrewartha [58, 59, 60, 61, 62, 63, 64], Suratteau Cadilhac and Petit [65] and, Tayeb and Petit [66]. The method is not presented here but is detailed in J. Le Perchec's thesis [18] and references therein.

1.3.3.1 The numerical results of the exact modal method

The application of the exact modal method to nano-scaled metallic groove gratings [18, 17] shows for the first time that it is possible to excite an EM resonance in the visible spectral range in rectangular grooves of height h << ($\lambda/4 \sim 100$ nm). We reproduce here, in figure 1.15, the results of a numerical calculations for gratings made of silver with a period d=30 nm and rectangular grooves of width w=5 nm and of height h ranging between 8 and 30 nm. The dips in the specular reflectivity, as shown in figure 1.15(d), points out the existence of EM resonances for these gratings when they are illuminated by visible light. In the case of the grating with a groove depth of height h=15 nm, the calculation shows that at the resonance energy E=2.6 eV, the spectra of the magnetic field intensity at the bottom of the groove exhibit a maxima, as shown in figure 1.15(a) as well as the spectra of the electric field at the top of the groove, as shown in figure 1.15(b). The map of the magnetic field modulus calculated at this resonance is shown in figure 1.15(a) and confirms that the mode is a Fabry-Perot like one. Moreover, we note that the electric field intensity at the aperture of the groove, in figure
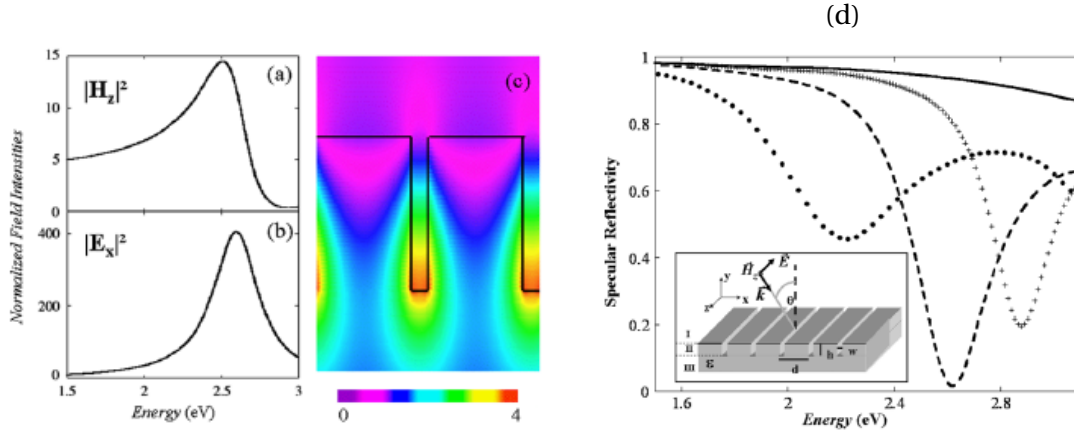
Figure 1.15: *Figures taken from [18] calculated by the exact modal method. The gratings are all made of silver with a period d=30 nm and rectangular grooves of width w=5 nm. Normalized intensities of the magnetic (resp. electric) field at the bottom (resp. aperture) of the groove (a) resp. (b) and normalized modulus magnetic field maps at resonance (2.6 eV) (c) for a groove height of h=15 nm. Specular reflectivity for three gratings with grooves height h of 8 (crosses), 15 (dashed line) and 30 nm (dots). The incidence angle θ_i=0°. Inset of (d) presents the geometry and the grating.*

1.15(b), has an intensity $|E|^2 \sim 400$ about 25 times larger than the magnetic field intensity at resonance.

It all adds up to show that metallic gratings may exhibit a Fabry Perot-like EM mode in the visible spectral range, able to localize the fields in a groove of width w~ λ/100 and of height h~ λ/30 and which are associated with high EF for the electric field. The question that arises is what mechanisms can explain such Fabry-Perot resonance of a groove of height h=15 nm excited by a wave of wavlength $\lambda \approx 500$ nm instead of the expected $\lambda_{FP} \sim 4h = 60$ nm?

In order to have a deep understanding of this phenomena we have to look further into the cavity modes. We have seen that a dielectric channel of sub-wavelength width in between two perfect metal walls guides an EM mode in the direction parallel to the walls. If we consider a real metal instead of perfect metal, the EM mode is built by the out of phase coupling of two SPPs propagating along each vertical wall of the groove, see figure 1.16.

Because the SPPs are bound to the surface, i.e. evanescent in the perpendicular direction to the walls, the EM field can be confined in a sub-wavelength volume. As mentioned previously, in the visible range, the behavior of SPPs on a single metal/dielectric interface is light-like which means that their wavevector in the direction of propagation is close to the one of light ie $\Lambda_0 \sim k_0\sqrt{\epsilon^+}$. The decaying length of the SPPs away from the wall in the dielectric is of the order of magnitude at the wavelength which is why the SPPs on each side of the sub-wavelength groove ($w < \lambda$) interact and make a guided mode. If the width of the cavity

33
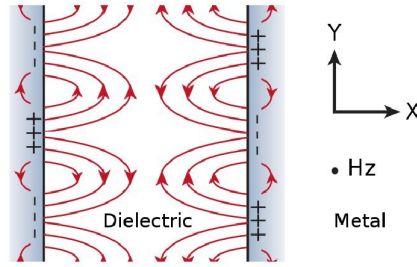
Figure 1.16: *Sketch of the electric field lines of the EM guided mode built by the coupling of the two SPP and the associated charge density (+) and (-) inside the grooves of a metallic grating*

is not too small (the meaning of not too small will be detailed later), the coupling of the two SPPs is weak and the guided mode is also light-like. The SPPs propagate in the direction parallel to the vertical walls towards the bottom of the groove. They are reflected at the bottom of the metallic groove where their phases are shifted of a value close to π (it is exactly π in the case of the perfect metal). A stationary wave is established in the groove if the phase of the SPPs during a back and forth route $\Lambda_0 h + \pi + \Lambda_0 h$ is equal to 2π ie $\Lambda_0 h = \pi/2$. We have, therefore, a Fabry-Perot type resonance $\lambda \sim 4h$. The light-like coupled SPPs channeled in the groove have a resonance in what we will call the **optical regime**.
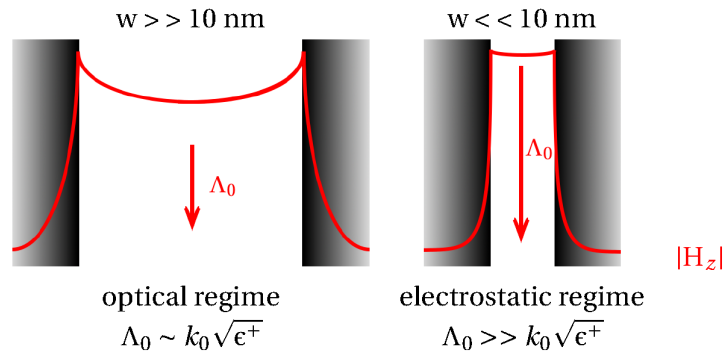
Figure 1.17: *Sketch of the SPP guided mode magnetic field in the optical regime (left) and electrostatic regime (right).*

We have seen that for very tiny grooves, there also exists a guided mode whose physics is totally different. The magnetic field channeled in the groove, sketched in figure 1.17, is confined differently as a function of the width of the cavity. In the optical regime the SPP guided mode is spatially limited by the skin depth of the metal due to the repulsion of the EM wave away from it. When the width of the groove decreases and becomes smaller than the skin depth of the metal (of the order of 20-30 nm), it also becomes the new spatial limitation for the SPP guided mode and therefore drives the physics. Indeed when the width of the groove decreases, the SPPs on each side of the groove have a stronger interaction. The strong coupling of the two SPPs is responsible for an increase of the modulus of the wavevector Λ_0.

34

And for widths lower than 10 nm for silver, the wavevector is not proportional to k_0 anymore but follows

$$\Lambda_0 = \frac{2}{w|\epsilon^-|} \quad .$$

The combined effects of the decrease of the metal permittivity $|\epsilon^-|$ in the visible range and the very narrow grooves permit the existence of an SPP guided mode whose wavevector becomes much bigger than the one of the exciting light, $\Lambda_0 >> k_0\sqrt{\epsilon^+}$. We have seen that for huge wavevectors the SPP on a flat surface is more "electron wave-like". In a similar way, the mode therefore enters in an **electrostatic regime**. There exist two main consequences for the cavity mode to have a huge wavevector Λ_0. The first one is that the Fabry Perot like resonance of the SPP guided mode happens for grooves of height h ~ $\pi/2\Lambda_0 << \lambda/4$. It explains why grooves of dimensions of 5 nm by 10 nm can resonate in the visible. The second consequence of an electrostatic SPP guided mode is that the electric field, associated with the oscillation of the charge density with a very small period, is huge. The electric field in the groove is therefore enhanced greatly.
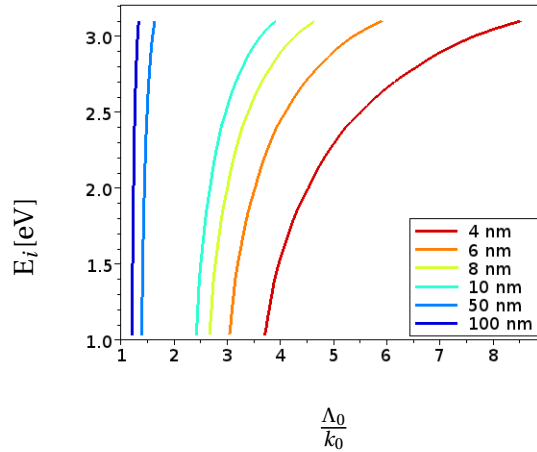
Figure 1.18: *Dispersion of the SPP guided mode in the groove ie plot of the incident wave energy* $E_i = \hbar k_0$ *as a function of the wavevector* Λ_0 *in the y direction of the SPP guided mode, normalized by the wavevector of light in vacuum, for different width w of the groove (4 to 100 nm) and considering a silver grating (in air).*

Two asymptotic regimes have been differentiated. For large widths the SPP guided mode resembles the flat surface SPPs: it is the optical regime. For small widths, the SPP guided mode is strongly confined and enters in the electrostatic regime. The two behaviors are illustrated in figure 1.18 where the energy of the mode is plotted against the SPP guided mode wavevector Λ_0 normalized by the wavevector of light k_0. One may observe at a fixed energy that for large widths (50-100 nm) the variation of the width of 50 nm results in a little change of Λ_0 with respect to k_0 and the ratio Λ_0/k_0 is close to one. For small width (w<10

35

nm) however, a decrease of the width results in a much stronger increase of Λ_0 and the ratio Λ_0/k_0 becomes much bigger than 1. A divergence in the dispersion curve happens at lower wavelengths because of the decrease of the permittivity in silver.

These results are very close to the observations made on cold films and prove that the SERS phenomena may indeed be caused by the plasmonic resonances induced in very little cavities formed by the roughness of the metallic surface. To extend the study to more complex shapes of grooves, one cannot apply the modal method as it is restricted to the rectangular groove. Therefore, more general methods have to be investigated.

1.4   conclusion

In this chapter, we have described two interesting phenomena associated with cold films illuminated by EM wavesin the visible spectral range: the Surface Enhanced Raman Scattering, and the Abnormal Optical Absorption. It was stressed that both phenomena are related, since the SERS, the AOA and the roughness of cold films disappear simultaneously when the films are warmed up at room temperature. The surface of the cold films, albeit difficult to characterize experimentally, shows deep crevices whose widths are less than 5 nm and separated by 5 to 30 nm.

The work of our group aims at understanding the mechanism triggering the optical properties of such metallic surfaces with defects of sizes much smaller than the wavelength. The plasmonic resonances of metallic gratings with grooves of sub-wavelength dimensions are studied for that purpose. We first described the surface plasmon polaritons and, second, the resonances of the grooves. A particular emphasis was put on these cavity modes, for which a standing wave is established inside the groove at the resonance frequency, and thus localizes the EM field into a sub-wavelength volume. Moreover, the EM field in the cavities are larger than that of the incident field.

An introduction to the modal method was given since it was chosen by our group for its relevance to study rectangular groove metallic gratings. An exact modal method was necessary to treat gratings with rectangular grooves whose dimensions match the realistic size of the cold films and was thus developed in our group. It was shown that the cavity modes is built by the coupling of the SPP belonging either to the optical or to the electrostatic regime depending on the width of the rectangular groove. The resonance of the smaller grooves has electrostatic chracteristics: the wavevector of the guided surface plasmon wave and the electric field are greatly enhanced compared to the one of larger grooves. Tiny grooves of heights of an order of magnitude of ten nanometers can thus exhibit resonances in the visible. Moreover, the enhancement factors of the electric field at resonance is comparable to the ones that lead to SERS.

Hence, we aim at studying surfaces with very small grooves (of widths smaller than 10 nm for silver for instance), similar to the surfaces of cold films with deep crevices. The next

step for a quantitative estimation of SERS EF and for the qualitative understanding of the mechanisms of SERS, is to study surfaces with more complex shapes than the rectangular grooves in order to model in a more realistic way the topography of rough surfaces. The integral equation method has the flexibility needed for such studies and is presented in the next chapter.

Chapter 2

The surface integral equations method

In this chapter, we describe the method we used to calculate the harmonic EM field in TM polarization near a metallic grating of arbitrary shaped grooves with dimensions as small as $\frac{\lambda}{100}$. The Surface Integral Equation (SIE) method was chosen to solve the Maxwell equation and a few advantages of the method are given to justify this choice. The Green functions are a key ingredient of the method and are fully detailed. The numerical implementation of the equations have been done in C++ and is explained as well as how to retrieve the physical quantities such as the field intensity maps and the reflectivity. Eventually a few examples are given in order to prove the correct implementation of the method.

2.1 State of the art on the modeling of rough metallic surfaces by the surface integral equations

We want to study the EM near-field for large enough surfaces with very small defects in order to model as correctly as possible the surfaces of cold films. In the framework of this thesis, we will perform our study in the visible spectral range, $\lambda \approx 400 - 800$ nm and the roughness will be of $1 - 10$ nm so one to two orders of magnitude smaller than the visible wavelengths. The method we choose must be able to handle a large range of sizes, be accurate and be reliable. The numerical techniques to solve Maxwell's equation are numerous [67] and may be divided in two main categories [68]

- the methods which express Maxwell's equations as integrals such as the Method of Moment [69], the Discrete Dipole Approximation [70] or the Multiple MultiPole method [71].

- the methods which solve directly the Maxwell partial equations. Among the direct-space methods, we may cite the Finite Difference Time-Domain or Frequency-Domain method, Finite Element Method or the Discontinuous Galerkin method [72]. Part of

the differential methods are transposed into the Fourier space such as the differential method in the Fourier space [73, 74], the coupled wave method [75, 76] and the C method [77].

The first category has been used preferentially to solve problems of rough metallic surfaces. One of the main advantage of using integral equations is that the problem of finding the EM field in the volume can be reduced to finding it on the boundaries, thus on the surface under study. A very good history of Boundary Integral Equations is given in [78]. It includes short biographies (and portraits) of all the great men that contributed to it. From Laplace and Poisson who contributed to the potential theory, to Green, Ostrogradsky and Strokes who presented the fundamental theorems which allow one to go from a 3D problem to a 2D one. It does not forget the mathematicians who worked on integral equations such as Cauchy, Hadamard and Fredholm as well as the physicists who extended Green's formula, designed for electrostatics, to other fields (such as acoustics, mechanics...) as Helmholtz, Betti or Lord kelvin and Lord Rayleigh.

The calculation of the EM field near rough surfaces has been made possible only very recently with the developpement of exact formalisms. The history and the issues of the calculation of the EM field close to rough surfaces is merged with the one of metallic gratings whose periodic modulation of the surface amplitude plays the role of the roughness. At the beginning of the 20th century, it was already known that diffraction gratings, whose surface profiles have dimensions of the order of magnitude of the wavelength, separate the incident white light into a continuum spectrum. Each spectral component is diffracted at a different angle. The observations of dark and bright bands in the reflectivity spectra depending on the polarization of the incident light illuminating a metallic grating by Wood in 1902 was, however, unexpected [1], and much attention was drawn to such metallic gratings. Lord Rayleigh was a pioneer in the modeling of such gratings and did so by using the so-called Rayleigh hypothesis. The surface integral equation can be simplified with the Rayleigh hypothesis in the same way the modal method is simplified with the surface impedance approximation and the next paragraph considers it.

2.1.1   The Rayleigh hypothesis: almost a century long debate

The Rayleigh hypothesis is of crucial importance in the theory of gratings and therefore its validity was discussed a lot, and still is. It was recently the subject of a whole chapter in the book *Light Scattering and Nanoscale Surface Roughness* [79]. In its paper of 1907 [2], Rayleigh expands the field as a sum of upwards propagating waves, particularly on the boundary of a shallow grating, without a proof. The scattered field would then be

$$u^s(x, y) = \sum_{m=-\infty}^{+\infty} R_m e^{ik_0(\gamma_m x + \beta_m y)} \tag{2.1}$$

with $\gamma_m = \sqrt{\epsilon^+}\left(\sin(\theta_i) + m\frac{\lambda}{d}\right)$ and $\beta_m^2 = 1 - \gamma_m^2$. An integral replaces the sum in the case of the non-periodic space.
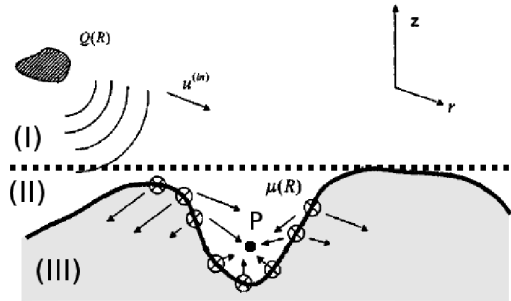
Figure 2.1: *Sketch modified from [79] to illustrate the Rayleigh hypothesis debate. The sources μ on the surface are represented by crosses in dots and the propagating fields by arrows.*

This is why writing any wave as a sum of outgoing waves is called a Rayleigh expansion. While the expansion above the grating, i.e. above the upper ordinate of the grating profile which is the region (I) in figure 2.1, is exact, there was a strong argument about its validity below the upper ordinate which is region (II). Using the Rayleigh expansion in the region (II) was therefore called the Rayleigh hypothesis. The first protest against that practice came many years later from Lippmann [80] as a "Note on the Theory of Gratings" and his remark is still pertinent for an infinite non-periodic surface. The expansion inside the grooves (II) seemed physically wrong to him. He argued that any point inside the groove will receive waves propagating downwards after a reflection on the sides of the grating. In a more general way, the magnetic field at any point of space is the result of the propagation of the field from the source point as well as from the boundaries of the space which act as source points. It is schematically represented in figure 2.1: a point P situated inside the groove will receive waves propagating down and upward from the sources μ on the boundaries. Of course the field in a groove may be written as a sum of upward and downward propagating waves, the issue here is whether it is the unique expression of the field or whether the downward propagating waves may be expressed as upward ones.

A strong debate commenced on whether the field expanded in series with the Rayleigh hypothesis was convergent. Petit and Cadilhac gave a proof that the sum was divergent for sinusoidal grating with a slope $h/d > 0.448/(2\pi)$ [81, 82]. Others however believed in the fact that the Rayleigh assumption was always true. Three years later, Millar proved the validity of the Rayleigh assumption for $h/d < 0.448/(2\pi)$ i.e. that the sum was convergent for all points above the grating [83]. A review summing up the subject may be found in [84]. Sometimes, contradictory results were given. As explained in [85], the Rayleigh assumption has to be differentiated with its application in various methods of resolution which depends on the weighting function used to project the field (the point matching method is equivalent to the choice of the Dirac function as a weighting function for instance). This is why the Rayleigh assumption gave an accurate result according to some and failed according to others. Eventually, the debate seems to have been settled in favor of the Rayleigh hypothesis. Theoretical

proofs were given [79] as well as successful numerical proofs of the convergence of the field expanded with the Rayleigh hypothesis wherever it is calculated [86, 85].

The efficiency of the Rayleigh hypothesis applied to the SIE would have enabled us to treat larger surfaces or surfaces with more defects. However, the Rayleigh expansion cannot be used in the modeling of gratings with deep and narrow grooves without tremendous numerical care and this counterbalances its advantages. The Rayleigh hypothesis will therefore not be used in our case.

2.1.2 The beginnings of the integral equations for the simulation of arbitrarily-shaped rough metallic surfaces

The development of integral equations for perfectly conducting gratings started in the sixties with the work of Petit *et al.* [81], Wirgin *et al.* [87] and Pavageau *et al.* [88]. A chapter by Maystre in [82] gives a description of the integral method applied to gratings as well as its early history. Successive new approaches of the method extended it to more general cases. For instance, Toigo *et al.* modeled a metallic grating of finite permittivity and with arbitrarily shaped grooves using a surface integral method [89]. He used a projective method on plane waves. It was common at the time to solve the system with a Rayleigh hypothesis as it reduces a lot the complexity of the projection. Therefore, the resolution was made by applying an expansion procedure equivalent to the Rayleigh expansion of the field and by looking for the coefficients in the wavevector space. As it was explained before, as correct as this description may be, the numerical implementation gives non convergent results for narrow grooves and it is also the conclusion of Toigo that,

> the expansion procedure suffers the same limitation as the original Rayleigh method, i.e., it does not converge in general

(An exact formulation of the integral formulation by Toigo *et al.* that does not apply the Rayleigh hypothesis was given by Desanto *et al.* [90] more recently.). This can be understood as follows: the magnetic fields at the surface of a rough grating can be highly localized and the magnetic field step-like variations are poorly described by a Fourier series because of the Gibbs phenomenon. The poor convergence in the wavevectors space will be commented on more in section 4.2.4. Consequently, shallow grooves gratings were extensively studied by different appropriate approximations but narrow and deep grooves gratings were not treated for a long time.

Advances in computer engineering, however, made it possible to solve the integral directly in the real space by discretizing it (approximating the area under the curve of the integrated function as a sum of rectangles). This resolution was first applied for infinite (non-periodic) surfaces successfully by Maradudin [91] and was exploited since then to study rough surfaces [92, 93, 94]. Some recent applications of the surface integral equation method in 3D with Green's function periodized in two directions can be found in the work

of Kobidze *et al.* [95], Søndergaard *et al.* [96] and Martin *et al.* [97]. The 2D surface integral equation method with Green's function periodized in one direction was applied for the first time to the field of plasmonic by Søndergaard *et al.* [98, 99, 100, 101, 102]. The method was used to study the resonances of gratings which have dimensions of the order of magnitude of 100 nm. For instance, a triangular-groove grating whose dimensions are a 500 nm period and a height of the groove between 150 and 300 nm exhibited very narrow resonances [98]. Another example is the one of a tapered gold slit grating with a period of 500 and 700 nm having a fixed taper angle of 20.5° for two different widths, 80 and 130 nm at the top and 25 and 65 nm at the bottom which showed field enhancement of 10^2 [102]. No gratings with width smaller than 20 nm were investigated to our knowledge.

Most of the work on rough surfaces has been done by considering self-affine surfaces since it seems that they correctly reproduce different rough surfaces which exist in nature [103]. Part of the studies focus on surfaces with a nano-scale roughness smoother than the one of the cold films for instance and are able to do so by considering the metal as a perfect one. These studies are of no interest in our case as the plasmonic resonances of nano-scaled grooves require treating the metal behavior exactly and to model it with a complex permittivity. That is why we will give a brief description in the next paragraph of self-affine surfaces and we will comment the study of a real-metal surface with the smallest roughness up to date with the use of the surface integral method.

2.1.3 The integral equations applied to self-affine surfaces

Self-affine surfaces are statistically scale invariant [103]. Let's see what this means for a surface defined by a function y with (x, y(x)) a point of the surface. If the lateral dimension is rescaled as ax then the horizontal one will also be rescaled as $a^H y$ with H the Hurst exponent which characterizes the roughness. The lower-scale cut-off ξ_L is the smallest scale that satisfies the scale invariant law and there is no variation of the surface at a smaller scale. It must be clear that the Hurst coefficient gives a relation between scales but does not give an absolute value for the heights and therefore does not describe the surface entirely. The statistical information on the absolute length of the profile is given by the root mean square (rms) of the height ie the mean height difference which is

$$\delta(\Delta x) = \left\langle \left(y(x + \Delta x) - y(x) \right)^2 \right\rangle^{\frac{1}{2}}$$

with $\langle \rangle$ the spatial average measured over a window of length Δx.
In the case of self-affine surfaces, the rms is $\delta(\Delta x) = l^{1-H} \Delta x^H$ with l the topothesy, a particular length for which $\delta(l) = l$. To sum-up, the self-affine properties are characterized by the Hurst exponent H for its roughness, the lower scale cut-off ξ_L for its smallest scale and its rms height δ. The self-affine surfaces are like fractal surfaces only at certain length scales. Therefore the term fractal will not be used although it is often seen in the literature. Nevertheless a fractal dimension is defined as D=2-H for a self-affine curve and as D=3-H for a self-affine surface.

The self-affine surfaces were studied extensively by Sánchez-Gil *et al.* [104, 105, 106, 107, 108, 109] taking up the method of Maradudin. The surfaces with the smallest defects whose optical properties were calculated are due to the same group [110]. Rough surfaces of length L= 5.14µm were illuminated by a Gaussian beam. The self-affine surfaces had an Hurst exponent of H=0.1 and the lower-scale cut-off started from ξ_L = 51.4 nm down to ξ_L = 6.425 nm with $\delta(L)$ = 51.4 nm in the first case and down to ξ_L = 12.85 nm with $\delta(L)$ = 257 nm in the second case. The resulting profiles have cavities whose dimensions are of the order of magnitude of several tens of nanometer, the smallest being about 30 nm by 30 nm i.e. a low aspect ratio of width over height equal to one. Only the case with the Husrt exponent H=0.1, the rms $\delta(L)$ = 257 nm and a lower scale cut-off ranging between ξ_L = 12.85 and ξ_L = 51.4 nm, is shown here. The profiles as well as an electric near-field map of the surface are shown as an example in figure 2.2. The rougher surfaces have SERS EF ($\propto |E|^4$) of approximately 10^{10}.
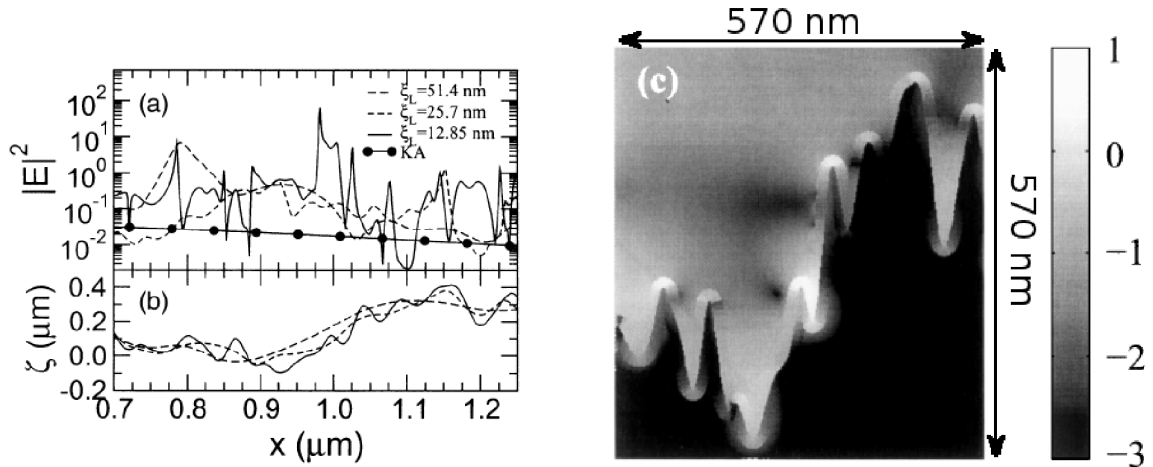
Figure 2.2: *(a) Surface electric field intensities along the center half of the illuminated area that results from TM polarized light scattering with* $\theta_i = 0°$, $\lambda = 629.9$ *nm for the silver self-affine surface represented in (b) with* $\delta=257$ *nm and H=0.1 and (c) a near-field intensity image in a log scale in an area of 570 × 570 nm^2 [110]*

The authors admit that they are limited in the choice of the defects dimension by the length of the surface in the micrometer range. To describe a localization of the field around defects whose sizes are of the order of magnitude of the nanometer, the surface profile has to be discretized with a step in the nanometer range or even smaller. Therefore, the accurate study of tiny defects requires the use of surface profiles whose length is smaller to avoid memory problem. This example also highlights that one issue of the resolution is its high number of unknowns. The higher the possible number of unknowns is, the more complex the surface can be.

The literature showed that one has to tackle several problems before being able to study nano-scaled rough surfaces. The methods which write the field as a plane wave expansion or as a Fourier series and apply the Rayleigh hypothesis, are suited for shallow sur-

faces and proved to be of no use for rough surfaces. The surface integral method enables one to study the EM field near arbitrary-shaped metallic surfaces and proved to be pertinent if the resolution is done by discretizing the equations in the real space. However, a compromise has to be done between the length and the complexity (or the size of the defects) of the surface profile. To our knowledge, no nano-scale rough surfaces with defects of the order of a few nanometers wide and tens of nanometers deep were studied. As we believe it was not investigated in previous studies, this is the path we want to explore in this thesis. We present this method as it was originally presented for non-periodic surfaces by Maradudin [91] in the next section.

2.2 The SIE for an arbitrary-shaped metallic surface

The method will be described in three steps. First, we present the system: an arbitrary-shaped metallic surface illuminated by an incident TM polarized plane wave and the differential equations for the magnetic field in the steady-state. Secondly, we get the surface integral equation for the magnetic field by applying the Green theorem to our problem. Eventually, we explain how to retrieve the physical quantities of our problem, the reflectivity and the electric and magnetic field in the whole space.

2.2.1 Description of the problem

2.2.1.1 The metallic surface

Our system consists of a metallic surface standing in a dielectric and excited by an incident field, typically a plane wave. The open domain of the media above (resp. below) the interface is denoted Γ^+ (resp. Γ^-). The notations of the figure 2.3 will be followed throughout the thesis.

The metallic surface may be seen as roughnesses added or subtracted from a planar surface in the xOz plane. It is invariant in the z direction and has a length d in the x direction. The direction perpendicular to this mean surface is then the y direction. Due to the invariance in z, the problem will only be solved in the xOy plane. A position $\vec{r}$ will be indifferently described by the Cartesian coordinates (x,y) and the polar ones (r,θ) with $r = \sqrt{x^2 + y^2}$ and $x = r\cos\theta, y = r\sin\theta$, the definition of θ being given in table 2.1

In order to be as general as possible, all surfaces S will be described by parametric functions. To avoid numerical problems, the parametric functions are differentiable twice. Each point of the surface has an abscissa $x_D(t)$ and an ordinate $D(t)$ associated with a parameter t. x_D and D are two functions in the space of continuous functions which have continuous derivatives up to the second order (the functions belong to $\mathscr{C}^{(2)}$). The surface is thus defined
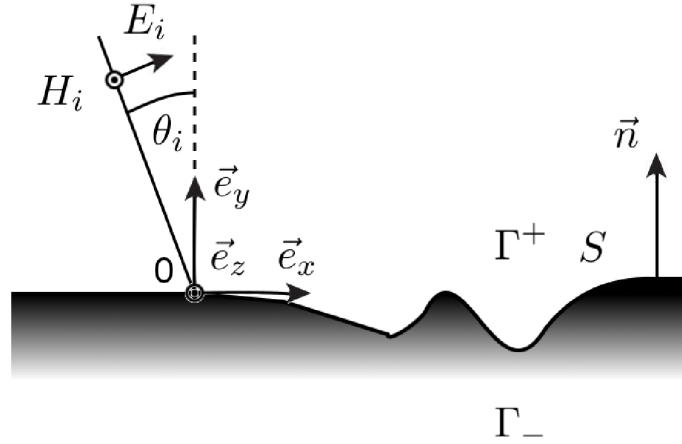
Figure 2.3: *Schematic representation of the surface profile and convention on the coordinates. S is the surface alone.*

x y	<0	>0
< 0	$\theta=-\pi-\mathrm{asin}\left(\frac{y}{r}\right)$	$\theta=\mathrm{asin}\left(\frac{y}{r}\right)$
> 0	$\theta=\pi-\mathrm{asin}\left(\frac{y}{r}\right)$	$\theta=\mathrm{asin}\left(\frac{y}{r}\right)$

Table 2.1: *Definition of the polar coordinate θ as a function of the Cartesian coordinates x and y and $r = \sqrt{x^2 + y^2}$. Asin the inverse sine.*

as:

$$S : t \in [0,\mathrm{T}] \rightarrow \vec{r}(t) = \left(\begin{array}{c} x_\mathrm{D}(t) \\ \mathrm{D}(t) \end{array} \right) \quad . \tag{2.2}$$

The normal vector at the interface going upwards, will therefore be:

$$\vec{n}(t) = \frac{1}{\gamma(t)} \left(\begin{array}{c} -\mathrm{D}'(t) \\ x_\mathrm{D}{}'(t) \end{array} \right) \qquad \gamma(t) = \sqrt{\mathrm{D}'(t)^2 + x_\mathrm{D}{}'(t)^2} \quad , \tag{2.3}$$

the derivation being with respect to the parameter t.

2.2.1.2 Maxwell's equation and radiation condition

To address the issues of plasmonic resonances of metallic surfaces, we will focus our research on the steady-state of harmonic and TM polarized waves near an interface between a dielectric in Γ^+ and a metal in Γ^- invariant in the z-direction. The EM problem in TM polarization is reduced to a single unknown H_z which follows the equations for a TM polarized wave from Maxwell's equations and boundary conditions. For convenience, the unknown

H_z will be described in the two domains Γ^+ and Γ^- by the functions H_z^+ and H_z^- respectively

$$H_z^+(\vec{r}) = \begin{cases} H_z(\vec{r}) & \text{if } \vec{r} \in \Gamma^+ \cup S, \\ 0 & \text{if } \vec{r} \in \Gamma^- \end{cases} \quad , \tag{2.4}$$

$$H_z^-(\vec{r}) = \begin{cases} 0 & \text{if } \vec{r} \in \Gamma^+, \\ H_z(\vec{r}) & \text{if } \vec{r} \in \Gamma^- \cup S \end{cases} \quad . \tag{2.5}$$

Moreover, we know that in a media of permittivity $\epsilon^\pm$, free of charges and current, we have $\forall \vec{r} \in \Gamma$

$$\Delta H_z^\pm(\vec{r}) + k^{\pm 2} H_z^\pm(\vec{r}) = 0 \quad ,$$

$$\frac{\partial H_z^\pm}{\partial y}(\vec{r}) = -\epsilon^\pm \epsilon_0 i \omega E_x^\pm(\vec{r}) \quad , \tag{2.6a}$$

$$-\frac{\partial H_z^\pm}{\partial x}(\vec{r}) = -\epsilon^\pm \epsilon_0 i \omega E_y^\pm(\vec{r}) \tag{2.6b}$$

and the boundary conditions are $\forall \vec{r} \in S$

$$H_z^+(\vec{r}) = H_z^-(\vec{r}) \quad , \tag{2.7a}$$

$$\frac{1}{\epsilon^+} \frac{\partial H_z}{\partial \vec{n}}^+(\vec{r}) = \frac{1}{\epsilon^-} \frac{\partial H_z}{\partial \vec{n}}^-(\vec{r}) \tag{2.7b}$$

with $k^\pm$ the wavevector of light in a media which follows the equation 1.15.

One last condition is required: having described the behavior of the wave in the whole space as well as at the interface, it lacked information on the boundaries at infinity to assure uniqueness of the solution. In order to have a physical solution, no wave can come from infinity (unless there exists a source at infinity) or there would be creation of energy. This concept was introduced as a general principle by Sommerfeld and has been known as the Sommerfeld radiation conditions since [111]. The radiation condition comes from the energy conservation: at infinity there can only be outgoing waves. With the convention $e^{-i\omega t}$, it writes:

$$\lim_{|\vec{r}| \to \pm\infty} \left(\frac{\vec{r}}{|\vec{r}|} \vec{\nabla} \mp i k_0 \right) H_z^\pm(\vec{r}) = 0 \quad . \tag{2.8}$$

The equations that governs the properties of the EM field, presented here, lead to a unique solution given a particular incident field impinging on a defined metallic surface.

2.2.1.3 The incident field

The incident field $\vec{H}_i = H_i \vec{e}_z$ is in the TM polarization and is harmonic

$$H_i(x, y, t) = e^{-i\omega t} H_i(x, y) \quad . \tag{2.9}$$

47

The incident field impinges on the grating from Γ^+ and is described by

$$H_i(\vec{r}) = \begin{cases} H_i(\vec{r}) & \forall \vec{r} \in \Gamma^+ \\ 0 & \forall \vec{r} \in \Gamma^- \end{cases} \quad .$$

In this thesis, the plane wave has been the only case investigated such that the incident field is written

$$H_i(\vec{r}) = H_i e^{ik_+(\sin\theta_i x - \cos\theta_i y)} \quad . \tag{2.10}$$

In order for the incident field to exist, it must be emitted by one or several source points $\vec{r}_i$ (in our case this or these points always being situated in Γ^+). The Maxwell equations, radiation and boundary conditions satisfied by the total field H_z^+ also hold for the incident field H_i in the space free of charges and currents. The only major difference occurs at the source points $\vec{r}_i$ from where the incident field is emitted. A source term ρ at these points must then be introduced to describe the equations satisfied by H_i. It is given here as an example but it will not be used later on:

$$\rho : \vec{r} \rightarrow \sum_i \rho(\vec{r}) \delta(\vec{r} - \vec{r}_i)$$

with $\vec{r}_i \in \Gamma^+$. What is of importance is the modification of the Helmholtz equation that H_i fulfills as

$$\Delta H_i + k^{+2} H_i = -\rho \tag{2.11}$$

and even more importantly the one that $H_z^\pm$ fulfills as

$$\begin{cases} \Delta H_z^+ + k^{+2} H_z^+ = -\rho & , \\ \Delta H_z^- + k^{-2} H_z^- = 0 & . \end{cases} \tag{2.12}$$

The problem described here by the description of a metallic surface, an incident field and the Maxwell equations, the boundary equation and the radiation condition, is uniquely solvable. We seek the solution by applying the surface integral method.

2.2.2 Where the Surface Integral Equations appear

We have chosen to solve the problem that has been presented in the previous section with the surface integral equation method. In a nutshell, the method consists of turning the differential equations into integral ones by applying the Green theorem. To do so, the Green function, which is the fundamental solution of the Maxwell inhomogeneous equation i.e. the solution in an infinite space free of charges and current, is needed. The magnetic field everywhere in the volume may then be expressed as an integral on the boundary of the Green function and its derivative and the magnetic field and its derivatives.

The surface integral equations method is particularly suited to plasmonic problems as the surface is the focus of the study: the unknown of the set of equations is the magnetic field at the surface S. Its three main advantages [112] are

- The boundary conditions, the radiation condition and the Helmholtz equation are contained in one and only one equation to solve. Moreover, the radiation condition assures that the problem is well-conditioned.

- As it is a semi-analytical method there are consequently no grid errors as can happen in FDTD. In the FDTD method, the spatial (time) derivatives of the field are approximated as the difference between two close points (time). The Maxwell equations are then solved for all the points of a grid in the volume at succeeding instants of time. The propagation of the field from a point to another is therefore done by discretized steps in space and time where as it is done with an analytical Green function in the surface integral method.

- The dimension of the problem is reduced from a 3D problem (to find the magnetic field in the volume) to a 2D one (to find the magnetic field on the surface). Thus, for a system invariant in one direction, the number of unknowns goes down from N^2 to N.

However a price has to be paid

- The Green function has to be known explicitly which is possible for homogeneous problems but can quickly become overcomplicated for inhomogeneous problems. Furthermore, the Green Function takes a long time to be evaluated.

- There are more numerical tricks than in a standard FDTD. For instance, the Green function is singular and the matrix to solve is dense.

We refer to the book *Boundary Integral Equations* by Hsiao and Wendland [113] for rigorous presentation of the method and to the dedicated chapter in *Light Scattering and Nanoscale Surface Roughness* [93]. Hereafter will be presented the important steps to generate integral equations for the magnetic field H_z as described in [91] and in a more detailed way in [114]. Let us first define the Green function.

2.2.2.1   Green's function in an infinite media

The Green function $G(\vec{r}' - \vec{r})$ enables one to describe the propagation of a field H created by a source term ρ at the point $\vec{r}$ to the point $\vec{r}'$ such that

$$H(\vec{r}') = \int_\Gamma \left[G(\vec{r}' - \vec{r})\rho(\vec{r}) \right] dV(\vec{r}) \quad .$$

The Green function is the distribution solution of the Helmholtz equation in a specific medium for a source point $\delta(\vec{r}' - \vec{r})$ under the same conditions of radiation at infinity as H_z. Starting from the analytical expression of the Green function, the Maxwell equation may be ex-

pressed as integral equations. Thus, great attention must be paid to the accuracy of the Green function.

Without loss of generality, the Green function may be looked for considering a source point located at the origin, i.e. having $\delta(\vec{r})$ in the Helmholtz equation. We make use of the Green function latter by substituting $\vec{r}' - \vec{r}$ for $\vec{r}$. In a media of permittivity $\epsilon^\pm$, the distribution satisfies the Helmholtz equation:

$$\forall (x, y) \in \mathbb{R}^2 \qquad \Delta G^\pm(x, y) + k^{\pm 2} G^\pm(x, y) = -\delta(x)\delta(y) \tag{2.13}$$

and the radiation condition:

$$\lim_{|\vec{r}| \to \pm\infty} \left(\frac{\vec{r}}{|\vec{r}|} \vec{\nabla} \mp i k_0 \right) G^\pm(\vec{r}) = 0 \quad . \tag{2.14}$$

The solution for the Green function is presented here in the real space, however there exists an equivalent spectral form of the Green function and its demonstration may thus be found in appendix B.2. The Helmholtz equation written in terms of the polar coordinates is equivalent to the Bessel Equations. The solution of equation 2.13 in the complex plane may consequently be looked for in terms of the Bessel functions of the first J_n and the second kind Y_n (The second kind is sometimes called the Neumann function N_n). The exact solution of the equation 2.13 is the Hankel function

$$\forall (x, y) \in \mathbb{R}^2 \qquad G^\pm(x, y) = \frac{i}{4} H_0^{(1)}(k^\pm r) \tag{2.15}$$

where $H_0^{(1)}$ denotes the modified Hankel function of the first kind and $r = \sqrt{x^2 + y^2}$.
The word "Modified" refers to the fact that the argument may be complex. This function is part of the Bessel family of functions and is defined by

$$\forall z \in \mathbb{C} \quad |z| \neq 0 \qquad \forall \nu \in \mathbb{R} \qquad H_\nu^{(1)}(z) = J_\nu(z) + i Y_\nu(z) \quad .$$

The Hankel function of the first kind is not defined at the point $|z|$=0 and its real part diverges for $|z| \to 0$ while its imaginary part tends to $i/4$. Due to this property, the Green function has a singularity at r=0 and its asymptotic behavior near the origin ($r \approx 0$) is

$$\frac{i}{4} H_0^{(1)}(k^\pm r) \approx -\frac{1}{2\pi} \log\left(\frac{\gamma |k^\pm r|}{2} \right) - \frac{i}{2\pi} \arg(k^\pm r) + \frac{i}{4} \tag{2.16}$$

where $\arg(k^\pm r)$ is the phase of $k^\pm r$ and γ is Euler's constant.

The asymptotic behavior of the Green function at infinity ($r \to +\infty$) is the plane wave (formula 9.2.3 p. 364 in [115])

$$\frac{i}{4} H_0^{(1)}(k^\pm r) \approx \frac{i}{4} \sqrt{\frac{2}{\pi k^\pm r}} e^{i(k^\pm r - \frac{\pi}{4})} \quad . \tag{2.17}$$

The Hankel function of the first kind is represented in figure 2.4 for $k^+ = 1$. In the limit $k^+ r \approx 0$, the real part (blue line) diverges and the imaginary part (red line) is equal to 0.25 substituting $\arg(k^+ r) = 0$ in the equation 2.16.

Now that we have presented the Green function, we present and apply the Green theorem.
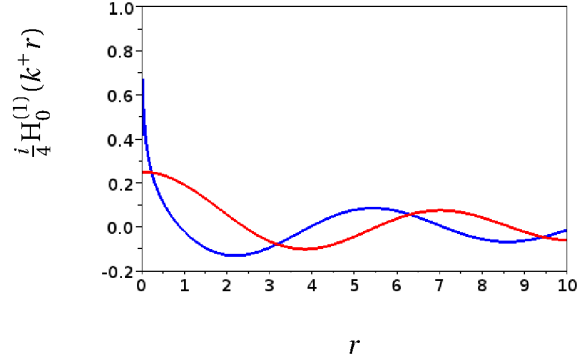
Figure 2.4: *Behavior of the real (blue) and imaginary (red) parts of the free space Green function* G_0 *for* $k^+ = 1$ *near the singularity r=0.*

2.2.2.2 The Green theorem
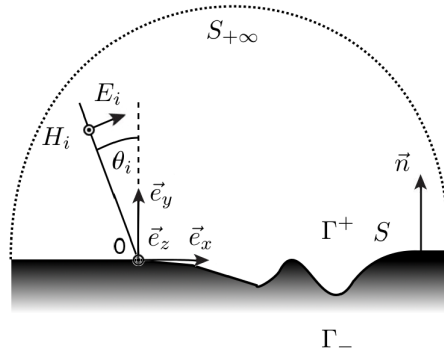
Figure 2.5: *Definition of the volume* Γ^+ *delimited by an oriented boundary: the surface* Σ *composed of the segment* S *(solid line) and the segment* $S_{+\infty}$ *(dashed line).*

The Green Theorem formulation for two continuous and derivable functions ϕ and ψ with a volume Γ enclosed by a smooth surface Σ oriented in the trigonometric direction is [1]

$$\int_{\Gamma} \left[\phi(\vec{r})\Delta\psi(\vec{r}) - \psi(\vec{r})\Delta\phi(\vec{r}) \right] dV(\vec{r}) = \oint_{\Sigma} \left[\phi(\vec{r})\frac{\partial\psi(\vec{r})}{\partial\vec{n}} - \psi(\vec{r})\frac{\partial\phi(\vec{r})}{\partial\vec{n}} \right] dS(\vec{r}) \tag{2.18}$$

where dV and dS are respectively the volume and surface element of Γ and Σ and $\vec{n}$ is the normal vector to the surface Σ oriented towards the exterior of the volume Γ^+.

We want to apply the Green function theorem for a volume Γ^+ whose boundary Σ can be divided in two segments: an arc $S^{+\infty}$ whose radius r tends to infinity and the metallic surface S as represented in figure 2.5. This approach is also valid in the volume Γ^- defined

---

[1]To quote Cheng and Chang [78]: " [to] put it simply the smoothness of a surface is such that on every point there exists a tangent plane but not necessarily a curvature"

51

in the semi-infinite metal, similarly to Γ^+, whose boundary is composed of an arc $S^{-\infty}$ whose radius r tends to infinity and the metallic surface S. The goal of the method is to connect the field at a defined point $\vec{r}\,'$ to any field in the whole space $\Gamma^\pm$. The field emitted at the point $\vec{r}$ which has propagated to the point $\vec{r}\,'$ may be written with the use of a Green function $G^\pm(\vec{r}\,' - \vec{r})$. The sum of all of the fields in the whole space $\Gamma^\pm$ that propagates to the point $\vec{r}\,'$ is mathematically equivalent to an integral over all the points in $\Gamma^\pm$. Applying the Green theorem, equation 2.18, on the volume Γ^+ for $\psi(\vec{r}) = G^\pm(\vec{r}\,' - \vec{r})$ and $\phi(\vec{r}) = H_z^\pm(\vec{r})$, we have

$$\int_{\Gamma^+} \left[H_z^\pm(\vec{r}) \Delta G^\pm\left(\vec{r}\,' - \vec{r}\right) - G^\pm\left(\vec{r}\,' - \vec{r}\right) \Delta H_z^\pm(\vec{r}) \right] dV(\vec{r})$$
$$= \oint_\Sigma \left[H_z^\pm(\vec{r}) \frac{\partial}{\partial \vec{n}_+} \left[G^\pm\left(\vec{r}\,' - \vec{r}\right) \right] - G^\pm\left(\vec{r}\,' - \vec{r}\right) \frac{\partial H_z^\pm}{\partial \vec{n}_+}(\vec{r}) \right] dS(\vec{r})$$

with $\vec{n}_+$, the normal vector of Σ oriented towards the exterior of Γ^+. Attention must be paid to the fact that the derivative is done with respect to $\vec{r}$ so $\frac{\partial}{\partial \vec{n}_+}\left[G^\pm(\vec{r}\,' - \vec{r}) \right] = -\frac{\partial G^\pm}{\partial \vec{n}_+}(\vec{r}\,' - \vec{r})$. There is therefore a minus in front of $\frac{\partial G^\pm}{\partial \vec{n}_+}$. Moreover, for convenience and from now on, the normal vector will be taken going upward i.e. $\vec{n} = -\vec{n}_+$ as shown in figure 2.3. The change is responsible for another minus in front of the entire integral over Σ. The two changes of sign give

$$\int_{\Gamma^+} \left[H_z^\pm(\vec{r}) \Delta G^\pm\left(\vec{r}\,' - \vec{r}\right) - G^\pm\left(\vec{r}\,' - \vec{r}\right) \Delta H_z^\pm(\vec{r}) \right] dV(\vec{r})$$
$$= \oint_\Sigma \left[H_z^\pm(\vec{r}) \frac{\partial G^\pm}{\partial \vec{n}}\left(\vec{r}\,' - \vec{r}\right) + G^\pm\left(\vec{r}\,' - \vec{r}\right) \frac{\partial H_z^\pm}{\partial \vec{n}}(\vec{r}) \right] dS(\vec{r}) \quad . \tag{2.19}$$

Let us take a close look at the integral on each segment of the boundaries of Γ^+ separately. To be at ease, we define the integrated part as a function $F(\vec{r}, \vec{r}\,')$ namely

$$F(\vec{r}, \vec{r}\,') = H_z^\pm(\vec{r}) \frac{\partial G^\pm}{\partial \vec{n}}(\vec{r}\,' - \vec{r}) + G^\pm(\vec{r}\,' - \vec{r}) \frac{\partial H_z^\pm}{\partial \vec{n}}(\vec{r}) \quad .$$

2.2.2.3 The integral at infinity

The boundary $S_{+\infty}$ is an arc of radius $|\vec{r}|$ that tends to infinity. The normal vector to this boundary is along $\vec{r}$ thus

$$\frac{\partial}{\partial \vec{n}} = \vec{n}\vec{\nabla} = \frac{\vec{r}}{|\vec{r}|}\vec{\nabla}$$

and the integrated piece therefore writes

$$F(\vec{r}, \vec{r}\,') = H_z^\pm(\vec{r}) \frac{\vec{r}}{|\vec{r}|}\vec{\nabla}G^\pm(\vec{r}\,' - \vec{r}) + G^\pm(\vec{r}\,' - \vec{r}) \frac{\vec{r}}{|\vec{r}|}\vec{\nabla}H_z^\pm(\vec{r}) \quad .$$

As we mentioned earlier the Sommerfeld radiation condition implies that only outgoing waves can exist at infinity. From 2.8 and 2.14 we can see that

$$\lim_{|\vec{r}|\to+\infty} \left(H_z^\pm(\vec{r}) \frac{\vec{r}}{|\vec{r}|} \vec{\nabla} G^\pm(\vec{r}'-\vec{r}) + G^\pm(\vec{r}'-\vec{r}) \frac{\vec{r}}{|\vec{r}|} \vec{\nabla} H_z^\pm(\vec{r}) \right)$$
$$= \lim_{|\vec{r}|\to+\infty} \left(H_z^\pm(\vec{r}) \left(-ik_0 G^\pm(\vec{r}'-\vec{r}) \right) + G^\pm(\vec{r}'-\vec{r}) ik_0 H_z^\pm(\vec{r}) \right)$$
$$= 0$$

such that

$$\int_{S_{+\infty}} F(\vec{r},\vec{r}') dS(\vec{r}) = 0 \quad . \tag{2.20}$$

Note that this term is often constructed differently because of the incident field being in most cases a plane wave and its source considered to be at infinity. An alternative approach is given in the next section.

2.2.2.4   The particular case of the incident field term

The rigorous way to treat the incident field is to apply once again the Green theorem to $G^+(\vec{r}'-\vec{r})$ and $H_i(\vec{r})$ on the volume $\Gamma^+ \cup \Gamma^-$ for $\vec{r}'$ in Γ^+. Similar result as obtained previously hold for the integrals on the boundaries at infinity, equation 2.20, such that

$$\oint_{S_{+\infty}\cup S_{-\infty}} \left[H_i(\vec{r}) \frac{\partial G^+}{\partial \vec{n}}(\vec{r}'-\vec{r}) + G^+(\vec{r}'-\vec{r}) \frac{\partial H_i}{\partial \vec{n}}(\vec{r}) \right] dS(\vec{r}) = 0 \quad .$$

The integral to look for is then given by the Green Theorem, equation 2.18,

$$\int_{\Gamma^+\cup\Gamma^-} \left[H_i(\vec{r}) \Delta G^+(\vec{r}'-\vec{r}) - G^+(\vec{r}'-\vec{r}) \Delta H_i(\vec{r}) \right] dV(\vec{r}) = 0$$

and because H_i is null in Γ^- we have

$$\int_{\Gamma^+} \left[H_i(\vec{r}) \Delta G^+(\vec{r}'-\vec{r}) - G^+(\vec{r}'-\vec{r}) \Delta H_i(\vec{r}) \right] dV(\vec{r}) = 0 \quad .$$

The relation between the source term ρ and the incident field H_i is obtained by substituting the Helmholtz relations of H_i and G^+, equations 2.11 and 2.13, into the function integrated over the surface such that

$$H_i(\vec{r}) \Delta G^+(\vec{r}'-\vec{r}) - G^+(\vec{r}'-\vec{r}) \Delta H_i(\vec{r})$$
$$= H_i(\vec{r}) \left(-\delta(\vec{r}'-\vec{r}) \right) - G^+(\vec{r}'-\vec{r}) \left(-\rho(\vec{r}) \right) \quad .$$

We can then obtain an explicit relation between the source term and the incident field, for $\vec{r}'$ in Γ^+

$$H_i(\vec{r}') = \int_{\Gamma^+} \left[G^+(\vec{r}'-\vec{r}) \rho(\vec{r}) \right] dV(\vec{r}) \tag{2.21}$$

which will appear and be needed later on for the equations on H_z.

2.2.2.5 An alternative to the particular case of the incident field and the integral at infinity

In the case of the incident field being a plane wave, its source may be considered at infinity i.e. on the boundary $S_{+\infty}$ (then $\rho = 0$ in Γ^+). In that case physicists often treat the boundary at infinity and the incident field at once, by assuming that the waves propagating downwards at infinity come from the incident field.

Let's now focus on the solution H_z^+ and separate it in outgoing H_{out}^+ and incoming H_{in}^+ waves. The integrated function therefore reads

$$\forall \vec{r} \in S_{+\infty} \qquad F^+(\vec{r}, \vec{r}') = H_{out}^+(\vec{r}) \frac{\partial G^+}{\partial y}(\vec{r}' - \vec{r}) + G^+(\vec{r}' - \vec{r}) \frac{\partial H_{out}^+}{\partial y}(\vec{r})$$
$$+ H_{in}^+(\vec{r}) \frac{\partial G^+}{\partial y}(\vec{r}' - \vec{r}) + G^+(\vec{r}' - \vec{r}) \frac{\partial H_{in}^+}{\partial y}(\vec{r}) \quad .$$

The radiation condition gives

$$\lim_{|\vec{r}| \to +\infty} \left(H_{out}^+(\vec{r}) \frac{\vec{r}}{|\vec{r}|} \vec{\nabla} G^+\left(\vec{r}' - \vec{r}\right) + G^+\left(\vec{r}' - \vec{r}\right) \frac{\vec{r}}{|\vec{r}|} \vec{\nabla} H_{out}^+(\vec{r}) \right) = 0 \quad .$$

The incoming waves from infinity can only corresponds to the incident field, then

$$\lim_{|\vec{r}| \to +\infty} \left(H_{in}^+(\vec{r}) \frac{\vec{r}}{|\vec{r}|} \vec{\nabla} G^+\left(\vec{r}' - \vec{r}\right) + G^+\left(\vec{r}' - \vec{r}\right) \frac{\vec{r}}{|\vec{r}|} \vec{\nabla} H_{in}^+(\vec{r}) \right) = H_z^i\left(\vec{r}'\right) \quad .$$

In that case, if the point of the source $\vec{r}_i$ tends to infinity, we have

$$\int_{S_{+\infty}} F^+(\vec{r}, \vec{r}') dS(\vec{r}) = H^i(\vec{r}') \quad .$$

For the solution H_z^- which is null in Γ^+, the result still is

$$\int_{S_{+\infty}} F^-(\vec{r}, \vec{r}') dS(\vec{r}) = 0 \quad .$$

Finally, we see that we obtain the same integral equations either by using this formulation or by using the formulation which makes explicit the source term ρ, as described in section 2.2.2.4 and 2.2.2.3. The demonstration here, however, is only valid for an incident field which comes from infinity whereas the other demonstration allows any sort of incident field.

2.2.2.6 The integral over S

We now comment on the integral on the last segment of the closed surface Σ, the integral on the segment S which is along the interface between the metal and the air

$$\int_S \left[\frac{\partial G^\pm}{\partial \vec{n}}\left(\vec{r}' - \vec{r}\right) H_z^\pm(\vec{r}) + G^\pm\left(\vec{r}' - \vec{r}\right) \frac{\partial H_z^\pm}{\partial \vec{n}}(\vec{r}) \right] dS(\vec{r}) \quad .$$

We have seen that the incident field H_i is created by a source ρ and the Green function, which appears in the integral of equation 2.21, plays the role of a propagator. In the same way, the magnetic field $H_z^\pm$ and its derivative $\frac{\partial H_z^\pm}{\partial \vec{n}}$ behave as source points on the metallic surface and the Green function $\frac{\partial G^\pm}{\partial \vec{n}}$ and $G^\pm$ are the propagators. The Green function, as the fundamental solution of the Maxwell equation, catches the laws of physics and is known analytically as a function of all the variables of the problem, for instance the wavelength or the angle. The characteristics of the geometry of the problem are also contained within the Green functions because the origin of the propagation of the field is the location of the source point $\vec{r}$. The source point $\vec{r}$ belongs to the surface S and is therefore written as $\vec{r} = (x_D(t), D(t))$, equation 2.2, whereas the point $\vec{r}' = (x', y')$ belongs to the whole space $\Gamma^\pm$.

To shed light on the expression of the Green function, it is given in Cartesian coordinates. The derivation is done with respect to the normal vector $\vec{n}$ which is $\frac{1}{\gamma(t)}(-D'(t), x_D'(t))$, equations 2.3. We stress here that the derivatives with respect to t are noted $'$ and must not be mistook for the notation of the coordinates of $\vec{r}'$. The Green function is thus expressed as

$$G^\pm \left(x' - x_D(t), y' - D(t) \right)$$

and its derivative as

$$\frac{\partial G^\pm}{\partial \vec{n}} \left(\vec{r}' - \vec{r} \right) = \frac{1}{\gamma(t)} \left(-D'(t) \frac{\partial G^\pm}{\partial x} + x_D'(t) \frac{\partial G^\pm}{\partial y} \right) \left(x' - x_D(t), y' - D(t) \right) \quad .$$

The Green functions contain the unique geometry of the profile through the coordinates of the vector $\vec{r}$ which belongs to the surface S. All the informations of the problem are therefore contained in the Green functions expression. On the contrary, the source points on the metallic surface ($H_z^\pm$ and $\frac{\partial H_z^\pm}{\partial \vec{n}}$) are the unknowns as they create the field in the whole space, specific to our problem.

2.2.2.7 Equations for t

We have expressed the integrals on the two parts of the enclosed surface Σ. We are now going to consider the integral on the volume Γ^+. Substituting the Helmholtz equations 2.41 and 2.12 into the function integrated on the volume one has

$$H_z^\pm(\vec{r}) \Delta G^\pm(\vec{r}' - \vec{r}) - G^\pm(\vec{r}' - \vec{r}) \Delta H_z^\pm(\vec{r})$$

$$= \begin{cases} -H_z^+(\vec{r}) \delta(\vec{r}' - \vec{r}) + G^+(\vec{r}' - \vec{r}) \rho(\vec{r}) \\ -H_z^-(\vec{r}) \delta(\vec{r}' - \vec{r}) \end{cases}$$

so given the expression of the incident field 2.21

$$\int_{\tilde{\Gamma}^+} \left[H_z^\pm(\vec{r}) \Delta G^\pm(\vec{r}' - \vec{r}) - G^\pm(\vec{r}' - \vec{r}) \Delta H_z^\pm(\vec{r}) \right]$$

$$= \begin{cases} H_i(\vec{r}') - H_z^+(\vec{r}') \\ -H_z^-(\vec{r}') = 0 \end{cases} \quad .$$

Eventually the Green Theorem, equation 2.19, yields $\forall \vec{r}\,' \in \Gamma^+$

$$\int_S \left[H_z^+(\vec{r}) \frac{\partial G^+}{\partial \vec{n}}(\vec{r}\,' - \vec{r}) + G^+(\vec{r}\,' - \vec{r})\frac{\partial H_z^+}{\partial \vec{n}}(\vec{r}) \right] dS(\vec{r}) = H_i(\vec{r}\,') - H_z^+(\vec{r}\,') \quad , \qquad (2.22)$$

$$\int_S \left[H_z^-(\vec{r}) \frac{\partial G^-}{\partial \vec{n}}(\vec{r}\,' - \vec{r}) + G^-(\vec{r}\,' - \vec{r})\frac{\partial H_z^-}{\partial \vec{n}}(\vec{r}) \right] dS(\vec{r}) = 0 \quad . \qquad (2.23)$$

Applying the Green Theorem on Γ^- defined in a similar manner as Γ^+, with the same orientation on the piece S (keeping in mind that the normal vector is now oriented in the same direction ie is $\vec{n}^- = \vec{n}$) in a similar manner $\forall \vec{r}\,' \in \Gamma^-$

$$-\int_S \left[H_z^+(\vec{r}) \frac{\partial G^+}{\partial \vec{n}}(\vec{r}\,' - \vec{r}) + G^+(\vec{r}\,' - \vec{r})\frac{\partial H_z^+}{\partial \vec{n}}(\vec{r}) \right] dS(\vec{r}) = 0 \quad , \qquad (2.24)$$

$$-\int_S \left[H_z^-(\vec{r}) \frac{\partial G^-}{\partial \vec{n}}(\vec{r}\,' - \vec{r}) + G^-(\vec{r}\,' - \vec{r})\frac{\partial H_z^-}{\partial \vec{n}}(\vec{r}) \right] dS(\vec{r}) = -H_z^-(\vec{r}\,') \quad . \qquad (2.25)$$

The expression of the field $H_z^+(\vec{r}\,')$ at the observation point, equations 2.22, can be interpreted as a sum of the propagated fields $G^+(\vec{r}\,' - \vec{r})\frac{\partial H_z^+}{\partial \vec{n}}(\vec{r})$ (respectively $\frac{\partial G^+}{\partial \vec{n}}(\vec{r}\,' - \vec{r})H_z^+(\vec{r})$) from the source points, $\frac{\partial H_z^\pm}{\partial \vec{n}}(\vec{r})$ (respectively $H_z^+(\vec{r})$) standing on the interface S. The Green function G^+ is the propagator in the media Γ^+ from the source point $\vec{r}$ to the observation point $\vec{r}\,' \in \Gamma^+$ whereas the Green function G^- is the propagator in the media Γ^-. We have obtained the integral equations for our problem. We see that the source functions, $\frac{\partial H_z^\pm}{\partial \vec{n}}$ and H_z^+ taken at the metallic surface boundary, are enough to deduce the field in the whole space. Therefore, we want to obtain a set of equations to calculate these two source functions.

2.2.2.8 Self coherent equations on the magnetic field

The integral equations 2.22 and 2.25 express explicitly the field at the observation point $H_z^\pm(\vec{r}\,')$ as a function of the field $H_z^\pm(\vec{r})$ and its derivative $\frac{\partial H_z^\pm}{\partial \vec{n}}(\vec{r})$ on the interface S only. Finding the expression of the field and its derivative on the surface is thus sufficient to obtain the field everywhere else. It corresponds to a direct formulation of the integral equations: we use directly the magnetic field as an unknown as opposed to looking for the charges and the currents on the surface and to deduce the magnetic field from these sources.
To solve the problem only at the boundary, only the field on the surface can appear in the equations i.e. we need to obtain self-coherent equations for $H_z^\pm(\vec{r})$ and its derivative $\frac{\partial H_z^\pm}{\partial \vec{n}}(\vec{r})$ with $\vec{r} \in S$. The two sets of equations, equations 2.22 and 2.23 and equations 2.24 and 2.25 can be used equally to do so. We will use the two unknowns H and L, continuous at the interface, and defined $\forall \vec{r} \in S$ by

$$H(\vec{r}) \qquad\qquad = H_z^+(\vec{r}) = H_z^-(\vec{r}) \quad , \qquad (2.26)$$

$$L(\vec{r}) \qquad\qquad = \frac{1}{\epsilon_+}\frac{\partial H_z^+}{\partial \vec{n}}(\vec{r}) = \frac{1}{\epsilon_-}\frac{\partial H_z^-}{\partial \vec{n}}(\vec{r}) \qquad (2.27)$$

and obtain self-coherent equations for them with the set of equations 2.22 and 2.23 (having two unknowns, one needs two self coherent equations to determine them).

The self coherent equations are obtained by having the observation point $\vec{r}^{\,'}$ tend to the surface S in the equations 2.22 and 2.23. This limit is not trivial at all since the Green function and its derivative are not defined for $\vec{r}^{\,'} = \vec{r}$. However, the integral of the singularity exists, making our equation an improper integral (ie the integral exists as a limit of a definite integral). Moreover, the discontinuity of the derivative of the Green function $\frac{\partial G^+}{\partial \vec{n}}(\vec{r}^{\,'} - \vec{r})$ when $\vec{r}^{\,'} = \vec{r}$ adds a term of the form $\frac{1}{2}H(\vec{r})$ in the equations. If the limit is taken from the $\Gamma^\pm$ side, an additional $\mp\frac{1}{2}H(\vec{r}^{\,'})$ appears , see (4.10) and (4.11) in [116]. Taking the limit from Γ^+ for the set of equations 2.22 and 2.23, one obtains:

$$\int_S \left[H(\vec{r}) \frac{\partial G^+}{\partial \vec{n}}(\vec{r}^{\,'} - \vec{r}) + \epsilon_+ G^+(\vec{r}^{\,'} - \vec{r})L(\vec{r}) \right] dS(\vec{r}) + \frac{1}{2}H(\vec{r}^{\,'}) = H_i(\vec{r}^{\,'}) \quad , \qquad (2.28)$$

$$\int_S \left[H(\vec{r}) \frac{\partial G^-}{\partial \vec{n}}(\vec{r}^{\,'} - \vec{r}) + \epsilon_- G^-(\vec{r}^{\,'} - \vec{r})L(\vec{r}) \right] dS(\vec{r}) - \frac{1}{2}H(\vec{r}^{\,'}) = 0 \quad . \qquad (2.29)$$

This system of equations consists in two Fredholm integral equations of the second kind with an integrable singularity of the Green functions. As Toigo said [89]:

" The self consistent equations above are quite unmanageable in general."

The resolution of the set of equations for an arbitrary-shaped surface is required to be done numerically. We will comment on the issues of doing so at the end of this chapter. Before solving the problem, we want to point out that when the method is to be used in the IR spectral range, it can be simplified, as the number of unknowns may be reduced with the use of the impedance of surface approximation.

2.2.2.9 Self coherent equations on the magnetic field in the impedance of surface approximation

In the spectral range where the noble metals are good conductors, one may apply the impedance of surface approximation as we have previously done in the modal method and which is presented in section 1.3.2. The approximation of impedance of surface 1.21 allows to establish a relation between the two unknowns: the field $H_z^+(\vec{r})$ and its derivative $\frac{\partial H_z^+}{\partial n}(\vec{r})$. The problem therefore admits only one unknown as the two unknowns are now linked by

$$\forall \vec{r} \in S \qquad L(\vec{r}) = i k^+ \xi H(\vec{r})$$

with $\xi = \sqrt{\frac{\epsilon^+}{\epsilon^-}}$. As there is only one unknown, the problem is thus reduced to the resolution of a single equation. We substitute the expression of L as a function of H in the equation 2.22 to obtain this equation which writes as

$$\int_S \left[\frac{\partial G^+}{\partial \vec{n}}(\vec{r}^{\,'} - \vec{r}) + \epsilon_+ i k^+ \xi G^+(\vec{r}^{\,'} - \vec{r}) \right] H(\vec{r}) dS(\vec{r}) + \frac{1}{2}H(\vec{r}^{\,'}) = H_i(\vec{r}^{\,'}) \quad .$$

As we want to study the visible range, this approximation cannot be used and we therefore have to solve a system of two equations for two unknowns.

2.2.3 Reflectivity and Magnetic and Electric field

The self-equations, once solved, only give us the field on the surface S. To explore the physics of metallic corrugated surfaces, it is also important to reconstruct the magnetic and the electric fields near and far from the surface. The magnetic field maps in the vicinity of the defects allow us to identify the resonances, and the electric field near the surface allow us to estimate its enhancement factor and compare it to SERS EF and the magnetic field far from the surface enables us to calculate the reflectivity whose dips at specific frequencies indicate plasmonic resonances. The next section will aim at relating the physical quantities we are interested in to the unknowns of the problem H and L.

2.2.3.1 Magnetic Field

The fields H_z at any observation point $\vec{r}'$ in the volume are built by substituting the two unknowns into the equations 2.22 and 2.25 respectively

$$H_z^+(\vec{r}') \quad = H_i(\vec{r}') - \int_S \left[H(\vec{r}) \frac{\partial G^+}{\partial \vec{n}}(\vec{r}' - \vec{r}) + \epsilon_+ G^+(\vec{r}' - \vec{r}) L(\vec{r}) \right] dS(\vec{r}) \quad , \qquad (2.30)$$

$$H_z^-(\vec{r}') \quad = \int_S \left[H(\vec{r}) \frac{\partial G^-}{\partial \vec{n}}(\vec{r}' - \vec{r}) + \epsilon_- G^-(\vec{r}' - \vec{r}) L(\vec{r}) \right] dS(\vec{r}) \quad . \qquad (2.31)$$

2.2.3.2 Electric Field

We substitute the integral formulation of the fields $H_z^\pm$ in functions of the two unknowns H and L, equation 2.30 in $\tilde{\Gamma}^+$ and equation 2.31 in $\tilde{\Gamma}^-$ into the Maxwell equations 2.6a and 2.6b to obtain the electric fields $\forall \vec{r}' \in \tilde{\Gamma}^+$

$$E_x^+(\vec{r}') = E_x^i(\vec{r}') + \frac{1}{i\omega\epsilon_+\epsilon_0} \int_S H(\vec{r}) \left[\frac{\partial}{\partial y'} \frac{\partial G^+}{\partial \vec{n}} \right] \left(\vec{r}' - \vec{r} \right) + \epsilon_+ \left[\frac{\partial}{\partial y'} G^+ \right] \left(\vec{r}' - \vec{r} \right) L(\vec{r}) dS(\vec{r}) \quad , \quad (2.32)$$

$$E_y^+(\vec{r}') = E_y^i(\vec{r}') - \frac{1}{i\omega\epsilon_+\epsilon_0} \int_S H(\vec{r}) \left[\frac{\partial}{\partial x'} \frac{\partial G^+}{\partial \vec{n}} \right] \left(\vec{r}' - \vec{r} \right) + \epsilon_+ \left[\frac{\partial}{\partial x'} G^+ \right] \left(\vec{r}' - \vec{r} \right) L(\vec{r}) dS(\vec{r}) \qquad (2.33)$$

and $\forall \vec{r}' \in \tilde{\Gamma}^-$

$$E_x^-(\vec{r}') = -\frac{1}{i\omega\epsilon_-\epsilon_0} \int_S H(\vec{r}) \left[\frac{\partial}{\partial y'} \frac{\partial G^-}{\partial \vec{n}} \right] \left(\vec{r}' - \vec{r} \right) + \epsilon_- \left[\frac{\partial}{\partial y'} G^- \right] \left(\vec{r}' - \vec{r} \right) L(\vec{r}) dS(\vec{r}) \quad , \qquad (2.34)$$

$$E_y^-(\vec{r}') = \frac{1}{i\omega\epsilon_-\epsilon_0} \int_S H(\vec{r}) \left[\frac{\partial}{\partial x'} \frac{\partial G^-}{\partial \vec{n}} \right] \left(\vec{r}' - \vec{r} \right) + \epsilon_- \left[\frac{\partial}{\partial x'} G^- \right] \left(\vec{r}' - \vec{r} \right) L(\vec{r}) dS(\vec{r}) \quad . \qquad (2.35)$$

2.2.3.3 Reflectivity

The calculation of the reflectivity depends on the incoming beam. Maradudin [91] chose to use a Gaussian beam and Sanchez-gil [114] details the case of an incident plane wave field.

The reflectivity, the ratio of the incident power to the reflected power, is calculated with the flux of the Poynting vector of the magnetic field through a plane surface $y = Cst$ with Cst a constant in $\mathbb{R}$ which is far away from the surface. Let us define the Poynting vector in the y direction

$$S_y = -i\frac{c^2}{8\pi\epsilon^+\omega}\frac{\partial H_z}{\partial y}H_z^*$$

and the flux of the Poynting vector through a plane surface $y = Cst$ of length L_z in the z direction

$$P = \left|L_z\int dx \quad \Re\left(S_y(x, y = Cst)\right)\right|$$

where $\Re$ denotes the real part of $S_y(x, y = Cst)$. The reflectivity is finally expressed as the ratio of the scattered flux P_r (the flux of the Poynting vector of the reflected far-field) to the incident flux P_i (the flux of the Poynting vector of the incident field)

$$R = \frac{P_r}{P_i} = \int d\theta_r \frac{\partial R}{\partial\theta}(\theta_r)$$

where $\frac{\partial R}{\partial\theta}$ is the angular reflection coefficient.

In the case of the incident wave being a plane wave, 2.10, the incident flux is:

$$P_i = \frac{c^2 L_z}{8\pi\epsilon^+\omega}k^+\cos\theta_i|H_i|^2 \quad . \tag{2.36}$$

The scattered field H_r is obtained by subtracting the incident field H_i to the total field H_z, hence

$$H_r\left(\vec{r}'\right) = -\int_S\left[H(\vec{r})\frac{\partial G^+}{\partial\vec{n}}\left(\vec{r}'-\vec{r}\right)+\epsilon_+G^+\left(\vec{r}'-\vec{r}\right)L(\vec{r})\right]dS(\vec{r}) \quad .$$

By substituting the asymptotes of the Green function for the Green function, when $\vec{r}'$ tends to infinity, H_r is expressed as a sum of propagating plane waves. The plane waves have a real wavevector $k^+(\sin\theta_r, \cos\theta_r)$ whose direction with respect to the normal to the surface is given by the angle θ_r. The demonstration is not given here as it is similar to the one done for the periodic case in the following section 2.3.5. The scattered flux is then

$$P_r = \frac{c^2 L_z}{8\pi\epsilon^+\omega}\int_{-\frac{\pi}{2}}^{\frac{\pi}{2}}|r_p(\theta_r)|^2 d\theta_r$$

with

$$r_p(\theta_r) = \int_0^T dt \quad e^{-ik^+(\sin\theta_r x_D(t)+\cos\theta_r D(t))}$$
$$\left[H(x_D(t), D(t))ik^+\left(-\sin\theta_r D'(t)+\cos\theta_r x_D'(t)\right)+\epsilon_+\gamma(t)L(x_D(t), D(t))\right] \quad .$$

The angular reflection coefficient is thus

$$\frac{\partial R}{\partial\theta}(\theta_r) = \frac{|r_p(\theta_r)|^2}{k^+\cos\theta_i|H_i|^2} \quad .$$

The specular reflection wave appears as a peak at $\theta_r = \theta_i$ in the plot of the angular reflection coefficient $\frac{\partial R}{\partial\theta}$ as a function of the reflected angle θ_r. The area under the peak gives the specular reflectivity.

59

2.2.4 Conclusion on the method

The problem of finding the EM field created when an incident plane wave impinges on an arbitrary-shaped metallic surface was converted into a set of equations. Two equivalent sets of integral equations were obtained for the two unknown source functions called H and L which are the magnetic field and its derivative on the surface S. As the source functions H and L appear in the reflectivity as well as in the expression of the magnetic and electric field at any point of the space, we see that they are central to the determination of the EM field and the optical properties of the system. In order to solve the surface integral equation numerically, the integral has to be expressed as a sum of discrete values of H and L on the surface. To do so, only a finite length of the metallic surface can be considered which is usually about 10 times the wavelength i.e. around a ten of micron. As the SPPs can propagate along the surface for lengths of several tens or hundreds of micron [51], there is no assurance that the physics can be correctly described. Moreover, the finite length of the profile is responsible for border effects and artifacts in the numerical simulations. To ensure that there is no border effect and that the solution is a physical one, we use periodic boundary conditions, which is equivalent to study gratings. There is another advantage to study gratings which is that we can choose the period of the system. By doing so, we can start by studying, in an exact way, very small grooves of gratings with a small period. We can then increase the complexity of the surface as well as the period to tend to the infinite rough surface. We present the surface integral equation method for the periodic system in the next section.

2.3 The SIE for an arbitrary-shaped periodic metallic surface

2.3.1 Description of the metallic grating and of the pseudo-periodic problem

Our system now consists of an incident TM polarized plane wave that impinges on a periodic metallic surface standing in a dielectric. The surface is periodized in the x direction with a period d as is represented in figure 2.6.

The entire surface S being periodic, it is sufficient to define it by the surface S_D of width d in the x-direction

$$S_D : t \in [0, T[\to \vec{r}(t) = \begin{pmatrix} x_D(t) \\ D(t) \end{pmatrix}$$

(2.37)

with $x_D(t)$ taking its values in [0,d[. Let us note that the interval is open at one end in order not to represent the border point twice.
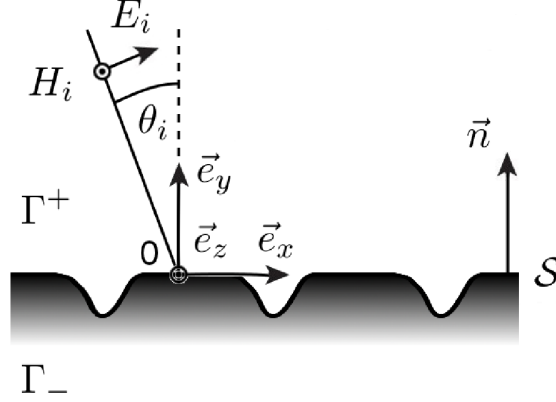
Figure 2.6: *Schematic representation of the grating profile and convention on the coordinates.*

The entire surface is deduced by translation of the first one as

$$S = \bigcup_{n=-\infty}^{\infty} S_n$$

with $\quad S_n : t \in [0, T[\to \vec{r}(t) = \begin{pmatrix} x_D(t) + nd \\ D(t) \end{pmatrix}$.

The surface is invariant by a translation of the period d in the x-direction however this is not the case of the problem. To see that, we consider that the entire space is divided in slices whose length in the x direction is equal to the period. As the surface is a grating, the profile in each slice is identical. However, the phase of the incident plane wave shifts of $\alpha_0 d$ where α_0 is the incident wavevector component along the x-direction, between two points where the second point is translated from the first one by the period d. When overlapping two slices, the incident field modulus is identical but the phase of two overlapping points is shifted by a number n of times $\alpha_0 d$ where n is equal to the number of period between the two points. The problem is then pseudo-periodic as the incident wave is and so are all the EM fields. The problem of an infinite metallic surface S can thus be reduced to the one of a surface over only one period when the pseudo-periodicity is taken into account. In the next paragraph, we define the pseudo-periodicity more rigorously and we describe the changes from the non-periodic problem.

2.3.2 Pseudo-periodicity of the problem

The system, i.e. the metallic surface standing in a dielectric, is periodic with a period d in the x-direction. In the same direction, the incident plane wave is also periodic but with a different period $2\pi/\alpha_0$ where α_0 is equal to the incident wavevector component along the x-direction $\alpha_0 = k_+ \sin \theta_i$. As a result, the incident field H_i is pseudo-periodic

$$H_i(x + d, y) = H_i(x, y) e^{i\alpha_0 d} \tag{2.38}$$

61

with a phase shift $\alpha_0 d$. While the incident plane wave is responsible for the pseudo-periodicity of the problem, it does not mean that it is the only admissible exciting wave. Any exciting field that is a harmonic TM polarized pseudo-periodic wave and fulfills the Maxwell equations and the radiation condition may be introduced in the surface integral equation as an incident field H_i. The EM field response is driven by the incident field and so the pseudo-periodicity of the incident field induces the pseudo-periodicity of the magnetic field in the whole space $\Gamma^+ \cup \Gamma^-$ (see more details in B.3.1.1). As the pseudo-periodicity comes from the incident field pseudo-periodic phase shift, the phase shift for H_z, $\alpha_0 d$, is the same, whatever the medium in which the magnetic field H_z is.

Let us examine the changes in the equations of the problem with respect to the non-periodic one. The Maxwell equations and the radiation condition are modified whereas the boundary conditions at the interface are exactly the same. The Maxwell equations are modified in the sense that the source term $\tilde{\rho}$ has to be pseudo-periodic. All the source points are repeated over each period of the grating and their phase is shifted by $\alpha_0 d$. The Dirac sum of all the source points above one period of the grating is now a pseudo-periodic Dirac. With the equation B.4 in appendix B, the Dirac becomes

$$\delta(\vec{r}' - \vec{r}) \rightarrow \sum_{n=-\infty}^{+\infty} \delta(\vec{r}' - (\vec{r} + nd\vec{e}_x))e^{i\alpha_0 nd} \quad .$$

Although it does not appear in the final equations, for the sake of clarity, $\tilde{\rho}$ may be defined as

$$\tilde{\rho} : \vec{r} \rightarrow \sum_{n=-\infty}^{+\infty} \sum_{i} \rho(\vec{r})\delta(\vec{r} - (\vec{r}_i + nd\vec{e}_x))e^{i\alpha_0 nd}$$

with $\vec{r}_i$ the source points being in Γ^+ with an abscissa belonging to [0,d[. The problem being "pseudo-invariant" by translation in the x-direction, there are incoming and outgoing waves in the x-direction at infinity and the radiation condition must change. In order to be well-conditioned, the problem only has to specify the behavior of the waves at the infinite in the y-direction as the behavior of the waves in the x-direction is managed by the periodic boundary condition. The radiation condition thus becomes

$$\lim_{y \rightarrow \pm\infty} \frac{\partial H_z^\pm}{\partial y} \mp ik_y H_z^\pm = 0 \quad . \tag{2.39}$$

Now that we saw the re-definition of the problem for a periodic profile of the metallic surface, we present how the Green function, which is a fundamental solution of the problem, is re-defined accordingly.

2.3.3   Pseudo-periodic Green's function

The Green function of a pseudo-periodic problem changes in only one way with respect to the non-periodic case: the Dirac in the Helmholtz equation becomes a pseudo-periodic

Dirac comb and the Green function itself becomes pseudo-periodic (demonstration in B.3.1.3). The phase shift on a period of the Green function depends on the convention taken for the Helmholtz equation i.e. whether the Dirac is $\delta\left(\vec{r}' - \vec{r}\right)$ or on the contrary $\delta\left(\vec{r} - \vec{r}'\right)$. In this thesis, I have chosen the first case. In order to have a lighter writing of the equations, (x, y) will stand from now on for the coordinates of $\vec{r}' - \vec{r}$. Thus the Dirac in the pseudo-periodic case becomes

$$\delta(x) \rightarrow \sum_{n=-\infty}^{\infty} \delta(x - nd) e^{i\alpha_0 nd} \quad .$$

The Green function must then be pseudo-periodic

$$\tilde{G}^{\pm}(x + d, y) = \tilde{G}^{\pm}(x, y) e^{i\alpha_0 d} \quad , \tag{2.40}$$

with a phase-shift $\alpha_0 d$. It also satisfies the Helmholtz equation

$$\forall (x, y) \in \Gamma^{\pm} \qquad \Delta\tilde{G}^{\pm}(x, y) + k^{\pm 2}\tilde{G}^{\pm}(x, y) = -\left(\sum_{n=-\infty}^{\infty} \delta(x - nd) e^{i\alpha_0 nd} \right) \delta(y) \tag{2.41}$$

and the radiation condition

$$\lim_{y \to \pm\infty} \frac{\partial \tilde{G}^{\pm}(\vec{r}, \vec{r}')}{\partial y} \mp i k_y \tilde{G}^{\pm}(\vec{r}, \vec{r}') = 0 \quad , \tag{2.42}$$

in order to be the pseudo-periodic Green function associated with our problem.

One way to express the pseudo-periodic Green function is to express the problem in terms of the free space one. Each term of the sum in the Helmholtz equation for the pseudo-periodic Green function, equation 2.41, resembles the Helmholtz equation of the Green function, equation 2.13, whose solution is the Hankel function as already seen in section 2.2.2.1. Therefore the solution of each term $\delta(x - md)\delta(y)$ is :

$$-\delta(x - md)\delta(y) \leftrightarrow \frac{i}{4} H_0^{(1)}(k^{\pm} r_m)$$

with $r_m = \sqrt{(x - md)^2 + y^2}$. The Green function $\tilde{G}_{HS}^{\pm}$, where the subscript HS stands for Hankel functions Sum, may thus be expressed as a sum of Hankel functions:

$$\tilde{G}_{HS}^{\pm}(x, y) = \frac{i}{4} \sum_{m=-\infty}^{\infty} H_0^{(1)}(k^{\pm} r_m) e^{im\alpha_0 d} \quad . \tag{2.43}$$

An example of this pseudo-periodic Green function may be seen in figure 2.7. The real part (blue line) diverges at every point of the x-axis whose abscissa is a multiple of the period d, whereas the imaginary part (red line) is finite in the same way as the Green function is in a non-periodic medium.

Another way of calculating the pseudo-periodic Green function is done by expressing the Green Function as a Fourier series and solving the equations 2.41 and 2.42 for each coefficient (see the demonstration in appendix B.3.2) which gives the Green function expressed as a sum of plane waves:

$$\tilde{G}_{WS}^{\pm}(x, y) = -\frac{1}{2id} \sum_{m=-\infty}^{\infty} \frac{e^{i\alpha_m x} e^{i\beta_m^{\pm}|y|}}{\beta_m^{\pm}} \tag{2.44}$$
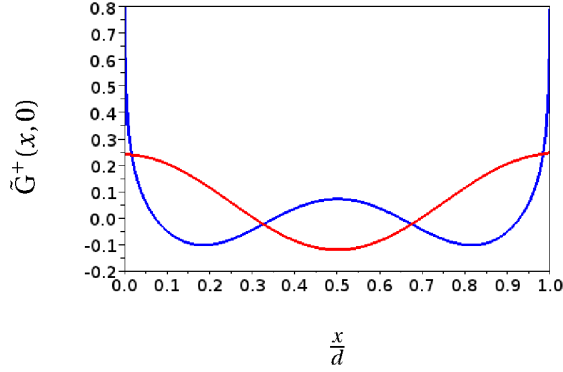
Figure 2.7: *Behavior of the real (blue) and imaginary (red) parts of the pseudo-periodic Green function $\tilde{G}^+$ for $\lambda = 0.75d$, $\epsilon_+ = 1$ and $\theta = 0°$ calculated by the method presented in section 2.4.1.4.*

with $\alpha_n = \alpha_0 + \frac{2\pi}{d}n$, $\beta_n^\pm = \sqrt{k^{\pm 2} - \alpha_n^2}$ and $\Re\beta_n^\pm > 0$. The subscript WS denotes a plane Wave Sum. In fact, there exists many different representations for the pseudo-periodic Green function $\tilde{G}$. For numerical reasons, another expression of $\tilde{G}$ has been needed in addition to the two presented here above. It will be described when we give further details on the numerical calculation of $\tilde{G}$ in the section dedicated to the simulation, section 2.4.

$\tilde{G}$ indicates from now on that the Green function which is used is the pseudo-periodic one. We present in the next section how the Green theorem is applied to the periodic case.

2.3.4 The Green theorem for a periodic system

The main difference in the application of the Green theorem is that the chosen volume is limited to a slice of the entire volume which contains the grating exactly over a period. The volume $\tilde{\Gamma}^+$ is chosen to be a unit cell of Γ^+. The with d of $\tilde{\Gamma}^+$ in the x direction is equal to the period d. Its boundary forms a rectangle except at the bottom where it is limited by the metallic surface S as represented in figure 2.8. Accordingly the boundary $\tilde{S}$ can be divided into four pieces, the left and right vertical boundaries S_{left} and S_{right}, the top horizontal boundary $S_{+\infty}$ at a fixed ordinate $y \to \infty$ and the bottom boundary that is identical to the metallic surface S_D. The Green theorem, equation 2.18, is applied in the same way to $H_z^\pm$ and $\tilde{G}^\pm$ for the volume $\tilde{\Gamma}^+$ and gives

$$\int_{\tilde{\Gamma}^+} \left[H_z^\pm(\vec{r})\Delta\tilde{G}^\pm\left(\vec{r}' - \vec{r}\right) - \tilde{G}^\pm\left(\vec{r}' - \vec{r}\right)\Delta H_z^\pm(\vec{r}) \right] dV(\vec{r})$$
$$= \oint_{\tilde{S}} \left[H_z^\pm(\vec{r})\frac{\partial\tilde{G}^\pm}{\partial\vec{n}}\left(\vec{r}' - \vec{r}\right) + \tilde{G}^\pm\left(\vec{r}' - \vec{r}\right)\frac{\partial H_z^\pm}{\partial\vec{n}}(\vec{r}) \right] dS(\vec{r}) \quad . \tag{2.45}$$

64
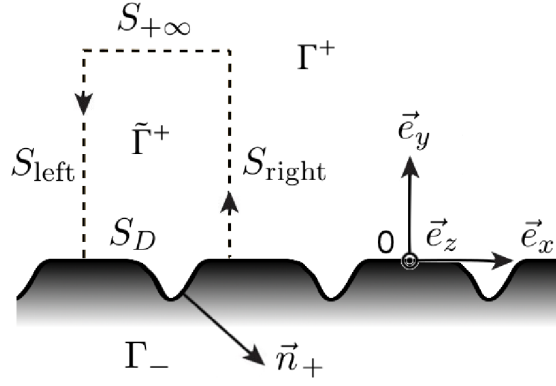
Figure 2.8: *Definition of the volume $\tilde{\Gamma}^+$ delimited by an oriented boundary: the surface $\tilde{S}$ composed of the segment S_D (solid line) and the segment S_{left}, S_{right} and $S_{+\infty}$ (dashed line).*

We define the new integrated function $\tilde{F}$ as

$$\tilde{F}\left(\vec{r}, \vec{r}'\right) = H_z^{\pm}(\vec{r}) \frac{\partial \tilde{G}^{\pm}}{\partial \vec{n}}(\vec{r}' - \vec{r}) + \tilde{G}^{\pm}(\vec{r}' - \vec{r}) \frac{\partial H_z^{\pm}}{\partial \vec{n}}(\vec{r}) \quad .$$

As the entire demonstration is similar to the non-periodic case, we just admit here that the integral over $S_{+\infty}$ is null due to the radiation condition at infinity. The integral over S_D is not modified either. Therefore, we detail only the integrals over S_{right} and S_{left} which are new.

The Green function $\tilde{G}^{\pm}$ and the magnetic field $H_z^{\pm}$ are pseudo-periodic with a phase shift $\alpha_0 d$. If we translate $\tilde{G}^{\pm}(\vec{r}' - \vec{r}) H_z^{\pm}(\vec{r})$ as a function of $\vec{r}$ by a vector $d\vec{e}_x$ we have

$$\tilde{G}^{\pm}(\vec{r}' - (\vec{r} + d\vec{e}_x)) H_z^{\pm}(\vec{r} + d\vec{e}_x) = e^{-i\alpha_0 d} \tilde{G}^{\pm}(\vec{r}' - \vec{r}) e^{i\alpha_0 d} H_z^{\pm}(\vec{r})$$

so $\tilde{G}^{\pm}(\vec{r}' - \vec{r}) H_z^{\pm}(\vec{r})$ is periodic as a function of $\vec{r}$. Hence $\tilde{F}$ is also periodic as a function of $\vec{r}$ which gives

$$\int_{\vec{r} \in S_{left}} \tilde{F}\left(\vec{r}, \vec{r}'\right) dS(\vec{r}) = \int_{\vec{r} \in S_{left}} \tilde{F}\left(\vec{r} + d\vec{e}_x, \vec{r}'\right) dS(\vec{r})$$

$$= \int_{\vec{r} + d\vec{e}_x \in S_{left}} \tilde{F}\left(\vec{r}, \vec{r}'\right) dS(\vec{r}) \quad .$$

The plane S_{right} is the translation of the plane S_{left} by the vector $d\vec{e}_x$ although they are oriented in opposite direction so

$$\int_{S_{left}} \tilde{F}\left(\vec{r}, \vec{r}'\right) dS(\vec{r}) = -\int_{S_{right}} \tilde{F}\left(\vec{r}, \vec{r}'\right) dS(\vec{r})$$

such that

$$\int_{S_{left}} \tilde{F}\left(\vec{r}, \vec{r}'\right) dS(\vec{r}) + \int_{S_{right}} \tilde{F}\left(\vec{r}, \vec{r}'\right) dS(\vec{r}) = 0 \quad . \tag{2.46}$$

65

As we mentioned earlier, there is no need for a radiation condition in the x-direction as we ensure having a physical solution with the periodic boundary condition. Indeed, the fluxes through the left and the right vertical boundaries cancel each others.

The rigorous way to treat the incident field is not different from the non-periodic case; we apply once again the Green Theorem for $\tilde{G}^+$ and H_i although we apply it for a different volume $\tilde{\Gamma}$ which is a slice of the entire volume with a width d. The new boundary forms a rectangle and follows the x and y axes. The vertical boundaries, S_{right} and S_{left}, are separated by a distance equal to the period d and the horizontal boundaries, $S_{+\infty}$ and $S_{-\infty}$, at the top and the bottom of the rectangle have their ordinates that tend to plus and minus the infinity respectively. Similarly, we have

$$H_i(\vec{r}^{\,'}) = \int_{\tilde{\Gamma}^+} \left[\tilde{G}^+(\vec{r}^{\,'} - \vec{r}) \tilde{\rho}(\vec{r}) \right] dV(\vec{r}) \tag{2.47}$$

The last steps to obtain the integral equations is to susbstitute the integral pieces on the segments S_{left}, S_{right} and $S_{+\infty}$ and to substitute the Helmholtz equations for $\tilde{G}^+$ and H_z in the integral over the volume Γ^+. We obtain a set of integral equations, $\forall \vec{r}^{\,'} \in \tilde{\Gamma}^+$

$$\int_{S_D} \left[H_z^+(\vec{r}) \frac{\partial \tilde{G}^+}{\partial \vec{n}}(\vec{r}^{\,'} - \vec{r}) + \tilde{G}^+(\vec{r}^{\,'} - \vec{r}) \frac{\partial H_z^+}{\partial \vec{n}}(\vec{r}) \right] dS(\vec{r}) = H_i(\vec{r}^{\,'}) - H_z^+(\vec{r}^{\,'}) \quad , \tag{2.48}$$

$$\int_{S_D} \left[H_z^-(\vec{r}) \frac{\partial \tilde{G}^-}{\partial \vec{n}}(\vec{r}^{\,'} - \vec{r}) + \tilde{G}^-(\vec{r}^{\,'} - \vec{r}) \frac{\partial H_z^-}{\partial \vec{n}}(\vec{r}) \right] dS(\vec{r}) = 0 \quad . \tag{2.49}$$

We can directly verify that the integral equation which is a function of $\vec{r}^{\,'}$ is pseudo-periodic from the pseudo-periodicity of $H_z^\pm$, H_i and $\tilde{G}^\pm$.
Eventually, we obtain self-coherent equations for the source functions H and L

$$\int_{S_D} \left[H(\vec{r}) \frac{\partial \tilde{G}^+}{\partial \vec{n}}(\vec{r}^{\,'} - \vec{r}) + \epsilon_+ \tilde{G}^+(\vec{r}^{\,'} - \vec{r}) L(\vec{r}) \right] dS(\vec{r}) + \frac{1}{2} H(\vec{r}^{\,'}) = H_i(\vec{r}^{\,'}) \quad , \tag{2.50}$$

$$\int_{S_D} \left[H(\vec{r}) \frac{\partial \tilde{G}^-}{\partial \vec{n}}(\vec{r}^{\,'} - \vec{r}) + \epsilon_- \tilde{G}^-(\vec{r}^{\,'} - \vec{r}) L(\vec{r}) \right] dS(\vec{r}) - \frac{1}{2} H(\vec{r}^{\,'}) = 0 \quad . \tag{2.51}$$

The source functions H and L are looked for only on a finite surface S_D so we will not have to deal with an infinite surface numerically.

We see that the pseudo-periodic surface integral equations can be retrieved from the non-periodic ones by substituting the pseudo-periodic Green function $\tilde{G}$ to G and by integrating over a period of the grating surface S_D instead of the entire surface S. The magnetic and electric field expressions in the pseudo-periodic problem are expressed accordingly. While the magnetic and electric field are expressed in a similar manner, the reflectivity expression changes as the reflection of a wave on a grating is done in particular directions, the diffracted orders. We detail the reflectivity in the next paragraph as it is now expressed as a function of the diffracted orders instead of all the possible directions.

2.3.5 Reflectivity

Maradudin [91] did not treat the reflectivity in the periodic case. A paragraph on this matter may however be found p.12 in [117].

To obtain the reflectivity of a periodic system, one has to seek the amplitude R_m of the mth diffracted orders. The reflectivity of the mth order is $|R_m|^2 \frac{\beta_m}{\beta_0}$ for real β_m with a Rayleigh expansion of the diffracted field H_r as

$$H_r(\vec{r}) = \sum_{m=-\infty}^{\infty} R_m e^{i\alpha_m x} e^{i\beta_m^+ y}$$

with $\alpha_m = \alpha_0 + \frac{2\pi}{d} m$, $\beta_m^+ = \sqrt{k^{+2} - \alpha_m^2}$ and $\Re\left(\beta_m^+\right) > 0$.

We want to highlight that the reflectivity is measured in the far-field region which is directly related to the fact that the mth diffracted orders have a real β_m. Indeed, we can see in the Rayleigh expansion that only the plane waves with a real β_m are propagating. The scattered far-field is obtained by subtracting the incident field H_i to the total field H_z, hence

$$H_r(\vec{r}') = -\int_{S_D} \left[H(\vec{r}) \frac{\partial G^+}{\partial \vec{n}}(\vec{r}' - \vec{r}) + \epsilon_+ G^+(\vec{r}' - \vec{r}) L(\vec{r}) \right] dS(\vec{r}) \quad .$$

In order to obtain the amplitude R_m by identification, we will substitute the Green function expressed as a sum of plane waves, equation 2.44 into the following equation. Using the parametric representation for $\vec{r}(t) = (x_D(t), D(t))$, the pseudo-periodic Green function $\tilde{G}$ and its derivative with respect to $\vec{r}$

$$\tilde{G}_{WS}^+(\vec{r}' - \vec{r}) = -\frac{1}{2id} \sum_{m=-\infty}^{\infty} \frac{e^{i\alpha_m(x' - x_D(t))} e^{i\beta_m^+|y' - D(t)|}}{\beta_m^+} \quad ,$$

$$\frac{\partial \tilde{G}_{WS}^+}{\partial \vec{n}}(\vec{r}' - \vec{r}) = -\frac{1}{2id\gamma(t)} \sum_{m=-\infty}^{\infty} \left(-i\alpha_m D'(t) + \text{sign}\left(y' - D(t)\right) i\beta_m^+ x_D'(t)\right) \frac{e^{i\alpha_m(x' - x_D(t))} e^{i\beta_m^+|y' - D(t)|}}{\beta_m^+} \quad .$$

As we evaluate the field in the far-field region, we consider the asymptotes of these two Green functions which are:

$$y' \to +\infty \qquad \tilde{G}_{WS}^+(\vec{r}' - \vec{r}) = -\frac{1}{2id} \sum_{m=-\infty}^{\infty} \frac{e^{i\alpha_m(x' - x_D(t))} e^{i\beta_m^+(y' - D(t))}}{\beta_m^+} \quad ,$$

$$\frac{\partial \tilde{G}_{WS}^+}{\partial \vec{n}}(\vec{r}' - \vec{r}) = -\frac{1}{2id\gamma(t)} \sum_{m=-\infty}^{\infty} \left(-i\alpha_m D'(t) + i\beta_m^+ x_D'(t)\right) \frac{e^{i\alpha_m(x' - x_D(t))} e^{i\beta_m^+(y' - D(t))}}{\beta_m^+} \quad .$$

Introducing these asymptotic expressions in that of H_r, one finds the expression of the reflected wave at infinity $y' \to +\infty$

$$H_r(\vec{r}') = \int_{S_D} \left[H(\vec{r}) \frac{1}{2id\gamma(t)} \sum_{m=-\infty}^{\infty} \left(-i\alpha_m D'(t) + i\beta_m^+ x_D'(t)\right) \frac{e^{i\alpha_m(x' - x_D(t))} e^{i\beta_m^+(y' - D(t))}}{\beta_m^+} \right.$$
$$\left. + \epsilon_+ \frac{1}{2id} \sum_{m=-\infty}^{\infty} \frac{e^{i\alpha_m(x' - x_D(t))} e^{i\beta_m^+(y' - D(t))}}{\beta_m^+} L(\vec{r}) \right] dS(\vec{r}) \quad .$$

The expression of H_r is then written in the form of a Rayleigh expansion such as

$$H_r(\vec{r}\,') = \frac{1}{2id} \sum_{m=-\infty}^{\infty} \frac{e^{i\alpha_m x'} e^{i\beta_m^+ y'}}{\beta_m^+} I_m \quad ,$$

$$I_m = \int_{S_D} \left[H(\vec{r}) \frac{1}{\gamma(t)} (-i\alpha_m D'(t) + i\beta_m^+ x_D'(t)) + \epsilon_+ L(\vec{r}) \right] e^{-i\alpha_m x_D(t)} e^{-i\beta_m^+ D(t)} dS(\vec{r}) \quad . \quad (2.52)$$

By identification with the Rayleigh expansion, the reflection coefficient is

$$R_m = \frac{1}{2id\beta_m^+} I_m \quad (2.53)$$

and the reflectivity of the mth order, $|R_m|^2 \frac{\beta_m}{\beta_0}$ is directly obtained for real β_m.

We have presented the modeling of the system. In order to solve the problem and to calculate the physical quantities we are interested in, we now have to choose a numerical method and to implement it. The simulation is described in the next section.

2.4   Simulation

There is no simple analytical solutions for surface integral equations over arbitrary-shaped metallic surfaces and a numerical resolution has to be done. We followed the lead of Maradudin who solved the equations by discretizing each integral into a sum of integrals over small segments of the metallic surface [91]. His method was, however, adapted to the periodic surfaces cases we treat and is presented in this section. First of all, we detail how the pseudo-periodic Green function is calculated. Then we present how we solved the system of self-coherent equations in the same way as Maradudin did. Eventually the magnetic and electric field maps as well as the reflectivity calculations are described.

2.4.1   The evaluation of the Pseudo-periodic Green function

There are many ways to express the pseudo-periodic Green function. All of them require to calculate series whose convergence depends on the initial parameters (θ, λ), the permittivity, and the point of space where the Green function is evaluated. Some recent work was published on rapidly convergent Green's functions (2D or 3D) since it is one of the most problematic issues [95, 118, 119]. However we found the work from Linton [120] comparing the different representations of the periodic 2D Green function to be the most comprehensive study. This section presents three of the Green function possible representation (two have already been introduced in the previous section) and shows the strategy we used to calculate the pseudo-periodic Green function in the most efficient way as possible.

To study and compare the convergence behavior of these three Green functions and their best domain of relevance, we have calculated them in two different regions of the

space: close to (resp. far) from the origin $\vec{r} = (10^{-4}, 0) \approx \vec{0}$ (resp. $\vec{r} = (0.5, 2) \gg \vec{0}$) and for two different values of the permittivity : $\epsilon = 1$ standing for a dielectric permittivity and $\epsilon = -17.0375 + i1.14963$ standing for a metallic permittivity. The coordinates have been normalized with the period d. The other parameters were chosen arbitrarily in the range of applications of this thesis $\theta = 22.5°$, $\lambda = 10d$, d= 65 nm. To be at ease with the legends of the following figures, each case is associated with a color as sketched in figure 2.9. I recall that (x, y) stands for the coordinates of $\vec{r}' - \vec{r}$ throughout the whole pseudo-periodic Green function section. For the evaluation of the Bessel family functions, I have used Amos *et al.* algorithms [121] implemented in Fortran 90 subroutines available at the ACM Digital Library.

$\epsilon = 1 > 0$
$\vec{r} = (0.5, 2) \gg \vec{0}$
$\epsilon = -17.0375 + i1.14963 < 0$
$\vec{r} = (0.5, 2) \gg \vec{0}$

$\theta_i = 22.5°$

d= 65 nm

$\lambda = 10d$

$\theta_i \; \vec{e}_y$

$\epsilon = 1 > 0$
$\vec{r} = (10^{-4}, 0) \approx \vec{0}$
$\epsilon = -17.0375 + i1.14963 < 0$
$\vec{r} = (10^{-4}, 0) \approx \vec{0}$

$0 \; \vec{e}_z$ $\quad \vec{e}_x$
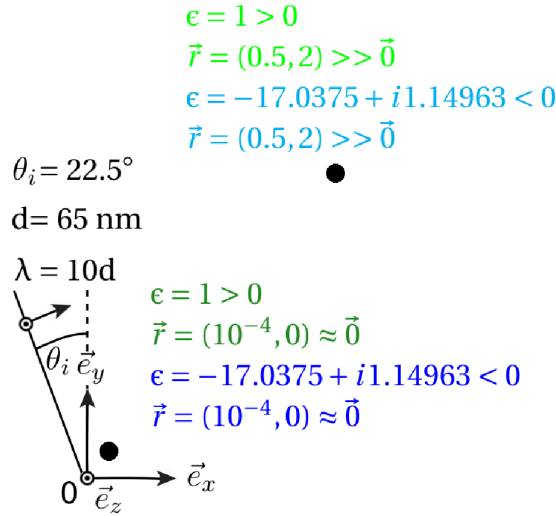
Figure 2.9: *Schematic representation of the four cases for which the Green functions are calculated and their associated colors. Green and blue colors are $\epsilon > 0$ and $\epsilon < 0$ respectively. Points which are close to the surface are represented in dark colors whereas points which are far from it are represented in light color. Coordinates have been normalized with the period d. The incident field parameters are given on the left.*

As the expression of the pseudo-periodic function derivatives was not found in the literature, their expressions will also be detailed. To be as general as possible we will seek the derivatives $\frac{\partial}{\partial \bar{n}_0} = n_x \frac{\partial}{\partial x} + n_y \frac{\partial}{\partial y}$ and do not express n_x and n_y more specifically. The derivatives up to the second order have been looked for. The second order derivatives may be found in the appendix B.3.4. The conditions of the convergence of the pseudo-periodic Green function derivatives are very similar to that of the Green function and are treated numerically in the same way.

2.4.1.1 Green's function $\tilde{G}_{HS}$ GHS expressed as a sum of the Hankel functions

We recall that the pseudo-periodic Green function $\tilde{G}^\pm$ may be written as a sum of Green functions $G^\pm$ i.e. as a sum of Hankel functions

$$\tilde{G}_{HS}^\pm(x,y) = \frac{i}{4} \sum_{m=-\infty}^{\infty} H_0^{(1)}(k^\pm r_m) e^{im\alpha_0 d} \quad .$$

with $r_m = \sqrt{(x-md)^2 + y^2}$.

Its derivative is obtained from that of the Hankel one, formula (9.1.27) p. 361 in [115], $\forall z \in \mathbb{C}$

$$\frac{\partial H_0^{(1)}}{\partial z}(z) = -H_1^{(1)}(z) \tag{2.54}$$

and is thus given by

$$\frac{\partial \tilde{G}_{HS}^\pm}{\partial \vec{n}_0}(x,y) = -\frac{i}{4} \sum_{m=-\infty}^{\infty} k^\pm \frac{n_y y + n_x(x-md)}{r_m} H_1^{(1)}(k^\pm r_m) e^{im\alpha_0 d} \quad .$$

To calculate $\tilde{G}_{HS}^\pm$, we consider the first 2M terms of the sum and we define $\left[\tilde{G}_{HS}^\pm\right]_M$ as this sum which can be written as

$$\left[\tilde{G}_{HS}^\pm\right]_M(x,y) = \frac{i}{4} H_0^{(1)}(k^\pm r_0) + \frac{i}{4} \sum_{m=1}^{M} \left[H_0^{(1)}(k^\pm r_m) e^{im\alpha_0 d} + H_0^{(1)}(k^\pm r_{-m}) e^{-im\alpha_0 d} \right] \quad . \tag{2.55}$$

The convergence of $\left[\tilde{G}_{HS}^\pm\right]_M$ is shown in figure 2.10 by plotting the value of $\left[\tilde{G}_{HS}^\pm\right]_M$ as a function of M. We see that the convergence depends on the asymptotic behavior of the Hankel function, equation 2.17. In a dielectric the wavevector k_+ is real and the convergence follows $\frac{e^{ik_+ r_m}}{\sqrt{k_+ r_m}} \approx \frac{1}{\sqrt{m}}$ (green curves) whereas, in a metal, the wavevector k_- is mostly imaginary. Therefore the convergence is exponential $\frac{e^{ik_- r_m}}{\sqrt{k_- r_m}} \approx \frac{e^{-|k_-|m}}{\sqrt{m}}$ (blue curves) and for good conductors, a relative precision of 10^{-16} is reached with only two terms. This expression of the Green function is thus very suitable in the metallic domain.

2.4.1.2 Green's function $\tilde{G}_{WS}$ GWS expressed a a sum of plane wave

Another way of calculating the pseudo-periodic Green function is done by expressing the Green Function as a Fourier series and solving the equations 2.41 and 2.42 for each coefficient (see the demonstration in appendix B.3.2) which gives

$$\tilde{G}_{WS}^\pm(x,y) = -\frac{1}{2id} \sum_{m=-\infty}^{\infty} \frac{e^{i\alpha_m x} e^{i\beta_m^\pm |y|}}{\beta_m^\pm} \quad ,$$

with $\alpha_m = \alpha_0 + \frac{2\pi}{d} m$, $\beta_m^\pm = \sqrt{k^{\pm 2} - \alpha_m^2}$ and $\Re \beta_m^\pm > 0$.

70
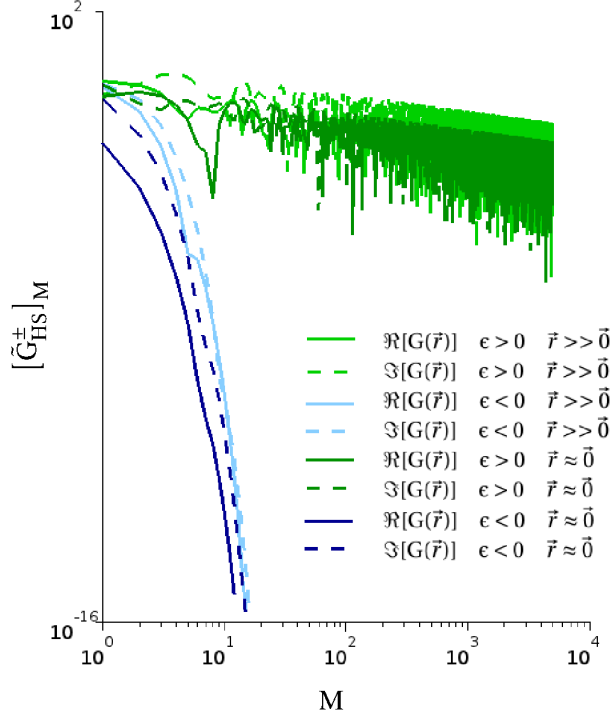
Figure 2.10: *Value of* $\left[\tilde{G}^{\pm}_{HS}\right]_M (x, y)$ *as a function of the number of added terms M in the sum defined in the equation 2.55 and calculated for the 4 cases shown in figure 2.9. We recall that green and blue colors are* $\epsilon > 0$ *and* $\epsilon < 0$ *respectively. Dark and light color are* $(x, y) = (0.5, 2)$ *and* $(x, y) = (10^{-4}, 0)$ *respectively. Real and imaginary part of* $\left[\tilde{G}^{\pm}_{HS}\right]_M$ *are shown in straight and dashed lines respectively.*

Its derivative expresses as

$$\frac{\partial \tilde{G}^{\pm}_{WS}}{\partial \vec{n}_0}(x, y) = -\frac{1}{2id} \sum_{m=-\infty}^{\infty} (i\alpha_m n_x + \text{sign}(y) i\beta^{\pm}_m n_y) \frac{e^{i\alpha_m x} e^{i\beta^{\pm}_m |y|}}{\beta^{\pm}_m}$$

with $\beta^{\pm}_m = \sqrt{k^{\pm 2} - \alpha^2_m}$.

The infinite sum is truncated in the same way as previously

$$\left[\tilde{G}^{\pm}_{WS}\right]_M (x, y) = -\frac{1}{2id} \frac{e^{i\alpha_0 x} e^{i\beta^{\pm}_0 |y|}}{\beta^{\pm}_0} - \frac{1}{2id} \sum_{m=1}^{M} \left[\frac{e^{i\alpha_m x} e^{i\beta^{\pm}_m |y|}}{\beta^{\pm}_m} + \frac{e^{i\alpha_{-m} x} e^{i\beta^{\pm}_{-m} |y|}}{\beta^{\pm}_{-m}} \right] \quad . \quad (2.56)$$

In this case, the convergence of $\left[\tilde{G}^{\pm}_{WS}\right]_M$, shown in figure 2.11, depends strongly on the point where the Green function is evaluated (light versus dark colored curves). With increasing M, the convergence is guaranteed by the terms $\frac{e^{i\beta_m |y|}}{\beta_m} \approx \frac{e^{-m|y|}}{im}$. Near the singularity and for $y = 0$, the method fails (dark curves). Otherwise, the convergence is exponential (light curves).

We may define a new sum $\tilde{G}_{WS\text{-bis}}$ from $\tilde{G}^{\pm}_{WS}$, whose convergence is quickened by using Kummer's transformation. In a nutshell, one subtracts a series u_m to $e^{i\beta^{\pm}_m |y|}/\beta^{\pm}_m$ for each m in
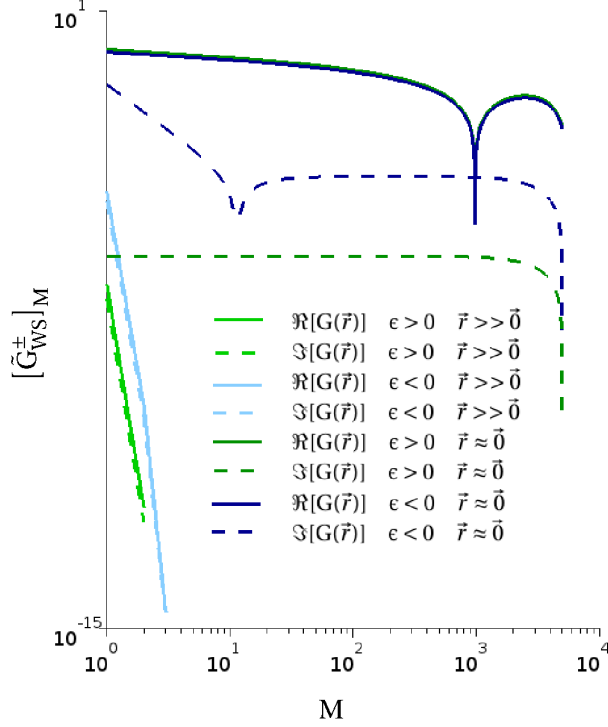
Figure 2.11: *Values of* $\left[\tilde{G}^{\pm}_{WS}\right]_M (x,y)$ *plotted as a function of the number of added terms M, as defined in equation 2.56, calculated for the 4 cases shown in figure 2.9.*

the sum of plane waves of $\tilde{G}_{WS}$ and then adds back the sum of u_m over all m, which appear in $\tilde{G}_{WS\text{-bis}}$ as the term S. The convergence of the sum of plane waves over m of $\tilde{G}_{WS}$ is improved near the singularity as u_m is chosen to be the asymptote of the plane wave term $e^{i\beta^{\pm}_m|y|}/\beta^{\pm}_m$ as m tends to infinity. We then write

$$\tilde{G}^{\pm}_{WS\text{-bis}}(x,y) = -\frac{e^{i\alpha_0 x}}{2id}\left\{\frac{e^{i\beta^{\pm}_0|y|}}{\beta^{\pm}_0} + S + \sum_{m=\mathbb{Z}\backslash\{0\}}\left(\frac{e^{i\beta^{\pm}_m|y|}}{\beta^{\pm}_m} - u_m(y)\right)e^{impx}\right\} \qquad (2.57)$$

$$\text{with} \qquad p = \frac{2\pi}{d} \quad,$$

$$S = e^{-\alpha_0|y|}\left(\frac{1}{p}Li_1(e^{-p(-ix+|y|)}) - \frac{2\alpha_0 - k^{\pm^2}|y|}{2p^2}Li_2(e^{-p(-ix+|y|)})\right)$$

$$+ e^{\alpha_0|y|}\left(\frac{1}{p}Li_1(e^{-p(ix+|y|)}) - \frac{2\alpha_0 + k^{\pm^2}|y|}{2p^2}Li_2(e^{-p(ix+|y|)})\right) \quad,$$

$$u_m(y) = \frac{e^{-(|m|p+sgn(m)\alpha_0)|y|}}{|m|p}\left(1 - \frac{\alpha_0}{mp} + \frac{k^{\pm^2}|y|}{2|m|p}\right) \quad.$$

Li_s is the polylogarithm function defined by $Li_s(z) = \sum_{m=1}^{+\infty}\frac{z^m}{m^s}$. Compared to the performance of the Green function $\tilde{G}^{\pm}_{WS}$ expressed as a sum of plane waves, the one of $\tilde{G}_{WS\text{-bis}}$ is improved near the singularity (comparison of the dark curves in figures 2.11 and 2.12). However, we will see in the next paragraph that the Green function $\tilde{G}_{LS}$ expressed with lattice

sums converges faster near the singularity. Moreover, the polylogarithm function is really long to calculate, therefore this expression of the Green function has been dropped out.
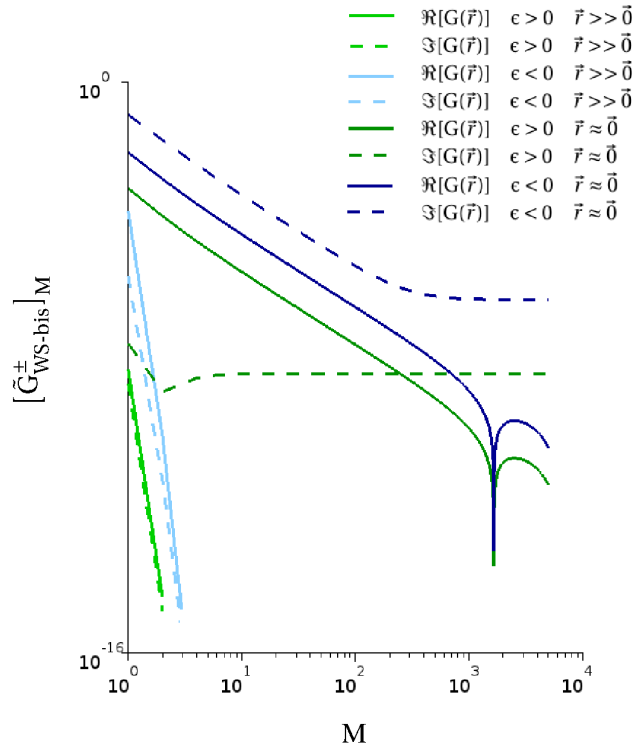
Figure 2.12: *Values of* $\left[\tilde{G}^{\pm}_{WS\text{-}bis}\right]_M (x, y)$ *as a function of the number of added terms M as defined in equation 2.57 calculated for the 4 cases shown in figure 2.9.*

2.4.1.3 Green's function $\tilde{G}_{LS}$GLS expressed with Lattice Sums

The last case we will study, is derived from $\tilde{G}_{HS}$. The convergence of the series is here quickened by using Graf's theorem to express the sum of the Hankel functions taken at r_m as a sum of the Bessel functions of the first kind near r (see more details in the appendix B.3.3). The Green function $\tilde{G}_{LS}$, where the subscript LS denotes the Lattice Sums, is

$$\tilde{G}_{LS}(x, y) = \frac{i}{4} \left\{ H_0^{(1)}(k^{\pm}r) + \sum_{l=0}^{\infty} (2 - \delta_{l,0}) S_l^{\pm} J_l(k^{\pm}r) \cos(\theta l) \right\}$$

$$\text{with} \quad S_l^{\pm} = \sum_{m=-\infty}^{\infty} e^{im\alpha_0 d} H_l^{(1)}(|m|k^{\pm}d) e^{il\phi_m}$$

$$\text{and} \quad \phi_m = \begin{cases} \pi & \text{if} \quad m < 0 \\ 0 & \text{if} \quad m > 0 \end{cases}$$

where (r, θ) are the polar coordinates equivalent to (x,y).

Let us now consider the derivative $\frac{\partial \tilde{G}_{LS}}{\partial \vec{n}_0}$. Since $\tilde{G}_{LS}$ is given in polar coordinates, the derivative operator $\vec{n}_0 \vec{\nabla}$ has to be in similar coordinates. The expression of the vector $\vec{n}_0$ in polar coordinates is

$$\begin{pmatrix} n_r(r,\theta) \\ n_\theta(r,\theta) \end{pmatrix} = \begin{pmatrix} \cos\theta & \sin\theta \\ -\sin\theta & \cos\theta \end{pmatrix} \begin{pmatrix} n_x \\ n_y \end{pmatrix} = \begin{pmatrix} n_y \sin\theta + n_x \cos\theta \\ n_y \cos\theta - n_x \sin\theta \end{pmatrix}$$

then

$$\vec{n}_0 . \vec{\nabla} = n_r \frac{\partial}{\partial r} + n_\theta \frac{\partial f}{r \partial \theta} \quad .$$

The sum terms are derived as

$$\frac{\partial}{\partial \vec{n}_0} J_l(k^\pm r) \cos(\theta l) = n_r \frac{\partial}{\partial r} J_l(k^\pm r) \cos(\theta l) + n_\theta \frac{\partial}{r \partial \theta} J_l(k^\pm r) \cos(\theta l)$$

$$= n_r J_l'(k^\pm r) \cos(\theta l) - l \frac{n_\theta}{r} J_l(k^\pm r) \sin(\theta l) \quad .$$

We have from [115], formula (9.1.27) p. 361, $\forall z \in \mathbb{C}$

$$J_l'(z) = \frac{J_{l-1}(z) - J_{l+1}(z)}{2}$$

and

$$\frac{J_l(z)}{z} = \frac{J_{l-1}(z) + J_{l+1}(z)}{2l} \quad .$$

Substituting the previous properties for every term in the sum which contains $J_l'(k^\pm r)$ and $\frac{J_l(k^\pm r)}{r}$, the expression of $\frac{\partial \tilde{G}_{LS}}{\partial \vec{n}_0}$ is found to be

$$\frac{\partial \tilde{G}_{LS}}{\partial \vec{n}_0}(x,y) = \frac{i}{4} \left\{ -n_r k^\pm H_1^{(1)}(k^\pm r) \right.$$

$$\left. + \sum_{l=0}^{\infty} (2 - \delta_{l,0}) S_l^\pm \frac{k^\pm}{2} \left[(n_r \cos(\theta l) - n_\theta \sin(\theta l)) J_{l-1}(k^\pm r) - (n_r \cos(\theta l) + n_\theta \sin(\theta l)) J_{l+1}(k^\pm r) \right] \right\} \quad .$$

There is a way to compact the sum in order to have a simpler form to use afterwards. First a simplification using (4.3.16-17) from [115]:

$$n_r \cos(\theta l) - n_\theta \sin(\theta l) = -n_y \sin(\theta(l-1)) + n_x \cos(\theta(l-1))$$
$$n_r \cos(\theta l) + n_\theta \sin(\theta l) = n_y \sin(\theta(l+1)) + n_x \cos(\theta(l+1))$$

yields:

$$\frac{\partial \tilde{G}_{LS}}{\partial \vec{n}_0}(x,y) = \frac{i}{4} \left\{ -n_r k^\pm H_1^{(1)}(k^\pm r) + \sum_{l=0}^{\infty} (2 - \delta_{l,0}) S_l^\pm \frac{k^\pm}{2} \left[-C_{l-1} J_{l-1}(k^\pm r) + C_{-(l+1)} J_{l+1}(k^\pm r) \right] \right\}$$

$$= -k^\pm \frac{i}{4} \left\{ n_r H_1^{(1)}(k^\pm r) + \sum_{l=0}^{\infty} (2 - \delta_{l,0}) \frac{S_l^\pm}{2} \left[C_{l-1} J_{l-1}(k^\pm r) - C_{-(l+1)} J_{l+1}(k^\pm r) \right] \right\}$$

74

with $\forall l \in \mathbb{Z}$ $\quad$ $C_l = n_y \sin\theta l - n_x \cos\theta l$.

Here again, in order to study the convergence, we define

$$\left[\tilde{G}_{LS}\right]_L (x, y) = \frac{i}{4} \left\{ H_0^{(1)}(k^{\pm} r) + \sum_{l=0}^{L} (2 - \delta_{l,0}) S_l^{\pm} J_l(k^{\pm} r) \cos(\theta l) \right\} \tag{2.58}$$

as the sum over the L first terms. The $S_l^{\pm}$ term hide another infinite sum which is truncated to the first 2M terms such as

$$S_l^{\pm} = \sum_{m=-M}^{M} e^{im\alpha_0 d} H_l^{(1)}(|m|k^{\pm} d) e^{il\phi_m} \quad .$$

The convergence of the $S_l^{\pm}$ terms is not presented here as it does not enter in the comparison between the different Green function. However, since they depend on the incident parameters (λ, θ), they only need to be calculated once for all the coordinates (x,y). A large number of terms M is required for each $S_l^{\pm}$ and the numerical evaluation is thus very long, of the order of several seconds.
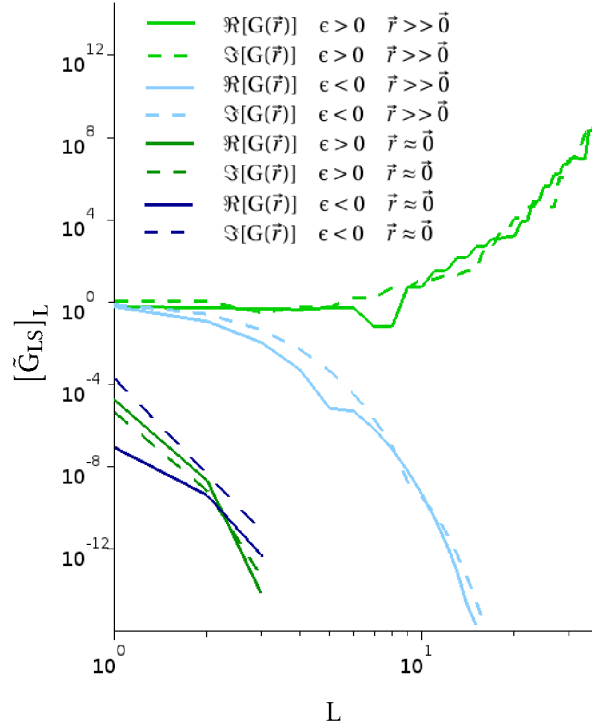
Figure 2.13: *Value of $\left[\tilde{G}_{LS}\right]_L (x, y)$ as a function of the number of added terms L in the sum as defined in equation 2.58 for the 4 cases shown in figure 2.9.*

The convergence of $\left[\tilde{G}_{LS}^{\pm}\right]_L$ shown in figure 2.13 depends mostly on the point where the Green function is evaluated (light versus dark colored curves).The convergence of the series is in $H_l^{(1)}(|m|k^{\pm} d) J_l(k^{\pm} r) \approx -i(\pi l)^{-1} \left(\frac{r}{md}\right)^l$ [120] ($H_l^{(1)}$ is in the S_l). The convergence is very

good near the singularity where $\frac{r}{d} << 1$ (dark curves) which leads to a exponential convergence. On the contrary for $\frac{r}{d} \approx 1$ the convergence is slow and may even fail in the dielectric case. As l increases, S_l becomes smaller and J_l bigger. As they are evaluated separately, their multiplication $S_l J_l$ may become highly inaccurate. If the convergence is not reached for a small number of terms L, the Green function may diverge. It is less likely in the case of the metal because S_l is evaluated as a sum of Hankel Functions which converge faster.

2.4.1.4   Numerical Calculation of the Green Function

We examined the convergence of three Green functions $\tilde{G}_{HS}^{\pm}$, $\tilde{G}_{WS}^{\pm}$ and $\tilde{G}_{LS}^{\pm}$ as a function of the medium they are associated with, i.e. of the value of permittivity $\epsilon^{\pm}$, and as a function of the proximity to the origin of the point where they are evaluated. We have summed up the efficiency of the convergence of the different Green functions in table 2.2. If the Green function converges with few terms, it is efficient and thus noted + otherwise it is noted -. We see that the Green function $\tilde{G}_{HS}$ expressed as a sum of Hankel functions is efficient in the case of the metal, both near and far from the origin. The Green function $\tilde{G}_{WS}$ expressed as a sum of plane waves and the Green function $\tilde{G}_{LS}$ expressed with a lattice sum are efficient for opposite conditions, far and near the singularity respectively indifferently from the value of the permittivity.

permittivity / position	$\epsilon^+ > 0$ (green)	$\epsilon^- < 0$ (blue)
close to the surface (dark color)	$\tilde{G}_{HS}^+$ - - $\tilde{G}_{WS}^+$ - $\tilde{G}_{LS}^+$ +	$\tilde{G}_{HS}^-$ ++ $\tilde{G}_{WS}^-$ - $\tilde{G}_{LS}^-$ +
far from the surface (light color)	$\tilde{G}_{HS}^+$ - - $\tilde{G}_{WS}^+$ + $\tilde{G}_{LS}^+$ -	$\tilde{G}_{HS}^-$ ++ G_{WS}^- + $\tilde{G}_{LS}^-$ -

Table 2.2: *Efficiency of the Green function as a function of the position where it is evaluated and the value of the permittivity. + is efficient and - is not.*

In order to choose between the three Green functions, the time of this evaluation was also checked. First a Green function of reference was calculated with at least ten significant figures by summing terms in one of the different Green functions until the tenth figure does not change anymore. Each Green function was then calculated with the same precision. The time taken by the Green functions to reach a relative error of 10^{-6} was compared in the different cases. In the metal case, the Green function $\tilde{G}_{HS}^-$ is faster than the other ones. In order to give more general results which do not take into account the processor efficiency, we convert the run time of the calculation into the number of cycles done by the processor. The number of cycles is obtained from the run time τ and the frequency of the processor f as $f\tau$.

In the dielectric case, we have to choose from $\tilde{G}^+_{WS}$ and $\tilde{G}^+_{LS}$. At first sight, $\tilde{G}^+_{LS}$ is more efficient, and fastest, near the singularity and $\tilde{G}^+_{WS}$ far from it. At the distance $r = 0.8d$, the time of evaluation of both function is comparable. Therefore it was chosen as a criteria to differentiate the area near the singularity versus the one far from it.

We have to highlight the fact that the use of the Green function $\tilde{G}^+_{LS}$ is worthwhile only for an important number of calls of the function for the same S_l terms (different calls of $\tilde{G}^+_{LS}$ at different coordinates (x,y)). The evaluation of the S_l, $l \in [0,L]$, which is calculated once for all the different evaluation of $\tilde{G}^+_{LS}$ in the matrix (as well as for its derivative), takes several seconds (18 10^9 cycles for L=25). The evaluation of the other Green function $\tilde{G}^+_{WS}$ takes between 10^4-10^7 cycles depending on its distance from the singularity. The Green function $\tilde{G}^+_{LS}$ therefore becomes competitive for at least 10^3-10^4 calls. This number is easily reached as a matrix for 10^3 unknowns calls 10^6 times $\tilde{G}^+$.

The chosen Green functions are summed up in table 2.3 and the order of magnitude of the number of cycles for the calculation of the Green functions is also given.

position ╲ permittivity	$\epsilon^+ > 0$ (dielectric)	$\epsilon^- < 0$ (metal)
close to the surface (r < 0.8 d)	$\tilde{G}^+_{LS}$, 10^4	$\tilde{G}^-_{HS}$, 10^3
far from the surface (r > 0.8 d)	$\tilde{G}^+_{WS}$, 10^4	$\tilde{G}^-_{HS}$, 10^3

Table 2.3: *The Green function which is used as a function of the position and the medium where it is evaluated. The order of magnitude of the number of cycles for the calculation is indicated.*

Because the Green Function is pseudo-periodic, there is a singularity at (x,y)=(0,0) as well as (x,y)=(nd,0) $\forall n \in \mathbb{Z}$. Thus the evaluation outside this perimeter of $x \in \left[-\frac{d}{2}, \frac{d}{2}\right]$ is brought back to the close perimeter with the pseudo-periodicity relation 2.40.

$$\tilde{G}(x, y) = \tilde{G}(x - md)\, e^{i\alpha_0 md}$$

with $m = \left\lfloor \frac{2x+1}{2d} \right\rfloor$ and $\lfloor\rfloor$ the floor function. The figure 2.14 shows the dielectric Green function $\left|\tilde{G}^+(x, y)\right|$ calculated for air (ϵ^+=1) with the use of $\tilde{G}_{LS}$ under the separation line of $r = 0.8d$ (black dashed line) and with $\tilde{G}_{WS}$ above it.

The determination of how to calculate the pseudo-periodic Green function efficiently was the first step to the numerical resolution of the surface integral equations. We now present in the next section how to transform the self-coherent integral equations in a matrix system.
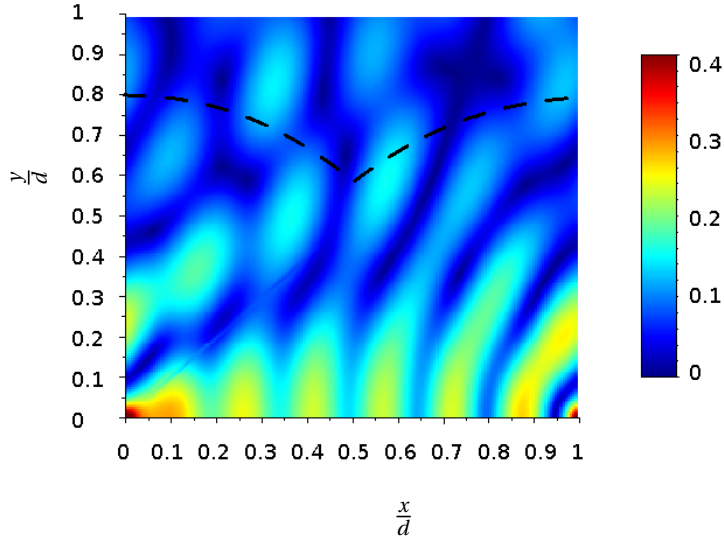
Figure 2.14: $\left|\tilde{G}^+(x,y)\right|$ *with* $\lambda = d/3, \theta = 45°$ *and* $\epsilon_+ = 1$. *The dashed line indicates the boundary* $r = 0.8$.

2.4.2 Setting the integral equations in a matrix form

2.4.2.1 Discretization of the integrals

Maradudin uses the Nyström method to solve the two self-coherent equations 2.50 and 2.51. This method essentially consists of two main steps. The first one is to discretize the integral by applying a quadrature formula [2] using N points of the surface S_D and the second one is to evaluate the equation at the exact same points. We then have a set of equations for the value of the source functions H and γL at these points which can be written in a matrix form and solved numerically.

We start by expressing the integral in terms of the parametric description of the surface S_D, $\forall t^{'} \in [0, T[$

$$\frac{1}{2}H(t^{'}) + \int_{S_D} \left[H(t)\frac{\partial \tilde{G}^+}{\partial \vec{n}}\left(\vec{r}(t^{'}) - \vec{r}(t)\right) + \epsilon_+ \tilde{G}^+\left(\vec{r}(t^{'}) - \vec{r}(t)\right)L(t) \right] \gamma(t)dt = H_i(t^{'}) \quad , \quad (2.59)$$

$$-\frac{1}{2}H(t^{'}) + \int_{S_D} \left[H(t)\frac{\partial \tilde{G}^-}{\partial \vec{n}}\left(\vec{r}(t^{'}) - \vec{r}(t)\right) + \epsilon_- \tilde{G}^-\left(\vec{r}(t^{'}) - \vec{r}(t)\right)L(t) \right] \gamma(t)dt = 0 \quad . \quad (2.60)$$

In order not to over-complicate the equations, it will be written indifferently $H(\vec{r}) = H(\vec{r}(t)) = H(t)$.

Let us define the discretization step h

$$h = \frac{T}{N} \quad \text{and} \quad \forall n \in [0; N-1] \quad t_n = \left(n + \frac{1}{2}\right)h \quad .$$

---

[2]A quadrature, sometimes called numerical quadrature, is another word for numerical integration.

We also write that the integral of a function f over T is approximated by the formula of the quadrature of rectangle as

$$\int_0^{\mathrm{T}} f\left(t^{'}, t\right) dt = h \sum_{n=0}^{N-1} f\left(t^{'}, t_n\right) \quad . \tag{2.61}$$

We want to apply directly

$$f\left(t^{'}, t\right) = \mathrm{H}(t) \frac{\partial \tilde{\mathrm{G}}^{\pm}}{\partial \vec{n}} \left(\vec{r}(t^{'}) - \vec{r}(t)\right) + \epsilon_{\pm} \tilde{\mathrm{G}}^{\pm} \left(\vec{r}(t^{'}) - \vec{r}(t)\right) \mathrm{L}(t) \tag{2.62}$$

in order to discretize the two equations 2.59 and 2.60. One obtains 2N unknowns ($\mathrm{H}(t_n)$ and $\mathrm{L}(t_n)$) in 2 equations $\quad \forall t^{'} \neq t_n \in [0, \mathrm{T}]$

$$\frac{1}{2}\mathrm{H}(t^{'}) + h \sum_{n=0}^{N-1} \left[\mathrm{H}(t_n) \frac{\partial \mathrm{G}^{+}}{\partial \vec{n}} (\vec{r}(t^{'}) - \vec{r}(t_n)) + \epsilon_{+} \mathrm{G}^{+}(\vec{r}(t^{'}) - \vec{r}(t_n))\mathrm{L}(t_n) \right] \gamma(t_n) = \mathrm{H}_i(t^{'}) \quad ,$$

$$-\frac{1}{2}\mathrm{H}(t^{'}) + h \sum_{n=0}^{N-1} \left[\mathrm{H}(t_n) \frac{\partial \mathrm{G}^{-}}{\partial \vec{n}} (\vec{r}(t^{'}) - \vec{r}(t_n)) + \epsilon_{-} \mathrm{G}^{-}(\vec{r}(t^{'}) - \vec{r}(t_n))\mathrm{L}(t_n) \right] \gamma(t_n) = 0 \quad .$$

These two expressions induce no problems as long as $\vec{r}(t^{'}) \neq \vec{r}(t_n)$. However, if there exists an integer m $\in [0, N-1]$ such that $t_m = t^{'}$, there will be a term $\mathrm{G}^{\pm}(\vec{r}(t^{'} = t_m) - \vec{r}(t_m))$ not defined because the Green function is singular. Similarly, there will be a term $f\left(t_m = t^{'}, t_m\right)$ in the sum of the quadrature formula, equation 2.61, which is not defined. That is due to the fact that we deal with improper integrals that exist only as a limit of $\vec{r}(t^{'})$ tending to the surface. In that sense, the Green function is singular at one point but is integrable. In order to have a function that is always defined, we add $\xi \vec{e}_y$ to $\vec{r}^{'}$ and take the limit for $\xi \to 0^{+}$. That will enable us to integrate the singularity while always considering a point above the surface. When considering the integral of the function $f(t_m, t)$ with m an integer of the interval [0,N-1], the formula of the quadrature of rectangle is then applied on the interval $[0, t_m - \frac{h}{2}[$ and $[t_m + \frac{h}{2}, \mathrm{T}[$ and treats separately the singular part of integral such that

$$\int_0^{\mathrm{T}} f(t_m, t) dt = h \sum_{n=0 \, n \neq m}^{N-1} f(t_m, t_n) + \lim_{\xi \to 0} \int_{t_m - \frac{h}{2}}^{t_m + \frac{h}{2}} f(\vec{r}(t_m) + \xi \vec{e}_y, \vec{r}(t)) dt \quad . \tag{2.63}$$

Applying the quadrature formula of equation 2.63 to the two equations 2.59 and 2.60, one obtains 2N unknowns ($\mathrm{H}(t_n)$ and $\mathrm{L}(t_n)$) in 2N equations $\forall m \in [0, N-1]$

$$\frac{1}{2}\mathrm{H}(t_m) + h \sum_{n=0 \, n \neq m}^{N-1} \left[\mathrm{H}(t_n) \frac{\partial \tilde{\mathrm{G}}^{+}}{\partial \vec{n}} (\vec{r}(t_m) - \vec{r}(t_n)) + \epsilon_{+} \tilde{\mathrm{G}}^{+}(\vec{r}(t_m) - \vec{r}(t_n))\mathrm{L}(t_n) \right] \gamma(t_n)$$

$$+ \lim_{\xi \to 0} \int_{t_m - \frac{h}{2}}^{t_m + \frac{h}{2}} \left[\mathrm{H}(t) \frac{\partial \tilde{\mathrm{G}}^{+}}{\partial \vec{n}} (\vec{r}(t_m) + \xi \vec{e}_y - \vec{r}(t)) + \epsilon_{+} \tilde{\mathrm{G}}^{+}(\vec{r}(t_m + \xi \vec{e}_y) - \vec{r}(t))\mathrm{L}(t) \right] \gamma(t) dt = \mathrm{H}_i(t_m) \quad ,$$

$$\tag{2.64}$$

$$-\frac{1}{2}\mathrm{H}(t_m) + h \sum_{n=0}^{N-1} \left[\mathrm{H}(t_n) \frac{\partial \tilde{\mathrm{G}}^{-}}{\partial \vec{n}} (\vec{r}(t_m) - \vec{r}(t_n)) + \epsilon_{-} \tilde{\mathrm{G}}^{-}(\vec{r}(t_m) - \vec{r}(t_n))\mathrm{L}(t_n) \right] \gamma(t_n)$$

$$+ \lim_{\xi \to 0} \int_{t_m - \frac{h}{2}}^{t_m + \frac{h}{2}} \left[\mathrm{H}(t) \frac{\partial \tilde{\mathrm{G}}^{-}}{\partial \vec{n}} (\vec{r}(t_m) + \xi \vec{e}_y - \vec{r}(t)) + \epsilon_{-} \tilde{\mathrm{G}}^{-}(\vec{r}(t_m) + \xi \vec{e}_y - \vec{r}(t))\mathrm{L}(t) \right] \gamma(t) dt = 0 \quad .$$

$$\tag{2.65}$$

79

Let us recall that $\gamma(t) = \sqrt{{\rm D}'(t)^2 + x_{\rm D}'(t)^2}$.

In the matrix associated with this set of equations, m is the index of the rows whereas n is the one of the columns. The two terms expressed with a limit correspond to the diagonal terms in the matrix (n=m). As already mentioned, they need a special attention because the Green functions diverge when the limit $\xi \to 0$ is taken but not the integral. An analytical approximation of the latter is presented in the next section.

2.4.2.2 The diagonal terms

To calculate the diagonal terms, the problem to tackle is the divergence of the Green functions at $r \approx 0$. To treat the singularity, we isolate the non-periodic Green function $G^\pm$, equation 2.15, which contains the singularity, from the rest of the periodic Green function $G_d^\pm = \tilde{G}^\pm - G^\pm$. The integral is thus divided in two parts, one for each part of the Green function $G^\pm$ and $G_d^\pm$,

$$\lim_{\xi \to 0} \int_{t_m - \frac{h}{2}}^{t_m + \frac{h}{2}} \left[{\rm H}(t) \frac{\partial \tilde{G}^\pm}{\partial \vec{n}} (\vec{r}(t_m) + \xi \vec{e}_y - \vec{r}(t)) + \epsilon_\pm \tilde{G}^\pm(\vec{r}(t_m) + \xi \vec{e}_y - \vec{r}(t)){\rm L}(t) \right] \gamma(t) dt$$

$$= {\rm H}(t_m){\rm L}_m^\pm + {\rm P}_m^\pm {\rm L}(t_m)\gamma(t_m) + \left[{\rm H}(t_m) \frac{\partial G_d^\pm}{\partial \vec{n}}(\vec{0}) + \epsilon_\pm G_d^\pm(\vec{0}){\rm L}(t_m) \right] \gamma(t_m) h$$

$$\text{with} \quad {\rm H}(t_m){\rm L}_m^\pm = \lim_{\xi \to 0} \int_{t_m - \frac{h}{2}}^{t_m + \frac{h}{2}} {\rm H}(t) \frac{\partial G^\pm}{\partial \vec{n}} (\vec{r}(t_m) + \xi \vec{e}_y - \vec{r}(t))\gamma(t) dt$$

$$\text{and} \quad {\rm L}(t_m)\gamma(t_m){\rm P}_m^\pm = \epsilon_\pm \lim_{\xi \to 0} \int_{t_m - \frac{h}{2}}^{t_m + \frac{h}{2}} G^\pm(\vec{r}(t_m) + \xi \vec{e}_y - \vec{r}(t)){\rm L}(t)\gamma(t) dt \quad .$$

The appendix B of Maradudin's paper [91] explains how, using a series expansion of the Green function $G^\pm$, the integrations of $G^\pm$ over the singular points are made i.e. how to approximately treat ${\rm L}_m^\pm$ and ${\rm P}_m^\pm$. First, to have a good approximation of the integral, h needs to be sufficiently small so that H and L are constant on the interval $[t_m - \frac{h}{2}, t_m + \frac{h}{2}]$ then

$$ {\rm L}_m^\pm = \lim_{\xi \to 0} \int_{t_m - \frac{h}{2}}^{t_m + \frac{h}{2}} \gamma(t) \frac{\partial G^\pm}{\partial \vec{n}} (\vec{r}(t_m) + \xi \vec{e}_y - \vec{r}(t)) dt \quad ,$$

$$ {\rm P}_m^\pm = \epsilon_\pm \left[\lim_{\xi \to 0} \int_{t_m - \frac{h}{2}}^{t_m + \frac{h}{2}} G^\pm(\vec{r}(t_m) + \xi \vec{e}_y - \vec{r}(t)) dt \right] $$

The analytical expression of ${\rm L}_m^\pm$ and ${\rm P}_m^\pm$, though not obtained in a mathematical rigorous way, is very efficient and accurate when compared to the numerical evaluation of these integrals. Let us therefore see how their analytical expressions are obtained.

2.4.2.3 The first diagonal term $P_m^\pm P$

We are looking for, replacing the non-periodic Green function $G^\pm$ by its expression, equation 2.15:

$$\lim_{\xi \to 0} \int_{t_m - \frac{h}{2}}^{t_m + \frac{h}{2}} G^\pm(x_D(t_m) - x_D(t), D(t_m) + \xi - D(t)) dt$$

$$= \int_{t_m - \frac{h}{2}}^{t_m + \frac{h}{2}} \frac{i}{4} H_0^{(1)}(k^\pm r_m(t)) dt$$

with $r_m(t) = \sqrt{(x_D(t_m) - x_D(t))^2 + (D(t_m) - D(t))^2}$.
Introducing the change of variable

$$t = t_m + u$$

and the series expansion of x_D and D

$$x_D(t) = x_D(t_m) + x_D'(t_m) u + o(u) \quad,$$
$$D(t) = D(t_m) + D'(t_m) u + o(u) \quad.$$

The variable r_m is approximately

$$r_m(t) \approx \sqrt{u^2(x_D'(t_m))^2 + u^2(D'(t_m))^2}$$

$$\approx |u| \sqrt{(x_D'(t_m))^2 + (D'(t_m))^2}$$

$$\approx |u| \gamma(t_m)$$

which gives

$$\frac{i}{4} \int_{t_m - \frac{h}{2}}^{t_m + \frac{h}{2}} H_0^{(1)} \left(k^\pm \sqrt{(x - x_m)^2 + (D(x) - D(x_m))^2} \right) dt = \frac{i}{4} \int_{-\frac{h}{2}}^{\frac{h}{2}} H_0^{(1)} \left(k^\pm |u| \gamma(t_m) \right) du$$

$$= \frac{i}{2} \int_0^{\frac{h}{2}} H_0^{(1)} \left(k^\pm u \gamma(t_m) \right) du \quad.$$

The series expansion of $H_0^{(1)}$ around z=0 is

$$i\pi H_0^{(1)}(z) \approx -2\log\left(\frac{\gamma z}{2}\right) + i\pi + \frac{z^2}{2}\left(\log\left(\frac{\gamma z}{2e}\right) - \frac{i\pi}{2}\right) + \dots$$

81

with γ the Euler constant. As $\int u^2 du \to h^3$ the last term is negligible at the first order of h such that

$$\frac{i}{2}\int_0^{\frac{h}{2}} H_0^{(1)}\left(k^\pm u \gamma(t_m)\right) du \approx \frac{i}{2i\pi}\int_0^{\frac{h}{2}} du\left[-2\log\left(\frac{\gamma k^\pm u \gamma(t_m)}{2}\right) + i\pi\right]$$

$$\approx \frac{1}{2\pi}[-2u(\log\left(\frac{\gamma k^\pm u \gamma(t_m)}{2}\right) - 1)]_0^{\frac{h}{2}} + \frac{1}{2\pi}[i\pi u]_0^{\frac{h}{2}}$$

$$\approx \frac{1}{2\pi}\left[-2u\log\left(\frac{\gamma k^\pm u \gamma(t_m)}{2e}\right)\right]_0^{\frac{h}{2}} + \frac{1}{2\pi}[i\pi u]_0^{\frac{h}{2}}$$

$$\approx \frac{1}{2\pi}\left(-2\frac{h}{2}\log\left(\frac{\gamma k^\pm h \gamma(t_m)}{4e}\right) + i\pi\frac{h}{2}\right)$$

$$\approx \frac{h}{4\pi} i\pi H_0^{(1)}\left(\frac{k^\pm h \gamma(t_m)}{2e}\right) \quad .$$

The first diagonal term is thus taken as:

$$P_m^\pm = \epsilon_\pm \frac{ih}{4} H_0^{(1)}\left(\frac{k^\pm h \gamma(t_m)}{2e}\right) \quad . \tag{2.66}$$

2.4.2.4   The second diagonal term $L_m^\pm L$

We are looking for

$$\lim_{\xi \to 0}\int_{t_m-\frac{h}{2}}^{t_m+\frac{h}{2}} \gamma(t)\frac{\partial G^\pm}{\partial \vec{n}}(x_D(t_m) - x_D(t), D(t_m) + \xi - D(t))dt \quad .$$

The derivative of the non-periodic function $G^\pm$ with respect to the vector $\vec{n}_0 = (n_x, n_y)$ is expressed with the derivative of the Hankel function, equation 2.54, as

$$\frac{\partial G^\pm}{\partial \vec{n}_0}(x, y) = -\frac{i}{4}k^\pm \frac{n_y y + n_x x}{r} H_1^{(1)}(k^\pm r) \quad .$$

Recalling that the normal vector $\vec{n}$ to the surface, equation 2.3, is $\frac{1}{\gamma(t)}(-D'(t), x_D'(t))$, the integral we are looking for thus becomes

$$\int_{t_m-\frac{h}{2}}^{t_m+\frac{h}{2}} dt(-k^\pm)\left(\frac{x_D'(t)(D(t_m) + \xi - D(t)) - D'(t)(x_D(t_m) - x_D(t))}{r_m(t)}\right)\frac{i}{4}H_1^{(1)}\left(k^\pm r_m(t)\right)$$

with $r_m(t) = \sqrt{(x_D(t_m) - x_D(t))^2 + (D(t_m) - D(t))^2}$.
Once again a change of variable and the series expansion of D and x_D are performed. The limit here has to be dealt with more precautions, keeping all the terms at the first order in ξ. Thus we need the series expansions

$$x_D(t_m) = x_D(t) - x_D'(t)u + \frac{x_D''(t)}{2}u^2 + o(u) \quad ,$$

$$D(t_m) = D(t) - D'(t)u + \frac{D''(t)}{2}u^2 + o(u) \quad .$$

In the same way as for $P_m^\pm$

$$r_m(t) = \sqrt{u^2 \gamma(t_m)^2} \quad .$$

In order to find the first term in u in the numerator of the fraction, the series expansion up to the second order is needed

$$x'_D(t)(D(t_m) - D(t)) - D'(t)(x_D(t_m) - x_D(t))$$

$$= x'_D(t)\left(-D'(t)u + \frac{D''(t)}{2}u^2\right) - D'(t)\left(-x'_D(t)u + \frac{x''_D(t)}{2}u^2\right)$$

$$= \left(x'_D(t)D''(t) - D'(t)x''_D(t)\right)\frac{u^2}{2}$$

$$= \left(x'_D(t_m)D''(t_m) - D'(t_m)x''_D(t_m)\right)\frac{u^2}{2} \quad .$$

The series expansions are then introduced in the integral and a change of variable $t = t_m + u$ is done which yields

$$\int_{-\frac{h}{2}}^{\frac{h}{2}} du \left(-\frac{k^{\pm 2}}{4\pi}\right)\left(\frac{x'_D(t_m)D''(t_m) - D'(t_m)x''_D(t_m)}{k^\pm |u\gamma(t_m)|}\frac{u^2}{2}\right) i\pi H_1^{(1)}\left(k^\pm |u\gamma(t_m)|\right) \quad .$$

The series expansion of Hankel's derivatives is

$$z \to 0 \qquad i\pi \frac{H_1^{(1)}(z)}{z} \approx \frac{2}{z^2} - \left[\log\left(\frac{\gamma z}{2e}\right) + \frac{1}{2} - i\frac{\pi}{2}\right] + \dots$$

Only the first term $\frac{2}{z^2}$ is kept, as $\int du\, u^2 \log(u)$ is not of the first order in h. Introducing the series expansion of $H_1^{(1)}$ into the integral, makes the variable u disappear in the integral

$$\left(-\frac{k^{\pm 2}}{4\pi}\right)\int_{-\frac{h}{2}}^{\frac{h}{2}} du \left[\frac{\left(x'_D(t_m)D''(t_m) - D'(t_m)x''_D(t_m)\right)}{k^{\pm 2}\gamma(t_m)^2}\right] \quad .$$

Eventually it leads to the expression

$$L_m^\pm = -\frac{\left(x'_D(t_m)D''(t_m) - D'(t_m)x''_D(t_m)\right)}{4\pi\gamma(t_m)^2}h \quad . \tag{2.67}$$

2.4.2.5 Matrix form, Library and Parallelisation

The system of equations 2.64 and 2.65 may be solved in a matrix form as $M\vec{X} = \vec{V}$ with $n, m \in [0, N-1]^2$ with

$$\vec{X} = \begin{bmatrix} \dots \\ H(\vec{r}(t_n)) \\ \dots \\ \gamma(t_n)L(\vec{r}(t_n)) \\ \dots \end{bmatrix} \qquad \vec{V} = \begin{bmatrix} \dots \\ H_i(\vec{r}(t_m)) \\ \dots \\ 0 \\ \dots \end{bmatrix} \tag{2.68}$$

83

and

$$
M = \left[
\begin{array}{ccc}
\begin{cases} \frac{1}{2} + L_m^+ + \gamma(t_n)\frac{\partial G_d^+}{\partial \vec{n}}(\vec{0})\, h & n = m \\ \gamma(t_n)\frac{\partial \tilde{G}^+}{\partial \vec{n}}(\vec{r}(t_m) - \vec{r}(t_n))\, h & n \neq m \end{cases} & \vdots & \begin{cases} P_m^+ + \epsilon_+ G_d^+(\vec{0})\, h & n = m \\ \epsilon_+ \tilde{G}^+(\vec{r}(t_m) - \vec{r}(t_n))\, h & n \neq m \end{cases} \\
\ldots & & \ldots \\
\begin{cases} -\frac{1}{2} + L_m^- + \gamma(t_n)\frac{\partial G_d^-}{\partial \vec{n}}(\vec{0})\, h & n = m \\ \gamma(t_n)\frac{\partial \tilde{G}^-}{\partial \vec{n}}(\vec{r}(t_m) - \vec{r}(t_n))\, h & n \neq m \end{cases} & \vdots & \begin{cases} P_m^- + \epsilon_- G_d^-(\vec{0})\, h & n = m \\ \epsilon_- \tilde{G}^-(\vec{r}(t_m) - \vec{r}(t_n))\, h & n \neq m \end{cases}
\end{array}
\right] . \quad (2.69)
$$

In the expression, $\gamma(t_n)$ was left before $\frac{\partial \tilde{G}^+}{\partial \vec{n}}(\vec{r}(t_m) - \vec{r}(t_n))$ because $\gamma(t_n)\frac{\partial \tilde{G}^+}{\partial \vec{n}}(\vec{r}(t_m) - \vec{r}(t_n))$ has a more simple expression to calculate since $n_x = -D'(t)/\gamma(t)$ and $n_y = x'_D(t)/\gamma(t)$. Filling the matrix M is long, however the operation is easily parallelized as each term of the matrix is independent. The system was solved using a standard LU decomposition via the Eigen library [122]. I found no clear criteria to decide of the total number of points N (or for the step h) as there is for FDTD, neither in the literature nor during discussions with other practitioners of 1D-surface integral method. As a consequence N is increased from N_i points to N_{i+1} until the difference between the solution H_i and H_{i+1} is negligible and the plots superimpose. I give further details on the convergence of the solutions and the estimation of the error for a practical case in section 2.5.2.1.

When the convergence is reached, we will consider that the unknowns are constant on the interval $\left[t_n - \frac{h}{2}, t_n + \frac{h}{2} \right]$. Usually, quick variations of the profile lead to quick variations of the unknowns and h is chosen such that the profile varies slowly on this interval. The needed step h is often less than the angström and can go down to 10^{-2} nm where the magnetic field varies quickly and huge electric field arises. Thus to perform calculations on roughnesses of the order of magnitude of several nanometers, a profile which is 10 nm long, for example, has to be discretized with several hundreds to several thousands of points. The simulation of a profile which is several micron long is then out of reach of a laptop capacity. We comment further on the matter of the length of the profile and the roughnesses dimensions which are possible to simulate in the next chapter. In the next paragraph, we detail the issues of memory space and time when using the surface integral method.

2.4.2.6 Memory space and run time requirements

The numerical resolution of our set of two Fredholm integral equations of the second kind is done in two main steps: (1) to fill the matrix M and (2) to solve the system MX=V. These two operations take time and occupy the memory space of the computer. We detail both aspects separately. Most of the memory space of the computer that is needed is due to the space occupied by the matrix M. The matrix M is filled with $4\,N^2$ double precision complex. The double precision complex (or two double precision float) is stored with two times 64-bits (16 octets). A computer with a memory space of 4 gigaoctets, like the Dell Precision M4400 which was used to do the simulations, may store $250\,10^6$ octets i.e. a matrix corresponding to a number N of unknowns equal to 7905. The resolution of the system requires, however,

more memory space than the memory space of the matrix itself to store intermediate results. It is thus possible to store and to solve a matrix with a number N up to about 6000.
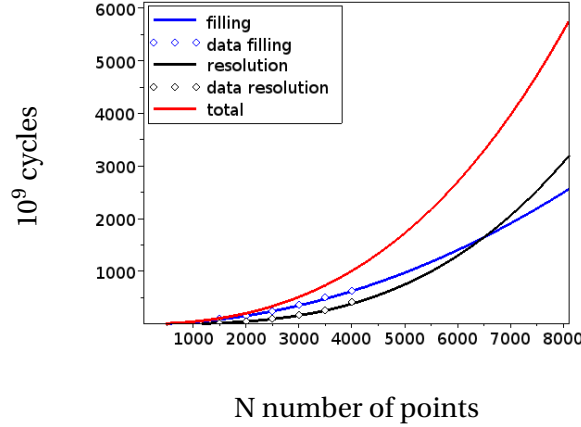
Figure 2.15: *Number of cycles for the two steps: to fill (blue solid line) and to solve (black solid line) the matrix as a function of the number of points N which discretize the boundary. The lines are extrapolated from the fitted dependencies of the data (resp. blue and black diamond). The total number of cycles is represented as a red solid line. Example with an incident plane wave λ^{-1}=2030 cm^{-1} and θ_i = 7.5° impinging on a gold grating of period d=1.75 μm with rectangular grooves (w=0.75 μm and h=1 μm).*

The second constraint is the time spent to do the resolution which includes (1) the time to evaluate the terms of the matrix and (2) the time to solve the matrix. The time spent to fill the matrix is proportional to the number of terms in the matrix $4\,N^2$. Each term of the matrix requires to calculate one of the pseudo-periodic Green function or its derivative. The evaluation of the Green function is a costly operation because a sum of multiplications and additions is made and the mean number of cycles for each evaluation is about 15000 cycles (we recall that the number of cycle is obtained by multiplying the run time of the operation by the frequency of cycles of the processor 3 GHz). As each term of the matrix is calculated independently, the different tasks can be done simultaneously on different processors. The time spent to fill the matrix may then be divided by the number of cores of the processor if the code is parallelized. To solve a dense matrix one needs to perform a number of operations proportional to $8N^3$ and the time spent to solve the matrix thus follows the same law in N^3. As the operations for solving a matrix are additions and multiplications, the number of cycles per operation is about 10. The total number of cycles to solve the matrix is therefore of the order of 10^2N^3 cycles whereas the one to fill it is 10^5N^2 cycles. The time to solve the matrix and to fill it are then equivalent for matrices with a number of unknowns N of several thousands. A parallelization may also be done but in a less efficient way than for the filling of the matrix. Overall, for matrices whose dimension 2N is less than 12000 and with a dual-core processor, the time to solve the matrix is less than the time to fill it. For example,

the number of cycles required to fill and to solve the matrix as a function of the number of unknowns N is represented in figure 2.15.

To summarize, in order to obtain the 2N unknowns from the system of 2N equations, one needs a memory space proportional to N^2 and one needs to wait for $10^5 N^2$ cycles to fill the matrix and $10^2 N^3$ cycles to solve it. To conclude, we are limited in the dimension of the matrix, or equivalently in the number of unknowns N, by the memory space. More over, the time to solve one matrix system being proportional to N^3 is multiplied by 8 each time that the number of unknowns is doubled and to solve very large system becomes a very long task. These requirements come from the fact that the matrix M is dense and we have to consider all its terms. Once the system is solved, the two source functions H and γL are known and the matter becomes that of their exploitation. The physics of the system is studied through three physical quantities which are the reflectivity, the magnetic field and the electric field as stressed in section 2.2.3. In the next paragraph, we explain how to calculate numerically these physical quantities from the source functions.

2.4.3 Calculation of the physical quantities

2.4.3.1 The reflectivity

The general expression of the mth diffracted order R_m, equation 2.53, is

$$R_m = \frac{1}{2id\beta_m^+} I_m$$

with I_m an integral described by the equation 2.52. Similarly to the integral equations, the integral I_m is discretized and approximated using the same quadrature formula (the quadrature of rectangle) as given in equation 2.61

$$I_m = \sum_{n=0}^{N-1} \left[H(\vec{r}(t_n))(-i\alpha_m D'(t_n) + i\beta_m^+ x'_D(t_n)) + \epsilon_+ \gamma(t_n) L(\vec{r}(t_n)) \right] e^{-i\alpha_m x_D(t_n)} e^{-i\beta_m^+ D(t_n)} h \quad .$$

This expression allows us to calculate the reflectivity in a precise way since once the convergence is reached the unknowns are quite constant on $[t_n, t_n + h]$. The $e^{-i\alpha_m x_D(t_n)} e^{-i\beta_m^+ D(t_n)}$ terms that comes from the Green function also vary slowly when the variations of the profile are small. Therefore, the quadrature formula with N points is already a good approximation of the integral and there is no need to push the calculation further.

2.4.3.2 The field intensities maps

To perform the map of the field intensities distributions, one would want to use integral representations of $H_z^\pm$ (equation 2.30 and 2.31), $E_x^\pm(\vec{r}')$ (equation 2.32 and 2.34), and $E_y^\pm(\vec{r}')$ (equation 2.33 and 2.35), and to apply the formula of the quadrature of rectangle once more.

This method works in most cases, however it produces incorrect results when $\vec{r}' \rightarrow \vec{r} \in S_D$ due to the strongly divergent Green functions at $\vec{r}' - \vec{r} = 0$. H and L are still constant on $[t_n, t_n + h]$ however it may not be the case for the Green function. The applied quadrature formula becomes then highly inaccurate. To ensure that we have a good approximation of the integral, a recurrent calculation was applied. The goal is to adapt the number of points of the quadrature formula in order not to impair the accuracy. The method will only be detailed for E_x^+ which expression, equation 2.32, is recalled here, $\forall \vec{r}' \in \tilde{\Gamma}^+$

$$E_x^+(\vec{r}') = E^i(\vec{r}') + \frac{1}{i\omega\epsilon_+} \int_S H(\vec{r}) \left[\frac{\partial}{\partial y'} \frac{\partial G^+}{\partial \vec{n}} \right] \left(\vec{r}' - \vec{r} \right) + \epsilon_+ \left[\frac{\partial}{\partial y'} G^+ \right] \left(\vec{r}' - \vec{r} \right) L(\vec{r}) dS(\vec{r}) \quad . \quad (2.70)$$

Nevertheless, it is valid for E_x^-, equation 2.34, E_y^+, equation 2.33, E_y^-, equation 2.32, H_z^+, equation 2.30, and H_z^-, equation 2.31.
The first step is to cut the integral into pieces

$$E_x^+(\vec{r}') = E_i(\vec{r}') + \frac{1}{i\omega\epsilon_+} \sum_{n=0}^{N-1} e_n$$

$$\text{with} \quad e_n = \int_{t_n}^{t_n+h} F(t', t) dt$$

$$\text{and} \quad F(t', t) = \left(H(\vec{r}(t)) \left[\frac{\partial}{\partial y'} \frac{\partial \tilde{G}^+}{\partial \vec{n}} \right] (\vec{r}(t') - \vec{r}(t)) + \epsilon_+ \left[\frac{\partial}{\partial y'} \tilde{G}^+ \right] (\vec{r}(t') - \vec{r}(t)) L(\vec{r}(t)) \right) \gamma(t) \quad .$$

Each part e_n of the integral on $[t_n, t_n + h[$ is approximated with a simple quadrature formula

$$e(t_i, t_{i+1}) = \frac{t_{i+1} - t_i}{2} \left(F(t', t_i) + F(t', t_{i+1}) \right) \quad . \quad (2.71)$$

A first approximated value for the integral e_n is thus $e(t_n, t_n + h)$. The piece of integral on $[t_n, t_n + h[$ is then cut in two integrals on $[t_n, t_n + h/2[$ and $[t_n + h/2, t_n + h[$. To evaluate these integrals we need the source functions H and L at other points than the t_n. A linear interpolation gives the source functions H and L for any points u in between t_n and $t_n + h$

$$H(u) = \left(\frac{u - t_n}{h} \right) H(t_n + h) + \left(1 - \frac{u - t_n}{h} \right) H(t_n) \quad .$$

The same quadrature formula, equation 2.71, is applied to the two halves whose values are $e(t_n, t_n + h/2)$ and $e(t_n + h/2, t_n + h)$. Their sum $(e(t_n, t_n + h/2) + e(t_n + h/2, t_n + h))$ should be a better approximation than the value obtained in the first place $(e(t_n, t_n + h))$. There is no need to continue the evaluation if

$$\left| e\left(t_i, t_i + \frac{t_{i+1} - t_i}{2} \right) + e\left(t_i + \frac{t_{i+1} - t_i}{2}, t_{i+1} \right) - e(t_i, t_{i+1}) \right| < K |e(t_i, t_{i+1})| \quad (2.72)$$

with K a variable fixed to control the accuracy (for example K=10^{-3}). If the condition, equation 2.72, is not met, the same procedure is repeated for each half. $e(t_n, t_n + h/4)$ and $e(t_n + h/4, t_n + h/2)$ are evaluated and their sum is compared to $e(t_n, t_n + h/2)$ and respectively for

the other half $e(t_n + h/2, t_n + h)$. If the condition is met, the integral on $[t_n, t_n + h[$ is evaluated as $e(t_n, t_n + h/2) + e(t_n + h/2, t_n + h)$. The integral is refined recurrently, each integral on $[t_i, t_{i+1}[$ being cut in two halves. If the condition, equation 2.72, is met, the recurrence stops and the part of integral on $[t_i, t_{i+1}[$ is added to the others to evaluate e_n otherwise the recurrence continues with the two halves of the integral on $[t_i, t_i + \frac{t_{i+1}-t_i}{2}[$ and $[t_i + \frac{t_{i+1}-t_i}{2}, t_{i+1}[$. The error may be controlled with precision by choosing the value of variable K.

Choosing K as small as wanted, we ensure that we will obtain an accurate calculation of every part of the integral. The value of K varies as a function of the numerical difficulty to approximate the integral. In order to have a relative precision of 10^{-2}, we choose to use $K = 10^{-3}$ for H_z, $K = 10^{-4}$ for E_x and $K = 0.5 \quad 10^{-4}$ for E_y.

The condition of equation 2.72 can take an indefinite time to be reached, especially if the part of the integral to calculate is small. To avoid overly long calculations, a maximum number N_{max} of iterations is set. If the number of iterations reaches the maximum, for the part of integral $[t_n, t_n+h/N_{max})[$ for instance, an approximation of the term $e(t_n, t_n+h/N_{max})$ is added to the error term and the part of integral on $[t_n, t_n + h/N_{max})[$ is set to zero. It is checked at the end of the calculation that the total error is negligible.

The simulation of a metallic grating excited by a TM polarized plane wave, described in this section, was implemented in a C++ program. We controlled the validity of the program by comparing it with the approximated modal method near-at-hand. We develop this matter in the next section.

2.5   Validation of the method

The surface integral equation (SIE) method program was put to the test by verifying that its results are the same than those calculated with the approximated or the exact modal method for different gratings. No approximations were used for the SIE method because we intend to use it in the visible spectral range where the surface impedance approximation cannot be used. The approximated modal method, described briefly in section 1.3.2, was implemented as a C++ program in the case of metallic gratings with multiple grooves per period [16]. The results from the exact modal method come from the previous student thesis [18]. Various examples were compared starting with gratings which have a single rectangular groove per period, to those which have several rectangular grooves per period, excited by a plane wave. Three examples are shown in this section and the convergence of the solution in the SIE method is demonstrated for one of them. First, we show the comparison between the results obtained from the SIE method with the results obtained from the approximated modal method program for two cases: a flat surface and a grating whose typical lengths scale is the micron and has thus resonances in the IR range. Finally, a comparison between the surface integral method and the exact modal method is given with gratings whose dimensions are between 5-30 nm and which have resonances in the visible. The values of the permittivity of

gold, silver and aluminum come from the Handbook of Optical Constants of Solids by Palik
[123].

2.5.1 Flat surface

The figure 2.16 shows the specular reflectivity of an incident plane wave impinging on a flat
surface of silver and gold. They were calculated using the surface integral method (red solid
line for silver and black solid line for gold) and the approximated modal method (dots for
silver and squares for gold). The excellent agreement between the two results enables us to
have a first validation of our program. The interband damping effect is responsible for the
decrease of reflectivity in the visible spectral range for both metal. The effect in gold may be
seen starting from 2.5 eV (λ = 500 nm) whereas it only starts around 3 eV (λ = 400 nm) for
silver and is less important. This is why silver is usually preferred over gold for studies in the
visible spectral range.
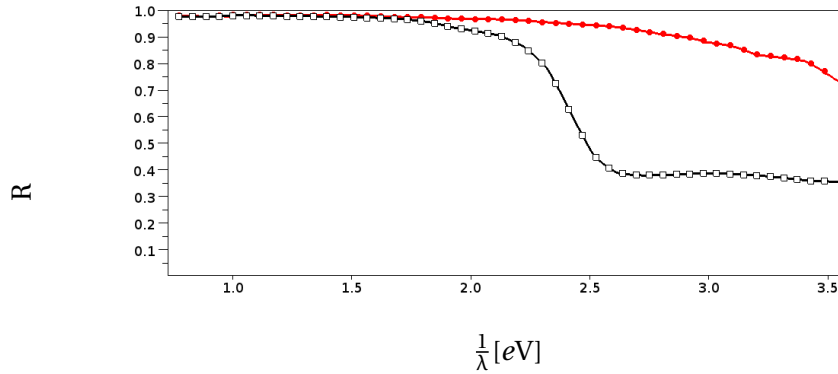
Figure 2.16: *Specular reflectivity of an incident plane wave impinging on a flat surface made
of silver and gold calculated by the surface integral method (red solid line for silver and black
solid line for gold) and the approximated modal method (dots for silver and squares for gold)
for an incident angle θ_i=0.1°.*

2.5.2 Grating studied in the IR spectral range

The profile of the rectangular grooves of width w and height h is approximated in the surface
integral equation method by the function D whose parameter β controls the slope of the
vertical walls

$$D : x \rightarrow -h \frac{2\cosh\left(\beta/4\right)^2}{\cosh\left(\beta/2\right)^2 + \cosh\left(\beta\frac{x}{w}\right)^2} \tag{2.73}$$

89

with $\beta \approx 100$. The approximation of the rectangular groove with an analytical function in the surface integral method is made in order to prevent corner effects and may be responsible for a small quantitative difference in the results obtained by both methods.
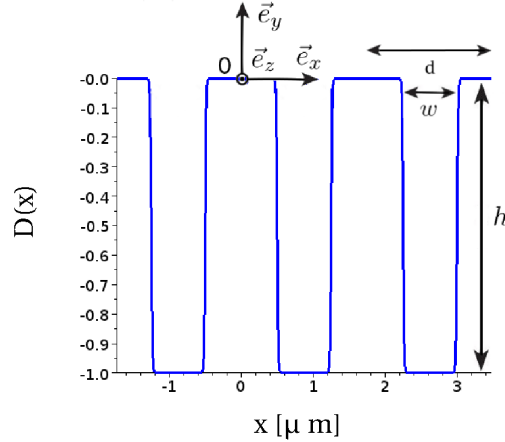
Figure 2.17: *Profile of a grating of period d=1.75 μm with rectangular grooves (w=0.75 μm and h=1 μm) and a parameter β = 100.*

The example of a gold grating with a rectangular groove which has resonances in the infrared will be shown here and was chosen because the approximation of surface impedance is valid in this spectral range [54]. The characteristics were chosen to be a period d=1.75 μm, a height h=1 μm and a width w=0.75 μm similar to [12]. The groove is centered in $d/2$. The profile of the grating is represented in figure 2.17. The validation of the surface integral method is done by a double check: first, that we have reached a convergent solution and secondly, that the solution of the SIE method agrees with the one of the approximated modal method. These checks are described in the two following paragraph.

2.5.2.1 Convergence of the solution

The resolution of the problem requires to solve the matrix system, equation 2.69 and 2.68, independently for each wavelength and angle. The solutions are the values of the source functions H_N and γL_N at the N points discretizing the metallic surface S_D (In this section, the subscript N exceptionally denotes the number of points the source functions were calculated with). These points of the metallic surface $\vec{r}(t_n) \in S_D$ for all $n \in [0, N-1]$ are described by $(t_n, D(t_n))$ i.e. $x_D(t_n) = t_n$ and sample the interval $[0,d[$ with a step d/N. We present here the convergence of the two source functions at a wavelength near the resonance of the first order cavity mode $\lambda^{-1} = 2030$ cm^{-1} and an incidence angle $\theta_i = 7.5°$. The reference solution is obtained by taking N_{ref}=4096 points on the surface S_D whereas the converging solutions have a number of points N equal to 128, 256, 512, 1024 and 2048. In the figure 2.18, the source functions H_N and γL_N are plotted as a function of $x_D(t_n) = t_n$ for a different number

90

of points N. We confirm that the difference between the solutions with an increasing number of points N is decreasing and we can take the solution with 4096 points as a reference.
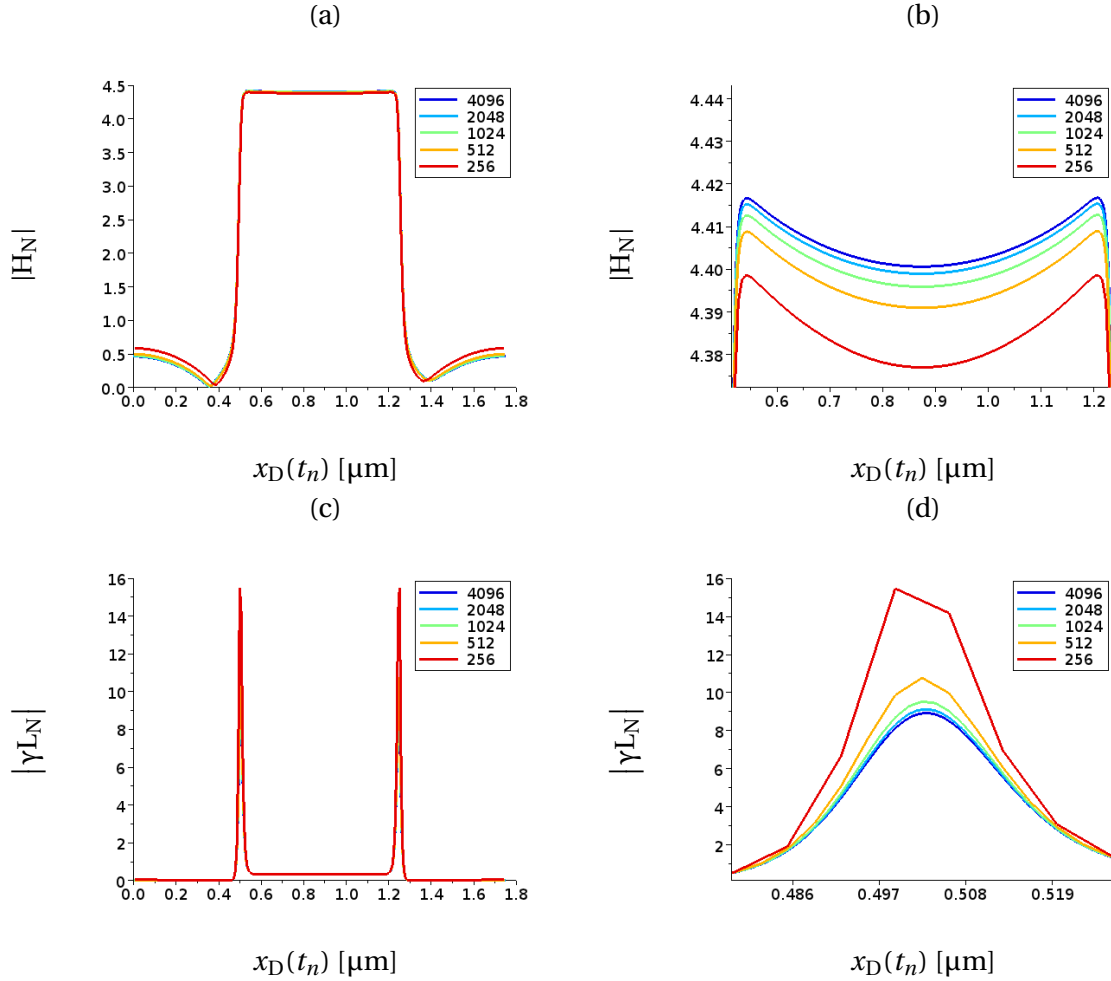
Figure 2.18: *Modulus of the source function* H, *(a) and close-up on its maximum values (b), and* γL, *(c) and close-up on its maximum values (d), as a function of the points* $\vec{r}(t_n) \in S_D$ $\forall n \in [0, N-1]$ *describing the profile of the grating. Different values of N were considered. The grating is made of gold with a period d=1.75* μm *and rectangular grooves (w=0.75* μm *and h=1* μm*) excited by a plane wave of incidence angle* $\theta_i = 7.5°$ *and a wavenumber* $1/\lambda = 2030$ cm^{-1}.

To study the convergence, let us define the relative error of the source function H_N calculated with N points discretizing the surface (or γL_N) compared to H_{ref}, calculated with a number of point N_{ref}, at the point $\vec{r}(t_n) \in S_D$ as

$$\left| \frac{H_N(t_n, D(t_n)) - H_{ref}(t_n, D(t_n))}{H_{ref}(t_n, D(t_n))} \right| = \left| \frac{H_N - H_{ref}}{H_{ref}} \right| (t_n, D(t_n))$$

and we define the mean relative error of the source function H_N (or γL_N) compared to H_{ref} as the spatial average

$$\overline{\left|\frac{H_N - H_{ref}}{H_{ref}}\right|} = \frac{1}{N}\sum_{n=0}^{N-1}\left|\frac{H_N - H_{ref}}{H_{ref}}\right|(t_n, D(t_n)) \quad .$$

The percentage of the mean relative error of the value of $|H_N|$ and $|\gamma L_N|$ is plotted as a function of the number of points taken on the surface in figure 2.19. We can see once again that the solution converges when taking an increasing number of points N, as the gap of the mean relative error between two consecutive numbers of points N and its double 2N decreases. The convergence is similar for $|H_N|$ and $|\gamma L_N|$.
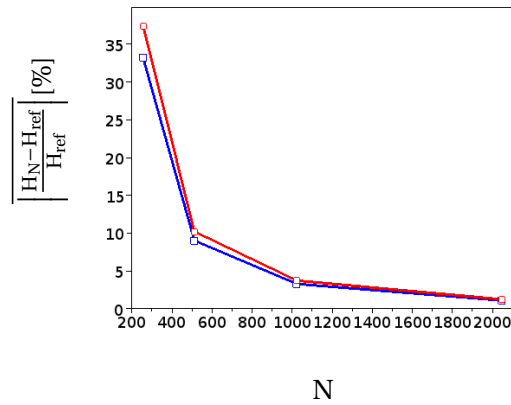
Figure 2.19: *Mean relative error of the modulus of the two unknowns* H_N *(blue line) and* γL_N *(red line) calculated by the surface integral method for a gold grating of period d=1.75 µm with rectangular grooves (w=0.75 µm and h=1 µm) at incident conditions* $\theta_i = 7.5°$, $1/\lambda = 2030$ *cm^{-1}.*

The relative error $\left|\frac{H_N - H_{ref}}{H_{ref}}\right|(t_n, D(t_n))$ in a logarithmic scale (blue line) with N=1024 points is also plotted as a function of the abscissa $x_D(t_n) = t_n$ in figure 2.20(a) and the one of L in figure 2.20(b). When examining the two curves, one sees that the convergence is not uniform on the surface. The reference source functions (red line) are plotted together to indicate where the source functions are high and low. The relative error is greater than 10 % (above the dashed line y=−1) locally at about x=0.3 µm when $|H_{ref}|$ and $|\gamma L_{ref}|$ have values close to zero. The absolute error due to this point is then negligible. Elsewhere, the error is lower than 10 % (below the dashed line y=−1) and the error on the value of $|H_N|$ and $|\gamma L_N|$ at the bottom of the groove, between 0.5 and 1.25 µm, is under 1 % (below the dashed line y=−2). The most important error is on the vertical walls of the groove where there are less points to describe the profile.

The accuracy of the physical quantities retrieved from an integral expression of the two solutions H and γL is even more important to know. To study it, the reflectivity, shown
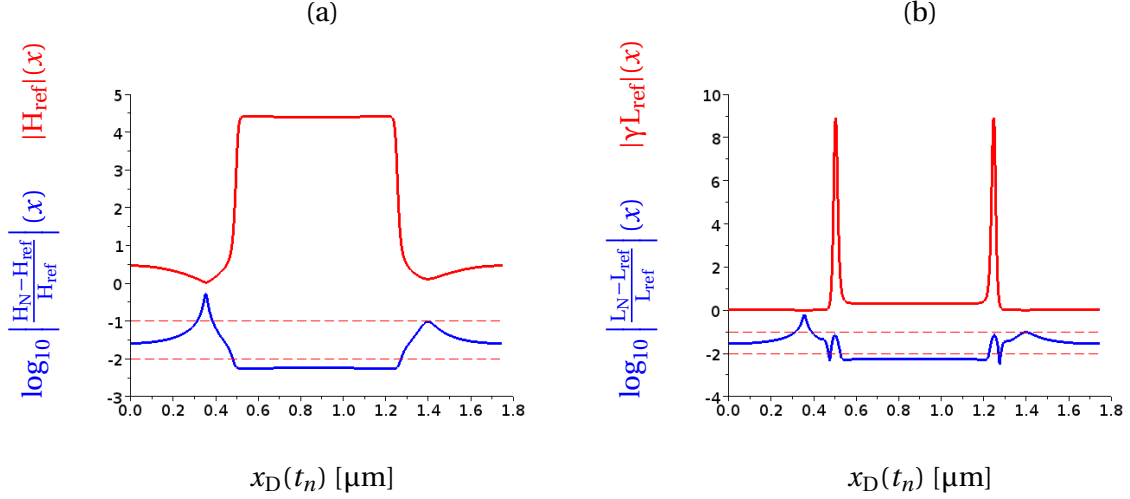
Figure 2.20: *Modulus of the two unknowns* H_{ref} *(a) and* γL_{ref} *(b) calculated by the surface integral method with* N_{ref}*=4096 points (red line) for a gold grating of period d=1.75 µm with rectangular grooves (w=0.75 µm and h=1 µm) at incident conditions* $\theta_i = 7.5°$, $1/\lambda = 2030$ cm^{-1} *and the one of the relative error (blue line) in logarithmic scale with N=1024 points.*

in figure 2.21(a), and the magnetic and electric field modulus, shown in figure 2.21(b) and in figure 2.21(c) respectively, are plotted as a function of 10 wavelengths chosen near the resonance between 1800 and 2600 cm^{-1}, for different values of the number of points N used for the resolution. We can see that the physical quantities curves have a similar shape when converging towards the reference. For an increasing number of points N starting from 512 points, the dip in the reflectivity and the peaks in the magnetic and electric field indicate the same wavelength of resonance. Therefore, the physics of the plasmonic mode is already captured with 512 points and the choice of the number points used for the resolution then depends on the desired accuracy. The relative error of the reflectivity compares the reflectivity R_N calculated with the source functions H_N and γL_N calculated with N points to the one R_{ref} calculated with the reference source function at one of the wavenumber λ_i^{-1}. The mean relative error of the reflectivity averages over all the wavenumber such that

$$\left\langle \left| \frac{R_N - R_{ref}}{R_{ref}} \right| \right\rangle_{\lambda^{-1}} = \frac{1}{10} \sum_{i=0}^{9} \left| \frac{R_N(\lambda_i^{-1}) - R_{ref}(\lambda_i^{-1})}{R_{ref}(\lambda_i^{-1})} \right| \quad .$$

The mean relative error of the reflectivity, shown in figure 2.21(b), and that of the magnetic and electric field modulus, shown in figure 2.21(d) and figure 2.21(f) respectively, is represented as a function of the number of unknowns N. The mean relative error of the physical quantities is lower than the one of the source function H and γL although the physical quantities are calculated from H and γL. It is not paradoxical as the physical quantities are calculated as a weighted sum of H and γL (the weight being the Green function or one of its derivative). A low relative error of H and γL, where they are the higher, ensures that one will have a good level of precision in the calculation of all of the other variables.

93
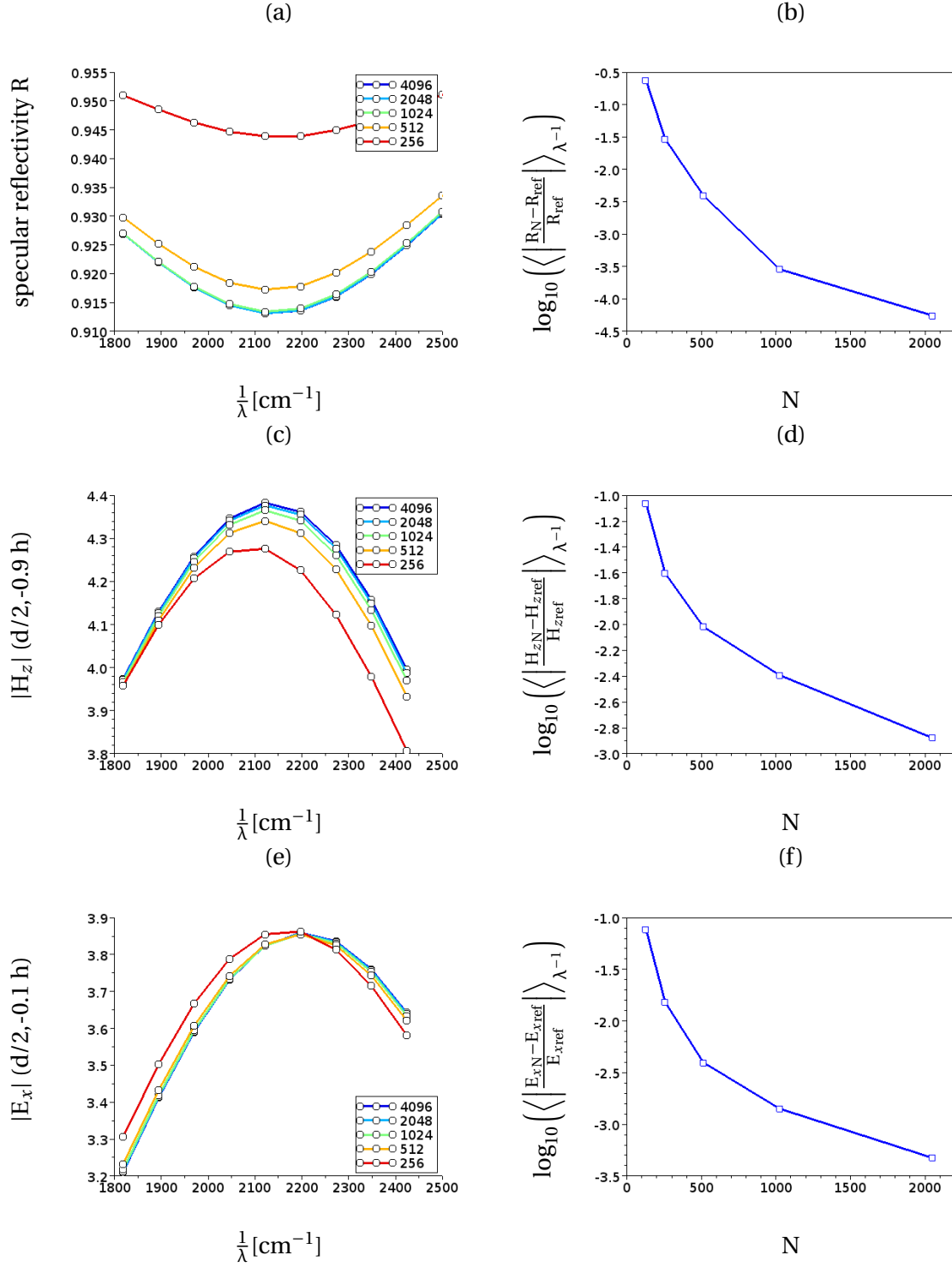
Figure 2.21: *(a)Specular reflectivity (c) magnetic field at (d/2,-0.9 h) and (e) the electric field at (d/2,-0.1 h) calculated by the surface integral method for different values of N for the 10 wavenumbers. On the right, their relative error averages on the 10 different wavelengths and with N_{ref}=4096 points are plotted in a logarithmic scale for (b) the reflectivity, (d) the magnetic field at (d/2,-0.9 h) and (f) the electric field at (d/2,-0.1 h). Same grating and conditions of incidence than figure 2.18.*

94

We can conclude that the two solved unknowns converge towards one single solution. The physical quantities such as the reflectivity and the magnetic and electric fields converge as well and the relative error is far below 1 % and can be as low as 0.1 %. Furthermore, having a few points of the surface having a relative error in the range of 5-10 % does not automatically prevent the physical quantities from being more accurate if the two unknowns are negligible at that point. We ensured in this example the stable convergence of the surface integral method. We verify in the next paragraph that the solution is physically the right one by comparing it with the one obtained from the approximated modal method.

2.5.2.2 Validation of the solution: comparison with the approximated modal method
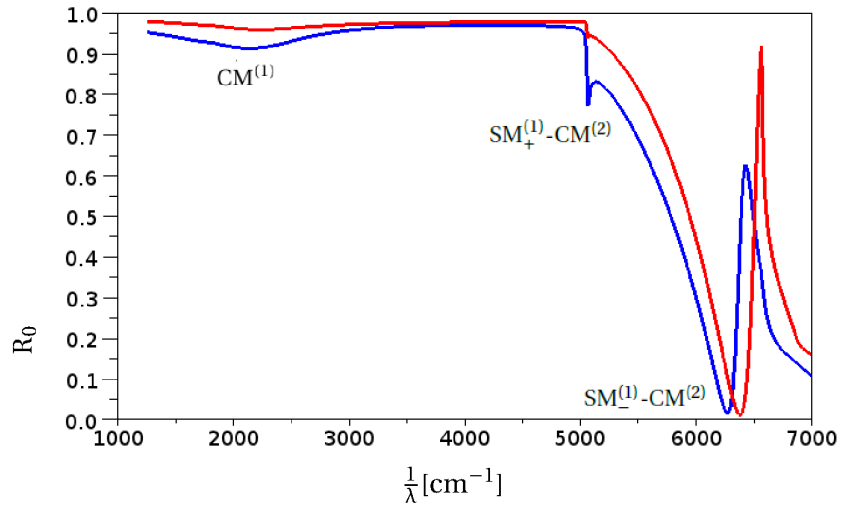
Figure 2.22: *Specular reflectivity of an incident plane wave impinging on a gold grating of period d=1.75 μm with rectangular grooves (w=0.75 μm and h=1 μm) similar to [12] at the incident angle $\theta_i = 7.5°$. Calculations are made by the surface integral method (blue) and the approximated modal method (red).*

As in the previous section, we have solved the problem of an incident plane wave impinging a gold grating of period d=1.75 μm with rectangular grooves whose width is w=0.75 μm and whose height is h=1 μm with an angle of incidence $\theta_i = 7.5°$ and in the IR spectral range. For this angle of incidence and in a range of wavenumber that goes from 1000 cm^{-1} (10 μm) to 7000 cm^{-1} (1.43 μm), both surface and cavity modes are expected. The m$^{\text{th}}$ order of the cavity modes is expected around $\lambda = \frac{4h}{m}$ (equation 1.27). The first order cavity mode CM$^{(1)}$ is thus approximately at 2000 cm^{-1} (5 μm) and the second order cavity mode CM$^{(2)}$ at 6000 cm^{-1} (1.6 μm). The surface mode SM$_\pm^{(m)}$ are expected at $\lambda_\pm^m = d(1 \pm \sin(\theta_i))/m$ (equation 1.17). Two surface modes are thus in the range of the chosen wavenumbers: SM$_+^{(1)}$ is at 5054 cm^{-1} (1.98 μm) and SM$_-^{(1)}$ is at 6572 cm^{-1} (1.52 μm).

Since the resonances of the cavity mode CM$^{(2)}$ and both surface modes SM$_\pm^{(1)}$ are close

95
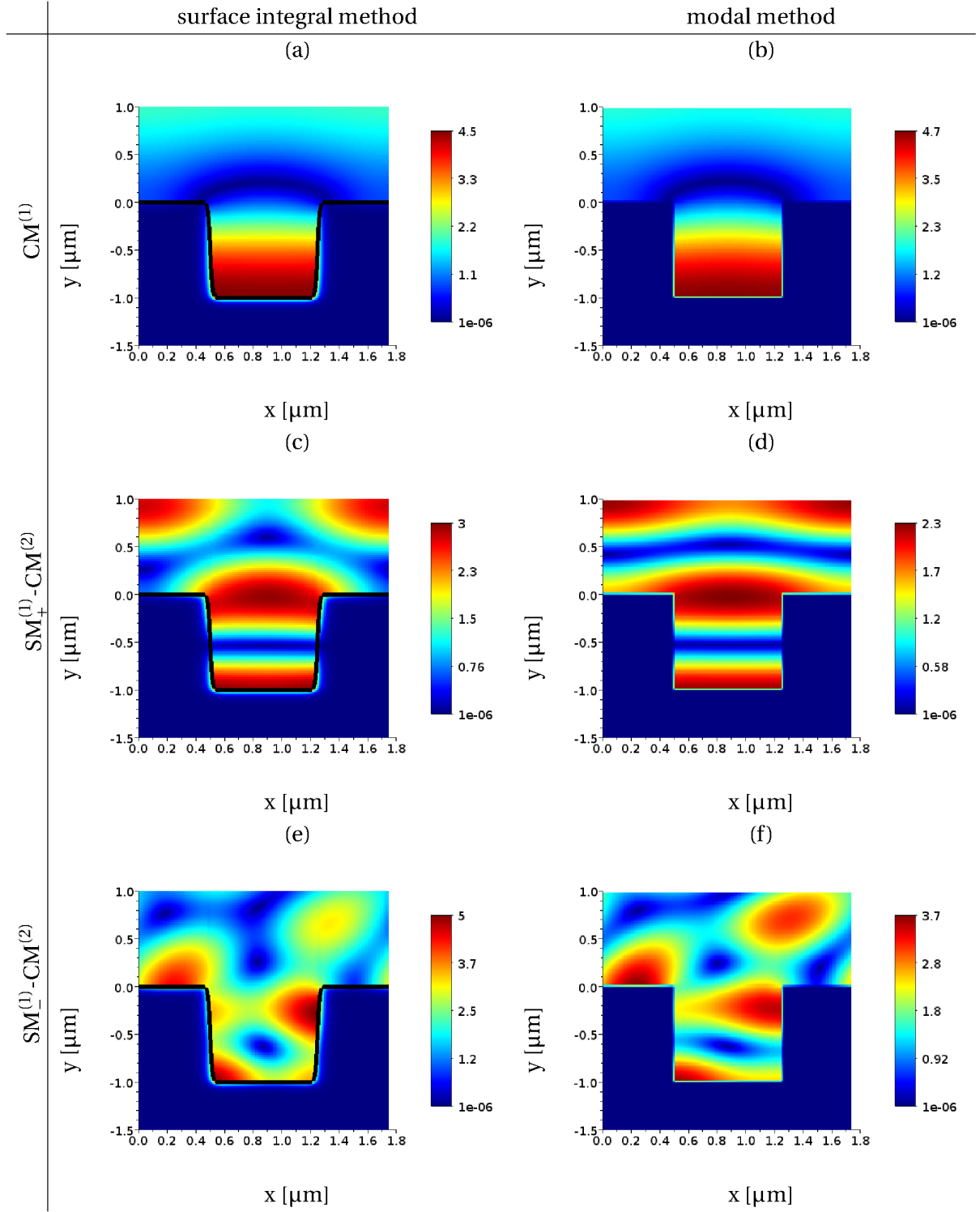
Figure 2.23: *Maps of the modulus of the magnetic field |H$_z$| calculated by the surface integral method (left column) and the modal method (right column) for a gold grating of period d=1.75 μm with rectangular grooves (w=0.75 μm and h=1 μm). The incident angle is θ$_i$ = 7.5° and the wavenumber is 2175 cm^{-1} (4.6 μm) (a,b), 5040 cm^{-1} (1.985 μm) (c,d) and 6250 cm^{-1} (1.6 μm) (e,f). The associated SPP modes are indicated on the left.*

96

Figure 2.24: *Maps of the modulus of the electric field $|E_x|$ calculated by the surface integral method (left column) and the modal method (right column) for a gold grating of period d=1.75 µm with rectangular grooves (w=0.75 µm and h=1 µm). The incident angle is $\theta_i = 7.5°$ and the wavenumber is $2175\ cm^{-1}$ (4.6 µm) (a,b), $5040\ cm^{-1}$ (1.985 µm) (c,d) and $6250\ cm^{-1}$ (1.6 µm) (e,f). The associated SPP modes are indicated on the left.*

97

to each other, the second cavity mode $CM^{(2)}$ supported by the grating is coupled with both surface modes. The three excited modes appear as three minima in the specular reflectivity in figure 2.22: the first order cavity mode $CM^{(1)}$ at 2175 cm^{-1} and two coupled surface and second order cavity mode $SM_+^{(1)}$-$CM^{(2)}$ at 5040 cm^{-1} and $SM_-^{(1)}$-$CM^{(2)}$ at 6250 cm^{-1}. We recall that the excitation of plasmonic modes by the incoming beam is responsible for a loss of energy of the diffracted orders. The plasmonic modes therefore appear as dips in the reflectivity. The magnetic and electric field intensities maps calculated using the two methods are shown in figure 2.23 and 2.24 for the sake of comparison of the two methods as well as the validation of the nature of each mode. The nature of the Fabry-Perot like resonance of the first cavity mode $CM^{(1)}$ is confirmed in both the magnetic and electric field maps as the field is localized in the cavity.

The field maps of the coupled surface modes and second order cavity mode $SM_+^{(1)}$-$CM^{(2)}$ and $SM_-^{(1)}$-$CM^{(2)}$ show both nature: a Fabry-Perot like resonance with a resonance wavelength three times smaller than the one of the first order cavity mode and a magnetic field at the interface which is the one of a stationary wave with a period d. The magnetic field is maximum above the groove for $SM_-^{(1)}$ and above the metallic surface for $SM_+^{(1)}$. The mode $SM_+^{(1)}$-$CM^{(2)}$ is weakly coupled as its wavenumber of resonance is close to the one of the surface mode $SM_+^{(1)}$ where as the wavenumber shift is more important for the $SM_-^{(1)}$-$CM^{(2)}$ mode. Moreover,the intensity of the field in the cavity at the resonance of $SM_+^{(1)}$-$CM^{(2)}$ is smaller than the one of $SM_-^{(1)}$-$CM^{(2)}$.

The spectrum of the electric field $|E_x|$ at the top of the groove i.e. at the point of coordinates $(d/2, -0.1h)$ and the one of the magnetic field at the bottom of the groove i.e. at the point of coordinates $(d/2, -0.9h)$ (where they are maximum) are compared for the modal method and the surface integral method in figure 2.25. We can see that the comparison of the integral and approximated modal method is good but the plots do not superimpose as it is the case for the reflectivity (figure 2.22). The differences have two origins: the difference in the geometry of the groove and the approximations used to describe the metallic surface behavior in the modal method. If the steepness of the groove is increased, the resonance wavenumber of the mode $SM_-^{(1)}$-$CM^{(2)}$ increases and the dip in the specular reflectivity of the integral method is shifted toward the one of the approximated modal one. The specular reflectivity of the two methods also get closer. We now detail how the approximation in the modal method intervenes.

In the approximated modal method, the vertical walls are considered to be a perfect metal. Hence, the energy losses due to a plasmonic cavity mode are under estimated. It results in a visible difference for the first cavity mode $CM^{(1)}$: the dip in the reflectivity is less important in that case than in the SIE method (the dips are also more pronounced in the experiments). The intensity of the magnetic field at the bottom of the groove as well as the electric field at the top of the groove at the resonance is also stronger in the modal method. The localization of the field is cost less in energy in the approximated modal method so the intensity of the magnetic field is higher than in the surface integral method. The minima of
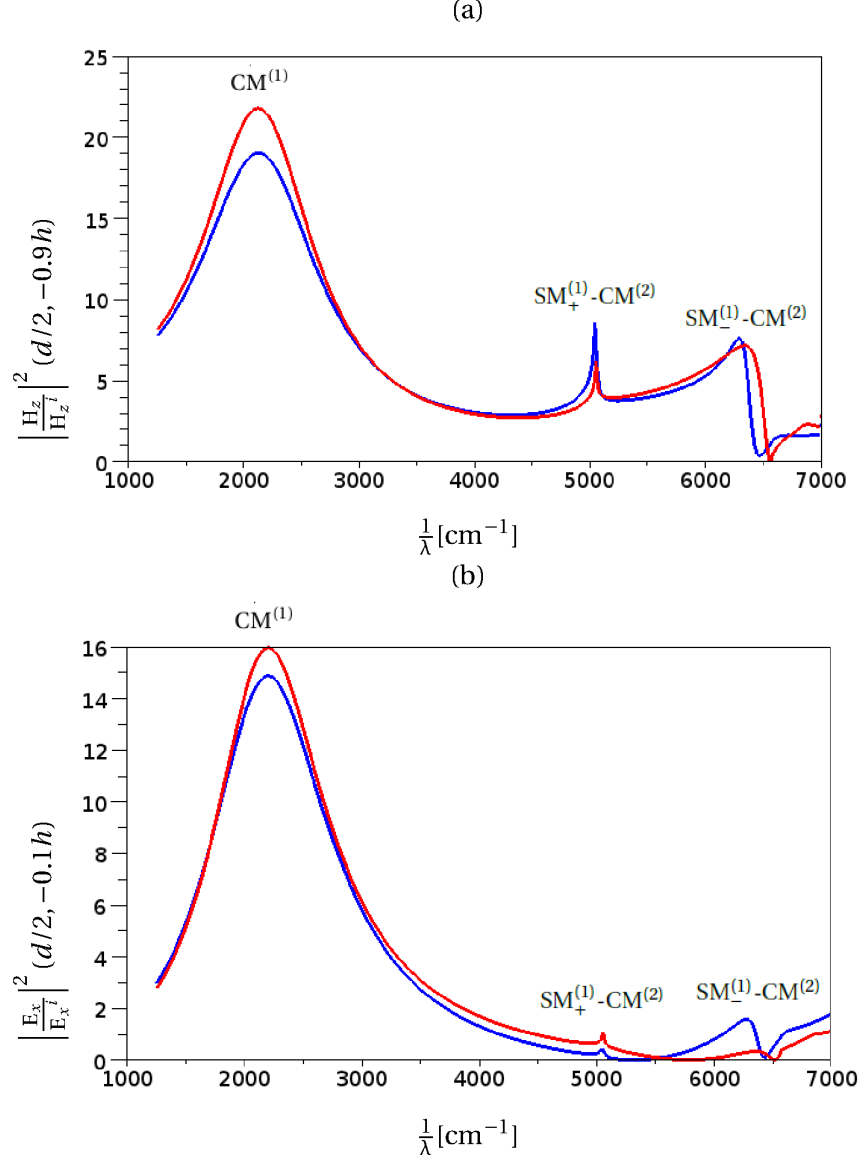
Figure 2.25: *Spectral dependance of the intensity of the magnetic field at the bottom of the groove (b) and of the electric field at the top (c) for an incident angle $\theta_i = 7.5°$ calculated with the surface integral method (blue) and the modal method (red) for a gold grating of period $d=1.75\,\mu m$ with rectangular grooves ($w=0.75\,\mu m$ and $h=1\,\mu m$) similar to [12].*

the reflectivity corresponding to the cavity modes are also translated due to the approximation, we will see why. The groove plays the role of a Fabry-Perot cavity. Considering a metal with a finite permittivity compared to a perfect metal is equivalent to consider a cavity filled with an effective index $n_{\mathrm{eff}} = \sqrt{1 + \frac{2i}{k_0 w \sqrt{\epsilon^-}}}$ compared to a cavity filled with an index $n = 1$. The surface integral method mode has thus a resonance at $1/\lambda_{\mathrm{res}} = 1/(\lambda n_{\mathrm{eff}})$ compared to the resonance of the modal method at $1/\lambda$. At $\lambda = 1.6\,\mu m$ with $\epsilon^- = -103 + 12i$, we find n_{eff}=1.03. The mode $SM_-^{(1)}$-$CM^{(2)}$ of the modal method at $1/\lambda = 6400$ cm^{-1} is translated to

$1/\lambda_{res} = 6200$ cm^{-1} in the case of the surface integral method. The difference is less important for the first cavity mode because $\epsilon^- \approx -600$ and the wavelength is bigger. This roughly explains the shift of the frequency of the cavity mode to the smaller wavenumbers (ie to the left) with the integral method.

To sum up, both methods permit us to obtain similar results: the reflectivity shows the similar minima due to the excitation of SPP surface and cavity modes and the magnetic and electric field intensity maps are in good agreement. The rectangular groove is, however, not reproduced exactly in the surface integral method and the approximated modal program models the vertical walls of the groove as a perfect metal and the horizontal walls of the grooves with the approximation of surface impedance. Expected little differences between the two numerical approaches are therefore visible such as a difference in the energy losses and a frequency shift. However, this comparison proves that the surface integral method program is correct in the IR spectral range.

2.5.3   Grating studied in the visible spectral range

Eventually, the results obtained from the surface integral method are compared to the exact modal method using an example extracted from Jerome Le Perchec's thesis [18]. In this case, three silver gratings are studied in the visible spectral range, the period of the grating is 30 nm, the width of the rectangular grooves is 5 nm and the heights of the groove are 8, 15 and 30 nm. The rectangular groove profile is approximated by an analytical function, equation 2.73, as for the study in the IR with $\beta = 60$ (β is lower than the one in the previous section because the ratio height over width is higher). The convergence of the solution of the surface integral equations is checked in the same way that it was done for the grating studied in the IR. The results of the surface integral method are plotted for two different number of points N in the resolution, N=500 and N=1000, in order to prove that the curves superimpose and that the convergence is reached. The excitation of the first order cavity mode of the three silver gratings, at normal incidence of the incident plane wave, is shown as a maximum in the magnetic field at the bottom of the groove in figure 2.26(a,c) and a dip in the reflectivity in figure 2.26(b,d). The map of the magnetic near-field modulus of the silver grating with a groove height equal to 15 nm is also shown in figure 2.27. It was calculated at the resonance energy E=2.6 eV using both methods for comparison.

We ensure that the surface integral method has been implemented correctly thanks to the agreement between the two independent methods. There is, however, once again a little difference which we attribute to the difference in the geometry of the groove.
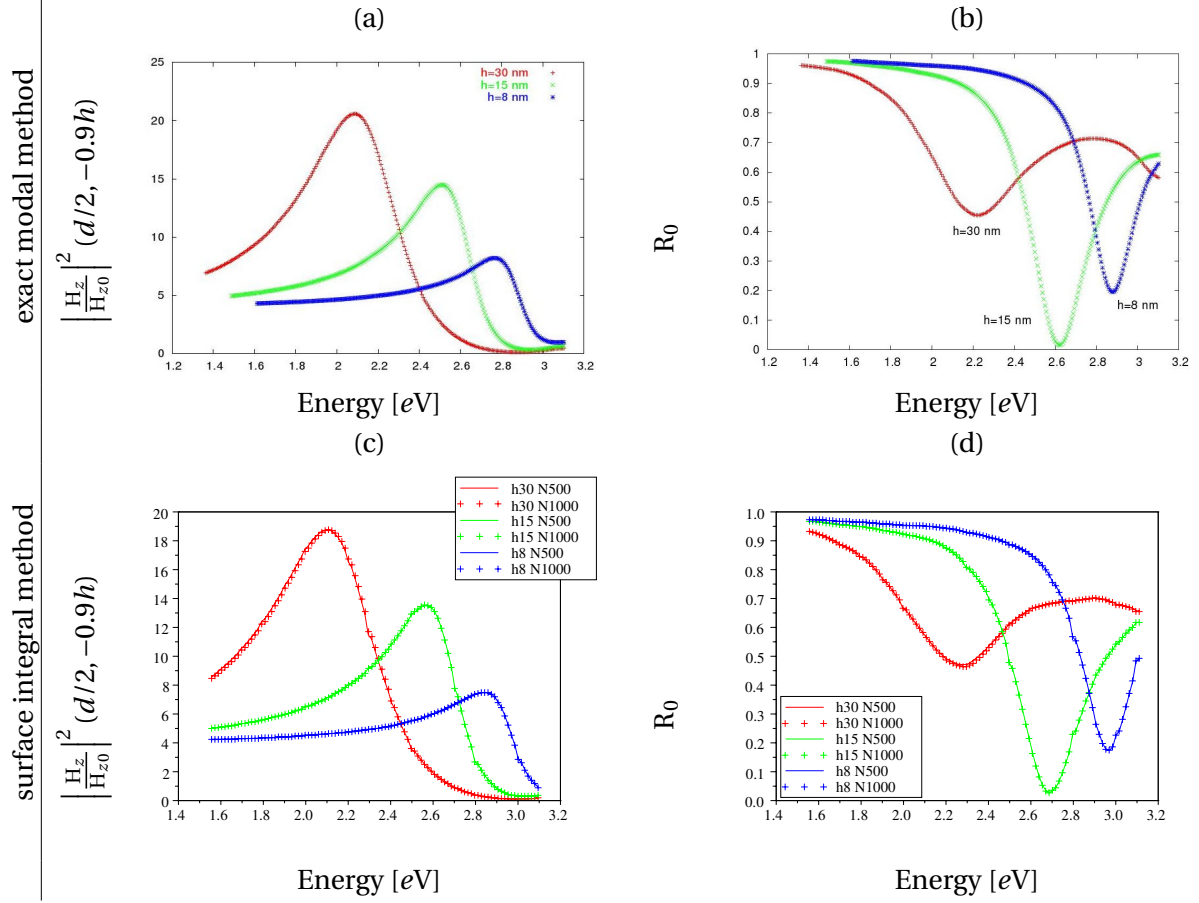
Figure 2.26: *(a) Intensities of the magnetic field at the bottom of the groove and (b) specular reflectivity calculated by the exact modal method [18] and compared to (c) intensities of the magnetic field at the bottom of the groove and (d) specular reflectivity calculated by the surface integral method respectively obtained with a number of points N=500 (solid line) and N=1000 (crosses) to discretize the profile. The gratings are made of silver with a period d=30 nm and rectangular grooves of width w=5 nm and height h=8 (blue), h=15 (green) and h=30 nm (red). The incidence angle is θ_i=0°.*

2.6 Conclusion

We have implemented the periodic surface integral equations described in this chapter in order to be able to calculate the field around nano-scale defects. We choose to periodize the problem to avoid border effects as well as to have a smaller length of surface thus enabling us to have smaller defects and to reach sizes of roughness under 10 nm. The surface integral equations method is based on the expression of the EM field at any point of the volume as the propagation of a known source on the boundary. The Green function or its derivative plays the role of the propagators. The magnetic field at any point of the surface is then expressed as the sum of the propagated fields created at all the points of the surface by the

(a)   (b)
surface integral method   exact modal method
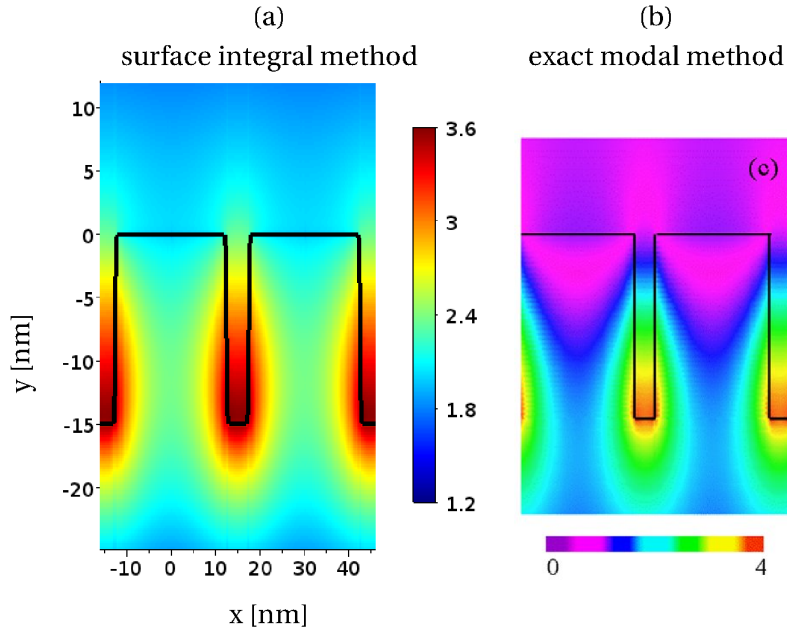
Figure 2.27: *Maps of the modulus of the magnetic field* $|H_z|$ *at an energy of 2.6 eV and* $\theta_i = 0°$ *calculated by the surface integral method (a) and the exact modal method (b) from [18]. The groove sizes are w=5 nm, h=15 nm and the period of the grating is d=30 nm.*

existence of the magnetic field H itself and its derivative, called L, which both play the roles of sources. The SIE method eventually consists in solving two self coherent equations on H and L which are functions of their coordinates on the surface.

To do so, we worked on how to calculate a pseudo-periodic Green function and how to retrieve physical quantities such as the reflectivity and the magnetic and electric field. We highlighted the numerical difficulties we had to overcome: the calculation of the sums in the pseudo-periodic Green function and the one of the integrals of the Green function needed for the magnetic and electric field. The pseudo-periodic Green function needs special attention as it can be written as different sums whose convergence depends on the media of propagation as well as on the traveled distance and we presented an efficient way to evaluate the Green function. The analytical expression of the derivatives, which were not found in the literature, were also derived. The calculation of the electric and magnetic fields require us to evaluate integrals carefully due to the divergence of the Green function at its origin. A recurrent algorithm was proposed to overcome this difficulty.

Eventually, we checked our program, compared it with both the approximated and the exact modal method and showed that it converges towards the right solution. We also showed that it is indeed able to solve problems in the nanometer range scale and we will use this method to study the nano-scale arbitrary shaped defects of metallic surface in the next chapter.

Chapter 3

Application of the surface integral equations method to nano-scale roughness and defects

The behavior of a metallic grating with sub-wavelength rectangular grooves studied in the visible spectral range exhibits two kinds of plasmonic modes: the surface modes which consist in the propagation of a SPP at the surface of the grating and the cavity modes which consist in the Fabry Perot resonance of an SPP guided mode into the grooves. Due to their strong confinement of the EM field in the groove, the cavity modes are of particular interest.

Maradudin *et al.* showed there exists the same phenomenon in differently shaped grooves (Gaussian shaped grooves and circular ones) than the rectangular one [124, 125] by calculating the dispersion relation of the EM modes of the structures made of perfect metal. They called the EM wave standing in the cavity a *Channel Plasmon Polariton* (CPP). They were not able to obtain accurate dispersion relations for structures made of a lossy metal and one of their conclusions was that in order to have an EM mode in the visible range ($\lambda = 632.8$ nm), the width of the groove had to be smaller than about 30 nm. The resonances of Channel Plasmon Polariton of dimensions within 100 nm - 1µm were then studied theoretically as well as experimentally for wedge and triangular-grooves at wavelengths within 0.5-1.5 µm [126, 127, 128, 129]. The aim of the studies was mainly to demonstrate the guiding of the CPP along the groove in view of circuitry applications. Some recent studies investigated the optical properties of triangular groove gold gratings with a groove height of 200 nm in the visible spectral range [99].

To our knowledge, the EM resonances of triangular or Gaussian-shaped grooves of smaller dimension were not studied. However, we saw in section 1.3.3, that if the width w of the groove is smaller than a few tens of nanometers (the exact value depends on the permittivity of the metal), the cavity mode enters in an electrostatic regime. The characteristics of this regime are: 1) a spectral resonance of the EM fields into the groove whose

frequency depends on the ratio w/h, with h the height of the groove, 2) a very strong electric field enhancement and 3) a very low reflectivity at this resonance. The aim of this chapter is to determine if the electrostatic behavior may also be observed for a grating with differently shaped grooves, here Gaussian shaped grooves similar to that of [125], and if the tiny Gaussian shaped grooves gratings may model random rough surfaces such as the coldly evaporated films surfaces. For simplicity, the Gaussian shaped grooves are hereafter called Gaussian grooves.

3.1   EM resonances of gratings with a single Gaussian groove per period

In this section, we start by studying the EM resonances of a grating with one Gaussian grooves per period. The Gaussian groove of height h, of full-width at half maximum w (called hereafter the width) and centered at the abscissa x_i has a profile function

$$D : x \rightarrow -he^{-\left((x-x_i)\frac{2}{w}\sqrt{\log 2}\right)^2} \tag{3.1}$$
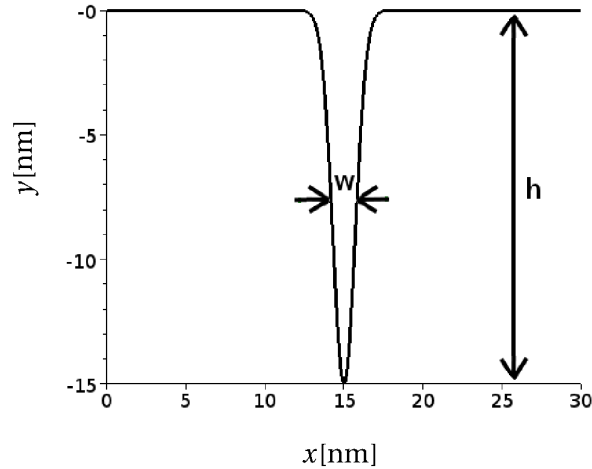
Figure 3.1: *Representation of the profile of the Gaussian groove of width w=1.66 nm and height h=15 nm grating of period d=30 nm.*

We take interest in a plane wave impinging on a silver grating of period d=30 nm with a Gaussian groove of width w=1.66 nm and height h=15 nm whose profile is shown in figure 3.1. We want to determine whether a plane wave of energy in the range of 1.5 to 3.5 eV, the visible spectral range, excites EM resonances and if so, to characterize them.

3.1.1 Identification of the EM resonances

The reflectivity of an incident plane wave impinging with an incidence angle $\theta_i = 10°$ on the grating presented here above, is shown in figure 3.2. Two dips in the reflectivity, at 1.97 eV and 2.75 eV, appear and are the signature of the EM resonances. These resonances hardly depend on the angle of incidence: the first dip starts to shift slightly in the spectrum from 1.97 eV toward higher energies to reach 2.14 eV when the incidence angle goes from 30° to 80° whereas the second dip stays at 2.75 eV within the range of $\theta_i = 0°$ to 80° (the reflectivity at other angles than 10° are not shown here).

$$E = \hbar \frac{2\pi}{\lambda} \text{ [eV]}$$
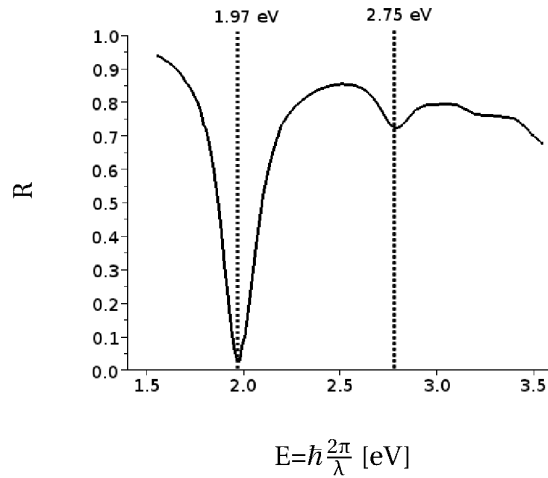
Figure 3.2: *Specular reflectivity of an incident plane wave impinging on a silver grating of period d=30 nm with a single Gaussian groove per period of width w=1.66 nm and height h=15 nm for an incident angle θ_i=10°.*

The maps of the modulus of the magnetic field $|H_z|$ and the modulus of the electric field $|E_x|$ at the resonance of the first dip (E=1.97 eV), when the grating is excited by a plane wave of incidence angle $\theta_i = 10°$, are plotted in figure 3.3. For comparison, we plot the maps of the modulus of the magnetic field $|H_z|$ and the modulus of the electric field $|E_x|$ for a plane wave with an incident angle $\theta_i = 10°$ and an energy of 2.14 eV impinging on a silver grating of period d=30 nm with a rectangular groove of width w=2 nm and height h=15 nm in figure 3.4. These conditions of incidence ($\theta_i = 10°$, E=2.14 eV) correspond to the resonance of the first order cavity mode for the rectangular groove. In both the rectangular and the Gaussian groove, the EM field is localized in the groove and much enhanced with respect to the incident light. We have seen that the EM field in the rectangular groove at resonance is the one of a guided wave built by the coupling of SPPs propagating on each side of the vertical walls. The Fabry-Perot like resonance of this guided SPP wave of wavevector Λ_0 results in cavity modes whose m^{th} order happens for

$$\left(\frac{\Lambda_0}{2\pi}\right)^{-1} \sim \frac{4h}{2m-1} \quad . \tag{3.2}$$

105
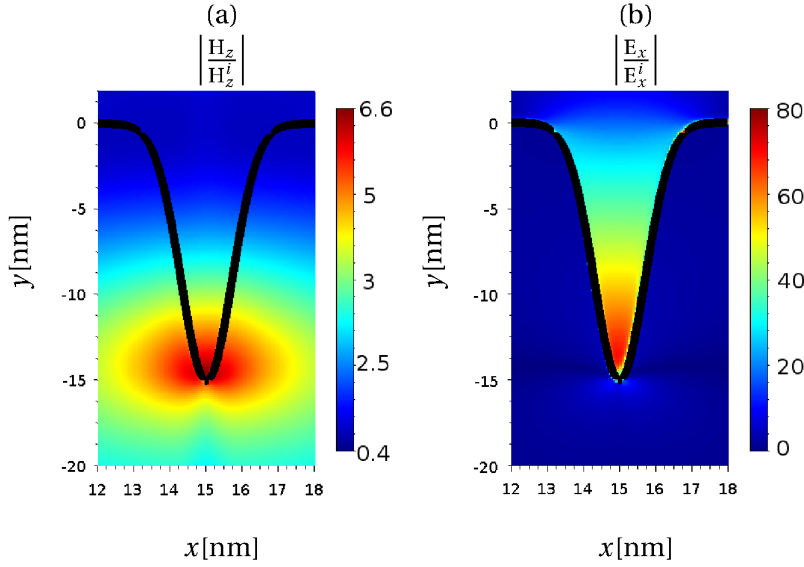
Figure 3.3: *Maps of the modulus of the magnetic (a) and electric (b) fields for a silver grating of period d=30 nm with a single Gaussian groove of width w=1.66 nm and height h=15 nm excited by an incident plane wave of energy E=1.97 eVm and angle* $\theta_i = 10°$. *The color scale gives the value of the* $\left|\frac{H_z}{H_z^i}\right|$ *and the* $\left|\frac{E_x}{E_x^i}\right|$ *respectively.*
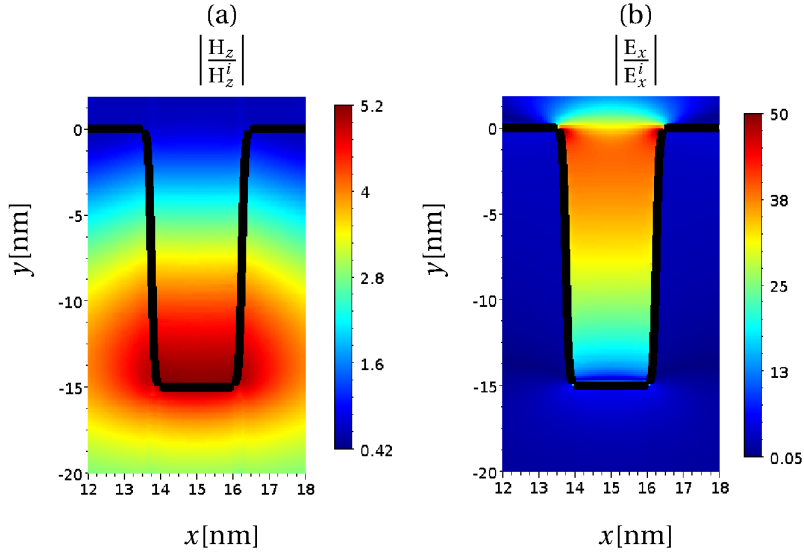
Figure 3.4: *Maps of the modulus of the magnetic (a) and electric (b) fields for a silver grating of period d=30 nm with a single rectangular groove of width w=2 nm and height h=15 nm excited by an incident plane wave of energy E=2.14 eVm and angle* $\theta_i = 10°$. *It corresponds to the first order cavity mode. The color scale gives the value of the* $\left|\frac{H_z}{H_z^i}\right|$ *and the* $\left|\frac{E_x}{E_x^i}\right|$ *respectively.*

The wavelength of the guided wave, $(\Lambda_0/2\pi)^{-1}$, of the first order cavity mode is therefore four times bigger than the height. In our case of the rectangular groove, a first order cavity

106

mode is excited and the EM field in the rectangular groove corresponds to a standing wave over a quarter of the wavelength. By analogy, the EM fields corresponding to the first dip in the reflectivity, in the case of the Gaussian groove, are identified as a standing wave standing in the groove due to the coupling of SPPs supported by the metallic surface of the groove and the EM resonance is identified as a first order cavity mode. We note that, due to the tightening of the Gaussian groove when going downward, the maximum of the electric field enhancement is situated at the bottom of the Gaussian groove whereas it is situated at the top of the rectangular groove.

The maps of the modulus of the magnetic field $|H_z|$ and the modulus of the electric field $|E_x|$ at the resonance of the second dip, an incident angle $\theta_i = 10°$ and an energy of 2.75 eV, are plotted in figure 3.5 (for the Gaussian groove grating). The electric field exhibits a maximum at the bottom of the groove and an intermediate maximum at the ordinate y=-9 nm. The magnetic field also has a maximum at the bottom of the groove although it is very weak. The EM field is localized in the groove and may be identified, in the same way as the first dip, as a standing wave over three quarters of the wavelength of the wave i.e. $\lambda_{\text{res}} \simeq 4h/3$. In the case of the rectangular groove, the wavelength of the guided wave $(\Lambda_0/2\pi)^{-1}$ of the second order cavity mode is according to equation 3.2 similar to $4h/3$. The standing wave of the second order cavity mode of the rectangular groove is expected to have a wavelength three times shorter than the first order cavity mode. By analogy with the rectangular groove grating, the second dip at 2.75 eV in the reflectivity of the plane wave impinging on the Gaussian groove grating is thus identified as the second order cavity mode.
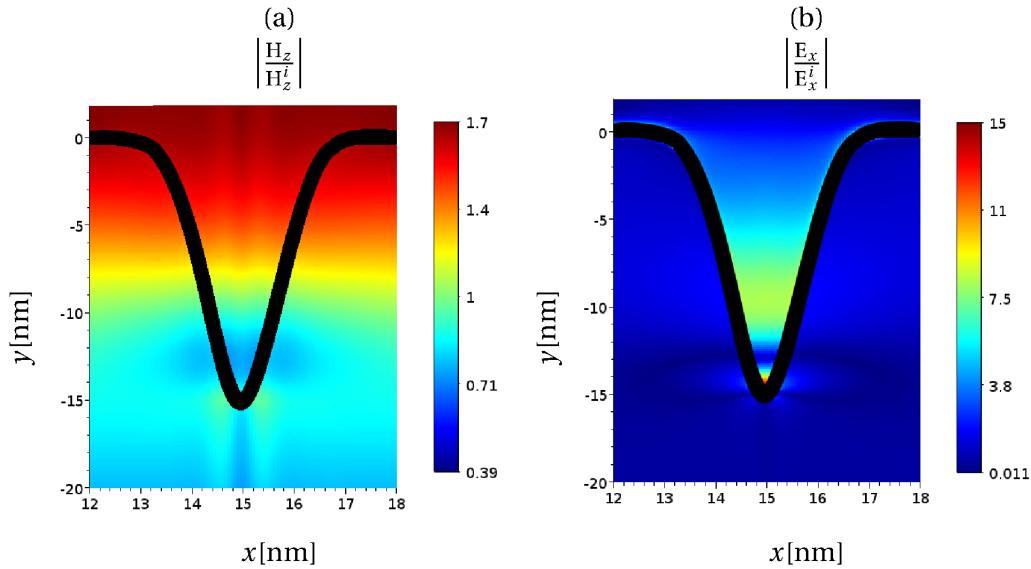
Figure 3.5: *Maps of the modulus of the magnetic (a) and electric (b) fields on a silver grating of period d=30 nm with a single Gaussian groove of width w=1.66 nm and height h=15 nm excited by an incident plane wave of energy E=2.75 eVm and angle $\theta_i = 10°$. The color scale gives the value of the $\left|\frac{H_z}{H_z^i}\right|$ and $\left|\frac{E_x}{E_x^i}\right|$ respectively.*

We see in the maps of the modulus of the magnetic field in figure 3.3(a) and 3.5(a) that in the groove, the magnetic field is invariant in the x-direction and therefore that the electric field in the y direction is almost zero. That is why the maps of the electric field E_y are not plotted. As a consequence the electric field in the x direction is comparable to the total one $|E_x| \approx |E|$.

By analogy with the EM resonances of the rectangular groove grating, we proposed that the two dips in the reflectivity of a plane wave exciting a Gaussian groove grating are due to a first order and a second order cavity mode. In the next paragraph, we want to verify that we have a resonance phenomenon.

3.1.2   Confirmation of the resonance of the EM field

In order to highlight the resonance phenomena, we examine the magnetic and electric field as a function of the energy. To do so, we have to consider specific points in the groove. Based on the maximum and the minimum which we have seen in the EM field maps, we look for the EM fields at the middle of the groove, x=15 nm, and for three ordinates corresponding to the opening of the groove y=-1.5 nm, the middle of the groove y=-9 nm and the bottom of the groove y=13.5 nm. We ensure that the EM field is accurately calculated by standing at a distance greater than one nanometer from the surface.

Let us first take a look at the magnetic field spectra shown in figure 3.6. The plots of the spectra for the three points are translated in the y-axis for sake of clarity. The peak at 1.97 eV in the spectrum of the magnetic field at the bottom of the groove confirms that the first dip is associated to a resonance phenomena. There is not really a peak at 2.75 eV in the magnetic field spectra which is not surprising as the magnetic field map in figure 3.5(a) shows a very weak magnetic field.

Let us now turn to the electric field. We plotted the real part of the electric field in figure 3.7 because we wanted to differentiate the directions toward which the electric field is pointed at. At E=1.97 eV, there is a peak in the three spectra for the electric field at the different ordinates translated along the y-axis. The electric field is uniformly increasing from the top to the bottom of the groove in agreement with the electric field being the one of a standing wave over one quarter of a wavelength and the resonance being the one of a first order cavity mode. At E=2.75 eV, there is a dip in the spectrum of the real part of the electric field at the bottom of the groove and a peak in the one at the top of the groove. The peak in the spectrum at the top of the groove corresponds to a maximum of the electric field in the same direction than the first order cavity mode whereas the dip in the spectrum at the bottom of the groove corresponds to a maximum of the electric field in the opposite direction than the first order cavity mode. When going downward, the electric field E_x is in fact turning from a maximum in one direction of the x-axis in the upper part of the groove to a maximum in the opposite direction at the bottom of the groove. This is in agreement with the electric field being the one of a standing SPP wave over three quarters of a wavelength.
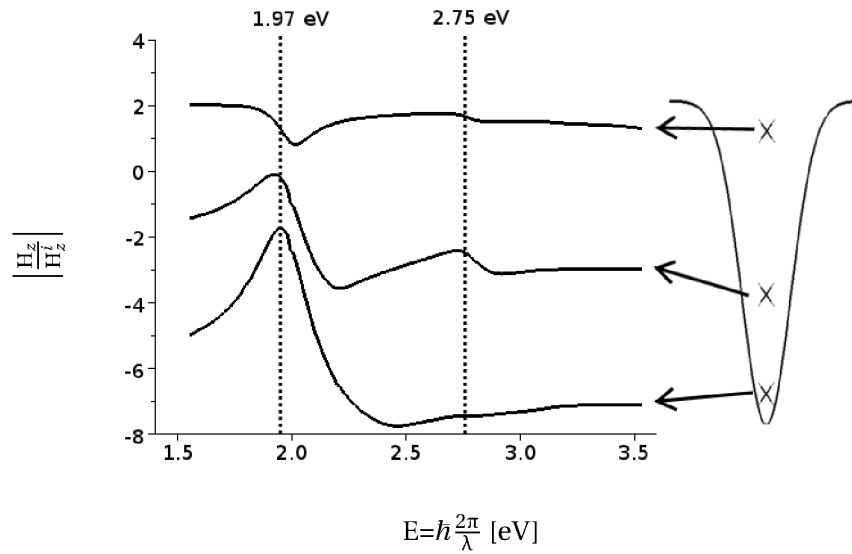
Figure 3.6: *Spectra of the modulus of the magnetic field* H_z *at three different heights, y=-1.5 nm, -9 nm and -15 nm, inside the groove and at the middle of it. The positions are marked by a cross on the groove profile sketched on the right. The magnetic fields are normalized by the intensity of the incident magnetic field* H_z^i *at the same point. The spectra of the two last ordinates are translated of respectively -4 and -8 in the y-axis. The system is a silver grating of period d=30 nm with a single Gaussian groove of width w=1.66 nm and height h=15 nm excited by an incident plane wave impinging with an angle* $\theta_i = 10°$.
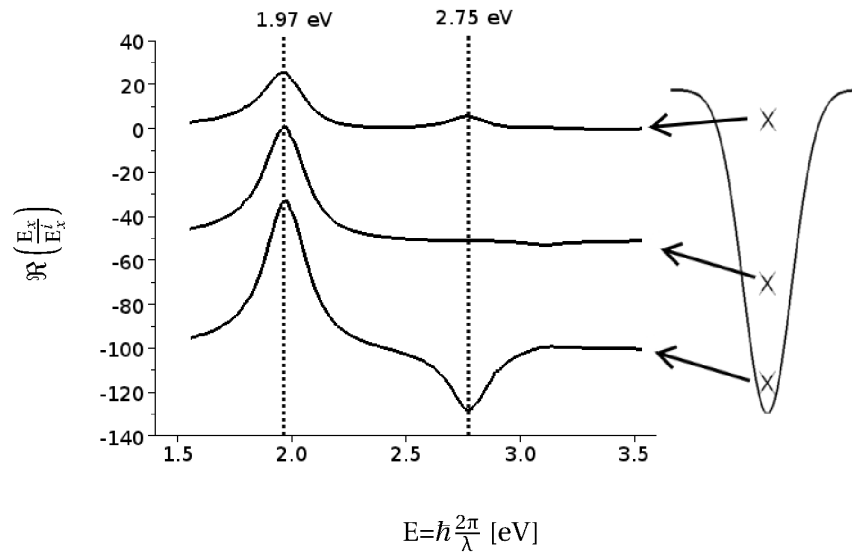
Figure 3.7: *Spectra of the real part of the electric field* E_x *at three different heights, y=-1.5 nm, -9 nm and -15 nm, inside the groove and at the middle of it. The positions are marked by a cross on the groove profile sketched on the right. The electric fields are normalized by the intensity of the incident magnetic field* E_x^i *at the same positions. The spectra of the two last ordinates are translated of respectively -50 and -100 in the y-axis. The system is the same as in figure 3.6.*

This confirms that the resonance is the one of a second order cavity mode.

The two dips in the reflectivity are thus associated to a peak at 1.97 eV and a dip at 2.75 eV in the real part of the electric field spectrum at the bottom of the groove. Additionally, there is a peak at 1.97 eV in the magnetic field spectrum at the bottom of the groove. We thus confirm that there exists two plasmonic resonances supported by the Gaussian groove grating, respectively a first order and a second order cavity mode as indicated by the EM field maps. We showed here that grooves of a few nanometers deep and wide, much smaller than the wavelength of the incident plane wave, with a different shape than the rectangular one may also exhibit cavity modes. In the next section, we study the first order cavity mode of Gaussian groove gratings more thoroughly.

3.2   First order cavity mode of the Gaussian groove gratings

3.2.1   Agreement of the behavior of the first order cavity mode with the electrostatic regime

In order to generalize the results on the electrostatic behavior of the tiny rectangular groove gratings in the visible spectral range, gratings with Gaussian shaped grooves of similar dimensions are studied.

Four Gaussian grooves gratings, whose dimensions qualify to be in the electrostatic regime, are put to the test. The profile of each grating is represented in figure 3.8. The gratings are all made of silver and their period is set to 30 nm. For this choice of period d, there exists no surface mode in the visible spectral range. Two heights and two ratios w/h are chosen in order to allow the comparison of the behavior of the four different gratings as described in table 3.1. The widths at half-heights are chosen to be less than 10 nm as it was shown that rectangular grooves gratings enter in the electrostatic regime in that range of width for silver.

width w [nm]	height h [nm]
1.66	15
3.32	15
3.32	30
6.64	30

Table 3.1: *Characteristics of the gratings of period d=30 nm with a Gaussian groove of width w and depth h. The width is the full-width at half maximum.*

We start by looking at the EM resonances of the first grating in table 3.1 with a Gaussian groove of width w=1.66 nm and height h=15 nm.
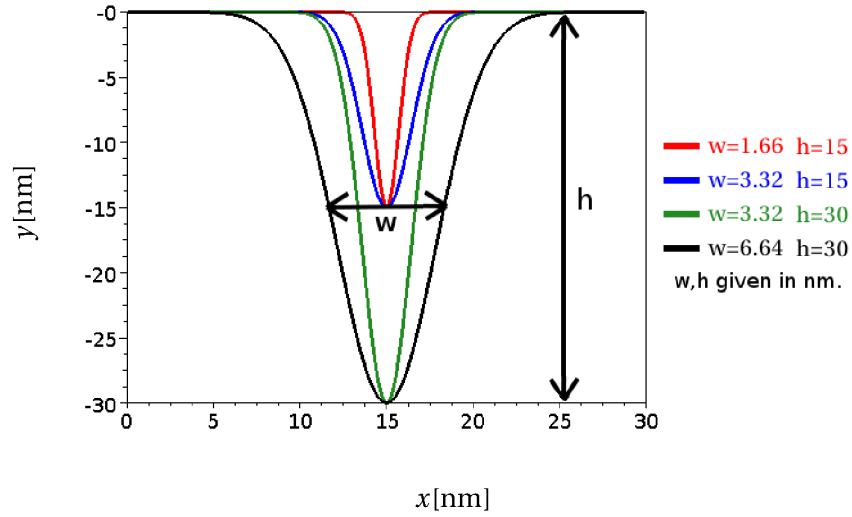
Figure 3.8: *Representation of the profile of the Gaussian grooves described in the table 3.1.*

3.2.1.1 Characterization of the cavity modes for small Gaussian groove gratings

We study the behavior of the first order cavity mode for the four gratings described in table 3.1. We want to determine how does the energy of the resonance depend on the width and the height, and if so, whether the electric field is enhanced and the reflectivity very low at this resonance.
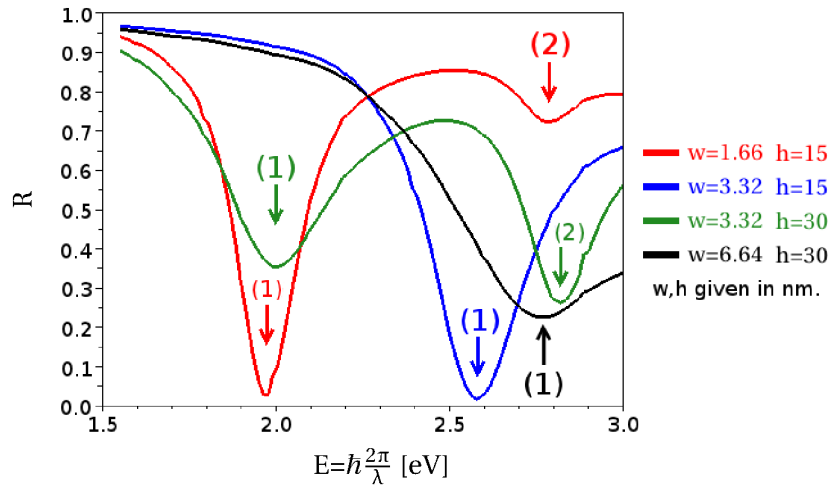
Figure 3.9: *Specular reflectivity for the four Gaussian grooves gratings described in the table 3.1 for an incident angle θ_i=10°.*

The specular reflectivity of a plane wave impinging on the four silver gratings at θ_i=10°, are represented in figure 3.9. We observe one or two dips in the reflectivity for each grating,

noted (1) and (2). The reflectivity at the minimums (1) is very low, less than 0.4 and goes down to almost zero for the dips (1) of the red and blue curves (grooves with a depth h=15 nm). The reflectivity of the silver grating with a Gaussian groove of width w=1.66 nm and height h=15 nm studied in the first paragraph appears again as a red line and the two dips are identified as the first and second order cavity mode. In order to identify the first order cavity mode for the three other Gaussian groove gratings, we look for a peak in the spectrum of the intensity of the magnetic field at the bottom of the groove shown in figure 3.10. We observe two regions of enhancement, at 1.95 eV for the grooves whose ratio w/h is 0.16 (red and green curves) and at 2.55 eV for the grooves whose ratio w/h is 0.32 (blue and black curves). The two different energies of resonance are indicated by dashed lines. They are the signature of the resonance of a first order cavity mode and correspond to the first dip (1) in the reflectivity of the respective gratings. The EM field maps at resonance, not reproduced here, are similar to the ones of the grating with Gaussian grooves of width w=1.66 nm and height h=15 nm. The energy of resonance of the first order cavity mode is thus similar for grooves with a similar ratio w/h and the energy of resonance therefore depends on the ratio w/h.
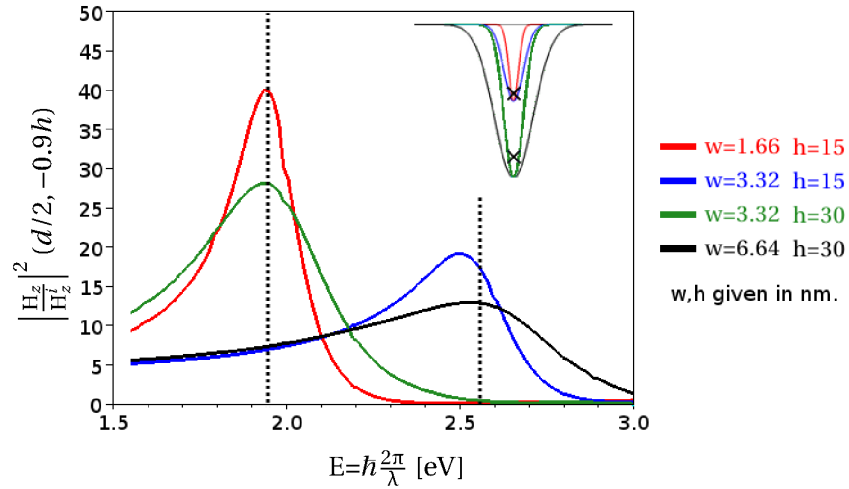
Figure 3.10: *Spectra of the intensity of the magnetic field H_z at the bottom of the grooves centered at x=d/2 (marked by a cross on the groove profile in the insert) and normalized by the intensity of the incident magnetic field $H_z{}^i$ at the same point for a plane wave impinging with an angle θ_i=10° on the four Gaussian grooves gratings described in table 3.1.*

The spectra of the intensity of the electric field enhancement at the bottom of the groove, shown in figure 3.11, also shows a peak around 1.95 eV for the red and green curves and at 2.55 eV for the blue and black curves as expected for a first order cavity mode in a Gaussian groove. The two different energies of resonance are indicated by dashed lines. We note that a second smaller peak around 2.75 eV for the green and red curves appears in the electric field spectra and corresponds to the second dip (2) in the respective curves of the reflectivity shown in figure 3.9. This second EM resonance is identified as a higher order cavity

112
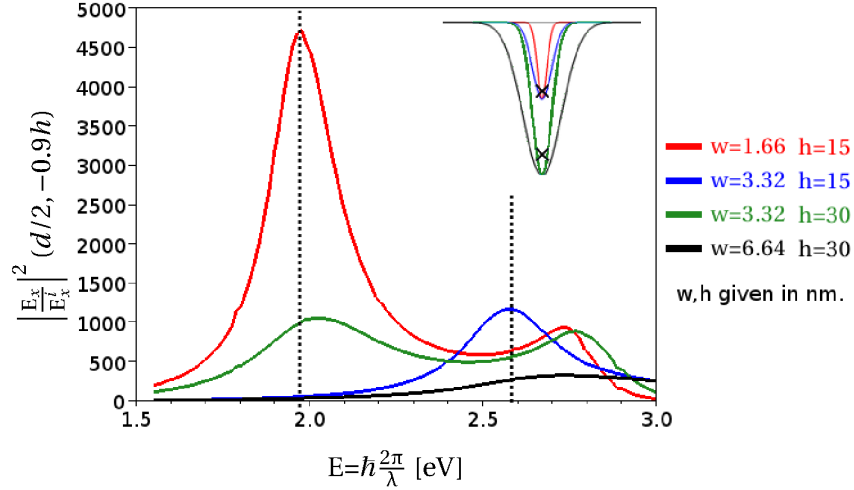
Figure 3.11: *Spectra of the intensity of the electric field* E_x *at the bottom of the groove centered at x=d/2 (marked by a cross on the groove profile in the insert) and normalized by the intensity of the incident electric field* E_x^i *at the same point for a plane wave impinging with an angle* $\theta_i=10°$ *on the four Gaussian grooves gratings described in table 3.1.*

mode and that is confirmed with the EM field maps at resonance which are not shown here since we focus on the first order mode.

The maximum of the enhancement of the intensity of the electric field is of several orders of magnitude higher than the maximum of the magnetic field one at the resonance of the first order cavity mode. The value of this maximum in the electric field intensity enhancement is of 5000 for the Gaussian groove with the smallest width w=1.66 nm (red curve), of a 1000 for the grooves with a width w=3.32 nm (green and blue curves) and of 300 for the groove with the largest width w=6.64 nm (black curve). These values range between 10^2 and 10^4 and it could give rise to SERS enhancement factor between 10^4 and 10^8.

We identified the first dip (1) in the reflectivity of a plane wave impinging on the four gratings as the first order cavity mode in the Gaussian groove and compared its behavior for the four gratings. In the next paragraph, these numerical observations are confronted with the characteristics of the resonances of the small rectangular grooves (the width w<10 nm) in the electrostatic regime.

3.2.1.2 Comparison of the resonance of the small Gaussian groove gratings with the electrostatic resonance of the small rectangular gratings

Let us first recall the characteristics of the electrostatic resonances of the silver rectangular grooves of width less than ten nanometer (w<10 nm) as seen in the section 1.3.3. In the electrostatic regime of the first order cavity mode of the tiny rectangular groove, the wavevector

of the guided SPP wave Λ_0 in the groove behave as [17]

$$\Lambda_0(\lambda) \simeq \frac{2}{w|\epsilon^-(\lambda)|} \tag{3.3}$$

where $\epsilon^-(\lambda)$ is the relative permittivity of the metal. As $w < 10 nm << \lambda \sim 400 - 800$ nm, the wavevector Λ_0 is very much bigger than the one of light k_0 i.e. $\Lambda_0 >> k_0$.

The electric field and the magnetic field are linked by the Maxwell equations, equation 1.4:

$$\left| \frac{E_x}{\frac{\partial H_z}{\partial y}} \right| = \frac{1}{\epsilon^+ k_0 \sqrt{\epsilon_0}}$$

and in the particular case of a wave having a wavevector in the y-direction equal to Λ_0, the ratio of the electric and magnetic field of the TM polarized wave becomes

$$\left| \frac{E_x}{H_z} \right| = \frac{\Lambda_0}{\epsilon^+ k_0 \sqrt{\epsilon_0}} >> \frac{1}{\sqrt{\epsilon_0}} \quad .$$

These are the general characteristics that qualify the resonance as an electrostatic one: a huge wavevector and a huge electric field compared to the magnetic one.

Let us now take a close look on the Fabry-Perot like resonance of the guided mode in the rectangular groove, which follows the equation 3.2. The huge wavevector Λ_0 and the Fabry-Perot like condition yield

$$\frac{2\pi}{\Lambda_0} << \frac{2\pi}{k_0} \Rightarrow 4h << \lambda$$

where λ is the wavelength of the incident plane wave. In the electrostatic regime, the resonance of the cavity mode happens for groove whose depth is small compared to the wavelength of the incident plane wave. Moreover, substituting the expression of Λ_0 in the electrostatic regime, equation 3.3, in the Fabry-Perot resonance condition, we have

$$\frac{w}{h} \simeq \frac{4}{\pi|\epsilon^-(\lambda)|} \quad . \tag{3.4}$$

For each wavelength λ of excitation, there exists a different ratio w/h of the groove parameters which fits the condition at the cavity resonance. The spectral dependence of the first order cavity mode is thus on the ratio w/h.

To summarize, the characteristics of the electrostatic resonance of the first order cavity mode in a groove of width w and height h are [18]:

- A resonance for the grooves of depth $h << \lambda$.

- A dependence of the resonance energy on the ratio w/h.

- An electric field $\left| E_x/E_x^i \right| >> \left| H_z/H_z^i \right|$.

114

- A low reflectivity. Such an extraordinary absorption was predicted for the rectangular groove gratings in the article *Why Metallic Surfaces with Grooves a Few Nanometers Deep and Wide May Strongly Absorb Visible Light* [17] and experimentally proved in [46].

Let us compare the observations made on the behavior of the first order cavity mode of the Gaussian groove with the characteristics of an electrostatic resonance step by step:

- The resonance wavelength of 490 nm (2.55 eV) and 640 nm (1.95 eV) is way bigger than the groove height h=15 nm or 30 nm.

- The dependence of the energy of resonance is on the ratio w/h. The grooves with a similar ratio w/h = 0.16 resonate at 1.95 eV whereas those with a ratio w/h=0.32 resonate at 2.55 eV.

- The electric field at the resonance is huge $\left|E_x/E_x^i\right|^2 \sim 10^3$ and more enhanced than the magnetic field $|E_x/H_z|^2 \sim 10^2 \left|E_x^i/H_z^i\right|^2$.

- The grooves with the smallest height, h=15 nm, are capable of absorbing almost entirely the incoming light energy as the specular reflectivity is almost zero for the dip (1) in the red and blue curve in figure 3.9.

We have shown the existence of a first order cavity mode in the visible range for Gaussian grooves of width less than 10 nm. The field maps at the resonance were consistent with a standing wave with a shorter wavelength, or a greater wavevector, than the one of the incident light and a maximum enhancement of the electric field greater than the magnetic field one. Furthermore, the excitation of the mode is dependent on the ratio w/h and leads to an almost total absorption of the incoming light. Therefore, by analogy with the rectangular groove grating, we may say that the first order cavity mode in the Gaussian groove of width w<10 nm is in the electrostatic regime.

3.2.2 Dispersion and enhancement factor of the first order cavity mode

In order to go further in our characterization of the first order cavity mode of the small Gaussian grooves (w<10 nm), we investigate the dispersion of the first order cavity mode and the enhancement factor (EF) at resonance. The energy and the EF factor of the electric field at the resonance of the first order cavity mode is determined for Gaussian grooves of width w=1.66 nm and for grooves twice wider w= 3.32 nm for several values of the height. As a comparison, the same study was performed for rectangular groove gratings of width w= 2.5 nm and twice bigger w=5 nm. All gratings are made of silver with a period d=30 nm.

3.2.2.1 Determination of some physical quantities at the resonance

As we have seen in the maps of the EM field at the resonance of the cavity modes, there is an EM field confined in the grooves. In the case of the rectangular groove, we know directly with the modal method (described in section 1.3.2) that the standing EM wave is due to the Fabry-Perot resonance of a fundamental mode of the cavity which is guided in the cavity and whose wavevector Λ_0 follows the equation 3.3 in the electrostatic regime. The fundamental mode of rectangular grooves of fixed width w, has the same wavevector Λ_0 whatever the height of the groove is. The dispersion of the fundamental mode of the cavity i.e. the energy of resonance of the fundamental mode as a function of its wavevector Λ_0 is known directly for each width w of the rectangular groove.

We have seen that the resonances of the cavity mode of the Gaussian groove have the same behavior than the rectangular groove in the electrostatic regime and in particular that the energy of resonance depends on the ratio w/h. By analogy with the rectangular groove grating, we can explain this dependence by the Fabry-Perot resonance of a guided mode in the cavity whose wavevector Λ_0 depends only on the width and not the height of the cavity. As explained in the previous section, if the wavevector follows $\Lambda_0 \simeq 2/w|\epsilon^-(\lambda)|$ and the Fabry-Perot resonance gives $\Lambda_0 h \simeq \pi/2$ then the ratio w/h follows the equation 3.4 and for each exciting wavelength, there exists only one ratio w/h which allows the cavity mode in the groove to resonate. In the same way as the rectangular groove, we may therefore look at the dispersion of the first order cavity mode for Gaussian grooves with a fixed width w and for different heights h. To plot the dispersion, one needs the energy and the wavevector of the mode in the cavity. At the resonance, an incident plane wave of wavelength λ_{res} (and of energy E=$\hbar k_0 = \hbar 2\pi/\lambda_{res}$) excites a standing wave whose wavevector Λ_0 normalized by the wavevector of light k_0 is approximated as

$$\frac{\Lambda_0}{k_0} \approx \frac{\lambda_{res}}{4h} \quad .$$

The physical quantity Λ_0/k_0 correspond to the enhancement of the wavevector of the EM wave standing in the cavity compared to the one of light. If $\Lambda_0/k_0 \simeq 1$, the EM wave resembles the one of light whereas $\Lambda_0/k_0 >> 1$ indicates that the resonance is in the electrostatic regime. By varying the height of the groove at fixed width w in the simulations, different values (λ_{res},h) at the resonance of the cavity mode are obtained. They give different values ($\hbar k_0$,Λ_0/k_0) of the dispersion curve for the groove of width w.

In order to calculate the dispersion curve ($\hbar k_0$ as a function of Λ_0/k_0), independent simulations are performed for gratings of period d=30 nm with a groove of fixed width w and with a height h ranging from 5 to 50 nm. The gratings are made of silver and illuminated by a plane wave with an incidence angle $\theta_i = 10°$. The spectra of the magnetic field enhancement at the bottom of the groove is calculated for each grating. The peak in each of the magnetic field spectra confirms the existence of the first order cavity mode and the spectral position of the maximum indicates the wavelength of the incident wave λ_{res} at the resonance. For each

of the height h, we thus have (λ_{res},h) which gives a point of the dispersion curve ($\hbar k_0$,Λ_0/k_0). The peak in the electric field spectra gives additionally the EF of the electric field at the resonance.
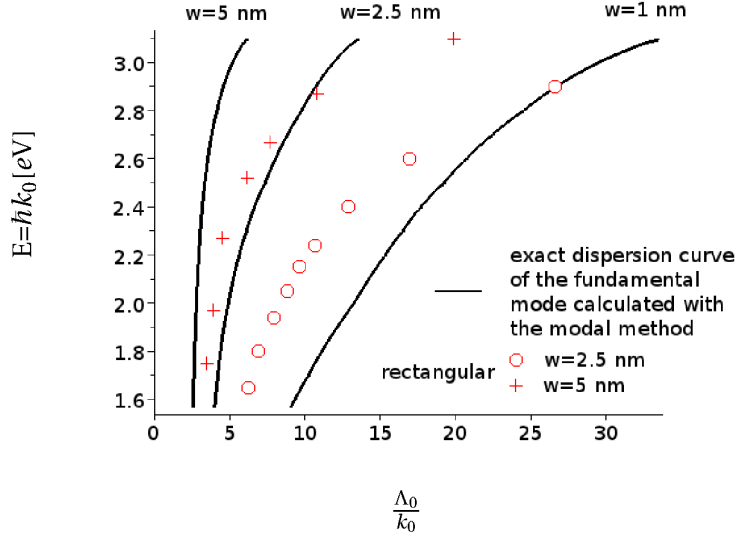
Figure 3.12: *Comparison between the exact dispersion curve of a rectangular groove silver gratings of period d=30 nm of width w calculated by the modal method and the approximate dispersion curve of the same grating calculated with the SIE method and the estimation $\frac{\Lambda_0}{k_0} \approx \frac{\lambda_{res}}{4h}$. The angle of incidence is θ_i=10°.*

In order to assess the relevance of this approach, we compare the exact dispersion curve of the fundamental mode calculated by the modal method for rectangular groove silver gratings of period d=30 nm of width w=1, 2.5 and 5 nm (black line) with the approximate dispersion curve calculated by the SIE method for rectangular grooves of width w=2.5 and 5 nm (red crosses and circles) in figure 3.12. One can see that the approximation of $\Lambda_0 \approx \pi/2h$ (Fabry-Perot resonance) is not accurate as there is approximately a factor two between the exact and the approximate dispersion curve. There is however a qualitative agreement between the two dispersion curves. The comments on the approximate dispersion curve shown in the next paragraph are therefore only qualitative.

3.2.2.2 The first order cavity mode dispersion

The dispersion curves ($\hbar k_0$,Λ_0/k_0), calculated with the SIE method and as explained in the previous paragraph, are plotted in figure 3.13 for silver Gaussian groove gratings (red) and as a comparison, for rectangular groove grating (blue). Independent simulations were performed for silver Gaussian groove gratings of width w=1.66 nm (red squares) and w= 3.32 nm (red crosses) and for silver rectangular groove gratings of width w=2.5 nm (blue squares) and w=5 nm (blue crosses).

117
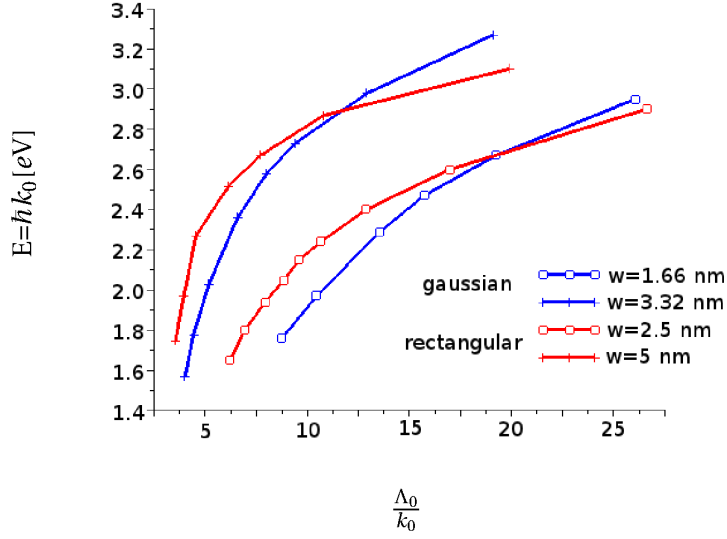
Figure 3.13: *Comparison of the energy of the incident plane wave $\hbar k_0$ at the first order cavity mode as a function of the ratio $\frac{\lambda_{res}}{4h} \approx \frac{\Lambda_0}{k_0}$ between a Gaussian groove grating of width w=1.66 nm (red squares) and w= 3.32 nm (red crosses) and a rectangular groove one of width w=2.5 nm (blue squares) and w=5 nm (blue crosses). The angle of incidence is θ_i =10°.*

The bigger width (crosses) is twice that of the smaller one (squares) and both are inferior to the limit of 10 nm to be in the electrostatic regime. The approximate dispersion curve of the first order cavity mode for the rectangular (red curves) and the Gaussian (blue curve) groove gratings is similar. This qualitative agreement in the approximate dispersion curve enables to draw a parallel between the EM resonances of the rectangular and Gaussian grooves. Some characteristics of the electrostatic regime which we have seen in the previous section are verified in figure 3.13: the wavevector Λ_0 increases when the width w decreases and additionally, $\Lambda_0/k_0 >> 1$. In the rectangular groove, these properties are due to a strong coupling of the SPP propagating on each vertical side of the groove facing each others. We may therefore generalize this explanation to the Gaussian groove. In the same way as for the rectangular groove grating, if the sides of the Gaussian groove are brought closer by diminishing the width w, the coupling of the surface plasmon supported by the metallic surface will be stronger, the coupled SPP wave will be more confined in the groove and the behavior of the mode will become more electrostatic.

3.2.2.3   Enhancement factor of the first order cavity mode

The maximum EF of the electric field is of interest because it gives a maximal value for the enhancement factor of SERS. We therefore compare the EF of the electric field at the resonance of the first order cavity mode, for different gratings, at the spot in the groove where

the EF is maximum. We thus calculated the spectrum of the electric field intensity for a point situated at the top of the groove for the rectangular groove gratings and at the bottom of the groove for the Gaussian ones, for the same gratings illuminated by a plane wave with an incidence angle $\theta_i = 10°$. The highest peak in each spectrum, appearing at the same energy as the one of the peak in the magnetic field spectrum, gives the maximum EF at the resonance of the first order cavity mode. The enhancement of the intensity of the electric field at the resonance of the first order cavity mode is represented in figure 3.14 for the same gratings as in the previous paragraph: silver Gaussian groove gratings of width w=1.66 nm (red squares) and w= 3.32 nm (red crosses) and as a comparison, silver rectangular groove gratings of width w=2.5 nm (blue squares) and w=5 nm (blue crosses). The enhancement is higher for the Gaussian groove gratings because the full-width at half height is smaller and the stranglehold formed by the Gaussian groove at the bottom confines the EM field.
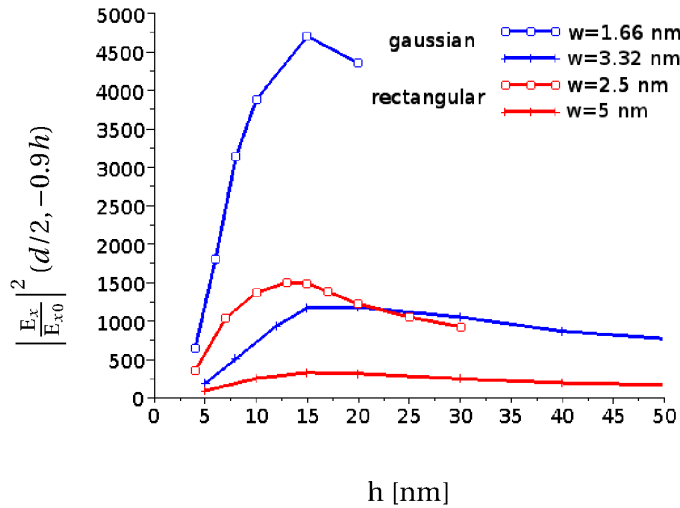
Figure 3.14: *Comparison of the enhancement of the intensity of the electric field at the first order cavity mode in function of the height h of the cavity between Gaussian groove grating of width w=1.66 nm (red squares) and w= 3.32 nm (red crosses) and rectangular groove ones of width w=2.5 nm (blue squares) and w=5 nm (blue crosses). The angle of incidence is θ_i=10°.*

There are clearly two behaviors for a groove whose width is fixed. When the height gets bigger, the enhancement of the intensity of the electric field increases until a critical point where it reaches its maximum and then decreases. On the one hand, if the height of the groove increases, the estimated wavevector of the guided wave in the cavity $\Lambda_0 \simeq \pi/2h$ decreases. The electrostatic behavior of the resonance is therefore weaker for the deep grooves and the EF of the intensity of the electric field is expected to decrease when the height increases. On the other hand, the analytical study of the resonance of the rectangular grooves showed that the quality factor of the resonance is proportional to the ratio h/w [18]. The energy is better confined in the deep grooves. The EF of the electric field is thus

expected to increase with the height. In the figure 3.14, the EF factor reaches a maximum and that seems to be due to a competition between the two opposite effects when the height increases:

- The EF of the intensity of the electric field decreases due to weaker electrostatic resonance.

- The EF of the intensity of the electric field increases due to a higher quality factor of the resonance proportional to h/w.

The first effect would be stronger at the highest energies whereas the second effect would be stronger at the lowest energies. This is a rough physical explanation and other parameters are expected to play a role, for instance the dispersion of the permittivity.

Lastly, we point out that the SERS EF expected for molecules that would migrate at the bottom of the grooves can be higher than 10^6. We see that the intrusion of very tiny grooves (w $\simeq$ 2 nm, h $\simeq$ 15 nm) on an otherwise flat metallic surface leads to a considerable change in the SERS effect at the surface in the visible spectral range. In the next section, we study the optical properties of nano-scale rough surfaces modeled as a grating of Gaussian grooves.

3.3 The Gaussian grooves grating as a model of nano-scale rough surfaces
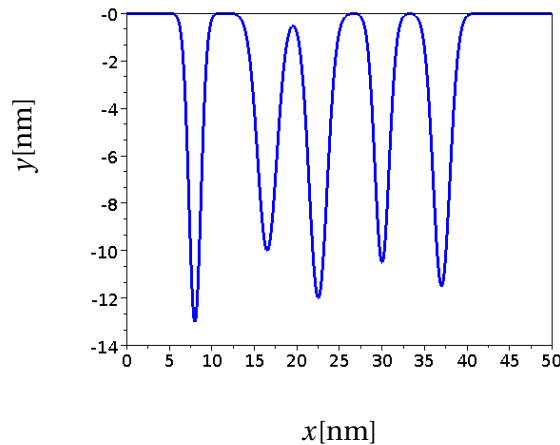
Figure 3.15: *Profile of the 5-Gaussian grooves grating of period d=50 nm.*

The coldly evaporated silver surfaces at low temperature are good SERS surfaces and they exhibit an Abnormal Optical Absorption as it was described in the subsection 1.1.2. We saw that Scanning Tunneling Microscopy measurements characterize the surface of cold films to be crevices of width less than 5 nm and separated by 5 to 15 nm. The height of the

groove, although greater than a few nanometers, is out of the reach of the experiments. In previous studies, our group modeled the surface of cold films as a grating of a tiny rectangular groove [18, 17]. In order to approach the surface in a more realistic way, we propose to model a crevice by a Gaussian groove and the surface of cold films by an ensemble of Gaussian grooves of different widths and heights separated by random lengths. The numerical simulations are compared to two experiments presented in the first chapter. The first experiment was performed by Hunderi *et al.* [35] and showed that silver surfaces have an important absorption around 2.5 eV (see figure 1.4). The second one was performed by Albano *et al.* [38] and proposed that the bottom of the crevices existing at the surface of coldly evaporated silver, excited by light, are the place of a huge electric field responsible for the SERS effect. A schematic of such surfaces was shown in figure 1.5.

A grating with several Gaussian grooves per period d=50 nm, whose profile is shown in figure 3.15, made of silver is chosen to model the rough surface. The widths of the grooves were chosen to be of a few nanometers and the heights around 10 nm. The characteristics of each groove are given in Table 3.2.

position	abscissa x [nm]	width w [nm]	height h [nm]
first groove	8	1.66	13
second groove	16.5	2.66	10
third groove	22.5	2.5	11
fourth groove	30	2	10.5
fifth groove	37	2.33	11.5

Table 3.2: *Characteristics of the 5 Gaussian grooves. The width is the full-width at half maximum.*

The specular reflectivity of the 5-Gaussian grooves gratings (blue line) is shown in figure 3.16. We can observe two dips, at 1.8 eV and the main one at 3 eV. This result agrees well with the observation of Hunderi *et al.* [35] (see figure 1.4) that the coldly evaporated rough silver surfaces have a strong absorption of the incoming light for a wide range of wavelengths around 2.5 eV. This absorption, called Abnormal Optical Absorption (AOA), is indeed unusual as the silver is a good reflector in the visible range. The reflectivity of a silver flat surface is given for comparison (red line) and confirms that in the absence of roughness the reflectivity is close to one. Fitting the exact position of the minimum of the reflectivity is possible by adjusting the height and the width of the grooves. However, the fit relies too much on the geometry of the groove to give a quantitative result to compare with the real surfaces.

Additionally, the electric field map is calculated and represented in figure 3.17 for the same incident wave illuminating the grating near the minimum in the specular reflectivity, at an energy E= 2.87 eV and angle $\theta_i = 0.1°$. We can see that all the grooves exhibit a strong electric field at their bottom, similar to the electric field distribution of the cavity mode of
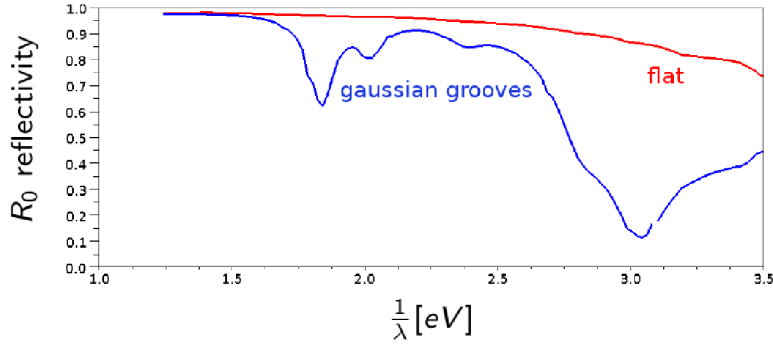
Figure 3.16: *Specular reflectivity for the silver grating represented in figure 3.15 for an incident angle θ_i=0.1°.*

the gratings with a single Gaussian groove per period. Albano's experiment pointed out that the bottom of the crevices existing at the surface of cold films as the active sites responsible for SERS [38] because the Raman scattering of the molecules is more enhanced if the molecules have migrated at the bottom of the crevices. This electric field repartition in the Gaussian grooves is consistent with Albano's experiment. The intensity of the electric field at the bottom of the groove is between 10^3 and $10^{3.5}$, the electromagnetic SERS enhancement factor at the bottom of the grooves is then of the order of magnitude of 10^6-10^7.
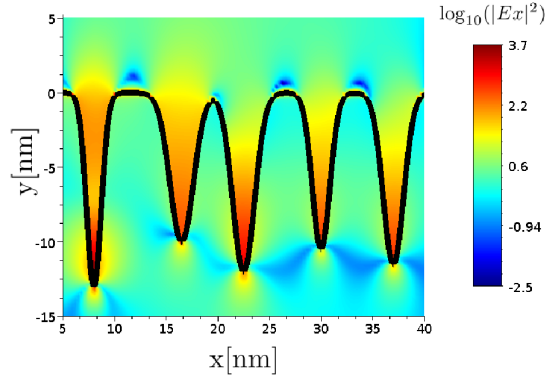
Figure 3.17: *Maps of the electric field E_x whose intensity is represented in a logarithmic color scale for a silver grating excited by an incident plane wave of energy E= 2.87 eV and angle $\theta_i = 0.1°$.*

Lastly, we comment on the geometry of the crevices. The geometry of the crevices determines the location of the active sites and is most probably closer to the Gaussian groove geometry, having a stranglehold at their bottom and not a square one. We saw that the stranglehold at the bottom of the Gaussian groove causes the electric field to be strongly confined at the bottom of the groove whereas it is confined at the opening of the groove for the rectangular groove. This observation advocates for the proposition of Albano that the

active sites responsible for SERS are located at the bottom of the crevices existing on the surfaces of cold films.

To sum up, the surface of cold films was modeled by a grating composed of five Gaussian grooves and the optical properties calculated by the numerical simulation and measured experimentally were compared. On one hand, the specular reflectivity showed a wide absorption in the visible spectral range similar to the AOA phenomena. On the other hand, the electric field maps showed a maximum of the intensity at the bottom of the grooves associated with a SERS enhancement factor of 10^6-10^7. The bottom of the Gaussian grooves at or near a plasmonic resonance can be active sites in agreement with Albano's experiment and his interpretation of the SERS phenomena. It therefore appears that the crevices at the surface of cold films may support cavity modes whose resonance in the visible spectral range would account for both the SERS effect and the AOA.

In order to go further in the study of the localization of the EM field on nano-scale rough surfaces, one may want to look for the dependence of the SERS EF or the reflectivity minimum on the grooves dimensions or on the grooves distribution, especially the mean length between the grooves. The modeling of the optical properties of a flat surface with Gaussian grooves could also be compared to the optical properties of self-affine surfaces in order to address the question of the modeling of the cold films. In the next paragraph, we comment on whether we have the ability to do this kind of simulations in a reasonable time and possibly on a laptop.

3.4 Discussion on the study of larger systems and Conclusion

As a conclusion, let us take a look at the number of unknowns needed to do the simulations presented in this chapter. We recall that the number of unknowns is the number of points discretizing the surface. We choose five representative systems, all gratings with one or several Gaussian grooves per period, in order to discuss the requirements of the simulations. For each system, we gather information on the grating: the period of the grating and the dimensions of the groove with the smallest ratio of width over height, and informations on the simulation: the highest enhancement factor of the electric field and the number of unknowns needed for the resolution in table 3.3. The number of unknowns in the table is the minimum of unknowns which is needed in order to have a convergence. However, in order to ensure that the convergence of the simulation is reached, the same simulation has to be done with a significantly larger number of unknowns.

One can observe with the three first gratings with a single Gaussian groove that the number of unknowns increases when the dimensions of the groove become smaller. For instance, the groove of width w=0.83 nm and height h=15 nm requires more unknowns than the groove of width w=1.66 nm and height h=15 nm. However, the increase is not linear as

system	period d [nm]	width/height w/h [nm]	EF of E_x	N
one Gaussian groove	30 nm	1.66/15 nm	70	500
one Gaussian groove	30 nm	1.66/30 nm	60	1500
one Gaussian groove	30 nm	0.83/15 nm	130	3000
5 Gaussian grooves	50 nm	1.66/13 nm	55	1000
5 Gaussian grooves	230 nm	1.66/13 nm	100	6000

Table 3.3: *Minimum number of unknowns N needed for the resolution of different systems. EF of*E_x*: maximum enhancement factor* $|E_x/E_x^i|$*. width/height: Smallest dimension of the width and height of the grooves.*

the width is divided by two but the number of points is multiplied by 6. We attribute the bigger required number of points to the bigger enhancement of the electric field.

We point out that the grating of 5 Gaussian grooves and of period d=230 nm, featured at the last line of table 3.3, required to be studied on a computer with more than 4 Go of memory space. We thank the IAPP for granting access to a computer server with 16 Go memory space which enabled to do so. Numerical simulations for gratings of period d=50 nm is therefore possible on a laptop but the numerical simulation of a grating of period d=230 nm is not. Furthermore, the resolution of a system with 6000 unknowns takes a very long time (several days for a spectrum). The extrapolation of the number of unknowns for the gratings with 5 Gaussian grooves predicts at least 30 000 unknowns for a grating with a period d=1 μm. This number may even increase if one wants to study grooves with a smaller width or a bigger height. The thorough study of nano-scale surfaces is thus only possible if the number of unknowns is reduced and the overall performances of the method are improved.

In this chapter, we studied the EM resonances of gratings with a Gaussian groove of height of one or several tens of nanometers in the visible spectral range, by analogy with the rectangular groove grating. We saw that the Gaussian groove gratings support cavity mode resonances in the electrostatic regime similarly to the rectangular groove. At the resonance, the EM field is confined in the Gaussian groove as a standing SPP wave. The excitation of such plasmonic resonances on a grating with 5 Gaussian grooves is responsible for a spectrally wide absorption of the exciting incident plane wave such as the AOA observed for cold films as well as an enhancement of the electric field localized at the bottom of the grooves which may give rise to a SERS enhancement factor of the order of magnitude of 10^7. Continuing the study of surfaces of length greater than 1 μm, and with a more complex shape, would be desirable. The actual performances of the SIE method requires, however, too many unknowns. The simulations are therefore out of reach of a laptop's capacity and even impossible for most of computer servers. Furthermore, the time of the simulations would be unreasonable. That is why this thesis was focused on improving the performances of the SIE. The wavelets were chosen to achieve this task. The next chapters introduce the theory of wavelets and synthesize our work on the application of the wavelets to the SIE method.

Chapter 4

The wavelets theory

4.1 Introduction

The method of resolution of the surface integral equations, which we presented in the previous chapter, consists mainly in solving a linear set of equations for the values of the magnetic field and its derivative at N equally spaced points of the metallic grating over a period. If one wants to study a phenomenon over a surface of a few microns but having a roughness whose size may be of the order of magnitude of the nanometer, this number of unknowns N may be then of several ten thousands. In the process, the matrix of $4N^2$ terms has to be stored and the system has to be solved, for each wavelength. Even with the help of a supercomputer, the limits are promptly reached. Moreover, the matrix is dense and the number of operations needed for the resolution is proportional to N^3.
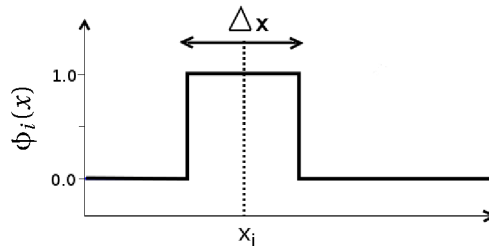
Figure 4.1: *Sketch of the rectangle function.*

In order to obtain the linear set of equations, the integrals were approximated as a sum of rectangles centered at the points x_i of the discretization of the surface. The area of each rectangle was then approximated by the multiplication of the discretization step Δx by the value of the integrated function at the point x_i. This method can also be viewed as expanding the integrated function on a specific basis whose basis functions are the rectangle function ϕ_i centered at the points x_i and of width equal to the discretization step Δx as sketched in figure 4.1. The basis functions are shifted of a length equal to this discretization

step Δx in relation to one another. The localized phenomena are well described by this method since the basis functions are defined on different intervals $[x_i - \Delta x, x_i + \Delta x]$ of the surface i.e. the basis functions differs from one another by their localization in space.

The expansion of the integrated function could be done on another basis: the plane waves basis, by using the Fourier transform. The basis functions do not differ from one another by their localization in space anymore but rather by their dilatation or compression in relation to one another as sketched in figure 4.2.
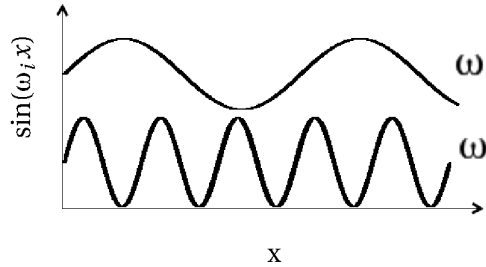
Figure 4.2: *Sketch of the plane wave basis function.*

An abrupt change of the integrated function in the real space is like a pseudo-discontinuity in the Fourier space. The Gibbs phenomenon appears in the function approximated as a Fourier series: around the sharp variation, oscillations appear in the approximated solution (see section 4.2.4). Localized phenomena are therefore approximated in a plane wave basis with difficulty. Inversely, a component of the integrated function whose length of modulation is of the order of magnitude of the period may be described by a sum of a few plane waves requiring thus only a few basis functions.

There exists on nano-scale rough surfaces, a priori, a mix of the two types of phenomena: on one hand the phenomena rather de-localized over the whole surface and, on the other hand, highly localized resonances at specific spots of the surface. In order to efficiently describe these phenomena, the integrated function has to be expanded, idealistically, on a basis capable of describing the phenomena at both huge and small scales. That is precisely the quality of the wavelet basis. That is why we consider the wavelets to solve our electromagnetic problem more efficiently.

Historically, the wavelet theory is quite recent (20-30 years) and is still under development. Their application in physics is not widespread. To our knowledge, for instance, this work is the first to use wavelets applied to a plasmonic problem. This first chapter thus introduces the principles of the wavelet theory by giving a general picture and focusing on the most important points. The application of the wavelet theory to the resolution of the surface integral equations is only given in the next chapter.

As Daubechies stated in [130] *"The wavelet transform is a tool that cuts data or function or operators into different frequency components, and then studies each component with a*

resolution matched to its scale". This mathematical tool has a wide range of applications that goes from signal processing to quantum physics. Its name comes from the French word *ondelette* which means small wave. Requirements upon it will differ hence all the techniques associated with a certain type of wavelets are often very specific to one wavelet family and an application field. I refer to the books of Chui [131] and Pan [132] for the application of wavelets to the fields of signal processing and electromagnetism respectively. The book by Mallat [133] was also really helpful. A very nice introduction to wavelets in scientific computing may be found in [134].

The common ground for all the wavelets is to build basis functions by the dilatation and the translation of a unique mother wavelet function. In a wavelet decomposition, the smooth and the sharp parts of a function are divided in different wavelet subspaces. The smooth part is described first and the little details are added step by step which makes the decomposition very efficient. Among others, as I already stated above, contrary to Fourier transforms, it can describe accurately rectangle functions. How could the wavelets be useful to our problem? In general, at the surface of a metal the magnetic field is simply reflected and its description is not particularly difficult. At a hot spot, however, the resonant magnetic field may have sharp variations and its derivative may become very large. The wavelets, and their ability to describe separately different levels of detail, seem thus appropriate to describe the magnetic field and its derivative on a rough surface.

The wavelets are a very wide subject and only a few families of wavelets will be considered within the scope of this thesis. A general and incomplete classification of the wavelets may be found in the appendix C.1.1. The investigation was limited to compactly supported wavelets, because they can be periodized, within the Multiresolution Approximation (MRA), also called Multi-Resolution Analysis. The MRA, theorized by Mallat [133], has been developed simultaneously with compactly supported orthogonal wavelets and scaling functions by Daubechies and others [135]. Together, they lead to efficient algorithms hence they are suited to numerical implementation. In order to understand the principles of the decomposition of a function on a basis of wavelets, wavelets and scaling functions will be described throughout this chapter.

4.2 Why decomposing on a wavelet basis?

4.2.1 Approximation of a square integrable function

All the functions we are dealing with are square integrable functions $f \in L^2(\mathbb{R})$. The scalar product of two functions f and g is

$$\langle f | g \rangle = \int_{-\infty}^{+\infty} f(x) g(x) dx \quad .$$

If the functions f and g are periodic of period T the scalar product is

$$\langle f | g \rangle = \frac{1}{T} \int_0^T f(x) g(x) dx \quad .$$

Any square integrable function $f \in L^2(\mathbb{R})$ may be approximated i.e. projected on a subspace V $\subset L^2(\mathbb{R})$. We will define P_V the projector on V and $f_V \in V$ the projection of the function f ($f_V = P_V f$). V is a vector space generated by an orthonormal basis $\{\phi^k\}_{k \in \mathbb{Z}}$. In an orthonormal basis, the basis functions ϕ^k are normalized

$$< \phi^k | \phi^k > = \int_{-\infty}^{+\infty} \left| \phi^k(x) \right|^2 dx = 1 \quad ,$$

and two basis functions ϕ^n and ϕ^k are orthogonal

$$< \phi^n | \phi^k > = \delta_{n,k} \quad . \tag{4.1}$$

Eventually, the projection f_V is thus written as

$$f_V(x) = \sum_{k=-\infty}^{+\infty} < f | \phi^k > \phi^k(x) \quad .$$

Additionally, we give the definition of the support of any function f. The support of f, Supp(f), is the closure of the set of all the points of $\mathbb{R}$ where f is not null. In other words, it is the smallest closed set such that

$$x \notin \text{Supp}(f) \quad \backslash \quad f(x) = 0 \quad .$$

For instance, if f is not null only on a closed interval [a,b] then the support of f is [a,b]. If f is not null only on the interval [a,b[then the support of f is [a,b].

4.2.2 Approximation of a square integrable function with the Haar scaling function

We begin with the simple example of the Haar wavelet. As a lot of wavelets, the Haar wavelets are functions built from a unique *mother scaling function* ϕ represented in figure 4.3. As we will see later, the mother scalling function (and also the mother wavelet) has no analytical expression (within the framework of the MRA). Exceptionally, the Haar's mother scaling function may be expressed analytically, it is:

$$\phi_0^0 : x \rightarrow \left\{ \begin{array}{ll} x \in [0, 1[& \phi_0^0(x) = 1 \\ x \in]-\infty, 0[\cup [1, +\infty[& \phi_0^0(x) = 0 \end{array} \right. \quad .$$

The support of the mother scaling function ϕ is [0,1], by definition, we will say that ϕ is *compactly supported* (a closed and bounded set of $\mathbb{R}$ is compact) .
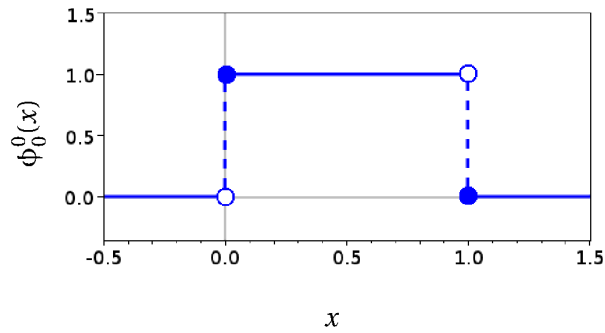
Figure 4.3: *The Haar mother scalling function* ϕ_0^0.

The translation of the mother scaling function ϕ defines an infinity of functions

$$\phi_0^k : x \rightarrow \phi(x - k)$$

with k an integer called the *shift parameter*.

A basis $\{\phi_0^k\}_{k \in \mathbb{Z}}$ can be built from these functions which generates a subspace V_0 included in $L^2(\mathbb{R})$. As the functions ϕ^k are non null only on the interval $[k, k+1]$, they form an orthogonal basis

$$\langle \phi_0^k | \phi_0^{k+1} \rangle = \delta_{k,k+1}$$

In order to give an example of the decomposition on the Haar basis, let us consider the function f

$$f : 0 < x < 4 \rightarrow \sin\left(\frac{\pi}{8}x\right) \tag{4.2}$$
$$\text{else } 0 \quad .$$

The function f_{V_0} is the approximation of f in the space V_0, we write

$$f_{V_0}(x) = \sum_{k=-\infty}^{+\infty} C_0^k(f)\phi_0^k$$

with $C_0^k(f) = \langle f | \phi_0^k \rangle$. This notation will be used later in the general case. The function f and its approximation f_{V_0}, are plotted in figure 4.4. The function f is badly approximated as f_{V_0} by steps of width equal to one.

In order to improve the approximation, we want to have successive bases which will approach $L^2(\mathbb{R})$ in a better way each time. The new basis, built again from the mother scaling function, has to generate a subspace which is a better approximation of $L^2(\mathbb{R})$. To do so we rescale the function ϕ so that the steps will have a width divided by two. The basis will then be $\{\phi_1^k\}_{k \in \mathbb{Z}}$ with

$$\phi_1^k : x \rightarrow \sqrt{2}\phi(2x - k) \quad .$$

129
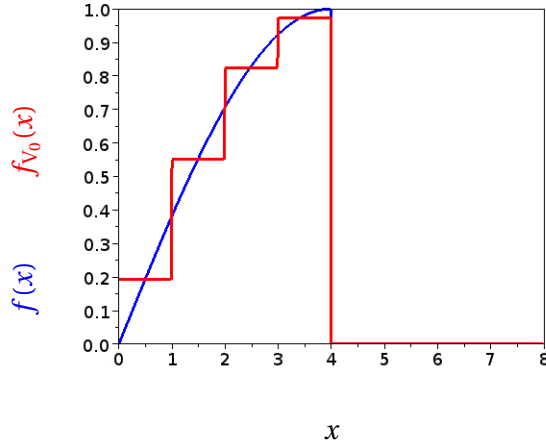
Figure 4.4: *Representation of the function f from equation 4.2 (blue solid line) and its decomposition on the Haar basis (red solid line).*

Continuing to do so, the basis rescaled j$^{\text{th}}$ times will then be $\{\phi_j^k\}_{k \in \mathbb{Z}}$ (generating the subspace V_j) with

$$\phi_j^k : x \to \sqrt{2^j}\phi\left(2^j x - k\right) \quad .$$

2^j is the *scale*, j the *scale parameter* and ϕ_j^k the *scaling function* or *scalet* at a scale 2^j and of shift parameter k. The rescaled basis functions of scale 2^j, for j=0 to j=3, and shift parameter $k = 0$ are shown in figure 4.5(a). The scaling function ϕ_j^k is shifted of $k/2^j$ and in the case of the Haar wavelet, the shift is therefore equal to a multiple of the length of the step. In V_0, V_1, V_2 and V_3, the shift is an integer number (equal to k) of times one, a half, a quarter and an eighth respectively as are the length of the step represented in figure 4.5(a). The higher the scale is, the better the approximation of the function f in the subspaces V_j is, as it is shown in figure 4.5(b). The resolution in the description of the function f at a scale 2^j is 2^{-j}.

In the case of the Haar wavelet, it is easy to demonstrate that a rectangle function of scale 2^j is equivalent to two neighbor rectangle functions of scale 2^{j+1} ie

$$\forall j \in \mathbb{N} \qquad \phi_j^k = \frac{1}{\sqrt{2}}\left(\phi_{j+1}^k + \phi_{j+1}^{k+1}\right) \tag{4.3}$$

This relation is called the *dilatation relation*. It contains all the informations necessary to rescale the mother scaling function into the scaling functions. As we will see later, each family of wavelet has a specific dilatation relation whose coefficients vary with the family. This relation is central in the use of wavelets, especially as the mother functions are generally not known analytically.

A direct consequence is that the generated subspace V_j is included in the next one V_{j+1}. It is a general property of scalets and they are chosen so that V_j tends to $L^2(\mathbb{R})$ as j tends to infinity.
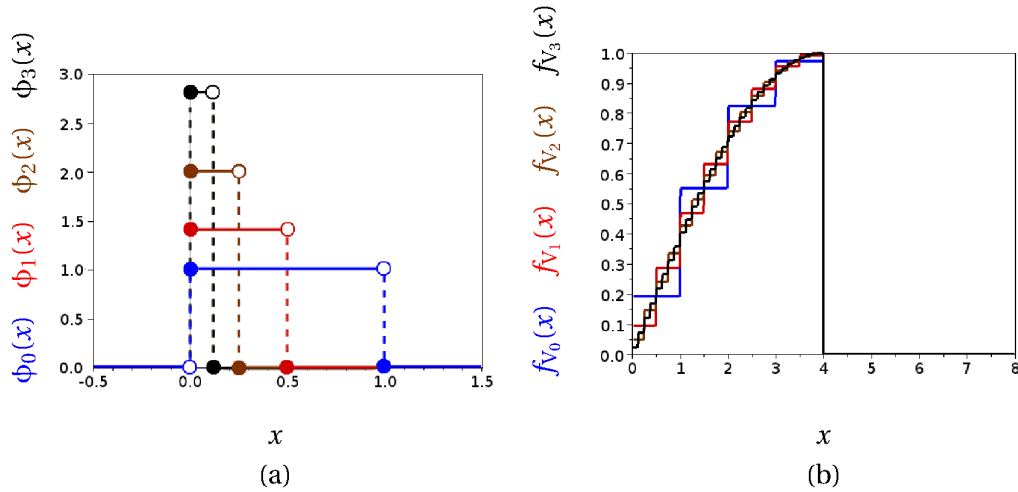
Figure 4.5: *(a) The basis function of V_0, V_1, V_2 and V_3 at k=0 in respectively blue, red, brown, black. (b) The corresponding approximation of f in the respective subspaces.*

The reader would have recognized that the discretization method described in the chapter 2 of the integrals as a sum of rectangles with a number of points $N=2^J$ is just the decomposition of the solution on the Haar scalet basis $\{\phi_J^k\}_{k\in\mathbb{Z}}$ in the subspace V_J.

4.2.3 Approximation of a square integrable function with the Haar wavelet
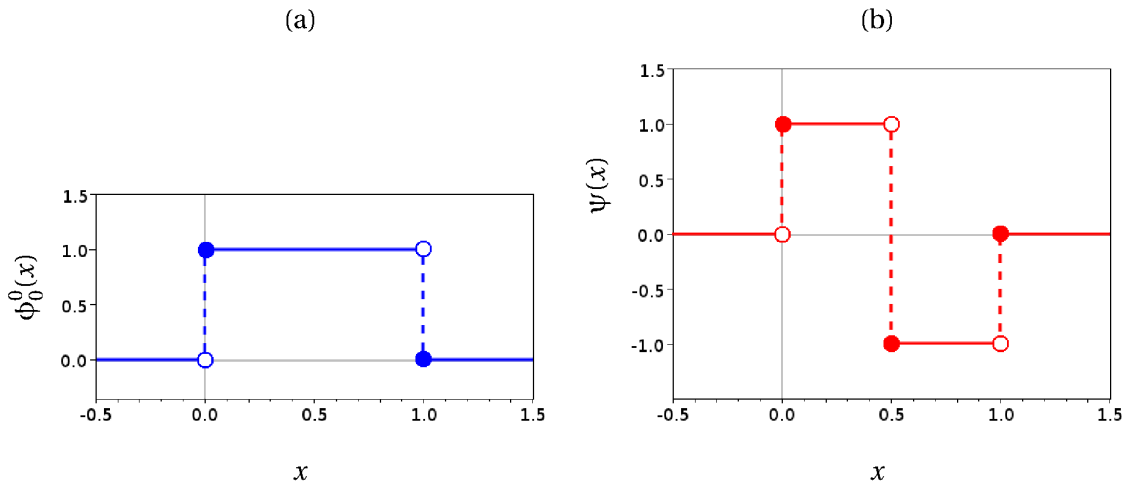
Figure 4.6: *(a) The Haar wavelet ψ_0^0. (b) The Haar mother scalling function ϕ_0^0.*

Apart from building the entire basis from a unique mother function, scaling functions are not a revolutionary basis. Indeed, there is a redundancy in the information given at two successive scales in the subspaces V_j and V_{j+1} since the first one is included in the second

131

one. To avoid this redundancy, the complementary space to V_j necessary to build V_{j+1} is defined as W_j

$$V_{j+1} = V_j \oplus W_j$$

By definition, the basis function ψ_j^k which generates the subspace $W_j = \{\psi_j^k\}_{k\in\mathbb{Z}}$ is called *wavelets* of scale 2^j and shift parameter k. The projector P_{W_j} on the space W_j is also defined as

$$\forall j \in \mathbb{N} \qquad P_{W_j} f = P_{V_{j+1}} f - P_{V_j} f$$

To generate the initial wavelets space W_0, one introduces the *mother wavelet* ψ_0^0. The way it is built will be explained later. In our example of the Haar family, ψ_0^0 is represented in figure 4.6(b), together with the mother scaling function ϕ_0^0 in figure 4.6(a). The knowledge of the two functions ϕ_0^0 and ψ_0^0 allows to produce a multi-resolution analysis of any function as follows.

Contrary to the scaling function at the scale 2^j, which approximates the function with a space resolution of 2^{-j}, the wavelet enables to represent the difference between the function approximated at a scale 2^j and the function approximated at a scale 2^{j+1}. As a consequence, the function must first be decomposed on a subspace of scaling function V_{J_0} with a resolution of 2^{-J_0}. J_0 is chosen arbitrarily (for example $J_0 = 0$). The precision may then be increased by decomposing the function on additional subspaces of wavelets W_{J_0} to W_J. The new direct sum $V_{J_0} \oplus_{j=J_0}^{J-1} W_j$ is equivalent to the subspace V_J. Indeed, by using $V_{j+1} = V_j \oplus W_j$ we find

$$V_{J_0} \bigoplus_{j=J_0}^{J-1} W_j = V_{J_0} \oplus W_{J_0} \bigoplus_{j=J_0+1}^{J-1} W_j = V_{J_0+1} \bigoplus_{j=J_0+1}^{J-1} W_j = ... = V_{J-1} \oplus W_{J-1} = V_J \quad .$$

The function f may then be approximated in $V_{J_0} \oplus_{j=J_0}^{J-1} W_j$. First the decomposition in the subspace V_{J_0} is

$$P_{V_{J_0}} f(x) = f_{V_{J_0}}(x) = \sum_{k=-\infty}^{+\infty} C_{J_0}^k(f) \phi_{J_0}^k(x)$$

with $C_j^k(f) = \langle f | \phi_j^k \rangle$. The C_j coefficients are the coefficients in the subspace V_j. In a similar way, the decomposition in the subspace W_j whose coefficients are called D_j is

$$P_{W_j} f(x) = f_{W_j}(x) = \sum_{k=-\infty}^{+\infty} D_j^k(f) \psi_j^k(x) \tag{4.4}$$

with $D_j^k(f) = \langle f | \psi_j^k \rangle$. Finally the decomposition of f in $V_{J_0} \oplus_{j=J_0}^{J-1} W_j$ is

$$P_{V_j} f = P_{V_{J_0}} f + \sum_{j=J_0}^{J-1} P_{W_j} f \tag{4.5}$$

132
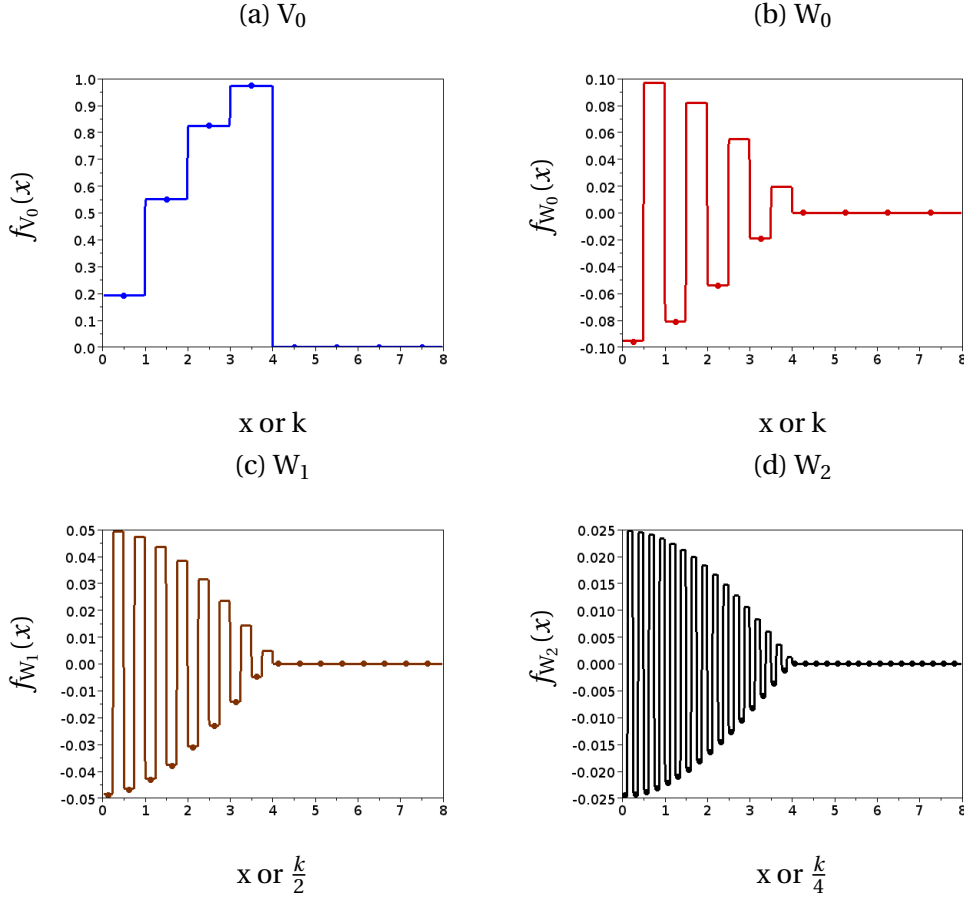
Figure 4.7: *The projection of f in the respective subspaces* V_0 *(a),* W_0 *(b),* W_1 *(c) and* W_2 *(d) is represented by solid lines. The coefficients* $\sqrt{2^j}D_j^k(f)$ *(resp.* $C_0^k(f)$*) are represented by dots in the middle of the interval* $[k/2^j, (k+1)/2^j]$ *where* $k/2^j$ *is the shift of* ψ_j^k *(resp.* ϕ_0^k*) from* ψ_j^0*. The function* f_{V_3}*, as represented in figure 4.5 is the sum of the four functions represented in (a), (b), (c) and (d).*

and f_{V_J} becomes

$$f_{V_J}(x) = \sum_{k=-\infty}^{+\infty} C_{J_0}^k(f)\phi_{J_0}^k(x) + \sum_{j=J_0}^{J-1}\sum_{k=-\infty}^{+\infty} D_j^k(f)\psi_j^k(x) \quad . \tag{4.6}$$

The number of subspaces W_j that are used is called the *depth*. In this example the depth is $J - J_0$.

Starting again with our previous example, we have a first decomposition of the function f in a scaling function subspace of scale parameter $J_0 = 0$, f_{V_0}. The projection of the function f in the subspace V_3, f_{V_3} as represented in figure 4.5, is obtained by adding the projection of f in the wavelet subspaces W_0, W_1 and W_2 to f_{V_0}. The projection $P_{W_j}f = f_{W_j}$ of f on the subspace W_j (or V_{J_0}) are represented by solid lines in figure 4.7. Hence, f_{V_3} is decomposed on scalet and wavelet bases, following the equation 4.6, with a depth of three. The

coefficients $\sqrt{2^j}\mathrm{D}_j^k(f)$ $\left(\mathrm{or}\mathrm{C}_{\mathrm{J}_0}^k(f)\right)$ are represented by dots at $k/2^j$ where $k/2^j$ is the shift of the basis function ψ_j^k from ψ_0^0. The exact correspondence between the coefficients and the ordinate of the steps is only due to the particular form of the Haar wavelet. In general, the coefficient may not be equal to the value of the projection of the function f at the point $k/2^j$. Similarly, the approximation f_{V_1} (resp. f_{V_2}), represented in figure 4.5, is obtained by adding the projection on the subspace W_0 (resp. W_0 and W_1) to the initial approximation on V_0.

4.2.4   Comparison of the wavelet transform with the Fourier transform

In this section, we show the utility of the wavelets to describe functions which have sharp variations. The same step-like function, equation 4.2, is chosen. For convenience with both the Fourier transform and the wavelets, the function is periodized of period d= 8. The Fourier transform is

$$\hat{f}(k) = \frac{1}{d}\int_0^d f(x)e^{-2i\pi kx}dx \quad .$$

(4.7)

The Fourier components are calculated by approximating the integral over the surface as a sum of rectangles. We apply the quadrature of the rectangles, equation 2.61, to the equation 4.7. The number of terms used for the quadrature is increased until the result converges and the absolute error on the Fourier coefficients is less than 10^{-10}. The approximated function is then

$$f_N^{\mathrm{F}}(x) = \sum_{k=-\frac{N}{2}}^{\frac{N}{2}} \hat{f}(k)e^{2i\pi kx} \quad .$$

The function recomposed from the Fourier space f_N^{F} is compared to a function f_N^{W} recomposed from a periodized wavelet space $V_{\mathrm{J}_0}\bigoplus_{j=\mathrm{J}_0}^{\mathrm{J}-1} W_j$ with a total of N= 2^{J} terms. To do so, we use a wavelet called Daubechies of order 8 described in section 4.3.4 and a decomposition called discrete wavelet transform, DWT, described in section 4.5.2. The decomposition, equation 4.6, was done on a scaling function subspace of scale parameter $\mathrm{J}_0 = 3$ and wavelet subspaces of scale parameter from $\mathrm{J}_0 = 3$ to $\mathrm{J}-1=5$. Both functions f_N^{F} and f_N^{W} with N=2^6=64 are represented respectively by blue dots in figure 4.8(a) and a black solid line in figure 4.8(c) as well as the absolute error $f - f_N$ with the same representation in figure 4.8(b) and (d). The Gibbs phenomenon, the presence of oscillations due to a step, is clearly visible for the Fourier series f_N^{F}.

To expand efficiently a function, the quick convergence of the coefficients is crucial. The Fourier coefficients of a rectangle function behave as $\hat{f}(k) \simeq \mathrm{sinc}(k)$ and converge slowly. On the contrary, the wavelet coefficients C_3^k and D_j^k from the scale parameter 3 to 5, shown in figure 4.9, converge much faster in the sense that there is fewer non-null terms at each scale 2^j when increasing j. The D_j^k (and C_3^k too) are the coefficients of the basis functions ψ_j^k which are shifted of $k2^{-j}$ from the mother basis function ψ_0^0. For sake of clarity, the
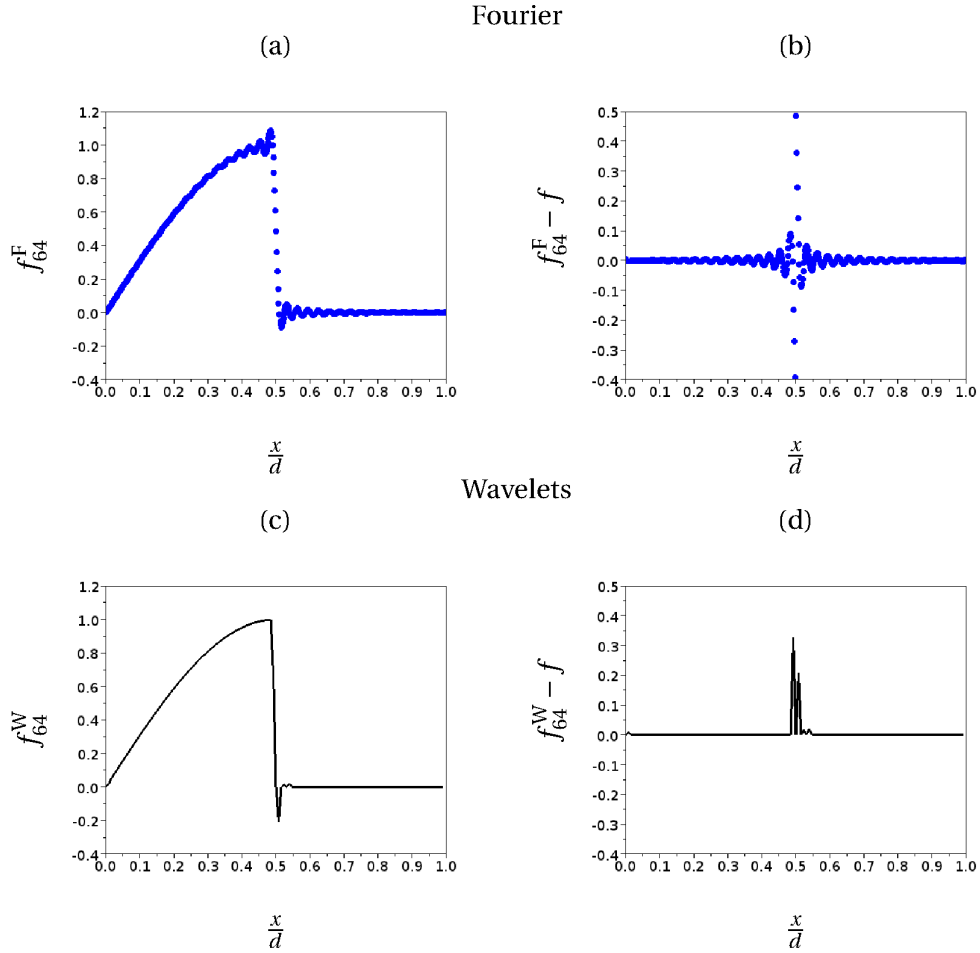
Figure 4.8: f_{64}^{F} and $f_{64}^{\mathrm{F}} - f$ are represented by blue dots in (a) and (b) respectively. f_{64}^{W} and $f_{64}^{\mathrm{W}} - f$ are represented by a black solid line in (c) and (d) respectively.

coefficients C_3^k and D_j^k are plotted at $k2^{-j}2^6$ in order to align in the figure the coefficients whose basis functions have the same shift compared with the mother scalet. The origin of the wavelet coefficients was also translated in the y-direction for better visibility. At the scale $2^{j=5}$ (brown line), the coefficients are almost all zero except one bump which corresponds to the jump. Setting the coefficients whose modulus is under 10^{-4} to zero, there are only 6 non-zero coefficients at the scale $2^{j=4}$ over a total of 16 coefficients and at the scale $2^{j=5}$, only 4 over a total of 32. The coefficients of the wavelet basis are not centered because of the high asymmetry of the Daubechies 18 wavelet. Of the 64 initial coefficients, only 42 wavelet coefficients are required to describe the approximated function. The function f projected in the wavelet space is efficiently recomposed by modifying the function only where the resolution has to be increased (the jump at x=0.5 d) whereas adding a Fourier coefficients affects the function over the whole profile to achieve the same goal.

The wavelet bases which represent only the changes of a function between two scales

135
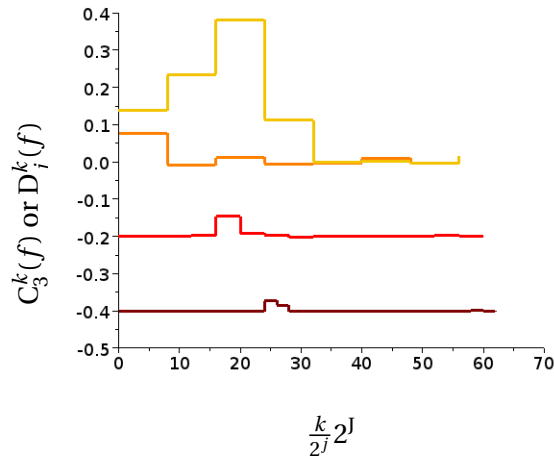
Figure 4.9: *The scalet coefficient $C_3^k(f)$ are represented as a function of $k2^{J-j}$ (J=6) by a yellow solid line and the wavelet coefficients $D_j^k(f)$ from j=3 to 5 by solid lines from orange to brown; The origin of the y-axis is arbitrarily translated for sake of clarity. The function f follows the equation 4.2.*

of resolution 2^{-j} and 2^{-j-1}, have shown in this example their efficiency to represent step-functions or abrupt variations contrary to the Fourier transform.

4.3   The basics of wavelets

We have introduced the principles of wavelets in the first section through the example of the Haar wavelet. We saw that the first goal of the wavelets is to describe functions by sorting the details as a function of their size. To do so, the space of integrable functions $L^2(\mathbb{R})$ may be split into wavelet subspaces which each contains functions with a different level of details. We briefly extend here the construction of the wavelets subspaces, seen in the previous section for the Haar wavelet, to the general case. The mathematical frame to this construction is given in the form of the Multi Resolution Analysis (MRA) by Mallat [133]. The exact formulation may be found in the appendix C.1.2, we present here the main relations necessary for the understanding. Some wavelets which fulfill the requirements of the MRA are also presented in the end of the section.

4.3.1   The scalet and wavelet bases

We introduce the single mother scaling function, or scalet, ϕ. This function is compactly supported. Two discrete transformations are applied to the mother scalet ϕ to obtain the scaling function children ϕ_j^k where j and k are integers.

136

The first one is a dilatation ruled by an integer power of two 2^j: the support of the function is divided by 2^j and the amplitude is multiplied by the square of 2^j:

$$\forall j \in \mathbb{Z} \qquad \phi_j : x \rightarrow \sqrt{2^j}\phi(2^j x)$$

and j is called the scale parameter. 2^j is the corresponding scale.

The second one is a translation of the mother scalet of $k/2^j$:

$$\forall j \in \mathbb{Z} \qquad \forall k \in \mathbb{Z} \qquad \phi_j^k : x \rightarrow \sqrt{2^j}\phi(2^j x - k) \tag{4.8}$$

and k is the shift parameter. At a fixed scale 2^j, all the scaling function children ϕ_j^k are therefore identical as they are the translation of the scaling function child ϕ_j^0.

As an example, the Daubechies 6 mother scalet $\phi_0^0(x)$ and its child $\phi_2^5(x)$ are represented by a blue and a red line respectively in figure 4.10. The dilatation and translation necessary to build ϕ_2^5 from ϕ_0^0 are represented by red and black arrows respectively.
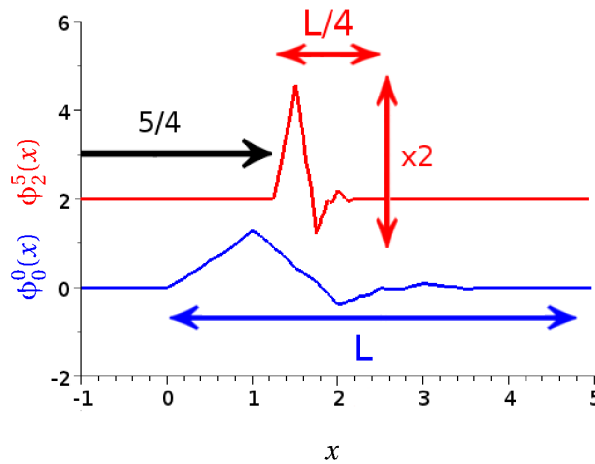
Figure 4.10: *The Daubechies 6 mother scalet $\phi_0^0(x)$ (blue line) and its child $\phi_2^5(x)$ (red line shifted of 2 in the y axis). The dilatation (resp. translation) are represented by red (resp. black) arrows. $L = Supp(\phi_0^0(x))$.*

At a fixed scale 2^j, all the scaling function children ϕ_j^k are an *orthonormal basis* of the subspace V_j which they generate :

$$\forall j \in \mathbb{Z} \qquad V_j : \left\{ \phi_j^k : x \rightarrow \sqrt{2^j}\phi(2^j x - k) \right\}_{k \in \mathbb{Z}} \quad .$$

Two points are important to notice about all the basis functions of V_j. First, the common size of the support of the basis functions ϕ_j^k is the one of ϕ divided by 2^j. The second is that, the translation step $1/2^j$ varies with the scale and matches the scale of the support $Supp(\phi_j^k) = Supp(\phi_0^0)/2^j$. In that way the basis functions can react locally to changes of the

137

function of the order of magnitude 2^{-j}. The resolution of the subspace V_j is 2^{-j} as it is the length between two successive basis functions.

In the subspace V_j, scalet children bases may approximate functions with details down to the resolution 2^{-j}. By choosing the scale parameter j, one may control the accuracy of the approximation of a function f belonging to $L^2(\mathbb{R})$. The subspaces V_j are nested subspaces such that

$$V_{j-1} \subset V_j \quad .$$

This property can be understood as follow: functions accurately approximated at a scale parameter j-1 will also be accurately approximated at a scale parameter j corresponding to a better resolution 2^{-j} compared with $2^{-(j-1)}$.

By definition, *The infinite sequence of nested subspaces* $\{V_j\}_{j \in \mathbb{Z}}$ *that are closer to* $L^2(\mathbb{R})$ *as j increases, are a Multi-Resolution Approximation of* $L^2(\mathbb{R})$. By increasing the scale parameter j, one may tend to an accurate description of the desired function f. If P_j is the projector on the subspace V_j then

$$\forall f \in L^2(\mathbb{R}) \quad j \to \infty \quad P_j f \to f$$

is an essential property of the scalet subspaces.

Now that we have seen how the functions f of $L^2(\mathbb{R})$ can be approximated with any desired accuracy in the scalet subspaces, the main goal is to sort out the functions f as a function of the size of their details along the x-axis. A function may be divided in components of different lengths L over which the function vary uniformly or equivalently the function may be divided in different levels of details of size L. The length L is small where the function changes abruptly and is long where the variation is smooth. We want to single out the functions with the same level of details. We consider all the functions with details down to the size of $2^{-(j+1)}$ (V_{j+1}) i.e. functions which are a sum of components which vary uniformly over different lengths all greater than $2^{-(j+1)}$. In this group of functions, we isolate the functions with details down to the size of 2^{-j} (V_j) from the functions with details of size included between 2^{-j} and $2^{-(j+1)}$ (W_j). We are interested in the last group, W_j. In that group, the functions have components which vary uniformly over lengths of controlled size included between 2^{-j} and $2^{-(j+1)}$. It corresponds to say that the subspace W_j is the *complementary* of the subspace V_j in the subspace V_{j+1}

$$V_{j+1} = V_j \oplus W_j \quad . \tag{4.9}$$

The projection of a function f of $L^2(\mathbb{R})$ in the subspace W_j is the difference between the approximations at two resolution $2^{-(j+1)}$ and 2^{-j}.

The subspace V_{J+1} may therefore be split into wavelet subspaces W_j ($j < J+1$) in order to single out the components with different resolutions. Repeating the step of the equation

4.9 N times starting from V_{J+1}, yields

$$V_{J+1} = V_J \oplus W_J = V_{J-1} \oplus W_{J-1} \oplus W_J = ... = V_{J-N} \bigoplus_{j=J-N}^{J} W_j \quad .$$

N+1 is called the depth of the decomposition into the wavelet subspaces. All the functions with a resolution of $2^{-(J+1)}$ are described in the subspace $V_{J-N} \oplus_{j=J-N}^{J} W_j$ because it is equivalent to V_{J+1}. The decomposition of the functions however distinguishes the components corresponding to the scales 2^{J-N} to 2^{J+1} from the rest.

If N tends to infinity and then J tends to infinity too, we have

$$\bigoplus_{j=-\infty}^{+\infty} W_j = L^2(\mathbb{R}) \quad .$$

The space of square integrable functions $L^2(\mathbb{R})$ may then be decomposed in an infinite sum of subspaces W_j, sorting out the functions in an infinity of detail ranges.
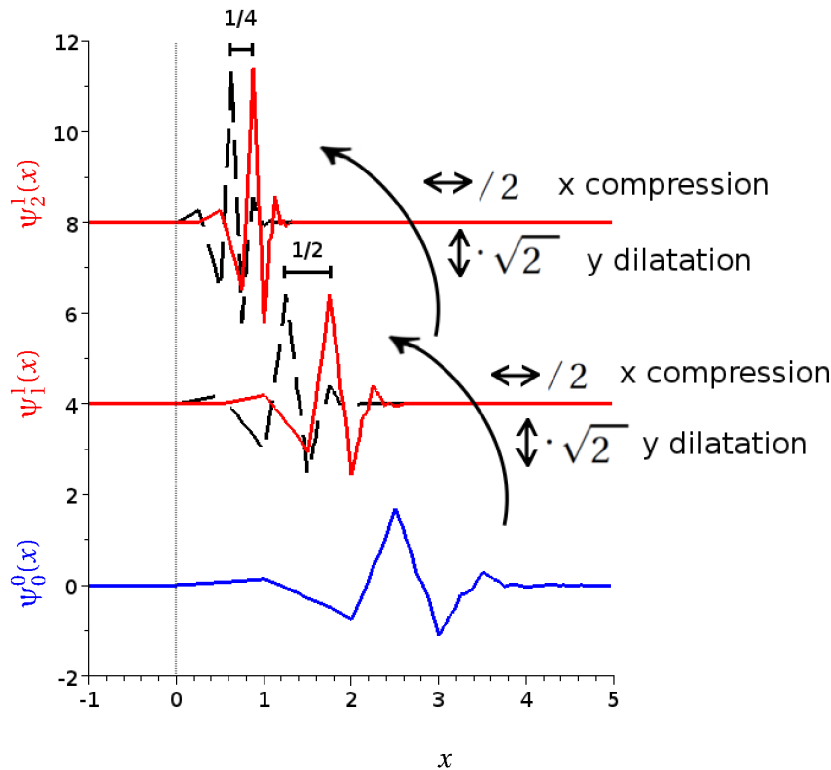
Figure 4.11: *The Daubechies 6 mother wavelet $\psi_0^0(x)$ is represented by a blue line as well as its children $\psi_1^0(x)$ by a black dashed line and $\psi_1^1(x)$ by a red line (resp. $\psi_2^0(x)$ and $\phi_2^1(x)$). They are shifted of 4 (resp. 8) along the y axis for sake of clarity.*

In the exact same way as for the scalet subspaces, the wavelet subspaces W_j are generated by basis functions issuing from a single function, *the mother wavelet ψ*. The wavelet

139

children ψ_j^k are an *orthonormal basis* of the subspace W_j such as

$$\forall j \in \mathbb{Z} \qquad W_j : \left\{ \psi_j^k : x \to \frac{1}{\sqrt{2^j}} \psi(2^j x - k) \right\}_{k \in \mathbb{Z}} \qquad .$$

The basis function ψ_j^0, the one of the wavelet subspace W_j which is not translated, is obtained from ψ_{j-1}^0, the one of the previous wavelet subspace W_{j-1}, by a dilatation of $1/2$ in the x direction and multiplied by $\sqrt{2}$ in the y direction. Equivalently it is obtained from the mother wavelet by a dilatation of $1/2^j$ in the x direction and of $\sqrt{2^j}$ in the y direction. The entire set of basis functions of a subspace W_j are then obtained by translating the initial dilated function ψ_j^0 by steps of $1/2^j$. Two successive basis functions of the wavelet subspace W_1 and W_2 are represented in figure 4.11. ψ_j^0 is represented by a black dashed line whereas the next basis function ψ_j^1 translated of $1/2^j$ is represented by a red line for j equal to 1 and 2.

The property of the wavelets that is to generate subspaces of functions with a predetermined range of details from a single function ψ, is unique and not given to any function. In order to be a wavelet, a function must be refinable i.e. by definition, to follow a dilatation relation which is the subject of the next paragraph.

4.3.2   The dilatation relation

The existence of the wavelets is no accident and in exchange of their ability to generate the subspace of integrable functions with a single mother function and to split it into subspaces of attributed scale, the scalling function must be refinable. The scalling function ϕ is refinable, by definition, if it satisfies a dilatation equation

$$\forall x \in \mathbb{R} \qquad \phi(x) = \sqrt{2} \sum_{k=k_0}^{k_1} a_k \phi(2x - k) \tag{4.10}$$

with k_0 and k_1 two integers and the a_k the *filter coefficients* [1]. We define the *wavelet genus* D as the number of terms in the sum D = $k_1 - k_0 + 1$ (it is called the *wavelet* genus since it concerns both the scalling function and the wavelet). We will now comment on the relation and these quantities.

The relation 4.10 states that it is possible to recompose the function ϕ from the sum of the same function ϕ squeezed and translated. From the unique way of the wavelet to recompose itself, there exist a bridge between scales that will determine everything else in the wavelet decomposition. The set of filter coefficients $\{a_k\}_{k \in [k_0, k_1]}$ by itself is enough to characterize a wavelet and all the properties verified by the wavelets have an equivalent for the set of filter coefficients $\{a_k\}_{k \in [k_0, k_1]}$.

---

[1] If the a_k are compactly supported, so is the scaling function ϕ and inversely. If they are not, k_0 and k_1 are equal to $\pm$ infinity. This case will not be considered in this thesis although it is possible to use non compactly supported wavelets.

The wavelet genus D is an important characteristic of the wavelet. The higher the wavelet genus D is, the more links there are between two scales. In a way, the wavelets with a larger wavelet genus D *averages* on more values and are thus smoother. The functions approximated by wavelets of larger wavelet genus D will also be smoother. Two successive basis functions of the scalet subspace V_1 are shifted of a fixed step 1/2 whatever the order of the wavelet is. The entire function ϕ is recomposed by D translated and squeezed scalets ϕ. As D increases, the support of ϕ is thus longer. There exists a link between the support and the wavelet genus and we will now look for it.

In order to find the support of ϕ, we suppose it is given by the real interval [r,s], r and s being two real numbers. We try to relate the support of ϕ and ϕ_1 through the dilatation equation which also writes as:

$$\forall x \in \mathbb{R} \qquad \phi(x) = \sum_{k=k_0}^{k_1} a_k \phi_1^k(x) \quad .$$

The support of ϕ_1^k is that of ϕ divided by two and translated of k/2 thus it is [(r+k)/2,(s+k)/2]. In the dilatation equation, the support of the term on the left, ϕ, must be equal to the support of the term on the right S_{right} which is the union of the supports of the ϕ_1^k for k $\in [k_0, k_1]$ i.e.

$$S_{\text{right}} = \bigcup_{k=k_0}^{k_1} \left[\frac{r+k}{2}, \frac{s+k}{2} \right] \quad .$$

The lower bound of the support S_{right} of all the functions ϕ_1^k in the sum is (r+k_0)/2 and the upper bound is (s+k_1)/2. The equality of the support on the left and on the right implies

$$r = \frac{r+k_0}{2} \quad ,$$
$$s = \frac{s+k_1}{2}$$

which implies $k_0 = r$ and $k_1 = s$. The support of ϕ therefore is $[k_0, k_1]$ and its length is D-1.

Now let us come to the mother wavelet ψ. Since $W_0 \subset V_1$, ψ may be written as a linear combination of the basis functions of V_1. It is thus the result of a dilatation and a translation from the mother scalet ϕ. So, there exists a second dilatation relation for the mother wavelet ψ [2]:

$$\forall x \in \mathbb{R} \qquad \psi(x) = \sqrt{2} \sum_{k=k_0}^{k_1} b_k \phi(2x - k) \tag{4.11}$$

with k_0 and k_1 the same integers as in the equation 4.10 and the b_k *the filter coefficients*. The set of filter coefficients $\{b_k\}_{k\in[k_0,k_1]}$ characterize by itself the mother wavelet whose support is $[k_0, k_1]$ and whose support length is D-1. Moreover, orthogonal wavelets have a set of filter coefficients which verify $b_k = (-1)^k a_{D-1-k}$.

---

[2]The formulation of the dilatation equation is not the same throughout the litterature.
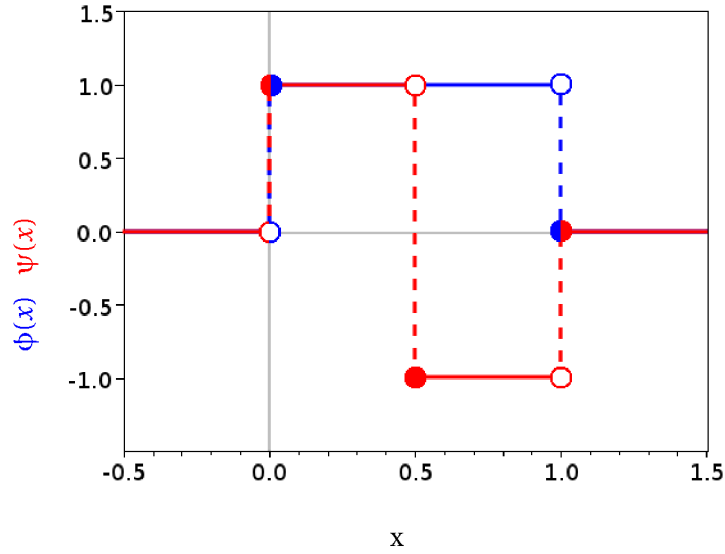
Figure 4.12: *Representation of the scaling function* φ *(blue solid line) and of the wavelet* ψ *(red solid line) of Haar.*

In order to illustrate this point, we start again with the Haar wavelet. We remind of the Haar mother scalet $\phi(x)$ and wavelet $\psi(x)$ in figure 4.12. We have seen that the Haar scalet follows a dilatation relation, equation 4.3, which can also write as

$$\forall x \in \mathbb{R} \qquad \phi(x) = \phi(2x) + \phi(2x - 1) \quad .$$

The genus D is therefore equal to 2, with $k_0 = 0$ and $k_0 = 1$, and its support is indeed [0,1]. The filter coefficients are exactly $a_0 = 1/\sqrt{2}$ and $a_1 = 1/\sqrt{2}$.

We can retrieve the other dilatation equation for the mother wavelet again from the knowledge of the two functions. The shape of the Haar wavelet at a scale $2^{j=0}$ may be reproduced by the juxtaposition of two neighbor scalet steps at a scale $2^{j=1}$ namely

$$\forall x \in \mathbb{R} \qquad \psi(x) = \phi(2x) - \phi(2x - 1) \quad . \tag{4.12}$$

The two integers $k_0 = 0$ and $k_1 = 1$, the wavelet genus D=2 as well as the support [0,1] are the same as the ones of the mother scalet. The filter coefficients b_k of the Haar wavelet are different and given by $b_0 = 1/\sqrt{2}$ and $b_1 = -1/\sqrt{2}$.

To summarize, a wavelet is characterized by an integer k_0, a wavelet genus D and by two sets of filter coefficients $\{a_k\}_{k \in [k_0, k_0 + D - 1]}$ and $\{b_k\}_{k \in [k_0, k_0 + D - 1]}$ associated to the mother scalet and the wavelet respectively (the integers and the wavelet genus are not independent as we have seen $D = k_1 - k_0 + 1$). The mother scalet and the wavelet have a common support equal to $[k_0, k_0 + D\text{-}1]$ of length equal to D-1.

One consequence of defining a wavelet through its filter coefficients is that *there often exists no analytical formula for the wavelet and scalet functions.* However, from the filter

coefficients of the scalet $\{a_k\}_{k\in[k_0,k_0+D-1]}$ and of the wavelet $\{b_k\}_{k\in[k_0,k_0+D-1]}$, it is possible to generate all the wavelets and the scaling functions by using the dilatation equations 4.10 and 4.11. The algorithm described in the next section retrieves the values of the mother scaling function with the use of the dilatation equation.

4.3.3 Evaluating the values of the mother scaling function and the mother wavelet function

The purpose of this section is to explain how to get the values of the mother scalet ϕ from the filter coefficients $\{a_k\}_{k\in[k_0,k_0+D-1]}$. The mother wavelet is then calculated through its dilatation equation 4.11 with the $\{b_k\}_{k\in[k_0,k_0+D-1]}$ and the values of ϕ and will not be presented here.

We look for the value of ϕ at any $x \in \mathbb{R}$ with a resolution on x of $1/2^j$ with j an integer (i.e. $m/2^j < x < (m+1)/2^j$) so we want to calculate $\phi(m/2^j)$ with m an integer. To scan the entire support of length D-1, m has to belong to $[0, 2^j(D-1)]$. We use a recurrent method to do so.

We first have to find D values of the wavelet, whose support is $[k_0,k_0+D-1]$, at integers values within the set i.e. $\{\phi(k)\}_{k\in[k_0,k_0+D-1]}$. A system of equations is obtained by writing the dilatation equation, equation 4.10, for all the integers within its support $[k_0, k_0 + D - 1]$. D equations are thus given as

$$\forall n \in [k_0, k_0 + D - 1] \qquad \phi(n) = \sqrt{2} \sum_{k=k_0}^{k_0+D-1} a_k \phi(2n - k) \tag{4.13}$$

As the term in the sum will also be ϕ at integers values and the value of ϕ at integers values outside of the support is null, the system will be a self coherent one of D unknowns. Once the system has been solved, the initialization of the recurrence is done as we have the values of ϕ at a scale $2^{j=0}$.

The recurrence relation is obtained easily from the dilatation equation. Let us suppose that we have the values of ϕ at a given scale parameter j-1 $\left\{\phi\left(\frac{k_0+k}{2^{j-1}}\right)\right\}_{k\in[0,2^{j-1}(D-1)]}$. We want to calculate the values of ϕ at the next scale parameter j. To do so we write the dilatation equation, equation 4.10, for any $x=(k_0 + n)/2^j$:

$$\forall n \in \left[0, 2^j(D-1)\right] \qquad \phi\left(\frac{k_0 + n}{2^j}\right) = \sqrt{2} \sum_{k=k_0}^{k_0+D-1} a_k \phi\left(\frac{k_0 + n - 2^{j-1}k}{2^{j-1}}\right) \quad . \tag{4.14}$$

Therefore, one can obtain by recurrence the values of ϕ at any given scale 2^j. We have $\{\phi(k)\}_{k\in[k_0,k_0+D-1]}$ from the resolution of the system 4.13 and we use recurrently the relation 4.14 to obtain ϕ at fraction points $m/2^j$ with m and j integers.

We saw that the knowledge of an analytical formula of the wavelet and scalet is not necessary. Indeed, we know how to calculate its value at any point with a desired resolution

143

by using the recurrence scheme that we have described. In the next paragraph, I present the wavelet decomposition of a function and the different wavelet families.

4.3.4 The wavelet decomposition of a function and the different wavelet families

The scalet and wavelet children form orthonormal bases of the subspaces they generate. A general decomposition of a function $f \in L^2(\mathbb{R})$ in V_J with a depth N is written as

$$f_J = \sum_{k=-\infty}^{+\infty} C_{J-N}^k(f)\phi_{J-N}^k + \sum_{j=J-N}^{J-1} \sum_{k=-\infty}^{+\infty} D_j^k(f)\psi_j^k$$

with $C_j^k(f) = \langle f | \phi_j^k \rangle$ and $D_j^k(f) = \langle f | \psi_j^k \rangle$ the coefficients in the scalet and wavelet bases respectively.
The set of coefficients C and D depends on the chosen scalet and wavelet ϕ and ψ. The wavelets with different properties form different wavelet families and we will introduce one of them before presenting the wavelet families.

One important property is to have vanishing moments. The moment of a wavelet of order p is the inner product of the mother wavelet function with the polynomial of order p. If the moment is null, so is the projection of the polynomial x^p in the wavelet subspace. If the wavelet ψ has N vanishing moments of order p

$$\forall 0 \le p \le N-1 \qquad \int_{-\infty}^{+\infty} x^p \psi(x) dx = 0 \quad , \tag{4.15}$$

the projections of the polynomials up to the order N-1 on the wavelet subspaces are null.

Moreover, the vanishing moments for the scalet ϕ are also interesting to develop high order quadrature formula. A scalet subspace with vanishing moments for $1 \le p \le N-1$ is orthogonal to all x at the power p. The projection of a function developed as a polynomial on such a scalet subspace will thus be simplified. The subject is developed further in the section 5.3.1.1.

From the specific properties attributed for each wavelet, different wavelet families have been created. The wavelet families which are of interest in this thesis are all compactly supported and are presented in the next paragraph. A new wavelet is generated by choosing enough properties to create a unique and solvable set of equations for its filter coefficients $\{a_k\}_{k \in [k_0, k_0+D-1]}$. A group of properties can create several sets of equations, one for each wavelet genus D. Each set of equations thus generates a member of a wavelet family with a different D. D is then the *order* of the wavelet and the wavelet is usually called Wavelet D (for instance Haar 2). They are constructed by a method presented in the appendix C.1.3.

We now present the main compactly supported wavelet families. The wavelets are often used for sampling purposes and their construction may be understood from the point

144

of vue of bandpass filters. The Haar wavelet, for instance, corresponds to the band pass filter in the real space. It is the worst case in terms of frequency localization optimization. Inversely, the Gaussian function would be the optimal case. The width at half height of the Gaussian function in the real space Δx and the width $\Delta \omega$ in the frequency domain satisfy the relation $\Delta x \Delta \omega = 1/2$. Unfortunately, the Gaussian function does not fulfill the criteria to be a wavelet.

The so-called Cardinal Splines families were designed with the aim to resemble the Gaussian more and more as their order m increased. The goal was to localize progressively the scalet in the real-space and to delocalize in the frequency domain. The limit of the width at half height of the mother scalet Δx_m and its Fourier transform $\Delta \omega_m$ are such that $\Delta x_m \Delta \omega_m$ tends to 1/2 when m tends to infinity. However, the Cardinal Splines wavelets do not form an orthogonal basis. Although they can be used as wavelets they cannot be used within the MRA efficient algorithms.

Daubechies thus wanted to build a new orthogonal wavelet family that would still be good in the frequency domain. Starting from the Cardinal Splines, she created the Daubechies family and different variants. All the new families have even orders. The D = 2m$^{\text{th}}$ order of the Daubechies family wavelet ψ_{2m}, in addition to be orthogonal, has m vanishing moments but that is not the case of the scalet.

On the request of Coifman to Daubechies, the Coifman wavelets (or Coiflet) were looked for to be orthogonal, as the Daubechies are, but to have also vanishing moments for the mother scalet ϕ in addition to those of the wavelet. *This property makes the Coifman wavelets very attractive for quadrature formulas.* In the same way, the wavelet family called Symmlets are orthogonal and more centered although they are only nearly symmetric. All these Daubechies-like wavelet may be used within the MRA.
The mentioned wavelet families and some of their properties are summed up in table 4.1 and represented in figure 4.13.

name	support	properties	V.M.
Haar	[0,1]	orthogonality, $\hat{\phi}(k) = \text{sinc}(\pi k)$	
Cardinal Spline	[0, D-1]	$\Delta x_m \Delta \omega_m \to 1/2$	
Daubechies	[0,D-1]	orthogonality, D=2N	$0 \leq p \leq N$ for ψ
Coifman	[-2N,4N-1]	orthogonality, D=6N	$0 \leq p \leq 2N$ for ψ $1 \leq p \leq 2N$ for ϕ
Symmlet	[-N+1,N]	orthogonality, D=2N nearly symmetric	$0 \leq p \leq N$ for ψ

Table 4.1: *The main properties of some compactly supported wavelets. V.M. : number of Vanishing Moments of order p (equation 4.15).*

In this thesis we will focus on the Daubechies and the Coifman wavelets as the or-
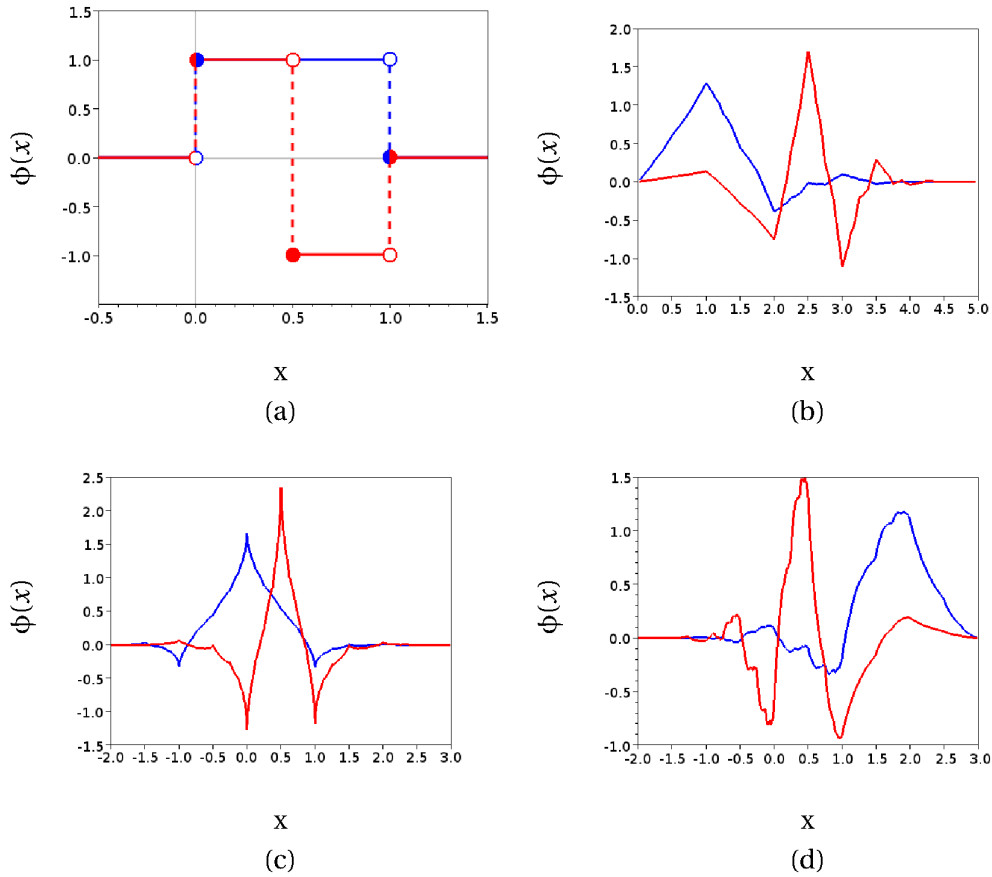
Figure 4.13: *Representation of the scaling function ϕ (blue solid line) and of the wavelet (red solid line) for (a) Haar, (b) Daubechies with D=6, (c) Coifman with D=6 and (d) Symmlet with D=6*

thogonality and the vanishing moments are the most important properties to our purposes (The filter coefficients of the 6th and 12th order of the Daubechies and the Coifman scalet and wavelet are given as an example in table C.2 and table C.3 in appendix C). Our problem being a periodic one, we present in the next section how to have periodic wavelet bases.

4.4 The periodized mother scaling function and wavelet

The best way to deal with periodic functions is to use periodic wavelets. In our problem we do not deal with a periodic function but with a pseudo periodic function of phase shift $\alpha_0 d$. The unknowns H, defined in equation 2.26, and L, defined in equation 2.27, may however be looked for as two unknown periodic functions u and v with $u(x) = H(x)/e^{i\alpha_0 x}$ and $v(x) = L(x)/e^{i\alpha_0 x}$ and therefore be easily expanded on a periodic wavelet basis. The easiest way to build periodic wavelets is to periodize regular wavelets. The period is always equal to one

for the wavelets (it is easier to normalize the variable of the function to be expanded than to change the wavelet basis each time the period changes). A periodic function may not be expanded on the wavelet basis straight away. Prior to the expansion, the variable of the periodic function has to be normalized by the period d to match the wavelet period equal to one. The functions we want to approximate will thus have to belong to $L^2([0,1])$ instead of $L^2(\mathbb{R})$. We show here how compactly supported wavelets can be periodized.

A periodic function may be defined only on its period and then evaluated at any point of $\mathbb{R}$ by translating it of an integer number of period. In the same way, the periodic wavelet basis function is defined within the period as the regular wavelet basis function and is then recomposed in $\mathbb{R}$ by translating it of the same period.

Any periodic scaling function $\tilde{\phi}_j^k$ of period equal to 1 is built from the initial scaling function ϕ_j^k by translating it of an integer number of times the period

$$\forall x \in \mathbb{R} \qquad \tilde{\phi}_j^k(x) = \sum_{n=-\infty}^{\infty} \phi_j^k(x-n) \quad . \tag{4.16}$$

The support of $\tilde{\phi}_j^k$ comes from the periodization of the support of ϕ_j^k which is $\left[\frac{k_0+k}{2^j}, \frac{k_0+k+D-1}{2^j}\right]$ and becomes:

$$\bigcup_{n=-\infty}^{+\infty} \left[\frac{k_0+k}{2^j} + n, \frac{k_0+k+D-1}{2^j} + n\right] \quad . \tag{4.17}$$

The period is one for every wavelet whatever its scale. The support at a scale parameter j is not the support at a scale parameter zero divided by 2^j, therefore $\tilde{\phi}_j^k(x) \neq \tilde{\phi}(2^j x - k)$. Consequently, the periodic scalet of higher scale is not the dilatation and translation of the periodic mother scalet but it does not loose their multi-resolution properties. This is a first important point.

The second important point is that the definition is not consistent if the support of the scaling function ϕ_j^k is longer than the period. Indeed, if that were the case, the scaling functions would overlap each other. The length of the support of ϕ_j^k is equal to $\frac{D-1}{2^j}$ and must be smaller than the period equal to one. The periodized scaling children $\tilde{\phi}_j^k$ exists if and only if

$$\frac{D-1}{2^j} < 1 \quad .$$

Hence there exists a minimum scale parameter J_{min} over which the scaling function ϕ_j^k can be periodized which is

$$J_{min} = \left\lceil \frac{\log(D-1)}{\log(2)} \right\rceil$$

where $\lceil \ \rceil$ is the ceiling function. $\forall j < J_{min}$, one cannot build periodic scalets.
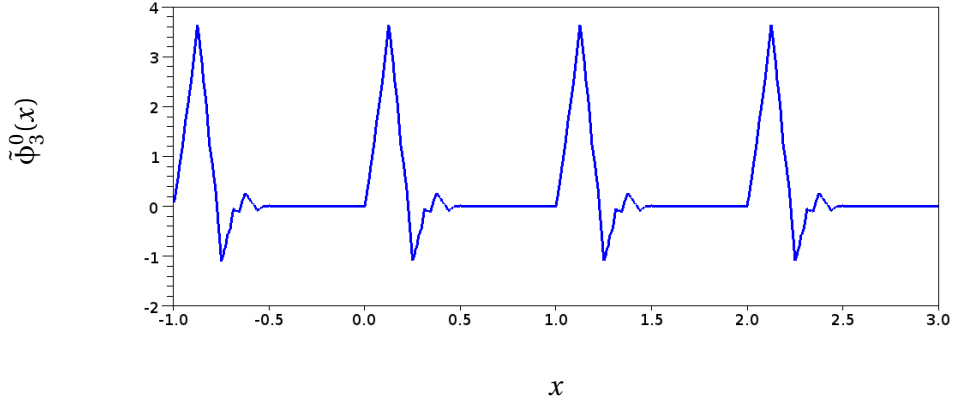
Figure 4.14: *The periodized Daubechies of order 6 scaling function children $\tilde{\phi}_3^0$ over 4 periods.*

For example, the minimum scale parameter $J_{\min}$ of the Daubechies of order D=6 is 3 since $\lceil \log(6-1)/\log(2) \rceil = 3$. The periodized scaling function $\tilde{\phi}_3^0$ obtained in that case is represented in figure 4.14.

As a results of the periodization of the scaling function, any scaling function children $\tilde{\phi}_j^k$ is equal to the same function shifted of an integer number of times 2^j ($\tilde{\phi}_j^{k+2^j}$). This is easily demonstrated as follows

$$
\begin{aligned}
\tilde{\phi}_j^{k+2^j}(x) &= \sum_{n=-\infty}^{\infty} \sqrt{2^j}\phi(2^j(x-n)-(k+2^j)) \\
&= \sum_{n=-\infty}^{\infty} \sqrt{2^j}\phi(2^j(x-(n+1))-k) \\
&= \sum_{n'=n+1=-\infty}^{\infty} \sqrt{2^j}\phi(2^j(x-n')-k) \\
&= \tilde{\phi}_j^k(x)
\end{aligned}
$$

This property is important: there exist only 2^j different periodized scaling function children of scale parameter j. Consequently, $\left\{ \tilde{\phi}_j^k \right\}_{k \in [0, 2^j-1]}$ is a finite basis of dimension 2^j and generates the subspace $\tilde{V}_j$ which has the same dimension, 2^j. As an example, the complete basis of periodized scaling function Daubechies 6 at the scale parameter J=3 is represented in figure 4.15. The dimension of the subspace $\tilde{V}_3$ (and the size of its basis) is $2^3 = 8$.

The periodized wavelets basis $\left\{ \tilde{\psi}_j^k \right\}_{k \in [0, 2^j-1]}$ and their generated spaces $\tilde{W}_j$ are defined in the same way as the periodized scaling function

$$
\forall j > J_{\min} \qquad \forall x \in \mathbb{R} \qquad \tilde{\psi}_j^k(x) = \sum_{n=-\infty}^{\infty} \psi_j^k(x-n) \tag{4.18}
$$

whose dimension is equal to 2^j.

148
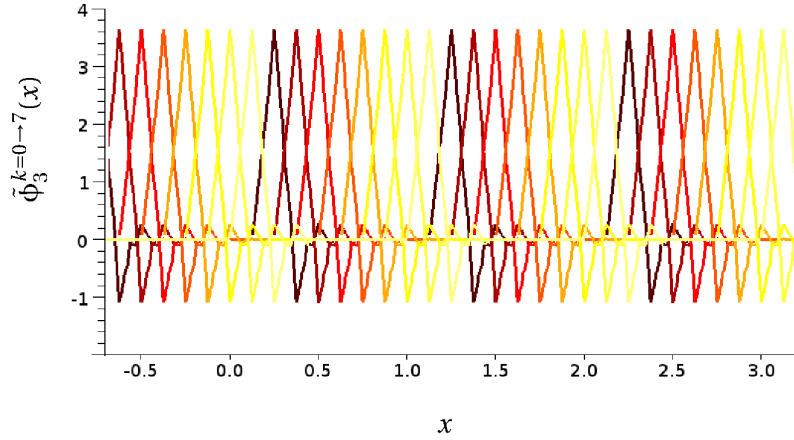
Figure 4.15: *The complete periodized scaling basis function at the scale parameter* $J = 3$ *($\tilde{V}_3$)* *for the Daubechies of order 6 . There are 8 basis functions $\tilde{\phi}_3^k$ with k from 0 to 7. They are represented by a solid line from brown (k=0) to yellow (k=7).*

The Multi-Resolution Approximation of $L^2([0,1])$ is the same as the Multi-Resolution Approximation of $L^2(\mathbb{R})$ apart from the fact that the scalet subspace is $\tilde{V}_j$ instead of V_j and the wavelet subspace is $\tilde{W}_j$ instead of W_j. In particular, the following properties are still verified by the periodized scalet and wavelet subspaces:

$$\tilde{V}_{j-1} \subset \tilde{V}_j \quad ,$$

and

$$\tilde{V}_{j+1} = \tilde{V}_j \oplus \tilde{W}_j \quad .$$

The Multi-Resolution Approximation of $L^2([0,1])$ is thus an infinity of nested subspaces $\tilde{V}_J$ of increasing scale parameter J whose dimension doubles each time. An equivalent approximation of $L^2([0,1])$ starts with a scalet subspace $\tilde{V}_J$ and adds up the wavelet subspaces $\tilde{W}_{j \geq J}$ of increasing dimension from 2^J to 2^{J+N-1} and doubling each time with increasing N. An approximation $\tilde{V}_{J+N}$ of $L^2([0,1])$ may be done equivalently by a scalet subspace or by a combination of a scalet and several wavelets subspaces such that

$$\tilde{V}_{J+N} = \tilde{V}_J \bigoplus_{j=J}^{J+N-1} \tilde{W}_j \quad . \tag{4.19}$$

The number of wavelet subspaces used in the decomposition is called, in the same way as the non-periodic case, the depth of the decomposition (on the left the depth is zero and on the right the depth is N). Both approximations have a total dimension equal to 2^{J+N} as

$$2^{J+N} = 2^J + \sum_{j=J}^{J+N-1} 2^j \quad .$$

149
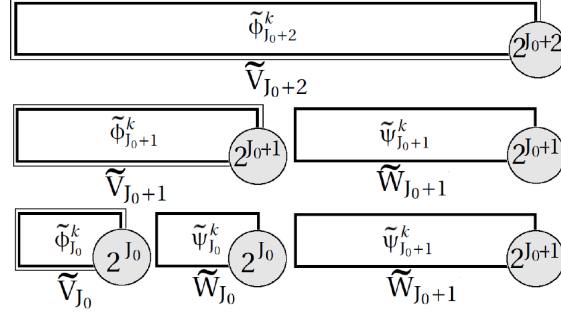
Figure 4.16: *Sketch of the periodized wavelet decomposition.*

In order to get a finer approximation, i.e. to go from $\tilde{V}_{J+N}$ to $\tilde{V}_{J+N+1}$, a wavelet subspace $\tilde{W}_{J+N}$ of dimension 2^{J+N} adds up to the initial subspace $\tilde{V}_{J+N}$ of dimension 2^{J+N} and the result is a subspace of dimension 2^{J+N+1} twice bigger.

The basis functions in $\tilde{V}_{J_0+2}$ with a depth of zero, one and two ($J=J_0$ and $N=0$, $N=1$ and $N=2$ in equation 4.19) are sketched from top to bottom in figure 4.16. The dimensions of each subspaces is indicated in the attached circles. The successive nested subspace $\tilde{V}_{J_0\leq j\leq J_0+2}$ are indicated by the double framed boxes. As an example, the basis functions corresponding to the subspaces $\tilde{V}_5 = \tilde{V}_2 \oplus_{j=2}^4 \tilde{W}_j$ with a depth equal to three are represented in figure 4.17 for the Daubechies of order 4.

Once the basis functions are known, any periodic function whose period is equal to one may be expanded on a wavelet basis. This is not a difficult task since the finite sums are easy to handle numerically. The decomposition of a function f in $\tilde{V}_j$ is thus a finite sum of exactly 2^j coefficients:

$$f_J = \sum_{k=0}^{2^J-1} C_J^k(f)\tilde{\phi}_J^k \tag{4.20}$$

as well as the decomposition with a depth N in $V_{J-N} \oplus_{j=J-N}^{J-1} W_j$:

$$f_J = \sum_{k=0}^{2^{J-N}-1} C_{J-N}^k(f)\tilde{\phi}_{J-N}^k + \sum_{j=J-N}^{J-1} \sum_{k=0}^{2^j-1} D_j^k(f)\tilde{\psi}_j^k \quad . \tag{4.21}$$

Attention must be paid to the fact that the subspaces of scale parameter j< J_{min} do not exist. Therefore, no decomposition can be done with less than $2^{J_{min}}$ points and the depth N must be chosen so that the lowest wavelet scale parameter in the decomposition $J - N$ is also greater than J_{min} (J_{min}, the minimum scale parameter for which the periodic wavelet exists, equation 4.18). The two decompositions (equation 4.20 and 4.21) are equal to the same approximated function although the decomposition coefficients will be different. The algorithms to decompose a periodic function in both ways and a few insights on the wavelet choice and the sparsity of the decomposition is given in the next section.

150
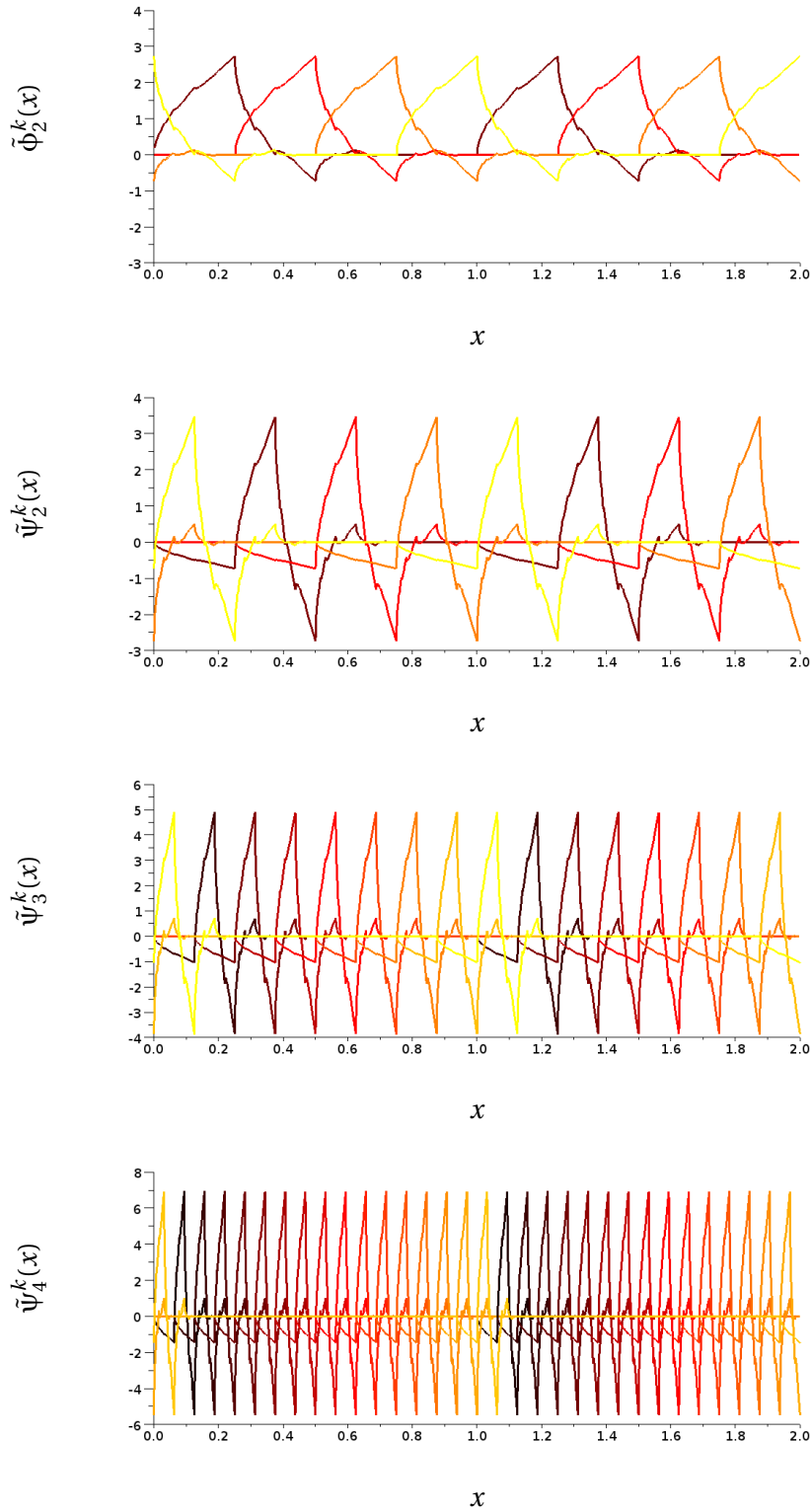
Figure 4.17: *The complete periodized basis of* $\tilde{V}_5$ *with a depth equal to 3 (*$J_0 = 2$*) corresponding to the subspace* $\tilde{V}_2 \bigoplus_{n=2}^{4} \tilde{W}_n$ *for the Daubechies of order 4. The scalet and wavelets* $\tilde{\psi}_2^k$ *of shifts k=0 to* $2^j - 1$ *are represented respectively by a solid line from brown to yellow.*

151

4.5 The common wavelet transforms

Two usefull tools to perform the wavelet decomposition described hereafter are

- the Discrete Scaling function Transform, DST: it calculates the 2^J discrete values of f in $[0, 1]$ from the 2^J scalet coefficients of f in $\tilde{V}_J$ and inversely.

- the Discrete Wavelet Transform, DWT: the DWT with a depth $J - J_0$ calculate the 2^J scalet and wavelet coefficients of f in $V_{J_0} \oplus_{j=J_0}^{J-1} W_j$ from the 2^J discrete values of f in $[0, 1]$ and inversely.

4.5.1 The Discrete Scaling function Transform (DST)

The Discrete Scaling function Transform (DST) is an efficient way to obtain the 2^J values of a periodic function $f \in L^2([0, 1])$, equally spaced in $[0, 1]$, from the scalet coefficients $\left\{ C_J^k(f) \right\}_{k \in [0, 2^J - 1]}$ in the subspace $\tilde{V}_J$ of scale 2^J. The function f may be approximated in $\tilde{V}_J$ by the equation 4.20. The DST consists in applying the general decomposition of equation 4.20 to the points $\frac{l}{2^J}$ for any integer $l \in [0, 2^J - 1]$

$$f_J\left(\frac{l}{2^J}\right) = \sum_{k=0}^{2^J-1} C_J^k(f) \tilde{\phi}_J^k\left(\frac{l}{2^J}\right)$$

and the sum may be easily written as a function of the mother scalet ϕ by using the definition of the scalet children, equation 4.8 after having expressed it as a

$$\tilde{\phi}_J^k\left(\frac{l}{2^J}\right) = \sum_{n=-\infty}^{+\infty} \phi_J^k\left(\frac{l}{2^J} + n\right)$$
$$= \sum_{n=-\infty}^{+\infty} \sqrt{2^J} \phi\left(l - k + 2^J n\right) \quad.$$

To use periodic wavelet the condition $D - 1 < 2^J$ has to be fulfilled. The abscissas of the terms $\phi\left(l - k + 2^J n\right)$ are all separated by 2^J which is greater than the length D-1 of the support of ϕ, $[k_0, k_0 + D - 1]$. Consequently, there can exist only one term in the sum over n that is within the interval $\left[k_0, k_0 + 2^J\right]$ of size 2^J and there exists only one $n_{k,l}$ for each couple (k,l) which fulfills $l - k + n_{k,l} 2^J \in \left[k_0, k_0 + 2^J\right]$. Equivalently, we say that $< l - k >_{2^J} = l - k + n_{k,l} 2^J$ is the integer value of $l - k$ modulo 2^J within the interval $\left[k_0, k_0 + 2^J\right]$. All the other terms than $< l - k >_{2^J}$ in the sum over n, are not included in the interval $\left[k_0, k_0 + 2^J\right]$, which contains the support of ϕ, and are therefore null. The DST can thus be written as

$$f_J\left(\frac{l}{2^J}\right) = \sum_{k=0}^{2^J-1} C_J^k(f) \sqrt{2^J} \phi\left(< l - k >_{2^J}\right) \quad.$$

Within the interval $\left[k_0, k_0 + 2^J\right]$, if the integer value $< l - k >_{2^J}$ belongs to the support of ϕ, $[k_0, k_0 + D - 1]$, then $\phi\left(< l - k >_{2^J}\right)$ is the value of ϕ at an integer value. Otherwise if $< l - k >_{2^J}$

belongs to $\left[k_0 + D - 1, 2^J\right]$ then $\phi\left(<l - k>_{2^J}\right) = 0$. In that transformation, *only the values of ϕ at integers are needed.*

That transformation may be written as a matrix S_J which transforms the vector of the coefficients $\left\{C_J^k(f)\right\}_{k\in[0,2^J-1]}$ into the vector of the values of f $\left\{f_J\left(\frac{l}{2^J}\right)\right\}_{l\in[0,2^J-1]}$, shown in the case of $k_0=0$ in figure 4.18. The matrix is a square one with a number of lines and columns equal to 2^J at a scale parameter J. The lines of the matrix are indexed by l from the point $l/2^J$ at which the values of f are taken and the columns are indexed by k, the shift parameter of the coefficients $C_J^k(f)$. The term (l,k) in the matrix is $\tilde{\phi}_J^k\left(\frac{l}{2^J}\right) = \sqrt{2^J}\phi\left(<l - k>_{2^J}\right)$. Each row (or column) only contains the values of ϕ at the D-1 integers included in its support and the rest of the terms are null.

Figure 4.18: *The Discrete Scaling Function Transform matrix is S_j with $k_0=0$.*

The matrix is highly sparse as the number of non-zero terms per line (resp. column) is constant, it is D-1, but the number of lines (resp. column), 2^J, doubles with the scale parameter J. The consequences are:

- The number of non-null terms the DST matrix is $D2^J$.

- The percentage of non-null terms is of the order of magnitude of $D2^{-J}$.

- The matrix gets sparser as the scale 2^J increases.

- The number of operations of this transformation is higher for wavelets of higher order D.

4.5.2 The Discrete Wavelet Transform (DWT)

A second important tool is the Discrete Wavelet Transform (DWT) of scale 2^J and with a depth $J - J_0$, which decomposes the functions f and its values $\left\{f_J\left(\frac{m}{2^J}\right)\right\}_{m\in[0,2^J-1]}$ directly into its wavelet coefficients. The wavelet decomposition with a depth equal to $J - J_0$ is done in

153

the subspace

$$\tilde{V}_{J_0} \bigoplus_{j=J_0}^{J-1} \tilde{W}_j \quad . \tag{4.22}$$

and is obtained by substituting N=J $-$ J$_0$ into the equation 4.21. J$_0$ is the scale parameter of the scalet subspace, $\tilde{V}_{J_0}$ and in the same time the lower scale parameter of the wavelet subspaces.

Throughout this thesis, the wavelet coefficients will be put in ascending order of scale, all the scalet coefficients first $\left\{ C_{J_0}^k(f) \right\}_{k=[0,2^{J_0}]}$ then the wavelet ones $\left\{ D_j^k(f) \right\}_{k=[0,2^j]}$ with j increasing from J$_0$ to J $-$ 1. The coefficients set (and corresponding vector) are

$$\left\{ \left\{ C_{J_0}^k(f) \right\}_{k=[0,2^{J_0}]} \left\{ D_j^k(f) \right\}_{k=[0,2^j]} \right\}_{j=[J_0,J-1]} \quad .$$

One way to obtain this set of coefficients, is first to decompose the function into its scalet coefficients and then to use a Fast Wavelet Transform (FWT) which decomposes further the scalet coefficients into scalet and wavelet ones with a desired depth J $-$ J$_0$ and is described in the section C.3 in appendix C. It corresponds to apply successively the inverse of the DST (S$_J$ matrix) and the FWT with a depth J $-$ J$_0$.

The other way is to look for the direct transformation matrix, and to do so, to apply the equation 4.21 to the points $m/2^J$ for $m \in [0, 2^J - 1]$

$$f_J\left(\frac{m}{2^J}\right) = \sum_{k=0}^{2^{J_0}-1} C_{J_0}^k(f) \tilde{\phi}_{J_0}^k\left(\frac{m}{2^J}\right) + \sum_{j=J_0}^{J-1} \sum_{k=0}^{2^j-1} D_j^k(f) \tilde{\psi}_j^k\left(\frac{m}{2^J}\right) \quad .$$

The same arguments as the ones issued in the previous section on the support of the periodic wavelet bases allows us to write that

$$f_J\left(\frac{m}{2^J}\right) = \sum_{k=0}^{2^{J_0}-1} C_{J_0}^k(f) \tilde{\phi}_{J_0}^k\left(< \frac{m}{2^{J-J_0}} - k >_{2^{J_0}}\right) + \sum_{j=J_0}^{J-1} \sum_{k=0}^{2^j-1} D_j^k(f) \tilde{\psi}_j^k\left(< \frac{m}{2^{J-j}} - k >_{2^j}\right)$$

with $< \frac{m}{2^{J-j}} - k >_{2^j}$ the value of $\frac{m}{2^{J-j}} - k$ modulo 2^j.

The columns in the matrix correspond successively to the scalet and wavelet basis function of ascending scale therefore it is possible to divide the matrix into sub-matrices corresponding to the different subspaces as sketched in figure 4.19(a) where solid lines represent the frontiers of the wavelet subspaces. In the first block starting from the left, the terms $\tilde{\phi}_{J_0}^k\left(m/2^J\right) = \psi\left(< \frac{m}{2^{J-J_0}} - k >_{2^{J_0}}\right)$ form a diagonal band of width equal to the support of the wavelet D-1. Next, in each block, the terms $\tilde{\psi}_j^k\left(m/2^J\right) = \psi\left(< \frac{m}{2^{J-j}} - k >_{2^j}\right)$ form diagonal bands of width equal to the support of the wavelet D-1 for each scale 2^j. As an example, the matrix coefficients of a decomposition starting at the scale parameter J$_0$ = 4 to J$_0$ + 2 = 6 for a Daubechies wavelet of order 6 is shown in figure 4.19(b) where the diagonal bands are materialized by dashed lines and the different subspaces are divided by solid lines.
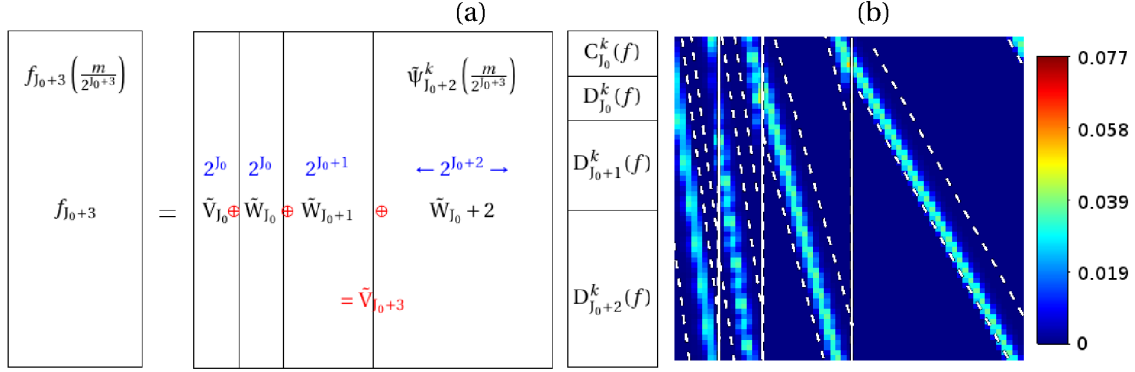
Figure 4.19: *(a) Sketch of the matrix of the DWT and ordering of the coefficients in the wavelet basis (b) Modulus of the values of the DWT matrix in the example of a Daubechies wavelet of order 6 with* $J_0 = 4$ *and* $J = 6$. *Solid lines divide the different wavelet subspaces and dashed lines indicate the frontiers of the non-null terms bands in the matrix.*

In the same way as for the DST, the sparsity of the matrix of size 2^J (corresponding to a development on the wavelet bases from J_0 to J-1) can be evaluated with the percentage P of non-null terms. Each subspace $\tilde{V}^j$ or $\tilde{W}^j$ of size 2^j by 2^J contains $D\,2^J$ terms. The total number of terms being 2^{2J}, the percentage P is

$$P = \frac{2^J D}{2^{2J}} \left[1 + \sum_{j=J_0}^{J-1} 1 \right] = \frac{D}{2^J}(J - J_0 + 1)$$

In the same way as for the DST, the characteristics of the DWT matrix of scale parameter J with 2^J coefficients are

- The number of non-null terms in the matrix is proportional to $DJ2^J$.

- The percentage of non-null terms is of the order of magnitude of $DJ2^{-J}$.

- The matrix gets sparser with higher scales.

- The number of operations of this transformation is higher for higher order wavelets.

4.5.3 Influence of the choice of the wavelet and its order on the wavelet decomposition

In order to compare different wavelets and to study the influence of the order, we use as an example, a new periodic function g, of period equal to one

$$g : \begin{cases} 0 \leq x < \frac{1}{2} & g(x) = \sin(11\pi x) \\ \frac{1}{2} \leq x < 1 & g(x) = 0 \end{cases} \tag{4.23}$$

The function is projected on the subspace $\tilde{V}_6$ with different wavelets of varying orders. The scalet coefficients of g in $\tilde{V}_6$ are obtained by using a DST and $g_{\tilde{V}_6}$ is then recomposed from

the scalet coefficients at any resolution 2^{-J} wanted. To evaluate the values of $g_{\tilde{V}_6}$, the ones of the basis functions are needed. Therefore, we use the algorithm to evaluate the values of the scaling function presented in section 4.3.3 and chose J = 9 because the step 2^{-9} cannot be distinguished. In figure 4.20(a), we show the approximated function $g_{\tilde{V}_6}$ with the Haar wavelet (yellow) as well as the Daubechies wavelet(orange), the Coiflet (red) and the symmlet (brown) of order 6.
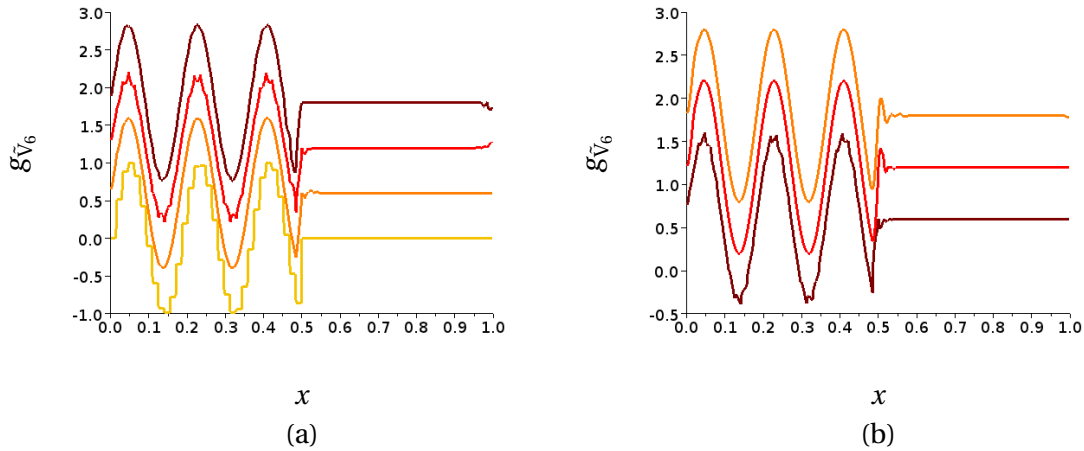
Figure 4.20: *(a) Approximation of the function of equation 4.23 in $\tilde{V}_6$ with a Haar wavelet (yellow), a Daubechies 6 wavelet (orange), a Coiflet 6 (red) and a Symmlet 6 (brown). (b) Approximation of the same function in $\tilde{V}_6$ with a Daubechies wavelet of order 4 (brown), 8 (red) and 16 (orange). The ordinates of the functions are translated of 0.6 from each other for sake of clarity.*

The values of $g_{\tilde{V}_6}$ at the points $x_l = l/2^6$ are identical to the ones of g. Indeed, recomposing the function from the scalet coefficients in $\tilde{V}_6$ with a resolution 2^{-6} is similar to apply a DST. Therefore, applying successively the inverse DST transform and the DST transform gives us the exact values of g at the x_l: $g_{\tilde{V}_6}(x_l) = g(x_l)$. Whatever wavelet is used, the values of $g_{\tilde{V}_6}$ at the x_l are thus identical. On the contrary, the recomposition of the entire function $g_{\tilde{V}_6}$ correspond to an interpolation of g between the x_l by the wavelet and is particular to each wavelet. The three functions approximated by Daubechies-like wavelets, Daubechies, Symmlet and Coiflet, are quite similar and they have the same resolution, 2^{-6}, so there is no reason at this stage, to prefer a wavelet to another.

The order of the wavelet depends on the kind of interpolation wanted for the function between the x_l. The wavelets with a higher order D draw a smoother curve between the x_l as shown in figure 4.21(b) with the Daubechies wavelet of order 4 (brown), 8 (red) and 16 (orange). The price one has to pay for a smoother approximation of the sinusoidal oscillations is a strongest residual oscillation on the right of x=0.5 due to the step. This effect is due to the fact that the scalet functions which interpolate smoothly the x_l on the left of x=0.5 go beyond the step because they are not localized at a point but over a length equal to

156

their support. As the support is proportional to D, if D is higher, the oscillations due to the interpolation goes past x=0.5 on a longer distance.
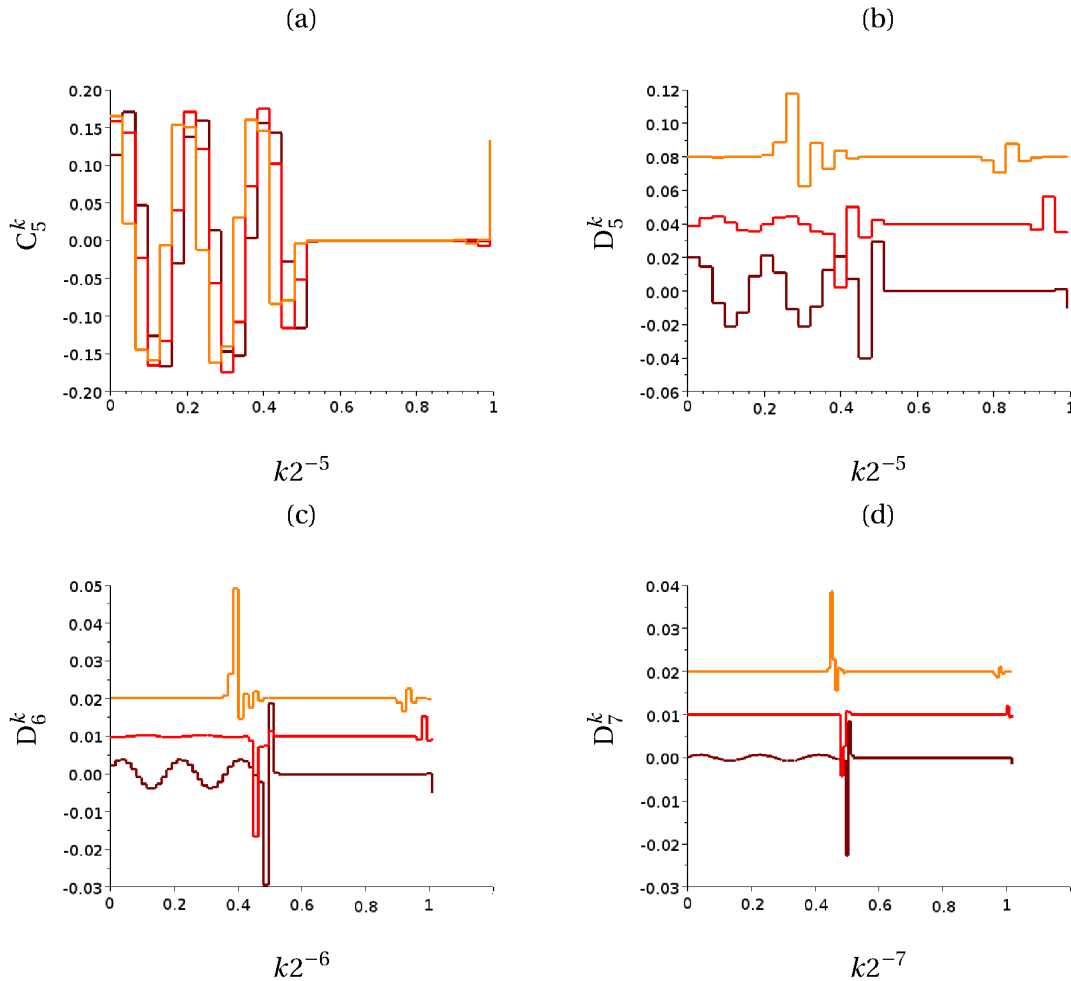
Figure 4.21: *The coefficients of the wavelet decomposition of the function of equation 4.23 on $\tilde{V}_8$ (J=8) with a depth 3 (J_0 = 5) are represented in (a) for $\tilde{V}_5$, (b) for $\tilde{W}_5$, (c) for $\tilde{W}_6$ and (d) for $\tilde{W}_7$ with three Daubechies wavelets of increasing order. The brown line corresponds to Daubechies 4, the red one to Daubechies 8 and the orange one to Daubechies 16. The D coefficients are translated in the y-axis for sake of clarity.*

The most important difference, however, is in the coefficients sparsity. The same function was decomposed on the subspace $\tilde{V}_8$ with a DWT with a depth equal to 3 (J_0 = 5). The wavelet coefficients on the subspaces $\tilde{V}_5$, $\tilde{W}_5$, $\tilde{W}_6$ and $\tilde{W}_7$, whose sum is equal to $\tilde{V}_8$, are shown in figure 4.21(a) to figure 4.21(d) with the Daubechies wavelet of order 4 (brown), 8 (red) and 16 (orange). The scalet and wavelet coefficients are plotted at equally spaced points on the interval [0,1]. The coefficient C_j^k is plotted at the point $x_k = k/2^j$ which is the shift of the scalet basis function ϕ_j^k from ϕ_j^0. The scaling function ϕ_j^k is therefore non-null around the point x_k where its coefficient is plotted. In that way, the coefficients may

be attributed to different parts of the function. The coefficients on the left part between 0 and 0.5 for instance correspond to the smooth sinus oscillation as shown in figure 4.21(a) whereas the coefficients between 0.5 and 1 correspond to the flat part. The sharp variations of the function appear most clearly in figure 4.21(d) as one big and one little spike. The highest spike in the coefficients at about x=0.5 correspond to the step. The second spike at about x=1 corresponds to the discontinuity of the derivative at x=0 and appears on the other side of the interval due to the asymmetry and the periodicity of the wavelet. The coefficient D_j^k of the Daubechies basis function ψ_j^k is linked to the projection of g over the interval $[2^{-j}k, 2^{-j}(k+D-1)]$. The interval $[2^{-j}k, 2^{-j}(k+D-1)]$ overlap the sharp variation of g at x=0.5 for D-1 values of k such that

$$2^{-j}k \ < \ 0.5 \ < \ 2^{-j}(k+D-1) \quad .$$

In these cases the inner product of ψ_j^k and g is different from zero. The coefficient D_j^k, which is associated to the step, is thus different from zero between 0.5 and $0.5 - (D-1)2^{-j}$. This explains why the spike due to the step at 0.5 is shifted to the left. The shift to the left is bigger if the order D is bigger or if the scale parameter j is smaller.

We observe that the repartition of the coefficients is different for the different orders D. If the order D is high, there is no coefficients which correspond to the smooth sinus oscillation on the wavelet subspace, only the two spikes due to the sharp variations as shown by the orange line in figure 4.21(b-d). On the contrary, if the order D of the wavelet is low, there are still coefficients between 0 and 0.5 to describe the sinus oscillations as shown by the brown line in figure 4.21(b-d). That is due to the fact that the projection on the scalet subspace $\tilde{V}_5$ done by the Daubechies 16 describes the smooth part of the function in a better way than the Daubechies 4. For the Daubechies 16, the sharp variations are thus the only part left to describe on the wavelet subspaces $\tilde{W}_5$, $\tilde{W}_6$ and $\tilde{W}_7$.

Let us focus on the coefficients of the sharp edges identified as the two spikes at about x=0.5 and x=1. The localization of the Daubechies 4 is so strong that only two big coefficients at 0.5 account for the step as shown in a brown line in figure 4.21(b-d). The Daubechies 16 has a support four times bigger than the one of Daubechies 4. The coefficients which make the spike close to 0.5 in the decomposition with the Daubechies 16 are thus more spread and more numerous as shown in an orange line in figure 4.21(b-d). As a consequence, the oscillations of the recomposed function $g_{\tilde{V}_6}$ after x=0.5 are also longer for Daubechies 16.

The order of the wavelet is used to adjust the localization of a wavelet in the real or the frequency space. The order of the wavelet influences its sampling properties whether it is better suited for smooth or sharp edges. The higher order wavelet approximates a function very quickly and as a result the decomposition is very sparse. Its wide support however slows down the approximation of sharp edges, requiring more coefficients at these precise points.

To sum up, the choice of the wavelet family depends on the kind of application it is used for and the properties that will therefore be needed. The choice of the order of the

wavelet depends on the kind of decomposition wanted which depends on the general profile of the function and more precisely on the density of sharp variations. If the density of sharp variations is low, it is more advantageous to chose a higher order wavelet. The result and the matrix will be more sparse and it will save memory space. The transformations of higher order wavelets require however more operations since the support is longer and are therefore more costly in time.

4.6   Conclusion

In this chapter, we have presented how to generate a complete periodic basis of $L^2([0,1])$ from the dilatation and translation of one single mother scaling function: the wavelet basis. A scaling function is defined by a set of filter coefficients $\{a_k\}_{k=[k_0,k_0+D-1]}$ where D is the order (or the wavelet genus) and $[k_0, k_0 + D - 1]$ is the support. The wavelet is defined by a set of filter coefficients $\{b_k\}_{k=[k_0,k_0+D-1]}$ and has the same support and order than the scalet. Different families of wavelets were introduced and two families draw our attention and are used in the next chapter: the Daubechies and the Coifman wavelet.

We have seen that the projection of a function on a wavelet basis of resolution 2^{-J} comprises two parts: the dense projection on the scalet subspace $\tilde{V}_{J_0}$ of scale parameter J_0 and the sparse projection on the wavelet subspace $\tilde{W}_j$ with j from J_0 to J. First, the projection of f on $\tilde{V}_{J_0}$ approximates the function f with a resolution 2^{-J_0}. Secondly, the projection on each wavelet subspace of increasing scale 2^j adds up details to go from a resolution 2^{-j} to $2^{-(j+1)}$ until the final resolution of 2^{-J} is reached. A function which varies abruptly at a few specific spots on the surface has only few details of the highest resolution 2^{-J}. Only a few coefficients in the higher scale wavelet subspaces are therefore needed for the decomposition. We commented on the repartition of the wavelet coefficients on the scalet and wavelet subspaces as a function of the order D of the wavelet. Efficients algorithms which perform the transformation from the real space into the wavelet subspaces were given.

In the next chapter, we see how to make use of the wavelets in the resolution of the surface integral equations.

Chapter 5

The application of wavelets to surface integral equation

We described in chapter 2, the modeling and the simulation of an incident plane wave impinging on a metallic grating standing in a dielectric with the SIE method. The method was used with periodic boundary conditions and applied to nano-scale rough surfaces with a small period (50 nm). As it is, the numerical implementation of the SIE method requires too much memory space and prevents one from treating larger surfaces. We saw that the EM physical quantities may all be expressed as an integral of the two source functions H and γL, which are the magnetic field and its derivative on the surface. The two surface integral equations over the metallic boundary discretized in a number N of points $\left\{\vec{r}_n \in S_D\right\}_{n\in[0,N-1]}$ gives us a set of 2N linear equations for the two source functions H ans γL. We call this method the Maradudin method as it was first introduced by Maradudin [91]. The set of linear equations are put in a matrix form MX=V such as

$$
\begin{bmatrix} \partial M^+ (\vec{r}_n, \vec{r}_m) & M^+ (\vec{r}_n, \vec{r}_m) \\ \partial M^- (\vec{r}_n, \vec{r}_m) & M^- (\vec{r}_n, \vec{r}_m) \end{bmatrix} \begin{bmatrix} H(\vec{r}_m) \\ \gamma L(\vec{r}_m) \end{bmatrix} = \begin{bmatrix} H_z^i (\vec{r}_n) \\ 0 \end{bmatrix} \tag{5.1}
$$

where $M^\pm (\vec{r}_n, \vec{r}_m)$ (resp. $\partial M^\pm$) is expressed with the pseudo-periodic Green function $\tilde{G}^\pm (\vec{r}_n, \vec{r}_m)$ (resp. of the derivative of $\tilde{G}^\pm$). Its resolution gives us the N values of the two source functions at these points. The resolution is not an easy task since the square matrix M is dense. Indeed, the dimension of the matrix M being 2N, the memory space needed to store the matrix is proportional to $4\,N^2$ and the number of cycles to fill and then solve the matrix is proportional to $10^5 N^2$ and $10^2 N^3$ cycles respectively (see section 2.4.2.6).

     The surface integral equation method was then applied to some examples of nano-scale rough surfaces with one to five defects, in chapter 3. It showed that grooves with dimensions of a few nanometers are able to sustain an electric field enhanced by 10^3 the incident one in the groove at a plasmonic resonance. The source function H can thus have sharp variations at the location of the sharp variations of the profile, and γL too. Therefore, the simulation requires a small step h=d/N (h $\lesssim$ 1Å), where d is the period, or equivalently a

high number N of points, to describe the source functions on the metallic surface correctly. This number of points N being limited by the computer capacity, we can only study small systems. Moreover, in order to study the plasmonic resonances, the whole spectra of the physical quantities in the visible has to be calculated and the time spent to calculate the solutions for a couple of values (θ_i, λ) of the incident conditions becomes critical.

In order to overcome this limitation, we have considered a new tool: the wavelets whose basic principles were presented in chapter 4. The use of wavelets within the framework of the multi-resolution analysis, enables one to study separately the details of a function with different scales. We want to take advantage of that to describe accurately the highly localized magnetic field of the hot-spots as well as the smooth variations of the magnetic field on the whole period.

The application of wavelets is proved to be successful for another integral method called the method of moment [136] and different wavelet techniques suited to large scale problems in electromagnetism have been developed [132]. Almost all the literature on the subject is found in IEEE Antennas and propagation. The closest example to our research, to our knowledge, is the problem of the scattering from 2D perfectly conducting random rough surfaces [137, 138, 139]. The most common technique is to sparsify the dense matrix obtained with the standard integral equations with a fast wavelet transform and then to solve it in a more efficient way by using an iterative technique. Another, more recent, technique has been developed by Pan which does not require calculating the initial dense matrix [140, 141].

Prior to the reading of this chapter, that of the previous chapter is recommended for those who are unfamiliar with the theory of wavelets. In this chapter, we start by highlighting why we believe that the wavelets can improve our current method, after having set a new frame for the simulation with the wavelets. We then describe two different ways to apply the wavelets to our problem. The first one sparsifies the initial dense matrix by applying a wavelet transform and the second one is based on the technique of Pan to calculate directly the sparse matrix in the wavelet bases.

5.1 Introduction to the application of wavelets to surface integral equation

In this section, we first make adjustments to apply the periodic real basis to a pseudo-periodic complex source function. We then address the question of the relevance of the wavelet for the study of the nano-scale rough surfaces.

5.1.1 A fresh start in the simulation of surface integral equation

Our goal is to develop a different way to do the simulation of the two surface integral equations 2.50 and 2.51. To do so efficiently, we want to benefit from the use of a periodic real wavelet basis. However, the unknowns are complex and pseudo-periodic with a period d, i.e. their phases shift of $\alpha_0 d$ over a period d in the x direction (H and L follow the same equation 2.38).

To circumvent the phase shift, we define the periodic unknowns $\tilde{H}$ and $\tilde{L}$ at a point $\vec{r} = (x, y)$ at the surface S_D

$$\tilde{H}(x, y) = H(x, y)e^{-i\alpha_0 x} \quad , \tag{5.2}$$

$$\tilde{L}(x, y) = L(x, y)e^{-i\alpha_0 x} \quad . \tag{5.3}$$

As γ is also periodic, the source function $\gamma\tilde{L}$ still is. To describe the two source functions $\tilde{H}$ and $\gamma\tilde{L}$, the wavelets will have to be periodic with respect to the variable x. However as the period of the wavelet is set to one, we define a normalized abscissa u= x/d. This normalized abscissa is now central to our problem. Indeed, the wavelet transforms require that the variable u is sampled at equally distant points and the inner products with a wavelet basis function also require an integral over the variable u. In order to apply the wavelet transform or to do an inner product with a wavelet basis function in the easiest way , the problem has to be expressed in function of the variable u. Therefore, the surface S may no longer be described by a general parametric function, the parameter has to be directly the variable u. The surface S_D is defined by

$$S_D : u \in [0, 1] \rightarrow \begin{pmatrix} ud \\ y_D(ud) \end{pmatrix} \qquad y_D \in \mathscr{C}^2 \quad .$$

This description of the surface profile is a little restriction with respect to the general one in the equation 2.2 [1]. It corresponds to the particular case of a parameter t ∈ [0, 1] and the function $x_D : t \rightarrow td$. All the results of the chapter 2 may then be applied in this chapter.

The fact that the two source functions are complex is not an issue. The expansion of a complex function on a real wavelet basis is the same as that of a real function except for the wavelet coefficients D_j^k which are complex. The real (resp. imaginary) part of the coefficients is then given by the projection of the real (resp. imaginary) part of the complex function on the scalet and wavelet subspaces, i.e. $\Re\left(C_j^k(f)\right) = \left\langle \Re(f) | \phi_j^k \right\rangle$. It is equivalent to treat separately the real and the imaginary part of the source function by dividing each equation in its real and imaginary part and by considering twice as many equations.

The new framework for developing a simulation with wavelets has been set. In the next paragraph, we make some comments on the usefulness of the wavelet basis to our problem.

---

[1] In this chapter, we call y_D the function which describes the ordinate of the surface profile in order to avoid confusion with the order D of the wavelet.

5.1.2 How can wavelet benefit our problem?

In this paragraph, we want to highlight how the source function $\tilde{H}$ decomposes on a wavelet basis. To do so, we studied an incident plane wave of energy 2.13 eV impinging at an incidence angle $\theta_i = 10°$ on a silver grating with a period equal to 230 nm. The surface contains five defects which are Gaussian grooves whose dimensions are about 1-2 nm for the width and 10-13 nm for the height. The grooves have the same dimensions as that of the grooves of the grating in chapter 3, indicated in table 3.2 and their espective abscissas are 18, 67, 112, 160 and 207 nm. The surface was chosen to resemble a flat surface with a few sharp grooves. The grating profile (blue line) is represented in figure 5.1 as well as the modulus of the source function $\tilde{H}$ on the metallic surface (red line) discretized with N = 8192 points calculated with the Maradudin method. The source functions superimpose for a resolution using a number of points equal to N = 4096 points and N = 8192 points so we consider that the solution converged. We can see that the magnetic field, at this wavelength, does not vary much along the flat surface whereas there are some quick variations in the groove.
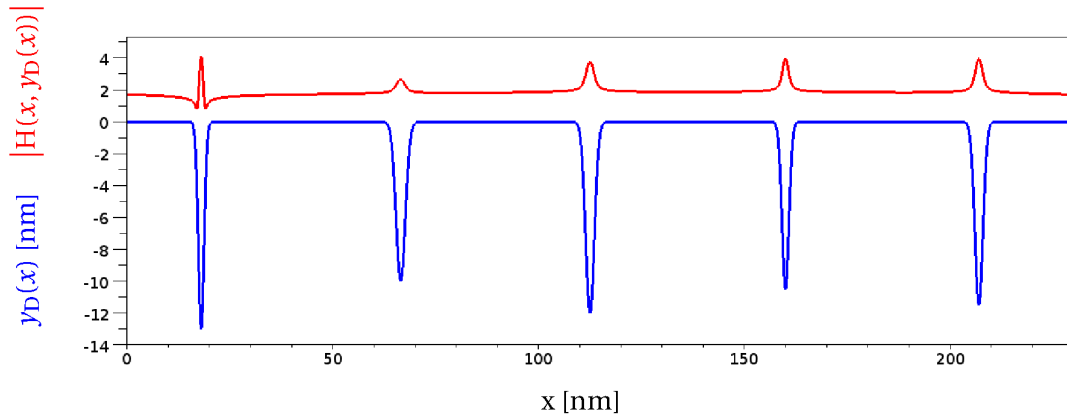
Figure 5.1: *Profile (blue solid line) of a silver grating of period d=230 nm with 5 Gaussian grooves and modulus of the source function H (red solid line) for an incident plane wave of energy 2.13 eV and $\theta_i = 10°$ impinging on the same grating calculated with the Maradudin method using N = 8192 points.*

The modulus of the source function $\tilde{H}$ is now projected on the subspace $\tilde{V}_{12}$ ($N_{12} = 4096$) and we choose a decomposition depth of 8, or equivalently $J_0 = 5$. We have a first decomposition on $\tilde{V}_{J_0} = \tilde{V}_5$ and next the complementary subspaces $\tilde{W}_5$ to $\tilde{W}_{11}$ are added

$$\tilde{V}_{J=12} = \tilde{V}_{J_0=5} \oplus \tilde{W}_5 \oplus \tilde{W}_6 \oplus \quad \ldots \quad \tilde{W}_{11} \quad .$$

From equation 4.21, we write the decomposition as

$$\tilde{H}_{\tilde{V}_{12}} = \sum_{k=0}^{2^5-1} C_5^k(\tilde{H})\tilde{\phi}_5^k + \sum_{j=5}^{11} \sum_{k=0}^{2^j-1} D_j^k(\tilde{H})\tilde{\psi}_j^k$$
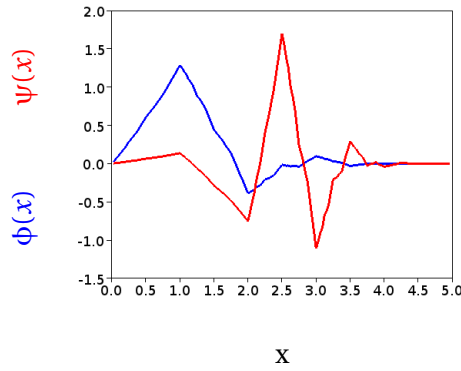
Figure 5.2: *Representation of the scaling function* φ *(blue solid line) and of the wavelet (red solid line) for the Daubechies of order 6.*

where the real (resp. imaginary) part of the coefficient corresponds to the projection of the real (resp. imaginary) part of the source function $\tilde{H}$. The wavelet is chosen to be Daubechies 6 whose mother scalet and wavelet are again represented in figure 5.2.

The projection of $\tilde{H}$ on the starting scalet subspace $\tilde{V}_5$ and the complementary wavelet subspaces $\tilde{W}_j$ for j from 5 to 9 are plotted in black as a function of the abscissa x, in figure 5.3(a) to figure 5.3(e) respectively. The profile of the grating is also plotted in blue as a guide for the eyes. The projection on $\tilde{V}_5$, represented in figure 5.3(a) added to the projection on $\tilde{W}_5$, represented in figure 5.3(b), is equivalent to a projection on $\tilde{V}_6$ such that

$$P_{\tilde{V}_5}(\tilde{H}) + P_{\tilde{W}_5}(\tilde{H}) = P_{\tilde{V}_6}(\tilde{H}) \quad .$$

$P_{\tilde{V}_6}(\tilde{H})$ is represented by a red line in figure 5.3(b). Similarly, each projection on a wavelet subspace $P_{\tilde{W}_j}(\tilde{H})$, plotted in black, is added to the projection on the complementary scalet space $P_{\tilde{V}_j}(\tilde{H})$, plotted in red in the previous figure. The sum, equivalent to the projection $P_{\tilde{V}_{j+1}}(\tilde{H})$ is plotted in red in the same figure as the projection on the wavelet subspace $P_{\tilde{W}_j}(\tilde{H})$.

The projection $P_{\tilde{V}_8}(\tilde{H})$, represented by a red line in figure 5.3(d) already resemble to $\tilde{H}$ (see figure 5.1). The overall description of the smooth part of the source function $\tilde{H}$ is thus done in the scalet subspace $\tilde{V}_8$. The decomposition on the subspace $\tilde{V}_8$ is done with only $2^8 = 256$ points. In order to have a more accurate description of the source function, additional projections $P_{\tilde{W}_j}(\tilde{H})$ on the complementary wavelet subspaces $\tilde{W}_j$, with j from 8 to 11, are necessary. However, the projection of $\tilde{H}$ on $\tilde{W}_j$ is localized at the sharp variations of the profile, here the deep grooves. The corresponding coefficients D_j^k of the decomposition in $\tilde{W}_j$, are not null only when the shifts $k/2^j$ of ψ_j^k from ψ_j^0 are close to a sharp variation of the profile. Therefore, the expansion of the source function $\tilde{H}$ is sparse on these wavelet subspaces. Additionally, the amplitude of the projected functions also decreases quickly as j increases.

In order to quantify the number of terms implicated in the description of the source

165

(a) $\tilde{V}_5$

(b) $\tilde{W}_5$

(c) $\tilde{W}_6$
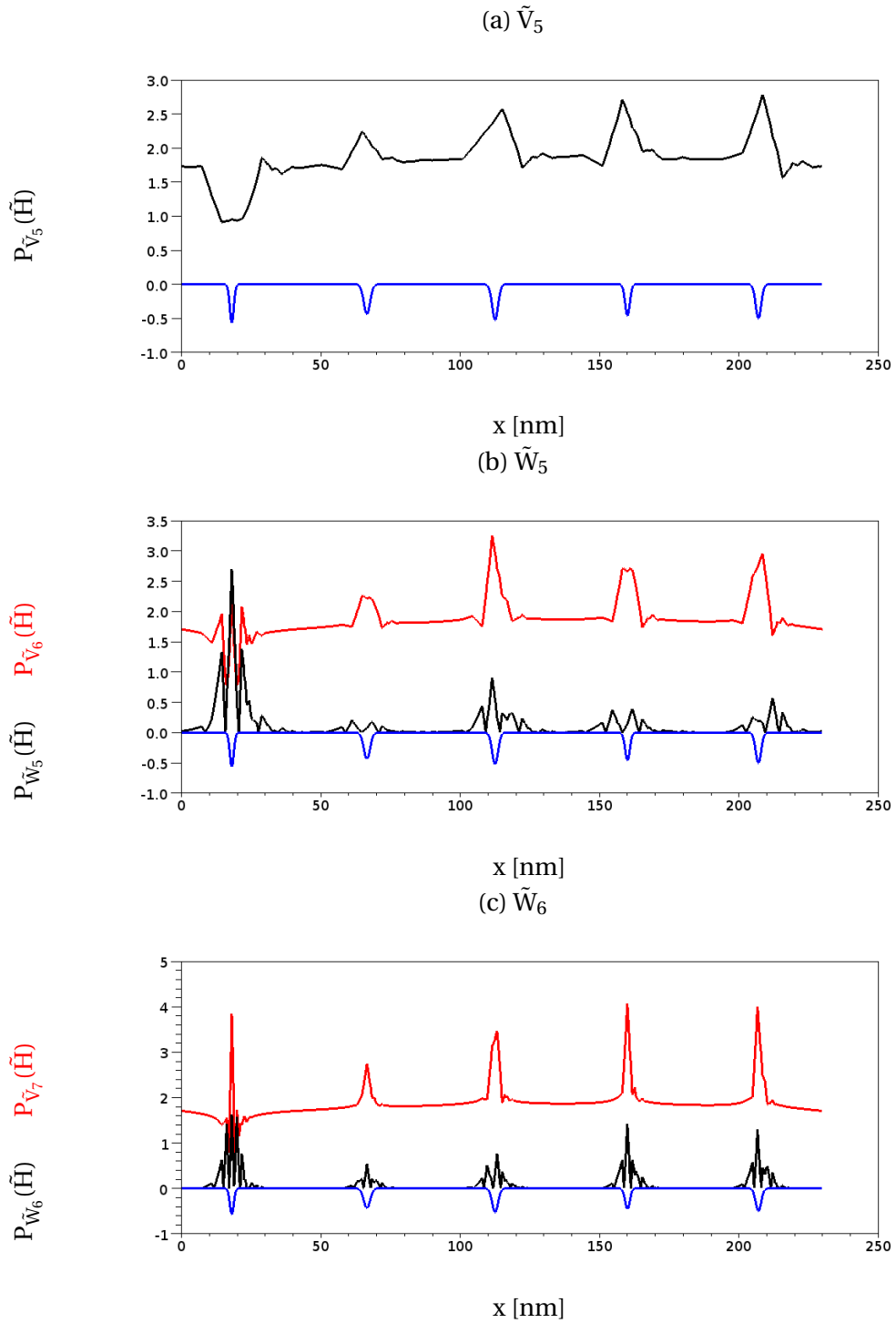
Figure 5.3: *(a) Projection* $P_{\tilde{V}_5}(\tilde{H})$ *of the source function* $\tilde{H}$ *calculated with the Maradudin method using* $N = 4096$ *points on the scalet subspace* $\tilde{V}_5$ *plotted in a black line as a function of the abscissa x. (b) The projection of* $\tilde{H}$ *on the wavelet subspace* $\tilde{W}_j$, $P_{\tilde{W}_j}(\tilde{H})$, *plotted in a black line, added to the projection* $P_{\tilde{V}_j}(\tilde{H})$ *on the complementary scalet subspace* $\tilde{V}_j$, *equals to the projection* $P_{\tilde{V}_{j+1}}(\tilde{H})$ *plotted in a red line for j=5. (c) Ibid for j=6. The wavelet is Daubechies 6. The grating and the conditions of incidence are the same than in figure 5.1.*

166
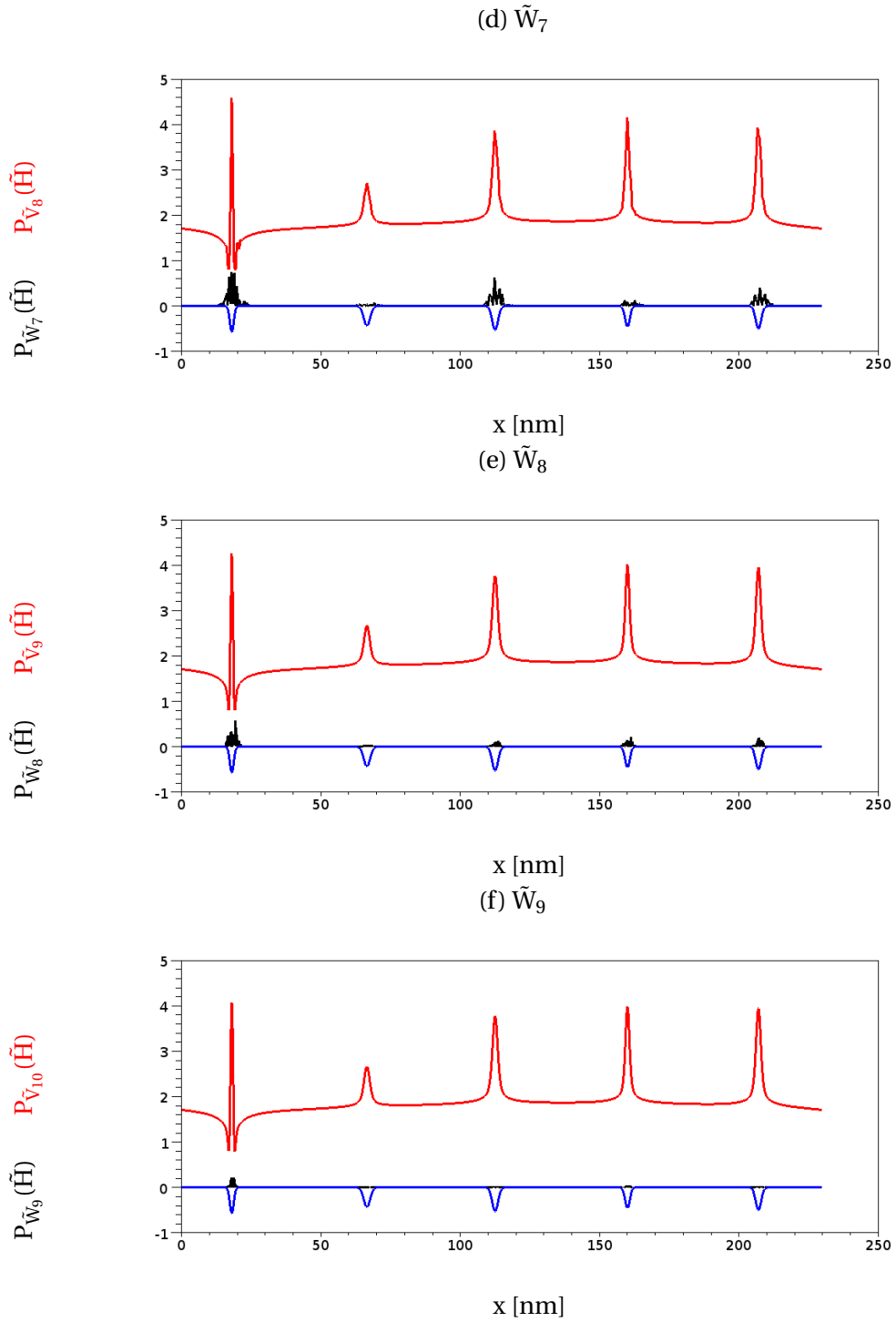
Figure 5.3: *Same as in figure 5.3. In (d) for j=7, in (e) for j=8 and in (f) for j=9.*
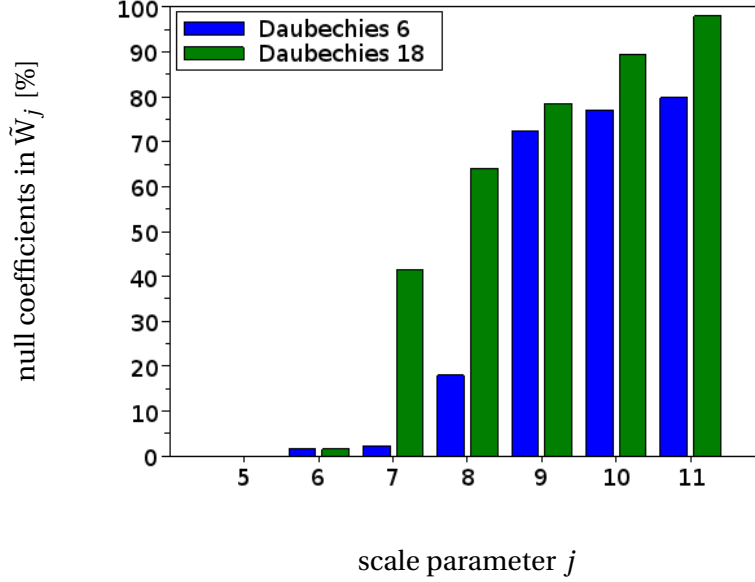
Figure 5.4: *Percentage of coefficients D_j^k whose modulus $\sqrt{2^j}|D_j^k|$ is less than 10^{-5} in the wavelet subspace $\tilde{W}_j$ of the wavelet decomposition of the source function $\tilde{H}$ calculated with* $N = 4096$ *points as a function of the scale parameter j from 5 to 11. The wavelet is Daubechies 6 (blue) and Daubechies 18 (green). The system is an incident plane wave of energy 2.13 eV and $\theta_i = 10°$ impinging on a silver grating of period d=230 nm with 5 Gaussian grooves.*

function $\tilde{H}$, we look for the number of coefficients which are null or negligible. The wavelet basis functions of the subspace $\tilde{W}_j$ has an amplitude $\sqrt{2^j}$ times larger than that of the subspace $\tilde{W}_0$. The coefficient D_j^k of the function projected on the subspace $\tilde{W}_j$ is responsible for a term of the order of magnitude of $\sqrt{2^j}|D_j^k|$ in the projection $P_{\tilde{W}_j}(\tilde{H})$. We therefore choose to consider the coefficients D_j^k whose modulus $\sqrt{2^j}|D_j^k|$ is less than 10^{-5} as null. 10^{-5} is chosen arbitrarily after having verified that the solution is not affected by the loss of those coefficients. The sparsity of the higher scale wavelet subspaces is evaluated by the percentage of coefficients D_j^k in the wavelet subspace $\tilde{W}_j$ which are considered null (as specified previously) out of the total number of coefficients in the subspace (which is equal to the dimension of the subspace), 2^j. This sparsity is plotted as a function of the scale parameter j in figure 5.4 for the same example as that of figure 5.1 with two Daubechies of order 6 and 18. First, we can immediately notice that as j increases, the sparsity also increases quickly. Secondly, we can see that the expansion in the higher order scale wavelet subspaces is more sparse for the Daubechies 18, between 80 and 90 % , than for the Daubechies 6, under 80 %. The wavelets of higher order approximate the smooth part of the source function $\tilde{H}$ with less wavelet subspaces and a very few number of coefficients is necessary to describe the details with a small resolution.

In this part we have only discussed the decomposition of $\tilde{H}$, but all the results are similar for the other source function $\gamma\tilde{L}$. To conclude, we have seen that the few coefficients D_j^k that are not null in the higher scale complementary wavelet subspaces $\tilde{W}_j$, come from the sharp variations of the source function at the location of the grooves. Where the profile varies quickly, so does the source function at or near a plasmonic resonance. Therefore, the only coefficients D_j^k of the wavelet children ψ_j^k that are necessary to describe the field accurately, are the ones whose intervals are not null around the shift $k/2^j$ approximately equal to the location of a groove. The expansion of the source functions $\tilde{H}$ and $\gamma\tilde{L}$ on a wavelet basis is thus sparse and the wavelet basis suited for the study of rough surfaces with sharp variations, even at nanometric scales. We believe that the sparsity of the wavelet decomposition may be used in order to reduce both the memory space and the time of the simulation.

In the next sections, we explore two different ways to take advantage of the sparsity of the representation of the field $\tilde{H}$ and $\gamma\tilde{L}$ for solving the surface integral equations.

5.2 The application of the wavelet transform to Fredholm integral equations of the second kind

The first method presented in this section, consists in applying a discrete wavelet transform to the dense matrix obtained from the surface integral equations. We investigate how to take advantage of the sparsity of the matrix in a wavelet basis, to improve the overall performances of the surface integral method. General technical aspects of this method are discussed in the literature like the needed storage and the computational cost in [142] or the wavelet choice in [143] where it is said that the compactly-supported wavelets of Daubechies are proved to be less costly in terms of matrix operations.

5.2.1 The method

Briefly, we recall how we have obtained the dense matrix of the surface integral method. The integral equations were discretized with a quadrature formula using the points $\left\{\vec{r}(t_m)\right\}_{m\in[0,N-1]}$ and evaluated at the same points $\left\{\vec{r}(t_n)\right\}_{n\in[0,N-1]}$. The set of linear equations on the values of the source functions H and γL at the point $\vec{r}(t_m)$ is put in the form of a matrix system, equation 5.1. We thus start again from the general system $MX = V$ previously obtained in chapter 2 with the matrix M, described by the equation 2.69, and the vectors X and V, described by the equation 2.68, and apply it to our particular case.

The Discrete Wavelet Transform (DWT), described in the section 4.5.2, retrieves the 2^J coefficients of the projection of a function f in $\tilde{V}_J$ from the 2^J values of f at the points of abscissa $n/2^J$ with $n \in [0,2^J[$. To be able to use the wavelet transform in the subspace $\tilde{V}_J$, the total number of points of the quadrature formula has to be a power of two i.e. $N_J = 2^J$.

Furthermore, the nth point of the quadrature formula taken at $\vec{r}(t_n)$ has to be equal to the nth point of the transform taken at the normalized abscissa $u_n = n/2^J$. Therefore, we substitute the points $\vec{r}(t_n) = (u_n d, y_D(u_n d))$ of the quadrature formula into the system, equations 2.69 and 2.68. The system to solve is $\forall n, m \in [0, 2^J[^2$ indexing each sub-matrix $K^\pm$ and $\partial K^\pm$ of the matrix

$$
\begin{bmatrix}
\partial K^+ \left(\frac{n}{2^J}, \frac{m}{2^J} \right) & K^+ \left(\frac{n}{2^J}, \frac{m}{2^J} \right) \\
\partial K^- \left(\frac{n}{2^J}, \frac{m}{2^J} \right) & K^- \left(\frac{n}{2^J}, \frac{m}{2^J} \right)
\end{bmatrix}
\begin{bmatrix}
H \left(\frac{m}{2^J} \right) \\
\gamma_m L \left(\frac{m}{2^J} \right)
\end{bmatrix}
=
\begin{bmatrix}
H_z^i \left(\frac{n}{2^J} \right) \\
0
\end{bmatrix}
$$

with

$$
\partial K^+ \left(\frac{n}{2^J}, \frac{m}{2^J} \right) =
\begin{cases}
\frac{1}{2} + L_m^+ + \gamma_n \frac{\partial G_d^+}{\partial \tilde{n}} (\vec{0}) \frac{d}{2^J} & n = m \\
\gamma_n \frac{\partial \tilde{G}^+}{\partial \tilde{n}} \left(\frac{m-n}{2^J} d, y_D \left(\frac{m}{2^J} d \right) - y_D \left(\frac{n}{2^J} d \right) \right) \frac{d}{2^J} & n \neq m
\end{cases}
$$

$$
K^+ \left(\frac{n}{2^J}, \frac{m}{2^J} \right) =
\begin{cases}
P_m^+ + \epsilon_+ G_d^+ (\vec{0}) \frac{d}{2^J} & n = m \\
\epsilon_+ \tilde{G}^+ \left(\frac{m-n}{2^J} d, y_D \left(\frac{m}{2^J} d \right) - y_D \left(\frac{n}{2^J} d \right) \right) \frac{d}{2^J} & n \neq m
\end{cases}
$$

$$
\partial K^- \left(\frac{n}{2^J}, \frac{m}{2^J} \right) =
\begin{cases}
-\frac{1}{2} + L_m^- + \gamma_n \frac{\partial G_d^-}{\partial \tilde{n}} (\vec{0}) \frac{d}{2^J} & n = m \\
\gamma_n \frac{\partial \tilde{G}^-}{\partial \tilde{n}} \left(\frac{m-n}{2^J} d, y_D \left(\frac{m}{2^J} d \right) - y_D \left(\frac{n}{2^J} d \right) \right) \frac{d}{2^J} & n \neq m
\end{cases}
$$

$$
K^- \left(\frac{n}{2^J}, \frac{m}{2^J} \right) =
\begin{cases}
P_m^- + \epsilon_- G_d^- (\vec{0}) \frac{d}{2^J} & n = m \\
\epsilon_- \tilde{G}^- \left(\frac{m-n}{2^J} d, y_D \left(\frac{m}{2^J} d \right) - y_D \left(\frac{n}{2^J} d \right) \right) \frac{d}{2^J} & n \neq m
\end{cases}
$$

and with $\gamma_n = \sqrt{(u_n d)^2 + (y_D(u_n d))^2}$, $H \left(\frac{m}{2^J} \right) = H(\vec{r}(t_m))$ and $L \left(\frac{m}{2^J} \right) = L(\vec{r}(t_m))$. The diagonal terms are composed of two terms (or three with the $\pm 1/2$) which come from the splitting of the Green function into the Green function $G^\pm$ in a non-periodic problem containing the singularity and the rest of it $G_d^\pm = \tilde{G}^\pm - G^\pm$. An analytical approximation of the piece of integral containing the singularity of the Green function or that of its derivative, appears in the form of $P_m^\pm$ or $L_m^\pm$ (equations 2.66 and 2.67). The discretization step $d \Delta u = d(u_{n+1} - u_n) = d 2^{-J}$ has already been replaced by its value in the equations.

The system has to be written as a function of the periodic unknowns $\tilde{H}$ and $\tilde{L}$ by introducing $e^{i\alpha_0 \frac{m}{2^J} d} e^{-i\alpha_0 \frac{m}{2^J} d} = 1$ in between the matrix term M(n,m) and the unknown term $H \left(\frac{m}{2^J} \right)$. The columns of the matrix indexed m are thus multiplied by $e^{i\alpha_0 \frac{m}{2^J} d}$ whereas the lines of the vector H indexed m are multiplied by $e^{-i\alpha_0 \frac{m}{2^J} d}$. Moreover, each line of the system is multiplied by $e^{-i\alpha_0 \frac{n}{2^J} d}$, in order to have a periodic incident field $\tilde{H}_z^i$ too. The periodized system is $\forall n, m \in [0, 2^J[^2$

$$
\begin{bmatrix}
\partial \tilde{K}^+ \left(\frac{n}{2^J}, \frac{m}{2^J} \right) & \tilde{K}^+ \left(\frac{n}{2^J}, \frac{m}{2^J} \right) \\
\partial \tilde{K}^- \left(\frac{n}{2^J}, \frac{m}{2^J} \right) & \tilde{K}^- \left(\frac{n}{2^J}, \frac{m}{2^J} \right)
\end{bmatrix}
\begin{bmatrix}
\tilde{H} \left(\frac{m}{2^J} \right) \\
\gamma_m \tilde{L} \left(\frac{m}{2^J} \right)
\end{bmatrix}
=
\begin{bmatrix}
\tilde{H}_z^i \left(\frac{n}{2^J} \right) \\
0
\end{bmatrix}
\tag{5.4}
$$

with $\tilde{K}^+ \left(\frac{n}{2^J}, \frac{m}{2^J} \right) = e^{-i\alpha_0 \frac{n}{2^J} d} K^+ \left(\frac{n}{2^J}, \frac{m}{2^J} \right) e^{i\alpha_0 \frac{m}{2^J} d}$. Now that the system is set up, we can apply the DWT to it.

The source functions $\tilde{H}$ and $\gamma\tilde{L}$ are expanded in $\tilde{V}_J$ with a depth of $J - J_0$. We call $\left[W_{J_0}^J(\tilde{H})\right]$ the vector composed of the coefficients of the decomposition of the source function $\tilde{H}$ in $\tilde{V}_J$ with a depth of $J - J_0$:

$$\left[\tilde{H}\left(\frac{m}{2^J}\right)\right] \xrightarrow{\text{DWT}} \left[W_{J_0}^J(\tilde{H})\right] = \left[C_{J_0}^k(\tilde{H}) \quad D_{J_0}^k(\tilde{H})\ldots D_{J-1}^k(\tilde{H})\right]^{\text{T}}$$

with T indicating a transpose vector. The transformation is thus in the matrix form:

$$\begin{bmatrix} \tilde{H}\left(\frac{m}{2^J}\right) \\ \gamma\tilde{L}\left(\frac{m}{2^J}\right) \end{bmatrix} = \begin{bmatrix} \text{DWT} & 0 \\ 0 & \text{DWT} \end{bmatrix} \begin{bmatrix} W_{J_0}^J(\tilde{H}) \\ W_{J_0}^J(\gamma\tilde{L}) \end{bmatrix} \quad . \tag{5.5}$$

The incident field is also expanded as

$$\begin{bmatrix} \text{DWT}^{-1} & 0 \\ 0 & \text{DWT}^{-1} \end{bmatrix} \begin{bmatrix} \tilde{H}_z^i\left(\frac{m}{2^J}\right) \\ 0 \end{bmatrix} = \begin{bmatrix} W_{J_0}^J(\tilde{H}_z^i) \\ 0 \end{bmatrix} \quad . \tag{5.6}$$

First, we substitute the vector of the expansion of the source functions in the wavelet basis, equation 5.5, into the system, equation 5.4. Then, the matrix of the inverse DWT is applied to the left of the system, equation 5.4. Finally, the multiplication of the matrix of the inverse DWT to the vector of the incident field, equation 5.6, is replaced to obtain a new system $M_W(J_0, J)W_{J_0}^J(X) = W_{J_0}^J(V)$ such that

$$M_W(J_0, J) = \begin{bmatrix} \text{DWT}^{-1} & 0 \\ 0 & \text{DWT}^{-1} \end{bmatrix} \begin{bmatrix} \partial\tilde{K}^+\left(\frac{l}{2^J}, \frac{m}{2^J}\right) & \tilde{K}^+\left(\frac{l}{2^J}, \frac{m}{2^J}\right) \\ \partial\tilde{K}^-\left(\frac{l}{2^J}, \frac{m}{2^J}\right) & \tilde{K}^-\left(\frac{l}{2^J}, \frac{m}{2^J}\right) \end{bmatrix} \begin{bmatrix} \text{DWT} & 0 \\ 0 & \text{DWT} \end{bmatrix} \quad . \tag{5.7}$$

The matrix $M_W(J_0, J)$ to solve is thus obtained by multiplying each sub-matrix $\tilde{K}^+$, $\tilde{K}^-$, $\partial\tilde{K}^+$ and $\partial\tilde{K}^-$ of the system by the DWT on the left and its inverse DWT^{-1} on the right (each sub-matrix is named after the function it contains). This operation is sketched in figure 5.5 (a). The functions $\tilde{K}^{\pm}(u, u')$ are thus projected on the scalet and the complementary wavelet subspaces with respect to the variable u (resp. u') by the multiplication of the inverse wavelet transform matrix DWT^{-1} with the matrix of $\tilde{K}^{\pm}$ (resp. that of the matrix of $\tilde{K}^{\pm}$ with the wavelet transform matrix DWT). The horizontal divisions in the matrix $\text{DWT}^{-1}\tilde{K}\text{DWT}$ thus split the matrix in different blocks, each one of those blocks corresponding to the projection of $\tilde{K}$ on each of the scalet and wavelet subspaces with respect to u. At the same time, the vertical division split the matrix $\text{DWT}^{-1}\tilde{K}\text{DWT}$ in blocks corresponding to the projection of $\tilde{K}$ on each of the scalet and wavelet subspaces with respect to u'. The structure of the transformed matrix $M_W(J_0, J)$ is thus composed of squares and rectangles of size 2^j by $2^{j'}$ which contain the projection of each sub-matrix of M on the subspaces $\tilde{W}_j$ and $\tilde{W}_{j'}$ (or the scalet subspace $\tilde{V}_{J_0}$) with respect to u and u' respectively. The matrix terms, indexed (k, k') within the rectangle associated to $\tilde{W}_j$ and $\tilde{W}_{j'}$, is $< \tilde{\psi}_j^k(u)|K(u, u')|\tilde{\psi}_{j'}^{k'}(u') >$. In the sketch, the projection of $\tilde{K}$ on the wavelet subspace $\tilde{W}_{J_0+1}$ with respect to u, is the multiplication of the matrix $\tilde{K}$ by the red block in the DWT^{-1} matrix. In the same way, the
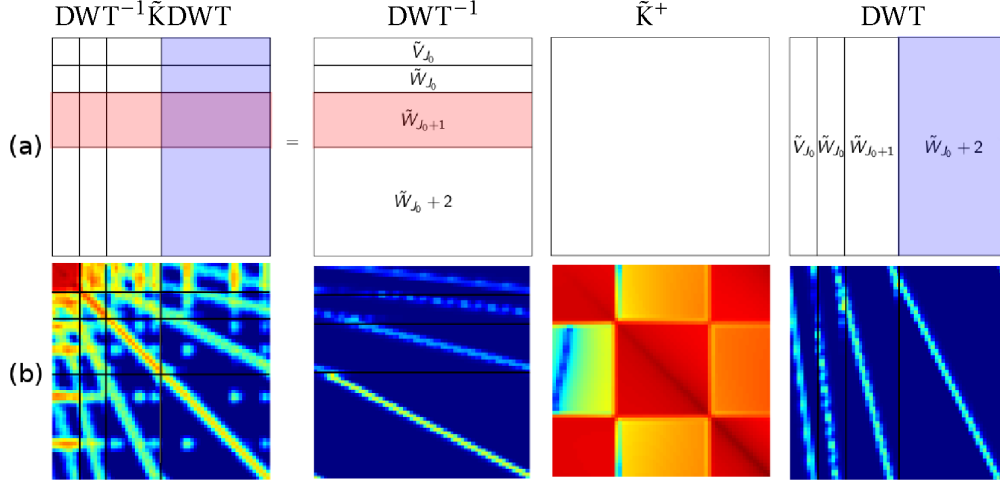
Figure 5.5: *(a) Sketch of the wavelet transform of one matrix K, equation 5.7, with J=6, $J_0=3$. (b) One example of matrices with the Daubechies 6 wavelet. The imaginary part of $\left(\tilde{K}^+\left(\frac{l}{2^j}, \frac{m}{2^j}\right)\right)$ is shown in logarithmic scale as well as its transformed counterpart (The color scale varies from 10^{-2} (red) to 10^{-6} (blue)). $\tilde{K}^+$ was calculated for a plane wave ($\theta_i = 7.5°$, $\lambda^{-1} = 2500\ cm^{-1}$) impinging on a gold grating of period d=1.75 μm with rectangular grooves (w=0.75 μm and h=1 μm).*

projection of $\tilde{K}$ on $\tilde{W}_{J_0+2}$ with respect to u' is the multiplication of the matrix $\tilde{K}$ by the blue block in the DWT matrix. Finally, the projection of $\tilde{K}$ on $\tilde{W}_{J_0+1}$ and $\tilde{W}_{J_0+2}$ yields a purple block of size $2^{J_0+1} \times 2^{J_0+2}$ in the $DWT^{-1}\tilde{K}DWT$ matrix ($\langle \tilde{W}_{J_0+1}|\tilde{K}^+|\tilde{W}_{J_0+2}\rangle$).

In order to illustrate this point, the wavelet transform performed on a quarter of the matrix, $\tilde{K}^+$, corresponding to the system of a plane wave of wavenumber $\lambda^{-1} = 2500\ cm^{-1}$ impinging with an angle $\theta_i = 7.5°$ on a gold grating of period d=1.75 μm with rectangular grooves (w=0.75 μm and h=1 μm) is shown in figure 5.5(b). The projection of the matrix $\tilde{K}^+$ on the scalet subspace $\tilde{V}_{J_0}$ with respect to u and u' ($\langle \tilde{V}_{J_0}|\tilde{K}^+|\tilde{V}_{J_0}\rangle$) results in the top-left square corner in the matrix $DWT^{-1}\tilde{K}DWT$. This square, in a bright red color in figure 5.5(b), has the largest terms in the matrix and no terms equal to zero. This is not surprising as the decomposition on a scalet subspace is not sparse. On the contrary, the bottom-right square corner corresponds to the projections on the largest scale subspaces ($\langle \tilde{W}_{J_0+2}|\tilde{K}^+|\tilde{W}_{J_0+2}\rangle$) is the more sparse. Attention must be paid here to the fact that a numerical threshold is needed in order to decide at which scale a quantity is negligible and can be considered as null. In this particular case, all the terms less than 10^{-6} were set to zero.

Once the system is solved, the values of the source functions are evaluated in the interval [0,1[by performing once more an inverse wavelet transform corresponding to the equation 5.5. The solution obtained through a wavelet transform depends on the threshold chosen for the terms that are put to zero and thus on the sparsity of the matrix. In the next paragraph, we comment on the precision of the solutions and the sparsity of the matrix.

172

5.2.2 The sparsity

We briefly saw in the last paragraph that the matrix M_W, which is the result of the wavelet transformation of M, has many null or negligible terms. The question that arises is, therefore, for which condition a term is considered negligible. The main goal of this paragraph is thus to study how the setting to zero of some terms in the matrix M_W, impacts the error of the solution $\tilde{H}$.

The threshold, below which the terms of the matrix are considered negligible and thus set to zero, is the variable here. Let us define the threshold T such that all the terms of the matrix M_W whose modulus is less than T are set to zero i.e. $\forall n, m \in [0, N[^2$

$$\text{if} \quad |M_W(n, m)| < T \qquad \text{then} \quad M_W(n, m) = 0 \quad .$$

To examine the consequence of setting a threshold T, we calculate the source functions using a wavelet transform for different thresholds T. We then address the question of the admissible threshold. The admissible threshold does not change the error that is made with and without wavelets relatively to the physical solution.

We choose to return to the same example the convergence was studied with, in the section 2.5.2.1. The system, once again, is a plane wave of wavenumber $\lambda^{-1} = 2030$ cm^{-1} impinging with an angle $\theta_i = 7.5°$ on a gold grating of period d=1.75 μm with rectangular grooves (w=0.75 μm and h=1 μm). As in figure 5.5, we used the Daubechies 6 wavelet and the starting scale $J_0 = 3$ which is equal to the minimum scale J_{min} for which the basis of the periodic scalet of order D=6 exists. We investigate here the best case scenario because we choose J_0 to be the lowest scale parameter possible. Indeed the blocks of size $2^{J_0} \times 2^{J_0}$ of the matrix $M_W(J_0, J)$ corresponding to the projection of M on the scalet subspaces ($\langle \tilde{V}_{J_0} | \tilde{K}^\pm | \tilde{V}_{J_0} \rangle$ and $\langle \tilde{V}_{J_0} | \partial \tilde{K}^\pm | \tilde{V}_{J_0} \rangle$) are dense whereas the blocks of the projection on the wavelet subspaces are sparse. The smaller the starting scale 2^{J_0} is chosen to be, the smaller is the dense block.

We calculate a reference source function $\tilde{H}_{N_J}$ by the Maradudin method using $N_J = 2^J$ points. From the corresponding matrix M of size $2N_J$, we calculate the matrix $M_W(J_0, J)$ using the wavelet transform DWT, and apply a threshold T to the matrix by setting all the terms less than the threshold to zero. Next, the system in the wavelet basis is solved and we obtain the solution $\tilde{H}_{N_J T}$ by applying the inverse wavelet transform. $\tilde{H}_{N_J T}$ is the source function $\tilde{H}$ calculated with a system of size $2N_J$ using a wavelet transformation and a threshold T. We want to compare the source functions $\tilde{H}_{N_J T}$ to the source function $\tilde{H}_{N_J}$, for the same number of points N_J, using different thresholds. The relative error of $\tilde{H}_{N_J T}$ compared with $\tilde{H}_{N_J}$ is then averaged over the interval [0,1[such as:

$$\overline{\left| \frac{\tilde{H}_{N_J T} - \tilde{H}_{N_J}}{\tilde{H}_{N_J}} \right|} = \frac{1}{N_J} \sum_{n=0}^{N_J-1} \left| \frac{\tilde{H}_{N_J T}\left(\frac{n}{2^J}d, y_D\left(\frac{n}{2^J}d\right)\right) - \tilde{H}_{N_J}\left(\frac{n}{2^J}d, y_D\left(\frac{n}{2^J}d\right)\right)}{\tilde{H}_{N_J}\left(\frac{n}{2^J}d, y_D\left(\frac{n}{2^J}d\right)\right)} \right| \quad .$$

Let us note that if no threshold is applied, the two source functions, with and without wavelets, are exactly the same as expected when a change of basis is performed.

The relative error of $\tilde{H}_{N_J T}$ compared with $\tilde{H}_{N_J}$ is plotted in a logarithmic scale, as a function of the number of points N_J used for the discretization, in figure 5.6(a). The relative error of $\tilde{H}_{N_J T}$ for decreasing thresholds from 10^{-2} to 10^{-5} are plotted together in orange to brown. The larger the threshold is set, the larger the relative error is and the solution is thus less accurate. We notice that in the range of the number of points N_J studied, the error is quite constant as a function of the number of points N_J.
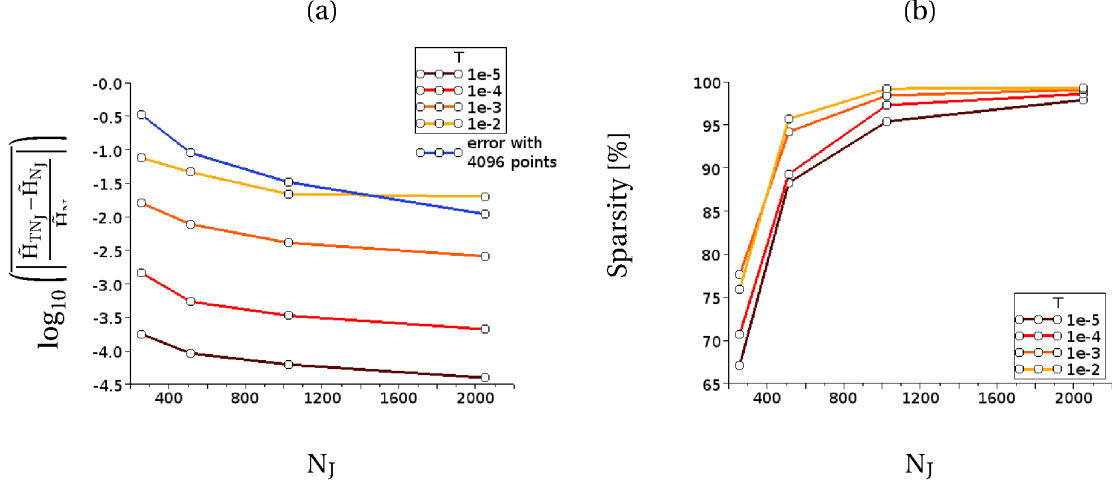
Figure 5.6: *(a) Spatial mean of the relative error of the modulus of the source function $\tilde{H}_T$ in a logarithmic scale as a function of the number of points N_J for different values of the threshold T. The blue curve is $\log_{10}\left(\left\|\frac{\tilde{H}_{N_J}-\tilde{H}_{4096}}{\tilde{H}_{4096}}\right\|\right)$. (b) Percentage of null-terms in the matrix. Example for a gold grating of period $d=1.75\ \mu m$ with rectangular grooves ($w=0.75\ \mu m$ and $h=1\ \mu m$) at incident conditions $\theta_i = 7.5°$, $1/\lambda = 2030\ cm^{-1}$.*

We also plotted in blue the spatial average of the relative error of $\tilde{H}_{N_J}$ compared with $\tilde{H}_{4096}$ $\left(\left\|\frac{\tilde{H}_{N_J}-\tilde{H}_{4096}}{\tilde{H}_{4096}}\right\|\right)$ as a function of N_J in figure 5.6(a). The relative error of $\tilde{H}_{N_J T}$ compared with $\tilde{H}_{4096}$ may be related to that of $\tilde{H}_{N_J}$ compared with $\tilde{H}_{4096}$. As $\tilde{H}_{N_J T} - \tilde{H}_{4096} = \tilde{H}_{N_J T} - \tilde{H}_{N_J} + \tilde{H}_{N_J} - \tilde{H}_{4096}$ and assuming $|\tilde{H}_{N_J}| \simeq |\tilde{H}_{4096}|$ which is confirmed by the blue curve in figure 5.6(a), we have:

$$\left|\frac{\tilde{H}_{N_J T} - \tilde{H}_{4096}}{\tilde{H}_{4096}}\right| < \underbrace{\left|\frac{\tilde{H}_{N_J T} - \tilde{H}_{N_J}}{\tilde{H}_{N_J}}\right|}_{10^{-2}-10^{-4}} + \underbrace{\left|\frac{\tilde{H}_{N_J} - \tilde{H}_{4096}}{\tilde{H}_{4096}}\right|}_{10^{-1}-10^{-2}} \ .$$

As long as the relative error of $\tilde{H}_{N_J T}$ compared with $\tilde{H}_{N_J}$ is one or two orders of magnitude lower than the relative error of $\tilde{H}_{N_J}$ compared with $\tilde{H}_{4096}$, we consider that

$$\left|\frac{\tilde{H}_{N_J T} - \tilde{H}_{4096}}{\tilde{H}_{4096}}\right| \approx \left|\frac{\tilde{H}_{N_J} - \tilde{H}_{4096}}{\tilde{H}_{4096}}\right| \ .$$

174

$\tilde{H}_{N_J T}$ is the same as $\tilde{H}_{N_J}$ in the point of view of $\tilde{H}_{4096}$. The two solutions $\tilde{H}_{N_J T}$ and $\tilde{H}_{N_J}$ have converged towards the solution $\tilde{H}_{4096}$ with the same accuracy. We can see in figure 5.6(a) that the curves corresponding to the threshold T between 10^{-3} and 10^{-5} (orange to brown curves) are at least one order of magnitude below the relative error of $\tilde{H}_{N_J}$ compared with $\tilde{H}_{4096}$ (blue curve) except for the largest number of points 2048. For a number of points less than 2048, a threshold T=10^{-3} is enough to retrieve the same result with or without wavelets, whereas for the largest number of points in the figure, 2048, the threshold T can be 10^{-4} or lower. If the number of points N_J increases, the source function is more accurate. The accuracy of the terms in the matrix must therefore increase accordingly, less terms have to be neglected and the threshold must be lower. Now, we look at the influence of the threshold T on the sparsity of the matrix M_W.

Let us define the sparsity of the matrix M_W as the percentage of the terms which are below the threshold T out of all the terms in the matrix ($4N_J{}^2$). The sparsity of the matrix M_W is plotted as a function of the number of points N_J in figure 5.6(b). The sparsity for different thresholds is plotted in orange to brown with the same color as in figure 5.6(a). When doubling the number of points N_J to N_{J+1}, the decomposition in an additional complementary wavelet space whose size is N_J is more sparse than the decomposition in the wavelet subspaces of lower scales since it only contains the difference with the previous scale. Therefore, in order to have sparse matrices, whose sparsity is over 90%, a high number of points N_J have to be used. As the main goal is to employ wavelets for large scale systems, i.e. for a number of points N_J larger than 2048, the sparsity of the matrix is expected to be larger than 90% in any case. For N_J=1028, the sparsity is around 95% whatever the threshold T is chosen to be. The choice of the threshold could then seem irrelevant. A difference of several percent is, however, of significance when dealing with millions of terms in the matrices as it is the case. If the threshold T is higher, more terms are set to zero in the matrix and the sparsity of the matrix M_W is naturally larger. By choosing a higher threshold, however, the accuracy of the solution decrease as shown by the increase in the relative error of $\tilde{H}_{N_J T}$ compared with $\tilde{H}_{N_J}$ in figure 5.6(a). A balance has therefore to be found between the memory gain which comes from a larger number of terms set to zero in the matrix and the larger error of the solution induced by neglecting more terms in the matrix.

To summarize, the threshold has to be chosen as high as possible, as long as the solution is not affected by the setting to zero of the terms in the matrix. A sparsity higher than 90% is obtained with a threshold of 10^{-4} without sacrificing the accuracy of the solution for a number of points used superior to 1024.

We ensured that we can obtain an accurate solution by using the wavelet transform. Now, we want to know what we can gain from this approach by studying the memory space and the number of cycles compared to the ones of the standard method using the same number of points.

5.2.3 Discussion on the memory space and the time requirements

In this section, we comment on the evaluation of the memory space and the time necessary for: 1) the calculation of the matrix $M_W(J_0,J)$ and 2) the resolution of the system $M_W(J_0,J)W_{J_0}^J (X) = W_{J_0}^J (V)$ with 2N unknowns. The first step is achieved by applying a wavelet transform to each quarter of the matrix of the Maradudin method M, $\tilde{K}^\pm$ and $\partial\tilde{K}^\pm$, as in equation 5.7. In a general manner, we call G a quarter of M (G is $\tilde{K}^\pm$ or $\partial\tilde{K}^\pm$) which is a N by N matrix. The wavelet transform of G gives a sparse matrix DWT^{-1} G DWT with DWT the Discrete Wavelet Transform matrix as shown in figure 5.7.

Figure 5.7: *Sketch of the multiplication of the DWT matrix and its inverse in order to obtain the matrix in the wavelet basis* M_W.

The Sparse matrix class of the Eigen library was chosen to store the sparse matrices in the C++ program. The storage is done by Compressed Column (or Row) Storage scheme. The values of the nonzero terms of the matrix as well as the indexes of their row (or column) are stored in two arrays. A third array indicates where to find the first nonzero term of each column (or row) by storing the index of its position in the two arrays. We thus assume that the memory space occupied by a sparse matrix is proportional to its number of nonzero terms.

The first remark in the discussion is that the dense matrix containing $\tilde{K}^\pm$ and $\partial\tilde{K}^\pm$ has to be calculated first, before calculating the sparse one. The time to fill the dense matrix is, naturally, the same in both methods. The time of the multiplications in order to obtain the sparse matrix is added to the time to fill the matrix. As the wavelet transform matrices are sparse with a number of terms proportional to the number of points N, the time spent for the multiplication is proportional to $N^2 \log N$ [68]. The time to calculate the matrix when one uses wavelets is therefore longer itself. This additional time may be compensated by saving some time during the resolution which is an operation taking a time usually proportional to N^3 for a dense square matrix of size N.

The second step after the calculation of the sparse matrix M_W is the resolution of the system $M_W(J_0,J)W_{J_0}^J (X) = W_{J_0}^J (V)$. In order to improve the speed of the resolution, iterative methods which are specific to sparse matrices have to be used. The one that is mainly used in the literature is the stabilized variant of the bi-conjugated gradient method iterative solver

named Bi-CGSTAB [144]. In a nutshell, the Bi-CGSTAB solver searches for the solution X of the system MX=V by reducing iteratively the residual V-MX$_i$ starting from an initial guess X$_0$. Each step determines a new direction p_i orthogonal to the residual with the help of a preconditioner and then adds it to X$_i$ to determine X$_{i+1}$. Using a Bi-CGSTAB solver for the Method of Moment impedance matrix sparsified with wavelets is very beneficial according to Pan [132]. Although the iterative method are now more reliable than ever, their use requires an expertise in the choice of the preconditioner and the performances may vary greatly depending on the initial solution that is given. There was not enough time to acquire that expertise in the last months of this PhD. Without the use of an iterative method for the resolution of the matrix M$_W$, the time spent to calculate the matrix M$_W$ being always longer than the time spent to calculate the matrix M of the Maradudin method, the resolution of the problem with a wavelet transform is more costly in time than the resolution of the problem without wavelets.

As for the gain in memory space, the way to calculate the sparse matrix M$_W$ has to be looked over carefully. If the calculation, and therefore storage, of the matrix G is done prior to the multiplications, there is no definite gain in memory space. Let us explain why. The fastest way to calculate a quarter of the sparse matrix M$_W$, is to first fill a quarter of the matrix of the Maradudin method G, next, to multiply it on the right by the DWT matrix and eventually to multiply the product by the inverse of the DWT matrix on the left as shown in figure 5.7. In that scenario, a quarter of the matrix in the Maradudin method is stored at once as well as the non-sparse intermediary result G DWT. A memory space of 2N^2 is thus occupied. If one wants to sparsify the dense matrix of the Maradudin method with the wavelets in that way, there is only a gain of factor 2 in the occupied memory space in comparison with the Maradudin method whose dense matrix requires storing 4N^2 terms. We therefore looked for another way to calculate the sparse matrix M$_W$ (step1) where the matrix G is not stored all at once and calculated only once. We examine the performances in time and memory space since the gain in memory space can be accompanied by a longer calculation and inversely.

In that method, in order to save some memory space occupied in the random access memory (RAM), the memory which is easily accessed by the processor, some matrices are stored in an exterior file on the hard drive. We note that the calculation done by the processor requires that all the terms necessary for the calculation are stored in the RAM. If the terms of a matrix are stored in an exterior file, they have to be retrieved from the hard drive and stored in the RAM before being used. Moreover, to access the data on the hard drive takes a longer time than to access them in the RAM. Let us now describe this method shown in figure 5.8. The first multiplication of G and DWT is done by calculating the product of a row-vector of G (green horizontal line) with the sparse matrix DWT (blue vertical lines) and to immediately store the obtained row-vector of G DWT in a exterior file (green vertical dashed line) and to repeat the operation for each row. In that way, only a row-vector of N terms of G is stored at a given time in the RAM and each row of G is calculated only once. The whole matrix G DWT is calculated and stored in an exterior file line by line. The left
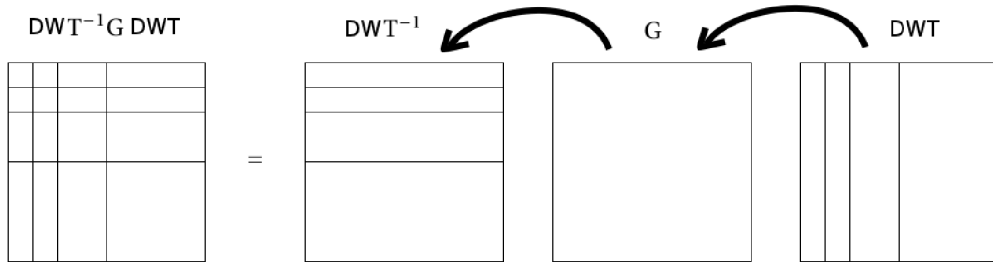
177
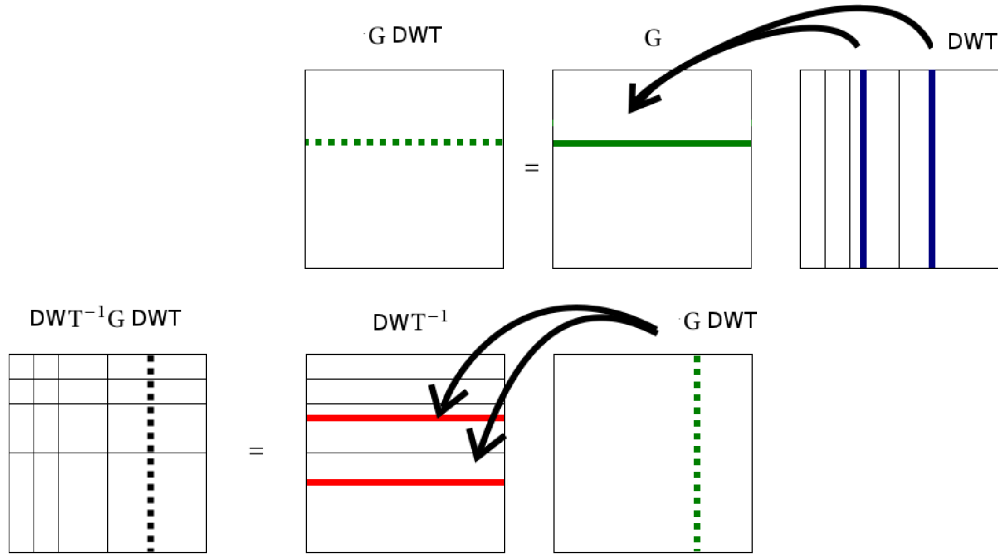
Figure 5.8: *Sketch of the multiplication of the DWT matrix and its inverse in order to obtain the matrix in the wavelet basis* M_W. *The blue and red lines are the columns of the DWT matrix and the rows of the* DWT^{-1} *matrix respectively. The green solid line is a row of the submatrices of* M_W *denoted G. The green dashed lines are a row or a column in the matrix* $G\,DWT$, *stored in an exterior file. The black dashed line is a column of the matrix* $DWT^{-1}\,G\,DWT$.

multiplication is done in a similar way by retrieving the matrix G DWT column by column from the exterior file. A vector-column of G DWT (green horizontal dashed line) is multiplied with DWT^{-1} on the left (red horizontal lines) which gives a vector-column of $DWT^{-1}\,G\,DWT$ (black vertical dashed line). The relevant terms of the vector-column of $DWT^{-1}\,G\,DWT$, the ones superior to the chosen threshold, are stored in the final matrix M_W.

In that scenario, the memory space necessary to calculate the final matrix M_W, is the memory space occupied by the sparse wavelet transform matrices (a number of terms proportional to N) and the memory space occupied by each of the sparse matrix $DWT^{-1}\,G\,DWT$ (a number of terms proportional to N log N) [68]. A lot of memory space is saved in that method since the wavelet transform matrices have a number of terms negligible compared with the final matrix M_W and the matrix G is not stored. The occupied memory space in this method is thus equivalent to that of the sparse matrix M_W. Despite a definite gain of memory space, this method is longer than the one that does directly the multiplication with the matrix G stored. The time spent to calculate the matrix $DWT^{-1}\,G\,DWT$ is the time spent to do the multiplication added with the time spent to store the intermediary matrix G DWT in an exterior file and to retrieve it. This method of calculation of the sparse matrix M_W is thus quite time-consuming but it offers a compromise between the time spent and the memory space occupied.

We have seen how to save memory space using the wavelet transforms with the SIE, by

storing only the sparse matrix M_W (N log N terms) compared with the Maradudin method whose matrix M is dense (N^2 terms). However, this method is very time-consuming and it does not make the most of the particular wavelets decomposition. In the next section, we shall give a proposal of application of the wavelet transform to optimize the number of points needed to solve the problem.

5.2.4   An optimization of the number of unknowns

As stated in the previous section 5.1.2, the level of detail needed to describe the source functions depends on the abscissa x which scans the profile of the surface. Indeed, we have seen that the source functions $\tilde{H}$ and $\gamma\tilde{L}$ have to be decomposed on higher scale wavelet subspaces where the field varies more abruptly. An optimization of the number of unknowns in the wavelet method may be done by changing the highest scale of the expansion as a function of the abscissa. Equivalently, the step of the dicretization of the surface in the Maradudin method needs to be smaller at the location of the abrupt variations of the field. In that case, the optimization of the number of unknowns consists in changing the discretization step as a function of the abscissa. In this section, we want to compare the optimization of the number of unknowns in the wavelet and the Maradudin method. Both methods can be considered as an optimization of the mesh. In the case of the Maradudin method it is literally the case. In the case of the wavelet method, the distance between two basis functions of the subspace of scale 2^J is $1/2^J$. Therefore, expanding the source function on more complementary wavelet subspaces at specific locations over the surface is equivalent to decrease the size of the discretization step at these specific locations. This second optimization of the number of unknowns with the use of the wavelets may therefore be considered as an optimization of the mesh.

In order to compare both strategies, let us come back to the example of the first section. We looked closely at the source function $\tilde{H}$ for an incident plane wave of energy 2.13 eV and $\theta_i = 10°$ impinging on a silver grating with a period equal to 230 nm with five defects which are Gaussian grooves whose dimensions are 1-2 nm for the width and 10-13 nm for the height at an abscissa 18, 67, 112, 160 and 207 nm. The source functions, as shown in figure 5.1, varies at the location of the Gaussian grooves and both methods focus the efforts on the areas of the grooves.

5.2.4.1   An optimization of the mesh

One way to reduce the number N of points of the resolution is to adapt the mesh. The discretization step has to be smaller where the variations of the source function $\tilde{H}$ are the more important, at the location of the groove. We use two discretization steps Δ and Δ^+, the first one on the flat surface and the second one at the location of the groove and choose Δ^+ to be smaller than Δ. The mesh is then refined by using the smaller step Δ^+ on an interval of

length l centered at the middle of the ith groove whose abscissa is called x_i. This interval is called $L_i = [x_i - l/2, x_i + l/2]$. The integral equations to solve (equation 2.59 and equation 2.60) are split in two parts. The first part is composed of the integral over the intervals L_i and the second part is the rest of the integral. A quadrature formula (the quadrature of rectangle in our case) is applied to the two parts using two different steps Δ^+ and Δ respectively such that

$$\int_0^d f\left(x',x\right)dx = \underbrace{\int_{\cup_{i=1}^5 L_i} f\left(x',x\right)dx}_{\Delta^+ \sum_n f\left(x',x_n^+\right)} + \underbrace{\int_{[0,d[\setminus\cup_{i=1}^5 L_i} f\left(x',x\right)dx}_{\Delta \sum_n f\left(x',x_n\right)}$$

$$x_{n+1}^+ = x_n^+ + \Delta^+ \qquad\qquad x_{n+1} = x_n + \Delta$$

where d is the period of the grating and $f(x',x)$ represent the integrated function, similarly to equation 2.62.

A simulation is therefore defined by the choice of the length l of the interval L_i and two discretization steps Δ and Δ^+. The intervals L_i are represented in figure 5.9 for three different lengths l=3 nm (blue), l=6 nm (green) and l=12 nm (black). For each length l, we solve numerically the integral equations using the Maradudin method with two different discretization steps and we obtain the source function $\tilde{H}_l$. The simulation is done for the system of the first section (described in figure 5.1). On the flat surface the discretization step Δ is chosen to be d/256. The choice of Δ is based on the fact that the smooth part of $\tilde{H}$ can be reproduced with 256 points as shown in figure 5.1(d). The discretization step Δ^+ in the intervals is increased from d/256 to d/8192. Only two cases are shown here Δ^+=d/4096 (Δ/16) and Δ^+=d/8192 (Δ/32) for which Δ^+ matches the discretization step of the solutions calculated by the Maradudin method with 4096 and 8192 points. The total number of unknowns N_{mesh} depending on the discretization steps Δ and Δ^+ and the length l is indicated in table 5.1.

legend	width l [nm]	discretization step Δ	smaller step Δ^+	N_{mesh}
482	3	d/256	d/4096	482
723			d/8292	723
717	6	d/256	d/4096	717
1209			d/8292	1209
1232	12	d/256	d/4096	1232
2273			d/8292	2273

Table 5.1: *Steps chosen on the flat surface and in the intervals around the grooves and resulting number of unknowns* N_{mesh} *for the different lengths l.*

At a fixed length l, if the discretization step Δ^+ is decreased from d/256 to d/8192 in the simulation, the solutions $\tilde{H}_l$ converge toward the ones obtained with the smaller discretization step Δ^+=d/8192. The source function $\tilde{H}_l$ obtained by increasing the number of points
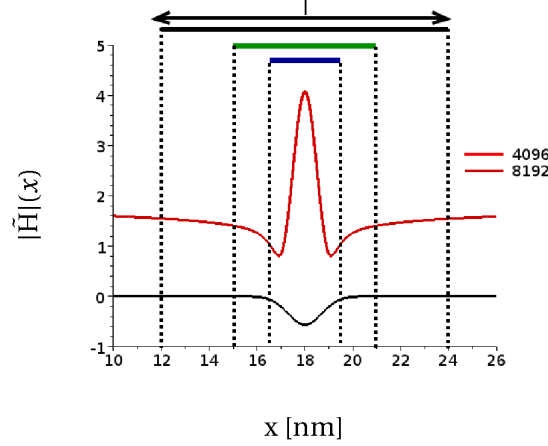
Figure 5.9: *Close-up of figure 5.1. The profile of the grating (blue line) is in arbitrary units. The intervals $[x_i - l/2, x_i + l/2]$ are represented by a bar for three different lengths l=3 (blue), l=6 (green) and l=12 nm (black). The limits of the intervals are represented by dashed lines .*

at the location of the grooves for the different cases indicated in table 5.1 are plotted in figure 5.10. As a comparison, we plot in the same figure the source function $\tilde{H}_{ref}$ calculated by the Maradudin method with N equally spaced points for N=4096 and N=8192. One can see that the solutions with $\Delta^+=d/4096$ and $\Delta^+=d/8192$ of the same length l (similar colors) almost superimpose in the close-ups, figure 5.10(b,c). By increasing the length l around the groove where the mesh is refined, the obtained $\tilde{H}_l$ is closer to $\tilde{H}_{ref}$. The source function $\tilde{H}_l$ obtained with a length l of 3 (blue lines) and 6 nm (green lines) are not matching with $\tilde{H}_{ref}$ obtained with a single discretization step $\Delta=d/8192$ (red lines) whereas the source function obtained with a length l of 12 nm (black lines) is. The close-ups, figure 5.10(b,c), show that the source function $\tilde{H}_l$ obtained with a length l=12 nm and the smallest discretization step $\Delta^+=d/8192$ (darkest black line), which requires $N_{mesh} = 2273$, almost superimposes the solution $\tilde{H}_{ref}$ obtained with N=4096 points (red line). The ratio between the number of unknowns required to solve the problem, N_{mesh} and N, is then only two.

Changing the discretization step as a function of the abscissa x in the Maradudin method can decrease the required number of unknowns, but in our example it is only divided by two. The area where the mesh is refined has to be large enough in order for the solution to be accurate and the benefits are then quite low. We believe it is possible to solve the problem with less unknowns by using the wavelets.

5.2.4.2 Adjusting the wavelet expansions

In the wavelet space, the decomposition of the source functions in different levels of detail offers new perspectives in order to adapt the accuracy of the description of the source functions over the surface profile. An exploratory work has been done in order to reduce the

181
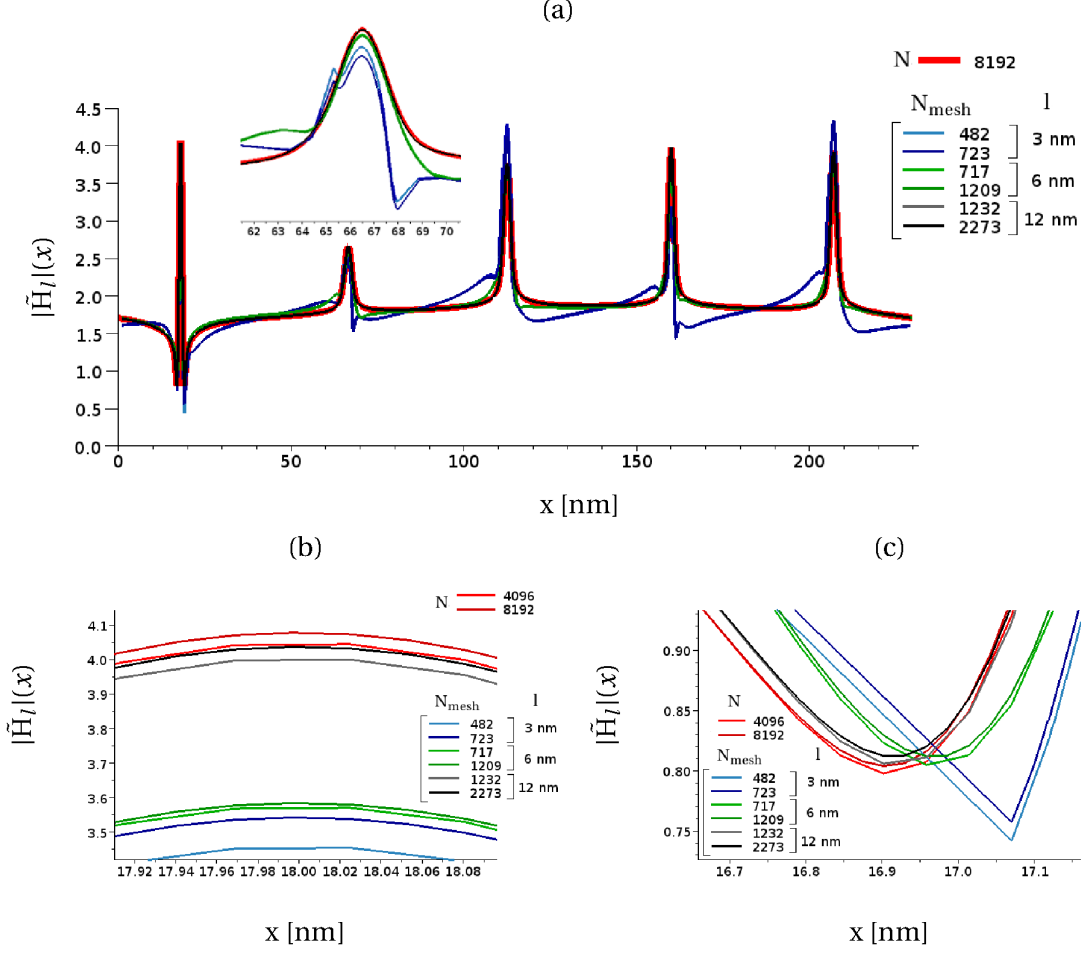
Figure 5.10: *(a) Modulus of the source function $|\tilde{H}_l|$ calculated by the surface integral method with the mesh described in table 5.1 for an incident plane wave of energy 2.13 eV and $\theta_i = 10°$ impinging on a silver grating of period d=230 nm with 5 Gaussian grooves. The modulus of the source function $|\tilde{H}_{ref}|$ calculated by the Maradudin method with N=4096 and N=8192 equally spaced points is represented with red lines. (b) and (c) close-ups.*

number N of unknowns which describes the source functions by using the wavelet transform approach. In the section 5.1.2, we saw that the projection of $\tilde{H}$ on the higher scale wavelet subspaces is highly localized at the location of the grooves. Since the support of the wavelet basis functions $\tilde{\psi}_j^k$ is $\left[\frac{k_0+k}{2^j}, \frac{k_0+k+D-1}{2^j}\right]$ (repeated periodically with a period of one), the basis functions are also localized around $k/2^j$ spread over a length $(D-1)/2^j$. A few wavelet basis functions are thus needed to describe the projection of $\tilde{H}$ in $\tilde{W}_j$. In the case of the Daubechies, $k_0=0$. To illustrate this point, the coefficients of the projection $\tilde{H}_{\tilde{W}_{10}}$ of $\tilde{H}$ in $\tilde{W}_{10}$ are plotted with the derivatives of the surface profile function y_D in figure 5.11. We observe that the coefficients are nonzero at the location of the groove, i.e. when their shift parameter k is such that the basis function $\tilde{\psi}_j^k$ has a support covering the area of the groove.
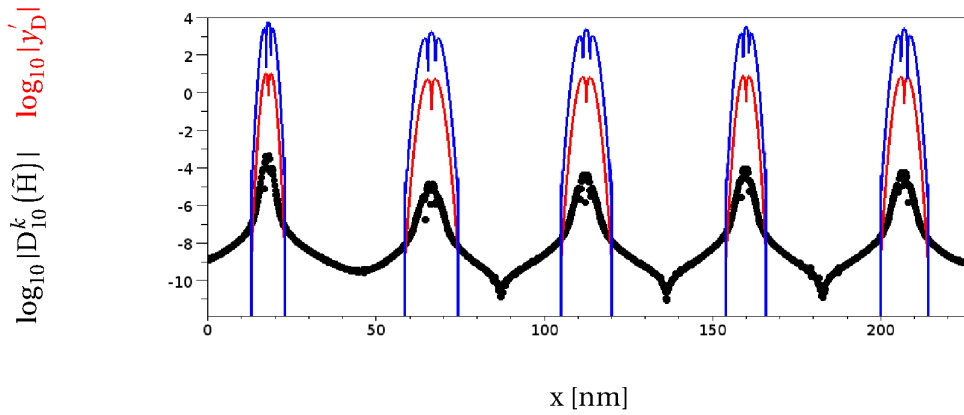
Figure 5.11: *First and second order derivatives of the surface profile function y_D are plotted in respectively red and blue lines in a logarithmic scale as a function of the abscissa (the derivatives which modulus is less than 10^{-8} are set to zero). The 2^{10} coefficients $|D_{10}^k|$ of the source function, calculated by the Maradudin method using 4096 points, projected in the subspace $\tilde{W}_{10}, \tilde{H}_{\tilde{W}_{10}}$ are also shown in a logarithmic scale for comparison. The coefficients D_{10}^k are plotted as black dots at $k/2^{10}\,d$ where $k/2^{10}$ is the shift of ψ_{10}^k from ψ_{10}^0. The wavelet is Daubechies 6. The system is the same as in figure 5.1.*

We recall that the decomposition of $\tilde{H}$ in the subspace $\tilde{V}_J$ of depth $J - J_0$ is done in the subspace

$$\tilde{V}_J = \tilde{V}_{J_0} \bigoplus_{j=J_0}^{J-1} \tilde{W}_j \quad .$$

In order to increase the resolution of the description of the source function $\tilde{H}$ where the abrupt variations are expected, the source function $\tilde{H}$ is not expanded in the same way in the different wavelet subspaces $\tilde{W}_j$. $\tilde{H}$ is first expanded in a scalet subspace of scale parameter $J_{init} > J_0$ and of low resolution. The decomposition of $\tilde{H}$ is thus done in

$$\tilde{V}_{J_{init}} = \tilde{V}_{J_0} \bigoplus_{j=J_0}^{J_{init}-1} \tilde{W}_j \quad .$$

Next, it is additionally expanded on a few basis functions of the wavelet subspace of higher scale $\tilde{W}_{J_{init} \leq j \leq J-1}$. We call K_j the set of k in $[0, 2^j[$ for which $d\,k/2^j$ corresponds to the area of the grooves. The decomposition on higher scale wavelet subspace $\tilde{W}_{J_{init} \leq j \leq J-1}$ is therefore done with the basis functions $\tilde{\psi}_j^k$ for which k belongs to the set K_j. This is equivalent to decompose the source function $\tilde{H}$ on the scalet subspace $\tilde{V}_J$ and then to cut the part of the decomposition which is useless such that

$$\tilde{V}_J = \tilde{V}_{J_0} \bigoplus_{j=J_0}^{J-1} \tilde{W}_j \xrightarrow{cut} \tilde{V}_J = \tilde{V}_{J_0} \bigoplus_{j=J_0}^{J_{init}-1} \tilde{W}_j \bigoplus_{j=J_{init}}^{J-1} \left\{ \tilde{\psi}_j^k \right\}_{k \in K_j} \quad .$$

The coefficients of the expansion of $\tilde{H}$ and $\gamma\tilde{L}$ in the wavelet subspaces $\tilde{W}_{J_{init} \leq j \leq J-1}$ whose shift parameter k does not belong to K_j are considered negligible and are set to zero prior to solving the matrix system (in fact, as it is explained later, the lines of the matrix corresponding to the coefficients set to zero are removed from the matrix). The expansion on the $2^{J_{init}}$ first terms is unchanged. The new representation of the source function therefore is

$$\left[W_{J_0}^J \left(\tilde{H} \right) \right] \xrightarrow{cut} \left[C_{J_0}^{k \in [0,2^{J_0}[} \left(\tilde{H} \right) \quad D_{J_0}^{k \in [0,2^{J_0}[} \left(\tilde{H} \right) \dots 0\, D_{J_{init}}^{k \in K_{J_{init}}} \left(\tilde{H} \right) 0 \dots 0\, D_{J-1}^{k \in K_{J-1}} \left(\tilde{H} \right) 0 \right]^T \quad .$$

The number of nonzero terms in the vector $\left[W_{J_0}^J \left(\tilde{H} \right) \right]_{cut}$ is called N_{cut}. N_{cut} is the dimension of $\tilde{V}_{J_{init}}$, $2^{J_{init}}$, added up with the dimensions of the sets $K_{j \geq J_{init}}$. Hence

$$N_{cut} = 2^{J_{init}} + \sum_{j=J_{init}}^{J-1} \dim \left(K_j \right) \quad .$$

To summarize, the two main parameters of the cut of the decomposition are:

- The scale parameter J_{init} of the smallest scale which is cut

- $\forall j \geq J_{init}$, the set K_j of shift parameters k for which the coefficients D_j^k of the decomposition in $\tilde{W}_j$ are kept. They are chosen such that the abscissas x=$k/2^j$d are close to a groove.

The number N=2^J of unknowns for each source function $\tilde{H}$ and $\gamma\tilde{L}$ of the system is reduced accordingly to N_{cut}. The new sparse matrix M_{Wcut} to be solved is now a matrix of $2\,N_{cut}$ by $2\,N_{cut}$ since the rows and the columns corresponding to the coefficients set to zero are removed. The process of cutting the matrix is shown in figure 5.12. The entire matrix M_W, whose decomposition depth equals to three, appears on the left whereas the new matrix M_{Wcut} with removed rows and columns appear on the right. The coefficients of the decomposition on the subspace $\tilde{V}_{J_0} \oplus_{j=J_0}^{J_0+2} \tilde{W}_j$ of the example of the first section 5.1.2 are sketched above the matrix M_W on the left. The profile of the grating is represented below the columns associated with the subspace $\tilde{W}_{J_0+2}$. The new matrix M_{Wcut} on the right keeps the columns which correspond to the coefficients in the area of the groove. The matrix M_{Wcut} is calculated by applying a DWT in the same way as presented in the beginning of this section, equation 5.7, except that some columns in the wavelet transform matrix DWT are removed as well as some lines in the inverse wavelet transform matrix DWT^{-1}. The calculation of a quarter of the matrix M_{Wcut} is done as

$$N_{cut} \updownarrow \underleftrightarrow[N_{cut}]{\left[DWT^{-1} G\, DWT \right]} = N_{cut} \updownarrow \underleftrightarrow[N]{\left[DWT^{-1} \right]} N \updownarrow \underleftrightarrow[N]{[G]} N \updownarrow \underleftrightarrow[N_{cut}]{[DWT]}$$

where G=$\{\tilde{K}^{\pm}, \partial\tilde{K}^{\pm}\}$ is a quarter of the matrix M_W, equation 5.7. The lines (respectively the columns) which are removed of the DWT^{-1} matrix (respectively of the DWT matrix) are indexed by $2^j + k$ for all j$\geq J_{init}$ with k$\notin K_j$. The source functions $\tilde{H}_{cut}$ and $\gamma\tilde{L}_{cut}$ are retrieved after solving the system of size $2N_{cut}$ and applying the DWT of size N $\times N_{cut}$ to $\left[W_{J_0}^J \left(\tilde{H} \right) \right]_{cut}$ and $\left[W_{J_0}^J \left(\gamma\tilde{L} \right) \right]_{cut}$.
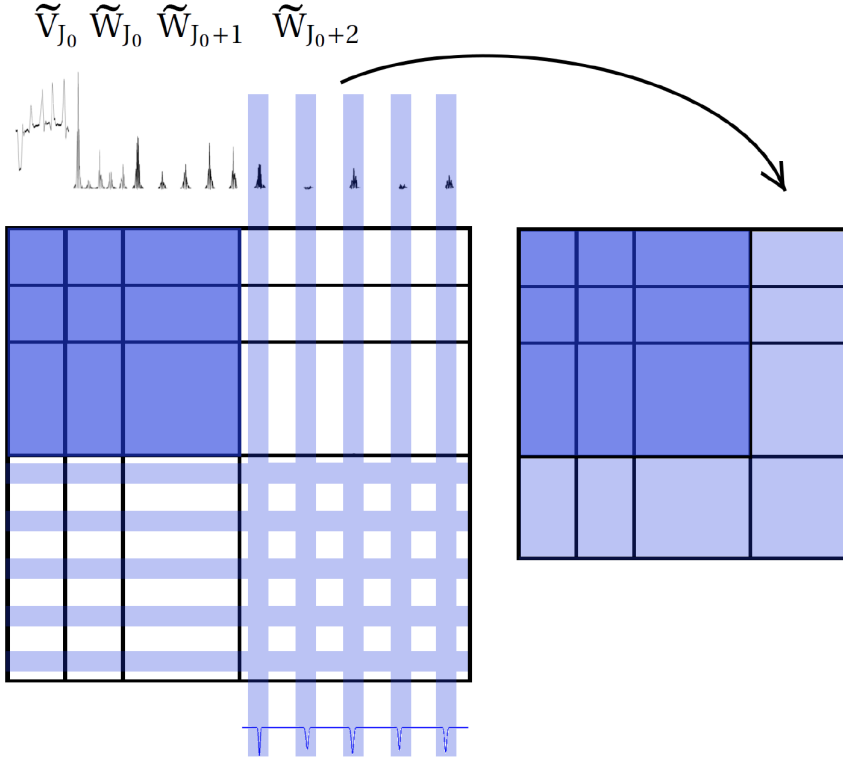
Figure 5.12: *Sketch of the cut of a quarter* DWT^{-1} G DWT *of the matrix in the wavelet basis* $M_W(J_0,J_0+2)$ *with* $J_{init} = J_0+2$ *(G={$\tilde{K}^{\pm}$,$\partial\tilde{K}^{\pm}$}, equation 5.7). The initial matrix is on the left and the matrix after the cut is on the right. The block in the matrix corresponding to* $\langle \tilde{V}_{J_{init}}|G|\tilde{V}_{J_{init}}\rangle$ *is in dark blue. The lines and the columns indexed by* $k \in K_j$ *are in light blue. The coefficients of the decomposition in* $\tilde{V}_5$, $\tilde{W}_5$, $\tilde{W}_6$ *and* $\tilde{W}_7$ *shown in figure 5.3 are recalled above the matrix on the left and the grating profile below.*

In order to outline the possibilities of this technique, the cut of the matrix is performed in the same case of an incident plane wave impinging on a silver grating with five Gaussian grooves presented in the first section (described in figure 5.1). For the example chosen, the kept terms are in five intervals corresponding to the basis functions localized around the middle of the grooves at $18, 67, 112, 160$ and 207 nm. The abscissa of the ith groove is called x_i. In the real space, the projection of $\tilde{H}$ in the subspace $\tilde{W}_j$ is spread over a length l_j centered at the x_i. The length l_j defined as

$$l_j = \frac{l_{J_{init}}}{2^{j-J_{init}}}$$

decreases when the scale parameter j increases. For each scale 2^j, it corresponds to keep the integer values k for which the shift $d\,k/2^j$ of the basis function ψ_j^k belongs to $[x_i - l_j/2, x_i + l_j/2[$. Each set K_j in then composed of the integer values within the five intervals

$$K_j = \bigcup_{i=1}^{5} \left[u_i - \frac{l_j}{2d}, u_i + \frac{l_j}{2d} \right[\quad .$$

where $u_i = x_i/d$ is the normalized abscissa of the middle of the ith groove. A sketch of the set K_j is shown in figure 5.13. The cut is done with $J_{init} = 8$ in order to have a resolution of $1/256$ over the whole period and different lengths $l_{J_{init}}$. The investigated values of l_8 are l_8=10.8 nm, l_8=21.5 nm, l_8=32.3 nm and l_8=64.7 nm corresponding to l_0/d=12, l_0/d=24, l_0/d=36 and l_0/d=72 respectively.
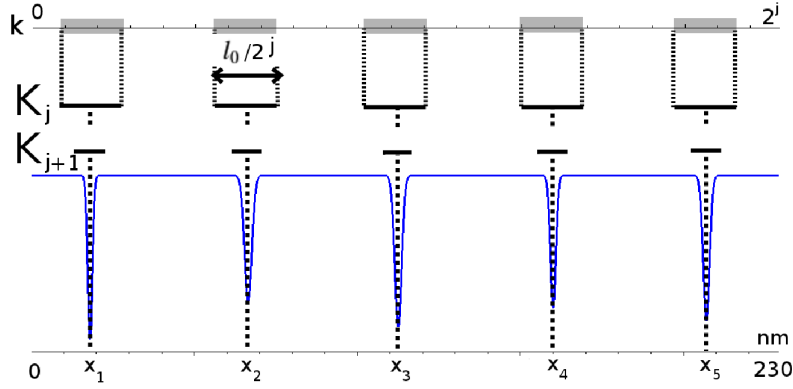
Figure 5.13: *Sketch of the set* K_j

We recall that the relative error of the source function $\tilde{H}$ (or $\gamma\tilde{L}$) compared with $\tilde{H}_{ref}$ at the normalized abscissa u is

$$\left| \frac{\tilde{H} - \tilde{H}_{ref}}{\tilde{H}_{ref}} \right| (u)$$

and its spatial average is

$$\overline{\left| \frac{\tilde{H} - \tilde{H}_{ref}}{\tilde{H}_{ref}} \right|} = \frac{1}{2^J} \sum_{n=0}^{2^J-1} \left| \frac{\tilde{H}\left(\frac{n}{2^J}\right) - \tilde{H}_{ref}\left(\frac{n}{2^J}\right)}{\tilde{H}_{ref}\left(\frac{n}{2^J}\right)} \right| \quad .$$

The source functions $\tilde{H}_{cut}$ is obtained by the resolution of M_{Wcut} after the wavelet transformation of the matrix in the Maradudin method in $\tilde{V}_J$ (2^J points) for different cuts. Two wavelets are used: the Daubechies of order 6 and the Daubechies of order 18. For comparison, the same system of the Maradudin method, with a number of points 2^J, is solved directly and gives us the source function of reference $\tilde{H}_{ref}$. The mean relative error of $\tilde{H}_{cut}$ for the different values of l_8 compared with $\tilde{H}_{ref}$ is plotted as a function of the number of points 2^J used in the resolution in figure 5.14. This relative error corresponds to the error done in the resolution of the system induced by the cut. The cases where the Daubechies of order 6 is used, are represented by solid lines whereas the ones where the Daubechies of order 18 is used, are represented by dashed lines. Identical colors indicate the same length l_8 used for the intervals of the sets K_j. In the case of the Daubechies of order 18 and the smallest length $l_8 = 10.8$ nm, the cut is too severe and the error is above the 10^{-2}. Except for that particular case, the relative error is below 10^{-4}. We can see that if the length l_8 is larger, the intervals
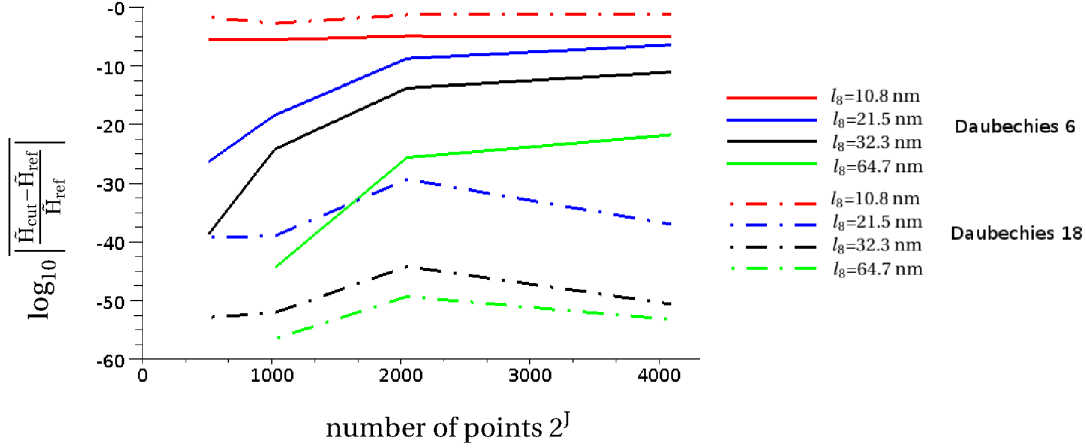
Figure 5.14: *Mean relative error of the magnetic field $\tilde{H}_{cut}$ calculated with a level J=12 (equivalent to 2^{12} = 4096 points) with the magnetic field computed with Maradudin's method H_{ref} with the same number of points in logarithmic scale as a function of the number of points 2^J. The different cuts are done with J_{init} = 8 and the set $K_{j \geq J_{init}}$ have interval of length $l_j = l_8/2^{j-8}$ with l_8=10.8 nm, l_8=21.5 nm, l_8=32.3 nm and l_8=64.7 nm. The system is the same as in figure 5.1.*

are wider and the relative error is therefore lower. At a fixed width of the interval l_8 (dashed and solid lines of the same colors), the relative error obtained by using a wavelet of higher order 18 is improved compared to the relative error obtained by using a wavelet of smaller order 6. This is due to the better approximation of the smooth part of the source function in the first wavelet subspaces $\tilde{V}_{J_{init}}$ by the higher order wavelet, leaving less to project on the higher scale complementary wavelet subspaces.

The error done in the resolution of the system was assessed. Now, let us take a look at the error done with respect to a solution which reaches a higher convergence. The relative error of $\tilde{H}_{cut}^{4096}$ calculated by the resolution of M_{Wcut} with a scale $2^J = 2^{12}$ (equivalent to 4096 points) for the different values of l_8 compared with $\tilde{H}_{ref}^{8192}$ calculated by the Maradudin method with 8192 points are plotted as a function of the normalized abscissa in figure 5.15. The cases where the Daubechies of order 6 is used, are represented as circles whereas the ones where the Daubechies of order 18 is used, are represented by dots. Identical colors indicate the same length l_8 of the intervals. As a comparison, the relative error of $\tilde{H}^{4096}$ with $\tilde{H}_{ref}^{8192}$ $\left(\left| \frac{\tilde{H}^{4096} - \tilde{H}_{ref}^{8192}}{\tilde{H}_{ref}^{8192}} \right| \right)$, both calculated directly by the Maradudin method, is represented in a black dashed line. Except for the Daubechies of order 18 and a length l_8=10.8 nm, the error induced by the cut in the wavelet matrix is negligible. There is no additional bias to the one that exists between the solutions obtained by the Maradudin method using 4096 and 8192 points. Provided with a width of the intervals of the set K_j superior or equal to $12/2^j$ (l_8=21.5 nm), the right source functions are obtained from this method whose expansion on higher

187
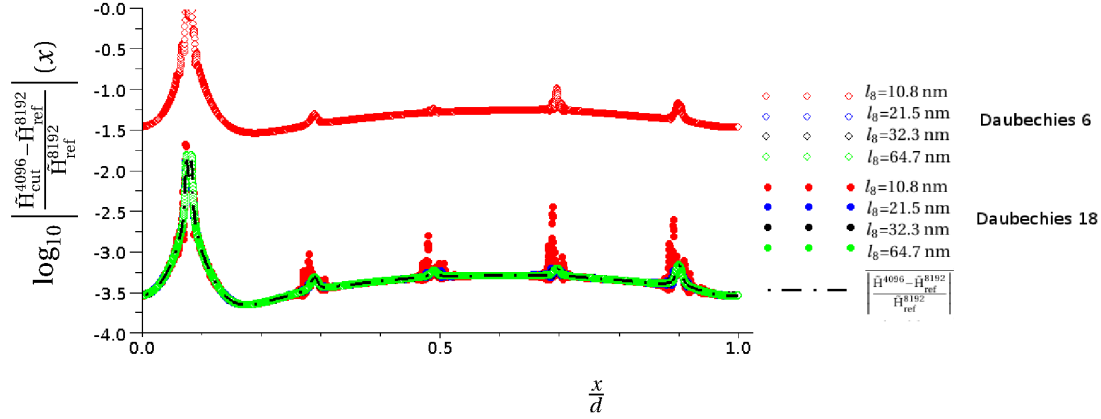
Figure 5.15: *Relative error of the magnetic field $\tilde{H}_{cut}^{4096}$ calculated with a level J=12 (equivalent to $2^{12} = 4096$ points) compared with the magnetic field computed with Maradudin's method $\tilde{H}_{ref}^{8192}$ with 8192 points in logarithmic scale as a function of the normalized abscissa. The different cuts are done with $J_{init} = 8$ and the set $K_{j \geq J_{init}}$ have interval of length $l_j = l_8/2^{j-8}$ with $l_8=10.8$ nm, $l_8=21.5$ nm, $l_8=32.3$ nm and $l_8=64.7$ nm. The system is the same as in figure 5.1.*

scale complementary wavelet subspaces is only done around the grooves.

Regardless of the performances of the method using a wavelet transform, these results show that it is possible to reduce significantly the number of unknowns. The number of unknowns N_{cut} obtained in the cases of the examples provided here are indicated in table 5.2. Except from the first column whose cut characteristics lead to an approximate solution, the other columns show that the initial number N of unknowns can be reduced in a significant way to N_{cut}. In the second column, we observe that the number of unknowns can go down to 736 instead of 4096 to obtain the same solution than by solving directly the Maradudin matrix.

length l_8 [nm]		10.8	21.5	32.3	64.7
length l_0/d		6	12	18	36
	512	316 (38.1 %)	376 (53.9 %)	436 (72.5 %)	
N	1024	376 (13.5 %)	496 (23.5 %)	616 (36.2 %)	872 (72.5 %)
	2048	436 (4.5 %)	616 (9 %)	796 (15.1 %)	1232 (36.2 %)
	4096	496 (1.5 %)	736 (3.2 %)	976 (5.7 %)	1952 (22.7 %)

Table 5.2: *Number of unknowns N_{cut} for the different values of the length of the intervals centered around the groove and in brackets, the percentage of memory space used in the wavelet method compared to the one in the Maradudin method.*

Let us say a few words on the advantages of this approach for the time and memory space requirements issues. As was previously said in section 5.2.3, the method using a wavelet transform makes it possible to save memory space if the matrix is filled adequately.

188

However, the calculation of the matrix in the wavelet basis M_W takes a longer time to perform and the total time spent for the resolution is longer than the one in the Maradudin method, especially if one does not use an iterative method. The method described in this section reduces the number of unknowns from N to N_{cut} and aims at reducing the time spent for the multiplication with the wavelet transform matrices accordingly. The multiplications then take a time proportional to $N_{cut}N \log N$ [68]. Additionally, if one uses the LU decomposition and not an iterative method for the resolution of the system, the number of cycles for solving the matrix is reduced from $8 N^3$ to $8 N_{cut}^3$. In the end the number of cycles necessary for the multiplication of the matrices and the resolution in the wavelet method (proportional to $N_{cut}N \log N$ added up with N_{cut}^3), is comparable with the number of cycles necessary for the resolution in the Maradudin method (proportional to N^3) but is still higher in the range of the number N of points which are used $N \approx 4096$. This new method using a cut in the wavelet matrices therefore becomes interesting as it compares to the Maradudin method in time and it enables to study wider surfaces by saving memory space. We note that the results are better with a wavelet of higher order D (Daubechies 18 in our example) but the multiplication step then takes more cycles to accomplish since the number of terms in the wavelet transform is proportional to the support of the mother wavelet D-1.

The method presented here enables us to gain time and memory space in comparison with the original method using a DWT. Thanks to that technique, we are able to adapt the description of the source functions as a function of the location over the profile. The source functions are described with a higher level of details at the location of the groove as they are expanded on higher scale wavelet subspaces at these precise locations. Due to the optimization of the number of unknowns N, larger systems with isolated grooves may be studied. To make use of this method requires, however, an analysis of a few solutions in order to determine a possible cut. Despite the definite gain of memory space, the time to calculate the solution is comparable to Maradudin's method and the dense matrix still has to be evaluated. Further improvements in the calculation of the matrix in the wavelet basis from the dense one can be expected. The evaluation of the discrete wavelet transformation of the dense matrix containing the Green function can probably be done more quickly. For instance, one may use the wavelets to interpolate the Green function in the real space where it is smooth and thus reduce the time spent to calculate the Green function. We believe that there is more to benefit from applying the wavelets to the surface integral equations in the way presented in the next section than from working on an improvement of the method presented in this section.

5.3 The application of the Coiflet as an expansion basis function and a testing function to Fredholm integral equations of the second kind

In this section, we will expand the unknown function $\tilde{H}$ and $\gamma\tilde{L}$ on a wavelet basis and then project the integral equations on the same basis (the basis functions then play the role of testing functions) in order to solve them. This method has been applied with the Coifman wavelet (Coiflet) in [140] and is described in [132]. The great advantage of the technique is to build the sparse wavelet matrix directly by using the unique properties of the Coiflet.

5.3.1 The method

5.3.1.1 The specificity of the Coiflet

This method rests on one property of the Coifman wavelet: it has vanishing moments. This allows to simplify the expression of the coefficients in the wavelet basis. Prior to expressing the coefficients, we give the main properties of the Coiflets.

The zero order moment of the mother scalet of order D=6P is

$$\int_0^1 \tilde{\phi}(x)\,dx = 1 \quad . \tag{5.8}$$

The mother scalet has also 2P-1 vanishing moments starting at the first-order one:

$$\forall 1 \le p \le 2P-1 \qquad \int_0^1 x^p \tilde{\phi}(x)\,dx = 0 \quad . \tag{5.9}$$

The mother wavelet of order D=6P has 2P vanishing moments, starting at the zero-order one:

$$\forall 0 \le p \le 2P-1 \qquad \int_0^1 x^p \tilde{\psi}(x)\,dx = 0 \quad . \tag{5.10}$$

The support of the Coiflet scalet and wavelet is $S_j^k = \left[\frac{-2P+k}{2^j}, \frac{k+4P-1}{2^j}\right[$. The periodic Coiflets have a larger support : the same support S_j^k and, in addition, the ones translated of an integer number of times. This support is $\tilde{S}_j^k = \bigcup_{l\in\mathbb{Z}} \left[\frac{-2P+k}{2^j}+l, \frac{k+4P-1}{2^j}+l\right[$.

A periodic function $f \in L^2([0,1[)$, of period equal to one, is projected on a scalet basis of scale 2^{J_0} of support $\tilde{S}_{J_0}^k$. We suppose that f may be developed on the interval $S_{J_0}^k$ of width $(D-1)/2^{J_0}$ as a polynomial of order P. This requires that f may be smooth enough or inversely that 2^{J_0} is high enough. For $x_0, x \in S_{J_0}^{k\,2}$, we have

$$f(x) = \sum_{n=0}^{P-1} \frac{f^{(n)}(x_0)}{n!}(x-x_0)^n + O\left((x-x_0)^P\right) \tag{5.11}$$

with $D = 6P$ the wavelet genus of the Coiflet. We are looking for an expansion of the wavelet coefficients $C_{J_0}^k(f) = < f | \tilde{\phi}_{J_0}^k >$. The inner product of a periodic Coiflet with a periodic function requires an integration on $\tilde{S}_j^k \cap [0, 1[$. In order to simplify the demonstration hereafter and without loss of generality, we choose a k for which $\tilde{S}_j^k \cap [0, 1[= S_j^k$. Otherwise, the integration is done on two compact intervals $[0, \frac{k+4P-1}{2^j}[$ and $[\frac{-2P+k}{2^j} + 1, 1[$ and the demonstration requires treating the two parts separately. The result is, however, valid for all $k \in [0, 2^{J_0}[$.

We aim at evaluating

$$C_{J_0}^k(f) = < f | \tilde{\phi}_{J_0}^k > = \int_{S_{J_0}^k} f(x) \tilde{\phi}_{J_0}^k(x) dx \quad .$$

Substituting the expansion of f, equation 5.11, we have

$$C_{J_0}^k(f) = \sum_{n=0}^{2P-1} \frac{f^{(n)}(x_0)}{n!} \int_{S_{J_0}^k} (x - x_0)^n \tilde{\phi}_{J_0}^k(x) dx + O\left(h^{2P}\right) \tag{5.12}$$

where $h = \max\left((-2P + k)/2^{J_0} - x_0, (k + 4P - 1)/2^{J_0} - x_0\right)$.
First, a change of variable $X = 2^{J_0} x - k$ is done under the integral, $\forall n \leq 2P - 1$

$$\int_{S_{J_0}^k} (x - x_0)^n \tilde{\phi}_{J_0}^k(x) dx = \int_{S_0^0} 2^{-nJ_0} \left(X + k - 2^{J_0} x_0\right)^n \sqrt{2^{J_0}} \tilde{\phi}_0^0(X) 2^{-J_0} dX \quad .$$

Secondly, $(X + k - 2^{J_0} x_0)^n$ is developed with the binomial theorem expressed as

$$\left(X + k - 2^{J_0} x_0\right)^n = \sum_{i=0}^{n} \binom{n}{i} X^i \left(k - 2^{J_0} x_0\right)^{n-i}$$

with $\binom{n}{i} = \frac{n!}{i!(n-i)!}$. Replacing the binomial theorem gives

$$\int_{S_{J_0}^k} (x - x_0)^n \tilde{\phi}_{J_0}^k(x) dx = 2^{-nJ_0} \sqrt{2^{-J_0}} \sum_{i=0}^{n} \binom{n}{i} \left(k - 2^{J_0} x_0\right)^{n-i} \int_{S_0^0} X^i \tilde{\phi}(X) dX \quad . \tag{5.13}$$

There is two cases for the moment of order i, $\int X^i \tilde{\phi}(X) dX$. For $2P - 1 \geq i \geq 1$, the moment of $\tilde{\phi}$ are null. We substitute the equation 5.9 into the equation 5.13

$$\int_{S_{J_0}^k} (x - x_0)^n \tilde{\phi}_{J_0}^k(x) dx = 2^{-nJ_0} \sqrt{2^{-J_0}} \binom{n}{0} \left(k - 2^{J_0} x_0\right)^n \int_{S_0^0} 1 \tilde{\phi}(X) dX + \sum_{i=1}^{n} 0 \quad .$$

For the zero-order moment we apply the equation 5.8 and obtain

$$\int_{S_{J_0}^k} (x - x_0)^n \tilde{\phi}_{J_0}^k(x) dx = 2^{-nJ_0} \sqrt{2^{-J_0}} \left(k - 2^{J_0} x_0\right)^n \quad . \tag{5.14}$$

As $k/2^{J_0} \in S_{J_0}^k$, we may choose $x_0 = k/2^{J_0}$ and the equation 5.14 has a very simple expression depending on the value of n

$$\int_{S_{J_0}^k} \left(x - \frac{k}{2^{J_0}}\right)^n \tilde{\phi}_{J_0}^k(x) dx = \begin{cases} n = 0 & \sqrt{2^{-J_0}} \\ n \geq 1 & 0 \end{cases} \tag{5.15}$$

Applying $x_0 = k/2^{J_0}$ and substituting the equation 5.15 into the equation 5.12, the expansion of the scalet coefficients of f are

$$C_{J_0}^k(f) = <f|\tilde{\phi}_{J_0}^k> = \sqrt{2^{-J_0}}f\left(\frac{k}{2^{J_0}}\right) + O\left(h^{2P}\right) \tag{5.16}$$

with h=$(4P-1)/2^{J_0}$.

The wavelet coefficients of f, $< D_j^k|f >$, are calculated in the same way. The requirement on f is now that f may be expanded as a polynomial of order p, equation 5.11 for x,x_0 $\in S_j^{k^2}$. We replace $\tilde{\phi}$ with $\tilde{\psi}$ (and $\tilde{\phi}_{J_0}^k$ with $\tilde{\psi}_j^k$), for all the equations from the equation 5.12 until the equation 5.13. The moments $\int X^i \tilde{\psi}(X)dX$ with $2P-1 \geq i \geq 0$ are all null (even for n=0) because of the equation 5.10. Therefore all the following equations from the equation 5.14 to the equation 5.16 are equal to zero and

$$D_j^k(f) = <\tilde{\psi}_j^k|f> = 0 + O\left(h^{2P}\right) \tag{5.17}$$

with h=$(4P-1)/2^j$.

For sufficiently smooth functions, the wavelet coefficients of the subspace $\tilde{V}_{J_0} \oplus_{n=J_0}^{J-1} \tilde{W}_n$ generated by a Coiflet basis are evaluated quickly by the equations 5.16 and 5.17. To be called smooth, the function has to satisfy the equation 5.11 with $x \in S_{J_0}^k$ and $x_0 = k/2^{J_0}$ for each k $\in [0,2^{J_0}[$, as well as the condition for higher scale parameter $j > J_0$. As for each (k,$j > J_0$) there exists a k' such that $S_j^k \subset S_{J_0}^{k'}$, if the condition, equation 5.11, is satisfied at the scale 2^{J_0} then the function is considered smooth on [0,1[.

5.3.1.2 The application of the Coiflet as an expansion basis function and a testing function

We want to express the problem directly in the wavelet basis, before building the matrix, in order to build the sparse wavelet matrix directly. We look for the equations on the coefficients of the source functions in the wavelet basis. We work with the wavelet subspace $\tilde{V}_{J_0} \oplus_{j=J_0}^{J-1} \tilde{W}_j$, generated by the Coifman wavelet basis $\left\{\left\{\tilde{\phi}_{J_0}^k\right\}_{k=[0,2^{J_0}-1]} \left\{\tilde{\psi}_j^k\right\}_{k=[0,2^j-1]}\right\}_{j=[J_0,J-1]}$ ($J_0 > J_{min}$).

First, we expand the periodic unknown $\tilde{H}$ as

$$\tilde{H} = \sum_{k=0}^{2^{J_0}-1} C_{J_0}^k\left(\tilde{H}\right)\tilde{\phi}_{J_0}^k + \sum_{j=J_0}^{J-1}\sum_{k=0}^{2^j-1} D_j^k\left(\tilde{H}\right)\tilde{\psi}_j^k \quad . \tag{5.18}$$

The second unknown in the resolution was chosen to be $\gamma\tilde{L}$, instead of $\tilde{L}$ alone, because it avoids adding a term in the integral. As a consequence $\gamma\tilde{L}$ is expanded similarly as $\tilde{H}$.

We present here the demonstration with one of the two integral equations, equations 2.59 and 2.60. The integral equation 2.59 has to be expressed in function of the normalized

192

variable u= x/d which scans [0,1[and is the parameter of the parametric equation of S_D

$$\frac{1}{2}H(u^{'}) + \int_0^1 \left[H(u)\frac{\partial \tilde{G}^+}{\partial \vec{n}}(u^{'},u) + \epsilon_+ \tilde{G}^+(u^{'},u)L(u) \right] \gamma(u)du = H_i(u^{'})$$

where $\tilde{G}^+(u^{'},u) = \tilde{G}^+(\vec{r}(u^{'}) - \vec{r}(u))$ and $\gamma(u) = \sqrt{1 + y_D'(u)^2}$. Attention must be paid to the fact that $\vec{r}(u^{'}) - \vec{r}(u) = (u^{'} - u, y_D(u^{'}) - y_D(u))$ and therefore the Green function does not depend on $u^{'} - u$ but on $u^{'}$ and u separately. $\tilde{G}$ denotes the pseudo-periodic Green function. We choose to call $\tilde{K}$ the periodic Green function. The periodic green function is defined similarly than the periodic unknowns as

$$\tilde{K}^\pm(u^{'},u) = \tilde{G}^\pm(\vec{r}(u^{'}) - \vec{r}(u))e^{i\alpha_0\left(u-u^{'}\right)d} \quad , \tag{5.19}$$

$$\frac{\partial \tilde{K}^\pm}{\partial \vec{n}}(u^{'},u) = \frac{\partial \tilde{G}^\pm}{\partial \vec{n}}(\vec{r}(u^{'}) - \vec{r}(u))e^{i\alpha_0\left(u-u^{'}\right)d} \quad . \tag{5.20}$$

The integral equation expressed with the periodic unknowns, $\tilde{H}$ and $\tilde{L}$, equations 5.2 and 5.3 and the periodic Green functions, equations 5.19 and 5.20, is

$$\frac{1}{2}\tilde{H}(u^{'}) + \int_0^1 \left[\tilde{H}(u)\frac{\partial \tilde{K}^+}{\partial \vec{n}}(u^{'},u) + \epsilon_+ \tilde{K}^+(u^{'},u)\tilde{L}(u) \right] \gamma(u)du = \tilde{H}_i(u^{'}) \quad . \tag{5.21}$$

Second, we substitute the decomposition of $\tilde{H}$ of equation 5.18, as well as the one of $\tilde{L}\gamma$ into the integral equation, equation 5.21

$$\sum_{k=0}^{2^{J_0}-1} C_{J_0}^k\left(\tilde{H}\right)\left[\frac{1}{2}\tilde{\phi}_{J_0}^k\left(u^{'}\right) + \int_0^1 \gamma(u)\frac{\partial \tilde{K}^+}{\partial \vec{n}}(u^{'},u)\tilde{\phi}_{J_0}^k(u)du\right]$$

$$+ \sum_{k=0}^{2^{J_0}-1} C_{J_0}^k\left(\tilde{L}\gamma\right)\epsilon_+ \int_0^1 \tilde{K}^+(u^{'},u)\tilde{\phi}_{J_0}^k(u)du$$

$$+ \sum_{j=J_0}^{J-1}\sum_{k=0}^{2^j-1} D_j^k\left(\tilde{H}\right)\left[\frac{1}{2}\tilde{\psi}_j^k\left(u^{'}\right) + \int_0^1 \gamma(u)\frac{\partial \tilde{K}^+}{\partial \vec{n}}(u^{'},u)\tilde{\psi}_j^k(u)du\right]$$

$$+ \sum_{j=J_0}^{J-1}\sum_{k=0}^{2^j-1} D_j^k\left(\tilde{L}\gamma\right)\epsilon_+ \int_0^1 \tilde{K}^+(u^{'},u)\tilde{\psi}_j^k(u)du = \tilde{H}_i(u^{'}) \tag{5.22}$$

The source functions in the integral have been expressed with the Coiflets as an expansion basis function. Lastly, we have to project the integral equation on the Coiflet basis to have a new set of equations. At this step, the Coiflets play the role of testing functions. Two kinds of equations are obtained: the ones which correspond to the scalet basis function $\left\{\tilde{\phi}_{J_0}^l\right\}_{l=[0,2^{J_0}-1]}$ and the ones which correspond to the wavelet basis function $\left\{\{\tilde{\psi}_i^l\}_{l=[0,2^i-1]}\right\}_{i=[J_0,J-1]}$.

The projection $\langle \tilde{\phi}_{J_0}^l | = \int_0^1 du' \, \tilde{\phi}_{J_0}^l(u')$ on the equation 5.22 is

$$\sum_{k=0}^{2^{J_0}-1} C_{J_0}^k(\tilde{H}) \left[\frac{1}{2}\delta_{k,l} + \int_0^1 du' \int_0^1 du \quad \tilde{\phi}_{J_0}^l(u')\gamma(u)\frac{\partial \tilde{K}^+}{\partial \vec{n}}(u',u)\tilde{\phi}_{J_0}^k(u) \right]$$

$$+ \sum_{k=0}^{2^{J_0}-1} C_{J_0}^k(\tilde{L}\gamma)\epsilon_+ \int_0^1 du' \int_0^1 du \quad \tilde{\phi}_{J_0}^l(u')\tilde{K}^+(u',u)\tilde{\phi}_{J_0}^k(u)$$

$$+ \sum_{j=J_0}^{J-1}\sum_{k=0}^{2^j-1} D_j^k(\tilde{H}) \int_0^1 du' \int_0^1 du \quad \tilde{\phi}_{J_0}^l(u')\gamma(u)\frac{\partial \tilde{K}^+}{\partial \vec{n}}(u',u)\tilde{\psi}_j^k(u)$$

$$+ \sum_{j=J_0}^{J-1}\sum_{k=0}^{2^j-1} D_j^k(\tilde{L}\gamma)\epsilon_+ \int_0^1 du' \int_0^1 du \quad \tilde{\phi}_{J_0}^l(u')\tilde{K}^+(u',u)\tilde{\psi}_j^k(u) = C_{J_0}^l(\tilde{H}_i)$$

where we substituted $\left\langle \tilde{\phi}_{J_0}^l | \tilde{H}_i \right\rangle = C_{J_0}^l(\tilde{H}_i)$ and $\left\langle \tilde{\phi}_{J_0}^l | \tilde{\phi}_{J_0}^k \right\rangle = \delta_{k,l}$ ($\delta_{k,l}$ is equal to one if k=l and equal to zero otherwise). We obtain 2^{J_0} equations for $l \in [0, 2^{J_0}[$.

The projection $\langle \tilde{\psi}_i^l | = \int_0^1 du' \, \tilde{\psi}_i^l(u')$ on the equation 5.22 is

$$\sum_{k=0}^{2^{J_0}-1} C_{J_0}^k(\tilde{H}) \int_0^1 du' \int_0^1 du \quad \tilde{\psi}_i^l(u')\gamma(u)\frac{\partial \tilde{K}^+}{\partial \vec{n}}(u',u)\tilde{\phi}_{J_0}^k(u)$$

$$+ \sum_{k=0}^{2^{J_0}-1} C_{J_0}^k(\tilde{L}\gamma)\epsilon_+ \int_0^1 du' \int_0^1 du \quad \tilde{\psi}_i^l(u')\tilde{K}^+(u',u)\tilde{\phi}_{J_0}^k(u)$$

$$+ \sum_{j=J_0}^{J-1}\sum_{k=0}^{2^j-1} D_j^k(\tilde{H}) \left[\frac{1}{2}\delta_{k,l}\delta_{j,i} + \int_0^1 du' \int_0^1 du \quad \tilde{\psi}_i^l(u')\gamma(u)\frac{\partial \tilde{K}^+}{\partial \vec{n}}(u',u)\tilde{\psi}_j^k(u) \right]$$

$$+ \sum_{j=J_0}^{J-1}\sum_{k=0}^{2^j-1} D_j^k(\tilde{L}\gamma)\epsilon_+ \int_0^1 du' \int_0^1 du \quad \tilde{\psi}_i^l(u')\tilde{K}^+(u',u)\tilde{\psi}_j^k(u) = C_i^l(\tilde{H}_i) \quad .$$

We obtain $2^J - 2^{J_0}$ equations for $j \in [J_0, J[$ and $k \in [0, 2^j[$. It is equivalent to see each term containing a double integration as a double projection. $\int_0^1 du' \, \tilde{\psi}_i^l(u') = \langle \tilde{\psi}_i^l |$ and $\int_0^1 du\, \tilde{\psi}_j^k(u) = |\tilde{\psi}_j^k\rangle$ so

$$\langle \tilde{\psi}_i^l | \tilde{K}^+ | \tilde{\psi}_j^k \rangle = \int_0^1 du' \int_0^1 du \quad \tilde{\psi}_i^l(u')\tilde{K}^+(u',u)\tilde{\psi}_j^k(u) \quad .$$

The second of the two integral equations gives the same number of equations by applying the same method to the equation 2.60 and substituting $\tilde{K}^-$ to $\tilde{K}^+$, ϵ^- to ϵ^+, 0 to $\tilde{H}_i$ and $-1/2$ to $1/2$ before the δ terms.

The new set of equations may be written as a matrix form MX =V such that

$$\begin{bmatrix} \partial M^+ & M^+ \\ \partial M^- & M^- \end{bmatrix} \begin{bmatrix} W_{J_0}^J(\tilde{H}) \\ W_{J_0}^J(\tilde{L}\gamma) \end{bmatrix} = \begin{bmatrix} W_{J_0}^J(\tilde{H}_i) \\ 0 \end{bmatrix}$$

with

$$\left[W_{J_0}^J(f) \right] = \left[C_{J_0}^k(f) \quad D_{J_0}^k(f)...D_{J-1}^k(f) \right]^T \quad .$$

The sub-matrices of M are

$$\partial M^\pm = \pm\frac{1}{2}\begin{bmatrix} \delta_{k,l} & 0 \\ 0 & \delta_{k,l}\delta_{j,i} \end{bmatrix}$$
$$+\begin{bmatrix} <\tilde{\phi}_{J_0}^l\left(u'\right)\left|\gamma(u)\frac{\partial\tilde{K}^\pm}{\partial\tilde{n}}(u',u)\right|\tilde{\phi}_{J_0}^k(u)> & <\tilde{\phi}_{J_0}^l\left(u'\right)\left|\gamma(u)\frac{\partial\tilde{K}^\pm}{\partial\tilde{n}}(u',u)\right|\tilde{\psi}_j^k(u)> \\ <\tilde{\psi}_i^l\left(u'\right)\left|\gamma(u)\frac{\partial\tilde{K}^\pm}{\partial\tilde{n}}(u',u)\right|\tilde{\phi}_{J_0}^k(u)> & <\tilde{\psi}_i^l\left(u'\right)\left|\gamma(u)\frac{\partial\tilde{K}^\pm}{\partial\tilde{n}}(u',u)\right|\tilde{\psi}_j^k(u)> \end{bmatrix} \quad (5.23)$$

and

$$M^\pm = \epsilon_\pm\begin{bmatrix} <\tilde{\phi}_{J_0}^l\left(u'\right)\left|\tilde{K}^\pm(u',u)\right|\tilde{\phi}_{J_0}^k(u)> & <\tilde{\phi}_{J_0}^l\left(u'\right)\left|\tilde{K}^\pm(u',u)\right|\tilde{\psi}_j^k(u)> \\ <\tilde{\psi}_i^l\left(u'\right)\left|\tilde{K}^\pm(u',u)\right|\tilde{\phi}_{J_0}^k(u)> & <\tilde{\psi}_i^l\left(u'\right)\left|\tilde{K}^\pm(u',u)\right|\tilde{\psi}_j^k(u)> \end{bmatrix} \quad (5.24)$$

The rows and columns of each sub-matrix of M are indexed in the same way as the vector $\left[W_{J_0}^J\left(f\right)\right]$ as shown in figure 5.16. The projection is done on the scalet first $\left\{\tilde{\phi}_{J_0}^k\right\}_{k=[0,2^{J_0}-1]}$ and then the wavelets of increasing order $\left\{\left\{\tilde{\psi}_j^k\right\}_{k=[0,2^j-1]}\right\}_{j=[J_0,J-1]}$. The row $l \in \left[0,2^{J_0}\right[$ corresponds to the projection on the scalet $\phi_{J_0}^l$ and the row $2^i + l$ with $l \in \left[0,2^i\right[$ corresponds to the projection on the wavelet $\tilde{\psi}_i^l$. The same is true for k and j respectively to index the columns. Throughout this section (i,l) index the rows and (j,k) index the columns as shown in figure 5.16.

The terms of the matrix which involve a double integration over $[0,1[$ may be evaluated by using a quadrature formula at the points $\left\{m/2^J\right\}_{m\in[0,2^J[}$. In this case the matrix terms are equivalent to the ones obtained by the wavelet transform method presented in the previous section 5.2.

5.3.1.3   The evaluation of the matrix M

We want to profit by the vanishing moments of the Coifman scalets and wavelets to evaluate directly the matrix M, equations 5.23 and 5.24. The functions which admit a polynomial expansion on an interval of size $(D-1)/2^{J_0}$, have Coifman scalet and wavelet coefficients which verify the equations 5.16 and 5.17 respectively. The functions of interest are the value of the Green function and its derivative at the points $\vec{r}(u) = (ud, y_D(ud))$ and $\vec{r}(u')$ of the surface, equations 5.19 and 5.20. The periodic Green functions are smooth functions except at the singularity $u = u'$ and $|u-u'| = 1$. It is therefore interesting to split the periodic Green function $\tilde{K}^\pm$ in two parts:

- the part $G_0^\pm$ containing the singularity

$$\begin{array}{lll} \text{if} & u' \approx u & G_0^\pm(u',u) = G^\pm(u',u) \\ \text{if} & u' \approx u \pm 1 & G_0^\pm(u',u) = G^\pm(u',u\pm1) \end{array}$$

with $G^\pm$ the non-periodic Green function, equation 2.15.

- the part far from the singularity $G_d^\pm = \tilde{K}^\pm - G_0^\pm$.

Figure 5.16: *Sketch of the sub-matrices of M, equations 5.23 and 5.24. On the left is indicated the wavelet subspaces on which the Green function is projected with respect to u' and on the right the index of the row $2^i + l$ corresponding to the basis function $\tilde\psi_i^l$. Above the matrix is indicated the wavelet subspaces on which the Green function is projected with respect to u and below the matrix is indicated the index of the row $2^j + k$ corresponding to the basis function $\tilde\psi_j^k$.*

The profile function y_D may be responsible for additional not smooth enough points $\vec{r}_a = (u_a d, y_D(u_a d))$ which prevent the Green function $\tilde K^\pm(u', u)$ (or its derivative) from being expanded as a polynomial of order P at u_a over an interval of width $6P/2^{J_0}$. Fortunately, it is possible to evaluate analytically the integrated functions $\tilde K^\pm$ and $\frac{\partial \tilde K^\pm}{\partial \tilde n}$, equations 5.19 and 5.20, to determine which points are critical.

The inner product of two functions is done by an integration over $[0,1[$. If the inner product is done with a scalet or wavelet basis function which are null outside their support by definition, the integration is reduced to the one over the support of the basis function . The periodic Coifman scalet and wavelet of scale parameter j and shift parameter k have a support $\tilde S_j^k$. The intersection of that support with the interval $[0,1[$, $\tilde S_j^k \cap [0,1[$ may be split in

two parts depending on the value of k and the limits of the integral are modified accordingly

$$0 \le k < 2P \qquad \tilde{S}_j^k \cap [0,1[= \left[0, \frac{k+4P-1}{2^j} \right[\cup \left[\frac{-2P+k}{2^j} + 1, 1 \right[$$

$$2P \le k \le 2^j - 4P + 1 \qquad \tilde{S}_j^k \cap [0,1[= \left[\frac{-2P+k}{2^j}, \frac{k+4P-1}{2^j} \right[$$

$$2^j - 4P + 1 < k \le 2^j \qquad \tilde{S}_j^k \cap [0,1[= \left[0, \frac{k+4P-1}{2^j} - 1 \right[\cup \left[\frac{-2P+k}{2^j}, 1 \right[$$

The integration of the inner product with the basis functions $\tilde{\psi}_j^k$ or $\tilde{\phi}_j^k$ on [0,1[may then be reduced to the compact support $\tilde{S}_j^k \cap [0,1[$ for all the terms of the matrix M.

First, we consider the case of a sufficiently smooth profile such that the singularity $u = u'$ of the Green function is the only point which prevents a polynomial expansion of the Green functions. $G_d^\pm(u',u)$ and $\gamma(u) \frac{\partial G_d^\pm}{\partial \tilde{n}}(u',u)$ may be developed as a polynomial everywhere on the profile (it satisfies the equation 5.11 for all (u',u)). $G_0^\pm(u',u)$ and $\gamma(u) \frac{\partial G_0^\pm}{\partial \tilde{n}}(u',u)$ may also be, except around $u' = u$ and $|u - u'| = 1$ (it satisfies the equation 5.11 for all (u',u) with $u' \ne u$ and $u' \ne u \pm 1$).

The evaluation of the top-left block $\langle \tilde{V}_{J_0} | \tilde{K}^\pm | \tilde{V}_{J_0} \rangle$ **of the sub-matrices** $M^\pm$ We present here how to calculate the terms in the top-left corner of the matrix $M^\pm$ which contains the inner products with the scalet basis functions only. We consider first the part due to the periodization of the Green function, $G_d^\pm$, which is smooth everywhere at the surface. For each inner product, we apply the expression of the inner product of the scalet basis function with a function expanded as a polynomial, equation 5.16,

$$\forall k,l \in [0, 2^{J_0}[^2 \qquad \left\langle \tilde{\phi}_{J_0}^l \left(u' \right) \middle| G_d^\pm(u',u) \middle| \tilde{\phi}_{J_0}^k(u) \right\rangle = \sqrt{2^{-J_0}} \left\langle G_d^\pm \left(\frac{l}{2^{J_0}}, u \right) \middle| \tilde{\phi}_{J_0}^k(u) \right\rangle + O\left(h^{2P} \right)$$

$$= 2^{-J_0} G_d^\pm \left(\frac{l}{2^{J_0}}, \frac{k}{2^{J_0}} \right) + O\left(h^{2P} \right) \quad .$$

The inner product with the non-periodic part, on the other hand is, $\forall l,k \in [0, 2^{J_0} - 1]^2$

$$\left\langle \tilde{\phi}_{J_0}^l \left(u' \right) \middle| G_0^\pm(u',u) \middle| \tilde{\phi}_{J_0}^k(u) \right\rangle = \int_{\tilde{S}_{J_0}^l \cap [0,1[} du' \int_{\tilde{S}_{J_0}^l \cap [0,1[} du \quad \tilde{\phi}_{J_0}^l \left(u' \right) G_0^\pm(u',u) \tilde{\phi}_{J_0}^k(u) \quad .$$

The singularity of $G^\pm$ at zero makes it impossible to develop the Green function as a polynomial. We thus have to identify the inner product where the supports $\tilde{S}_{J_0}^l$ and $\tilde{S}_{J_0}^k$ overlap, in order to treat this case separately.

Considering $k \le l$, the support $S_{J_0}^k$ is surrounded by $S_{J_0}^l$ on the right and $S_{J_0}^{l-2^{J_0}}$ on the left as shown in figure 5.17. There is no over-lapping of the two supports if and only if

$$\begin{cases} \frac{k+4P-1}{2^{J_0}} \le \frac{-2P+l}{2^{J_0}} & \Leftrightarrow & 6P-1 \le l-k \\ \frac{4P-1+l-2^{J_0}}{2^{J_0}} \le \frac{-2P+k}{2^{J_0}} & \Leftrightarrow & 2^{J_0} - 6P + 1 \ge l-k \end{cases} \quad .$$
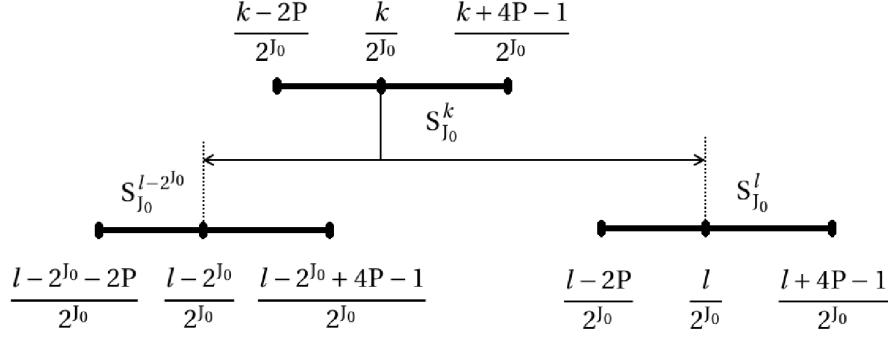
Figure 5.17: *Sketch of the supports of* $\tilde{\phi}_{J_0}^l$ *and* $\tilde{\phi}_{J_0}^k$, $\tilde{S}_{J_0}^l$ *and* $\tilde{S}_{J_0}^k$ *respectively, when* $k \in [l - 2^{J_0}, l[$. *The distance between the two dashed lines is the period equal to 1.*

On the contrary if $k \geq l$, the support $S_{J_0}^k$ is surrounded by $S_{J_0}^{l+2^{J_0}}$ on the right and $S_{J_0}^l$ on the left. The condition to have the singularity outside of the support is then $2^{J_0} - 6P + 1 \geq |l - k| \geq 6P - 1$ and in that case $G_0^{\pm}$ is considered smooth. The equation 5.16 may then be applied two times, for each inner product and the result is similar to the one of the matrix $G_d^{\pm}$

$$2^{J_0} - 6P + 1 \geq |l - k| \geq 6P - 1 \qquad \left\langle \tilde{\phi}_{J_0}^l\left(u'\right) \middle| G_0^{\pm}(u', u) \middle| \tilde{\phi}_{J_0}^k(u) \right\rangle = 2^{-J_0} G_0^{\pm}\left(\frac{l}{2^{J_0}}, \frac{k}{2^{J_0}}\right) + O\left(h^{2P}\right) \quad .$$

Otherwise the term cannot be approximated analytically and has to be evaluated numerically.

The evaluation of the other blocks of the sub-matrices $M^{\pm}$ We detail the case of the rest of the sub-matrices M, equations 5.23 and 5.24, which have at least one inner product with a wavelet i.e. the blocks $\langle \tilde{V}_{J_0} | \tilde{K}^{\pm} | \tilde{W}_j \rangle$, $\langle \tilde{W}_i | \tilde{K}^{\pm} | \tilde{V}_{J_0} \rangle$ and $\langle \tilde{W}_i | \tilde{K}^{\pm} | \tilde{W}_j \rangle$. We consider again the smooth part $G_d^{\pm}$ of the Green function, first. As the inner product of a function expanded as a polynomial with a wavelet is equal to zero, equation 5.17, we have $\forall i \quad \forall j$

$$\forall k \quad \forall l \quad \left\langle \tilde{\psi}_i^l\left(u'\right) \middle| G_d^{\pm}(u', u) \middle| \tilde{\psi}_j^k(u) \right\rangle = 0 + O\left(h^{2P}\right) \quad ,$$

$$\left\langle \tilde{\psi}_i^l\left(u'\right) \middle| G_d^{\pm}(u', u) \middle| \tilde{\phi}_{J_0}^k(u) \right\rangle = 0 + O\left(h^{2P}\right) \quad ,$$

$$\left\langle \tilde{\phi}_{J_0}^l\left(u'\right) \middle| G_d^{\pm}(u', u) \middle| \tilde{\psi}_j^k(u) \right\rangle = 0 + O\left(h^{2P}\right) \quad .$$

The Green function $G_0^{\pm}$ containing the singularity has, once again, to be treated differently when the supports of the two inner products overlap and the Green function diverges. The projection on two subspaces of scale parameter i and j, requires evaluating the inner product with two basis functions whose supports are $\tilde{S}_i^l$ and $\tilde{S}_j^k$. Let us see when these two supports overlap. The support S_j^k is centered around $k/2^j$. We have to compare its position with the center of S_i^l which is $l/2^i$. If $k/2^j \leq l/2^i$, the support S_j^k is surrounded by S_i^l on

198
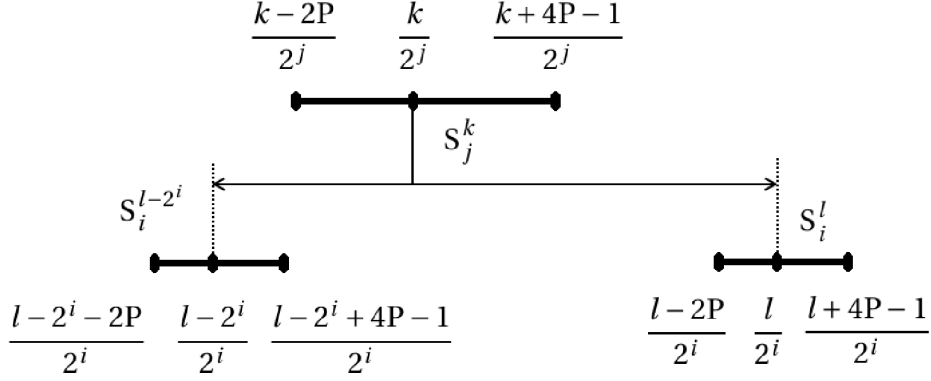
Figure 5.18: *Sketch of the supports $\tilde{S}_i^l$ and $\tilde{S}_j^k$, when $k \in [2^{j-i}l - 2^j, 2^{j-i}l[$. The distance between the two dashed lines is the period equal to 1.*

the right and $S_i^{l-2^i}$ on the left as shown in figure 5.18. There is no over-lapping of the two supports if and only if

$$
\begin{cases}
\frac{k+4P-1}{2^j} \le \frac{-2P+l}{2^i} & \Leftrightarrow & 2^i(4P-1) + 2^j(2P) \le 2^j l - 2^i k \\
\frac{l+4P-1-2^i}{2^i} \le \frac{-2P+k}{2^j} & \Leftrightarrow & 2^{j+i} - 2^i(2P) - 2^j(4P-1) \ge 2^j l - 2^i k
\end{cases}
$$

On the contrary, if $k/2^j \ge l/2^i$, the support S_j^k is surrounded by $S_i^{l+2^i}$ on the right and S_i^l on the left. The condition becomes

$$
\begin{cases}
\frac{k+4P-1}{2^j} \le \frac{-2P+l+2^i}{2^i} & \Leftrightarrow & 2^{i+j} - 2^i(4P-1) - 2^j(2P) \ge 2^i k - 2^j l \\
\frac{l+4P-1}{2^i} \le \frac{-2P+k}{2^j} & \Leftrightarrow & 2^i(2P) + 2^j(4P-1) \le 2^i k - 2^j l
\end{cases}
$$

Each condition corresponds to a band in the sub-matrix corresponding to the projection on the block $\langle \tilde{V}/\tilde{W}_i | \tilde{V}/\tilde{W}_j \rangle$, respectively above or below the diagonal of the block $2^j l - 2^i k = 0$. We call Zeros(l,i,k,j) the set of integer values such that the indexes (l,i,k,j) correspond to two supports $\tilde{S}_i^l$ and $\tilde{S}_j^k$ which do not overlap

$$
\text{Zeros}(l, i, k, j) = i, j \in [J_0, J[^2 \quad l, k \in [0, 2^i[[0, 2^j[\quad \backslash
$$
$$
\begin{cases}
2^j l - 2^i k \ge 0 & 2^i(4P-1) + 2^j(2P) \le 2^j l - 2^i k \le 2^{j+i} - 2^i(2P) - 2^j(4P-1) \\
2^i k - 2^j l \ge 0 & 2^i(2P) + 2^j(4P-1) \le 2^i k - 2^j l \le 2^{i+j} - 2^i(4P-1) - 2^j(2P)
\end{cases}
$$

Therefore the singularity is outside of the integration path if the indexes belong to Zeros(l,i,k,j). The Green function $G_0^\pm$ is then considered smooth and, for one of the inner product of $G_0^\pm$ with a wavelet basis function, we apply once more the equation 5.17, $\forall i, j$ and $\forall k, l$ belonging to Zeros(l,i,k,j)

$$
\left\langle \tilde{\psi}_i^l \left(u' \right) \left| G_0^\pm(u', u) \right| \tilde{\psi}_j^k(u) \right\rangle = 0 + O\left(h^{2P} \right) \quad ,
$$
$$
\left\langle \tilde{\phi}_{J_0}^l \left(u' \right) \left| G_0^\pm(u', u) \right| \tilde{\psi}_j^k(u) \right\rangle = 0 + O\left(h^{2P} \right) \quad ,
$$
$$
\left\langle \tilde{\psi}_i^l \left(u' \right) \left| G_0^\pm(u', u) \right| \tilde{\phi}_{J_0}^k(u) \right\rangle = 0 + O\left(h^{2P} \right) \quad .
$$

Summary on the matrix structure To summarize, the sub-matrices of M, equations 5.23 and 5.24, may be divided into blocks which contain the projection of the Green function on the scalet and wavelet subspaces. The structure is the same as in the previous method as shown in figure 5.19. The division between the projection on different scalet and wavelet subspaces is represented in black solid lines and the scalet and wavelet subspaces are indicated above and on the left of the matrix. We distinguish the areas far and close to the singularity of the Green function which correspond to the areas far and close to the diagonal of each block respectively, by a change of color. The diagonal of each block is represented as black dashed lines.
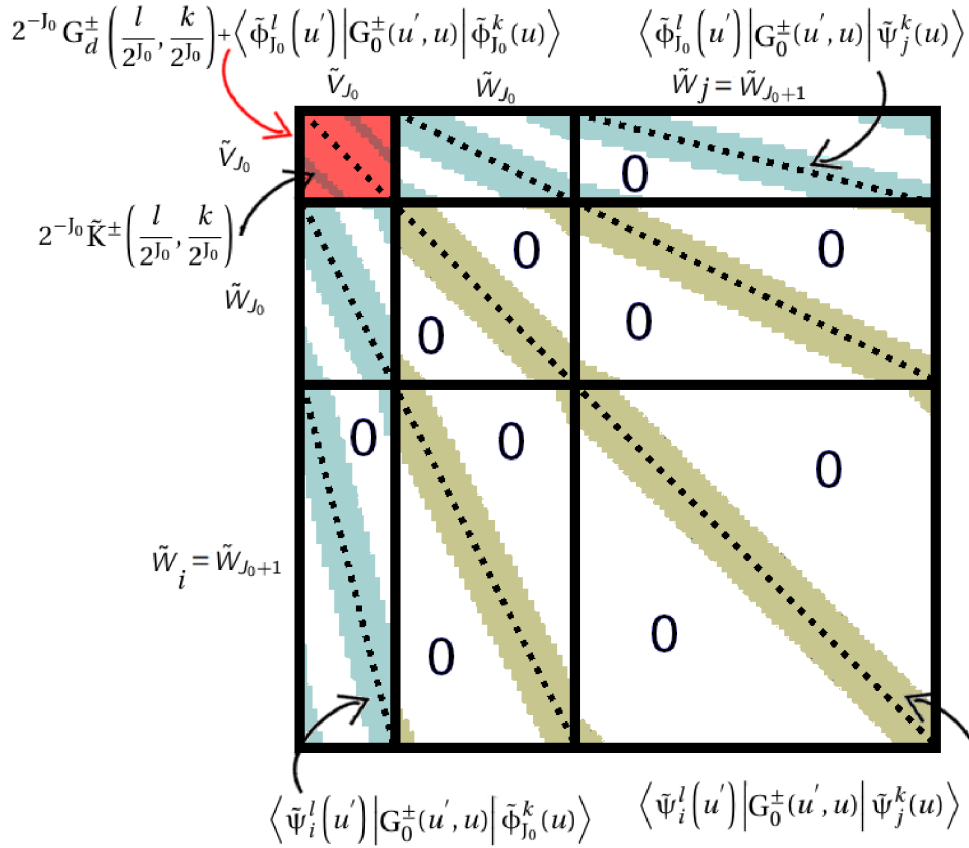
Figure 5.19: *Sketch of the sub-matrices of M, equations 5.23 and 5.24, with the use of the Coiflets. The indexes of the matrix are the same as in figure 5.16. On the left are indicated the subspaces corresponding to the projection with respect to u' and above the matrix is indicated the subspaces corresponding to the projection with respect to u. The dashed lines indicate the diagonals of each block.*

The red area corresponds to the scalet-scalet inner products. For all $k, l \in [0, 2^{J_0}[^2$

$$\mathrm{M}^\pm(l, k) = \pm\frac{1}{2}\delta_{l,k} + \left\langle \tilde\phi_{J_0}^l\left(u'\right) \middle| \tilde{\mathrm{K}}^\pm(u', u) \middle| \tilde\phi_{J_0}^k(u) \right\rangle$$

The terms of the sub matrix $M^\pm$ far from the diagonal (dark red area) are expressed, $\forall k, l$ such that $2^j - 6P + 1 \geq |l - k| \geq 6P - 1$, as

$$\left\langle \tilde{\phi}_{J_0}^l \left(u'\right) \left| \tilde{K}^\pm(u',u) \right| \tilde{\phi}_{J_0}^k(u) \right\rangle = 2^{-J_0} \tilde{K}^\pm \left(\frac{l}{2^{J_0}}, \frac{k}{2^{J_0}} \right) + O\left(h^{2P} \right) \quad .$$

Elsewhere in the top-left square (bright red areas), the terms of the sub matrix $M^\pm$ close to the diagonal are

$$\left\langle \tilde{\phi}_{J_0}^l \left(u'\right) \left| \tilde{K}^\pm(u',u) \right| \tilde{\phi}_{J_0}^k(u) \right\rangle = 2^{-J_0} G_d^\pm \left(\frac{l}{2^{J_0}}, \frac{k}{2^{J_0}} \right) + \left\langle \tilde{\phi}_{J_0}^l \left(u'\right) \left| \tilde{G}_0^\pm(u',u) \right| \tilde{\phi}_{J_0}^k(u) \right\rangle + O\left(h^{2P} \right) \quad .$$

The rest of the matrix corresponds to the inner products with at least one wavelet basis function. The white areas are the areas far from the diagonal and the corresponding terms are all null. The indexes of the null term of the matrix then belong to Zeros(l,i,k,j). The blue and brown areas, on the contrary, are the ones surrounding the singularity where the inner product of the basis function with the singular part of the Green function $G_0^\pm$ has to be evaluated numerically.

The first row of blocks, except the red one, is scanned by $l \in \left[0, 2^{J_0}\right[$ and for all $j \in [J_0, J[$, $k \in \left[0, 2^j\right[$

$$M^\pm(l, 2^j + k) = \begin{cases} i, l, j, k \in \text{Zeros}(i, l, j, k) & 0 + O\left(h^{2P} \right) \\ \text{else} & \left\langle \tilde{\phi}_{J_0}^l \left(u'\right) \left| \tilde{G}_0^\pm(u',u) \right| \tilde{\psi}_j^k(u) \right\rangle + O\left(h^{2P} \right) \end{cases}$$

and the first column of block, except the first red square, is scanned by $k \in \left[0, 2^{J_0}\right[$ and for all $i \in [J_0, J[, l \in \left[0, 2^i\right[$

$$M^\pm(2^i + l, k) = \begin{cases} i, l, j, k \in \text{Zeros}(i, l, j, k) & 0 + O\left(h^{2P} \right) \\ \text{else} & \left\langle \tilde{\psi}_i^l \left(u'\right) \left| \tilde{G}_0^\pm(u',u) \right| \tilde{\phi}_{J_0}^k(u) \right\rangle + O\left(h^{2P} \right) \end{cases}$$

The last blocks are for all $i, j \in [J_0, J[, l \in [0, 2^i[$ and $k \in [0, 2^j[$

$$M^\pm(2^i + l, 2^j + k) = \pm \frac{1}{2} \delta_{l,k} \delta_{i,j}$$
$$+ \begin{cases} i, l, j, k \in \text{Zeros}(i, l, j, k) & 0 + O\left(h^{2P} \right) \\ \text{else} & \left\langle \tilde{\psi}_i^l \left(u'\right) \left| \tilde{G}_0^\pm(u',u) \right| \tilde{\psi}_j^k(u) \right\rangle + O\left(h^{2P} \right) \end{cases}$$

The same arguments hold true for the sub-matrix $\partial M^\pm$ by substituting $\gamma \frac{\partial \tilde{K}^\pm}{\partial \tilde{n}}$ to $\tilde{K}^\pm$. The matrices $\partial M^\pm$ have the exact same structure than $M^\pm$ without the identity matrix $\pm 1/2$ I. In the next section, the sparsity of the matrix and the overall efficiency of the method are discussed. There was no time to implement the method and to test it during this PhD. This study therefore aims at assessing the relevance of this method to our problem in the view of a future implementation.

5.3.2 Critical study of the method

5.3.2.1 Technical difficulty of the numerical resolution

The main difference in this method compared to the one using the wavelet transform is that the inner products are not calculated by the discrete wavelet transform but rather individually. The question to address is how to calculate the following terms

$$\left\langle \tilde{\Psi}_i^l(u') \middle| G_0^\pm(u',u) \middle| \tilde{\Psi}_j^k(u) \right\rangle = \int_{\tilde{S}_i^l \cap [0,1[} du' \int_{\tilde{S}_j^l \cap [0,1[} du \quad \tilde{\Psi}_i^l(u') G_0^\pm(u',u) \tilde{\Psi}_j^k(u)$$

where $G_0^\pm$ is the non-periodic Green functions, $G^\pm(u'-u+m, y_D(u')-y_D(u-m))$ with m={−1,0,1}, which is singular over the surface $\tilde{S}_i^l \cap [0,1[\times \tilde{S}_j^l \cap [0,1[$ (the non-periodic Green function is defined by equation 2.15). Pan *et al.* explained that they used a two-dimensional quadrature formula using a number N_I of points $\vec{r}_i = (u'_i, u_i)$

$$\int_S du' \int_S du f(u',u) = 4h^2 \sum_{i=0}^{N_I} w_i f(u'_i, u_i) + O(h^4) \quad ,$$

with h the step and w_i the weights, in order to calculate the inner products [141]. In particular, they used the generalized Gaussian quadrature [145]. They reported needing only N_I = 5 points in order to have a sufficient accuracy. This is due to the fact that they study shallow surfaces and their discretization step is of the order of magnitude of $\lambda/4$. The required number of points N_I may be much larger than 5 in our case since our discretization step is around $\lambda/100$ or even less. As the Green function $G^\pm$ is considered near the singularity, the asymptotic behavior of the Hankel function near the origin may be used instead of the Hankel function which is costly to evaluate. The quadrature formula may be chosen so that it fits the asymptotic behavior of the Green function near the origin in order to optimize the number N_I of points which are necessary to evaluate the inner product accurately.

Attention must be paid to the fact that we have assumed that the integrated functions $\tilde{K}^\pm$ and $\frac{\partial \tilde{K}^\pm}{\partial \tilde{n}}$, equations 5.19 and 5.20, are smooth at a resolution 2^{-J_0} and therefore accurately described by a projection on the subspace $\tilde{V}_{J_0}$. If abrupt variations of the profile function y_D were to contradict this assumption, other nonzero terms than the diagonal band of each block would be missing. Fortunately both the Green function and the profile function are known analytically and the scale parameter J_0 may be chosen from the beginning to be high enough so that the condition to be considered as smooth, equation 5.11, is fulfilled. In his simulation, Pan uses 4 scalets per wavelength λ for a surface whose typical dimensions are of the order of 0.5λ [141]. If one supposes that there is the same scale ratio between its simulation and the one of Pan, for surfaces having typical dimensions of $\lambda/500$, one can assume that 1000 scalets per λ are required. For $\lambda \approx 500$ nm, the scalets would be separated of 0.5 nm. One can then make the very rough approximation that $d2^{-J_0} \approx 1$ nm. For a period d=230 nm, a scale parameter J_0=8 would be necessary. The approximation seems in agreement with the fact that the smooth part of the magnetic field is well described in the scalet subspace $\tilde{V}_8$ on a grating of period d=230 nm as shown in figure 5.3.

In the method using the coiflets, each nonzero diagonal term of the different blocks makes it necessary to perform a numerical integration. To find an efficient way to do so would be highly desirable. In the next paragraph, we evaluate the memory space that would be needed if the method was implemented.

5.3.2.2 Sparsity of the matrix

The sparse structure of the matrix in this method is determined before filling it. The sparsity may then be evaluated from the start. Let us examine the number of null terms for each block of a sub-matrix $M^\pm$ corresponding to the projection on two scalet or wavelet subspaces. The block of the projection on the scalet subspaces $\langle \tilde{V}_{J_0} | \tilde{K}^\pm | \tilde{V}_{J_0} \rangle$ is dense and has 2^{2J_0} coefficients. In each of the blocks corresponding to the projection on two wavelet subspaces $\langle \tilde{W}_i | \tilde{K}^\pm | \tilde{W}_j \rangle$ (or a scalet and a wavelet subspace) of scale parameters i and j, the nonzero terms form three bands. To evaluate the number of terms in the three bands of one of these blocks, one may count the number of nonzero terms in the first row of the block and multiply it by the number of rows of the block. Let us detail the counting. The set of the indexes of the null terms of the first row are given by Zeros(0,i,k,j) as

$$2^i(2P) + 2^j(4P-1) \le 2^i k \le 2^{i+j} - 2^i(4P-1) - 2^j(2P) \quad .$$

The nonzero terms of the first row are thus in the intervals $2^{-i} \left[0, 2^i(2P) + 2^j(4P-1) \right[$ and $2^{-i} \left[2^{i+j} - 2^i(4P-1) - 2^j(2P), 2^{i+j} \right[$ which gives

$$2^{-i} \left(2^i(2P) + 2^j(4P-1) + 2^{i+j} - (2^{i+j} - 2^i(4P-1) - 2^j(2P)) \right)$$

coefficients in the first row. Lastly, we multiply by the number of row, 2^i, and we obtain the number of nonzero terms in a block of size $2^i \times 2^j$

$$2^i(2P) + 2^j(4P-1) + 2^i(4P-1) + 2^j(2P) = \left(2^i + 2^j \right)(D-1) \quad .$$

The total number of terms of the matrix is the number of terms in $\langle \tilde{V}_{J_0} | \tilde{K}^\pm | \tilde{V}_{J_0} \rangle$, twice the number of terms in $\langle \tilde{W}_i | \tilde{K}^\pm | \tilde{V}_{J_0} \rangle$ and the number of terms in $\langle \tilde{W}_i | \tilde{K}^\pm | \tilde{W}_j \rangle$ for all $i, j \in [J_0, J[$. Hence, the total number of terms is

$$N_{M_{Coiflet}}(J, J_0) = 2^{2J_0} + 2 \left(\sum_{i=J_0}^{J-1} \left(2^i + 2^{J_0} \right)(D-1) \right) + \sum_{i=J_0}^{J-1} \sum_{j=J_0}^{J-1} \left(2^i + 2^j \right)(D-1) \quad . \tag{5.25}$$

For $J \gg J_0$, the number of points $N_{M_{Coiflet}}(J, J_0)$ is proportional to $JD2^J$. By comparison the number of nonzero terms in a quarter of the matrix M in the Maradudin method is 2^{2J} for 2^J unknowns .

We now want to compare the memory space required by this method using the Coiflets (4 $N_{M_{Coiflet}}(J, J_0)^2$ stored terms) with the memory space available on a laptop with 4 Go of RAM. To store a term in a sparse matrix requires storing as well its index, an integer value, so
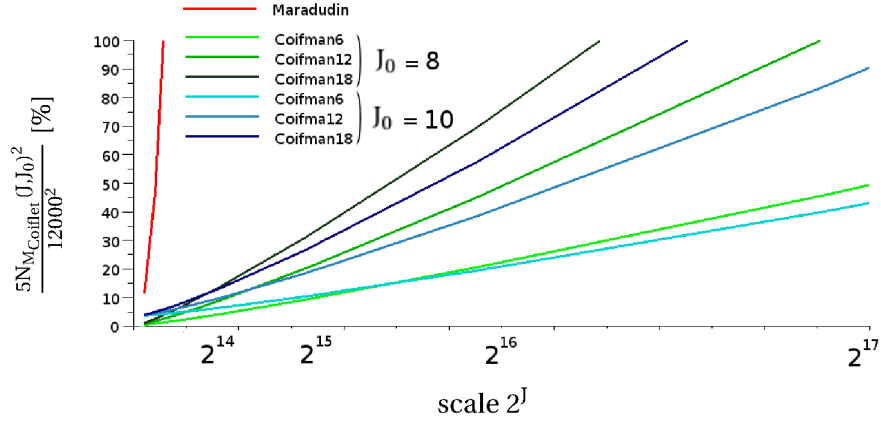
Figure 5.20: *Occupied memory space of* $M_{Coiflet}$ *is estimated as* $\frac{5N^2_{M_{Coiflet}}(J,J_0)}{12000^2}$, *equation 5.25, as a function of the scale* 2^J *with the Coifman of order 6,12 and 18 and two scale parameters* J_0 *of the scalet subspace* $J_0=8$ *and* $J_0=10$.

the number of terms is multiplied by a coefficient 1.25 (two doubles are 16 octets whereas one integer is 4 octets). The dense matrices which can be solved with 4 Go of RAM, have a maximum size of about 12000 (the complex terms are stored as two doubles). The percentage of occupied memory space is therefore estimated as the occupied memory space, 5 $N_{Coiflet}(J,J_0)^2$, out of the maximum memory space, 12000^2. We plotted the percentage of occupied memory space of the final matrix $M_{Coiflet}$ as a function of the scale 2^J in figure 5.20. Two scale parameters $J_0=8$ (green lines) and $J_0=10$ (blue lines) of the scalet subspaces are chosen to represent the cases of two surfaces with a period $d \approx 250$ nm and $d \approx 500$ nm with the rough assumption $d2^{-J_0} \approx 1$ nm. Three orders of the Coifman wavelet D=6, 12 and 18 are compared in the figure, the higher order being represented by the darkest line. We observe that the darkest lines are above the lightest. Indeed, the higher the order is, the larger the support is and the memory space increases with the order D=6P. This is in agreement with $N_{M_{Coiflet}}(J,J_0)$ being proportional to the order D as shown in equation 5.25. If the depth $J - J_0$ is small, the matrices with the lowest J_0 (blue curves) are the sparsest. However, as the dept $J - J_0$ increases (the depth increases with the scale 2^J in the figure), there is more and more nonzero diagonals in the matrix and the tendency reverses. Indeed, for the identical scale $J =16$, the matrix with a larger scale parameter $J_0=10$ (blue curve) has a smaller depth $J - J_0$ and less nonzero terms than the matrix with $J_0=8$ (green curve). In the end, the projection of the needed memory space when using this method shows that more complex systems or systems with sharper variations should be possible to study as it is possible to store matrices with a scale parameter as high as J=17.

Regardless of the exact number of scalets per period which is necessary, to study larger systems would require increasing the scale parameter J_0 of the scalet subspace. The step between the scalet basis functions, equally spaced over the period d, is $d/2^{J_0}$. To keep $d/2^{J_0}$ constant, the scale parameter J_0 has to be increased of one each time the period d doubles.

204

Therefore, J_0 is the parameter that gives the upper limit of the period d in this method. Let us give an estimation of this upper limit. As the block which contains the projection on the scalet subspace of size $2^{J_0} \times 2^{J_0}$ is dense, J_0 has to be inferior or equal to 12 (a dense matrix $2^J \times 2^J$ with $2^J = 2^{13}$ cannot be stored). In that case, based on the assumption that $d2^{-J_0} \approx 1$ nm, surfaces whose length is of the order of magnitude of d $\sim 4\mu$m may be studied. To have a scale parameter for the scalet subspace of J_0=12 and the highest scale parameter J=16 would occupy around 70% of the computer memory space with a Coifman scalet of order 6. Therefore, this method should enable us to store the matrix of EM problems for metallic surfaces of 1-2 microns with nano-scale roughness of the order of magnitude of a ten of nanometers with sharp variations.

Lastly, let us say a few words on the number of cycles that would be necessary to fill the matrix and then to solve it. The terms of the $2^{J_0} \times 2^{J_0}$ block which contains the projection on the scalet subspace have the same expression as the ones in the Maradudin method. The number of cycles that one needs to evaluate them, is the same. The difference of time spent to fill the rest of the matrix between the two methods depends on the number of cycles needed to calculate the nonzero diagonal terms in the method using Coiflets. The optimization of the double integration is therefore very important. We saw that the average number of terms in the method using Coiflets is proportional to $JD2^J$ instead of 2^{2J} in the Maradudin method. As long as the number of operations for calculating the double integral in the nonzero diagonal terms is not of the order of magnitude of 2^J, the filling time should be smaller than the one in the Maradudin method. As for the issue of the time spent to solve the system, it is the same as the one in the method using the wavelet transform. In the same way, the spent time may be improved by using an iterative method. To be realistic, the time of the resolution has to be improved if one wants to use the highest scale of 2^{16} as the number of cycles of the resolution is of the order of magnitude of 2^{16} cubed. We note that, for a system composed of isolated grooves, the optimization of the number of unknowns that was applied to the method using the wavelet transform may be applied in the same way in order to reduce the number of cycles necessary for the resolution.

To conclude, despite the lack of time to implement the method presented here, we performed a detailed analysis of it. This last method which uses Coiflets, seems the most appropriate for solving large problems with surfaces of nano-scale roughness as it may improve the original method both in the memory space and the time requirements.

5.4   Conclusion

In this chapter, we first saw how to make use of the wavelets with our Fredholm integral equations of the second kind of the source functions $\tilde{H}$ and $\gamma\tilde{L}$. The wavelet expansion of the source functions in different levels of details enables to treat separately the source function on the flat or smooth surface from the one on the strongest irregularities. The global description of the source function may be grabbed by its projection on a scalet subspace of

scale J_0. The sharp variations of the source function at the location of the abrupt variations of the surface profile are obtained by the projection on complementary wavelet subspaces of higher order.

Two methods which use wavelets have been presented: the first one rests on the discrete wavelet transform, DWT, and the second one on the use of the Coiflets as an expansion basis function and a testing function. The implementation of the first method showed that the problem may be solved in the wavelet basis and that the sparsity of the matrix in the wavelet basis is high with about 95% null terms. The optimization of the wavelet expansion as a function of the location over the surface reduced the number of unknowns of a problem which needed 4096 unknowns in the Maradudin method down to 736 unknowns. We thus confirmed the relevance of the wavelet expansion to our problem. This method, however, proved to be very costly in time in order to have a gain in occupied memory space.

Lastly, the Pan method using the vanishing moments of the Coiflets draw our attention [140]. The principles of this method were presented and a brief study of its time and memory space requirements was done. Due to the high number of vanishing moments of the Coiflets wavelet and scalet, the matrix terms in the wavelet basis may be evaluated straightforwardly. The sparse structure of the matrix in the wavelet basis is known prior to the filling. The method thus do not require calculating the whole matrix to select the nonzero terms afterward as it is done with the DWT. The matrix corresponding to the expansion of the unknowns on the subspace $\tilde{V}_J$ of the Coiflet of order D contains approximately $2^J JD$ terms. The total number of unknowns may be reduced in the same way as in the method using the DWT, reducing further the occupied memory but also the time spent to solve the matrix. These arguments lead us to believe this method may enable one to treat problems with surfaces of 1-2 microns with a nano-scale roughness. Prior to the implementation of this method, the question of the calculation of the inner product of the wavelet basis function with the Green function near the singularity has to be addressed. As we deal with rough surfaces contrary to Pan who applied the method to surfaces with smaller roughnesses [141], this issue may be more difficult to tackle.

General Conclusion and Outlook

General conclusion

In this thesis, the optical properties of metallic surfaces with nano-scale roughness were studied based on the former results of our group. On the surface of cold films, grown at low temperatures, crevices of a few nanometers wide and severals nanometers deep are formed between metallic pillars separated by 5-15 nm. At low temperature, the cold films exhibit simultaneously Abnormal Optical Absorption and Surface Enhanced Raman Scattering in the visible spectral range.

Prior to this thesis, these surfaces have been studied by considering metallic gratings with rectangular grooves as a model system. The EM modeling of these gratings with the exact modal method shows that there exists a channeled SPP wave along the walls of the groove for which the groove plays the role of a Fabry-Perot resonator. The resonance of the waveguided SPP wave results in a standing surface plasmon wave in the rectangular grooves which belongs either to an optical or an electrostatic regime depending on the width of the groove. In the optical regime, for grooves whose width is greater than 10 nm, the surface plasmon standing wave behavior is similar to the one of light and the Fabry-Perot resonance happens for depth h of the groove similar to the wavelength of excitation λ. In the electrostatic regime, for grooves whose width is under 10 nm, the wavevector of the surface plasmon standing wave is greatly enhanced compared to the one of light $\Lambda_0 >> k_0$ and the Fabry-Perot resonance therefore happens for very small depth $h << \lambda$. Moreover, in the electrostatic regime, the electric field is greatly enhanced compared to the incident one $|E| >> |E_0|$ and the electromagnetic enhancement factor of the resonance is close to the one of SERS $|E/E_0|^4 \simeq 10^6 - 10^8$. The high electric field is also responsible for high energy losses of the exciting incident field and results in a reflectivity near zero. Rectangular grooves way smaller than the wavelength may then support electrostatic resonances whose behavior explains some observations made for the SERS effect and the Abnormal Optical Absorption on rough surfaces.

We developed the surface integral equations method and implemented it in order to study profiles of arbitrary shape which are closer to the surface of cold films. Proceeding by analogy, we showed that electrostatic resonances are not limited to the rectangular grooves since tiny Gaussian grooves may resonate in the same way by supporting a standing SPP

wave and exhibit similar optical behavior. The plasmonic resonance of the Gaussian groove, whose width is a few nanometers and whose depth is a ten of nanometers, have the same characteristics as the rectangular groove in the electrostatic regime: a wavevector of the standing SPP wave greatly enhanced compared to the one of light which is shown by the resonance in the visible spectral range, an electric field greatly enhanced $|E| \simeq 100|E_0|$ and a dip in the reflectivity close to zero. Such a value of the electric field is able to give rise to the SERS effect with an expected enhancement factor of $|E/E_0|^4 \simeq 10^8$. A random repartition of 5 grooves of 1-2 nm wide and about 10 nm deep on a metallic surface showed that a spectrally broad absorption in the reflectivity similar to the AOA of the cold films is reproduced. In the same spectral range that of the broad absorption, a huge electric field at the bottom of the grooves is susceptible to play the role of active sites in the SERS effect.

The main work in this thesis was to address the question of the accurate calculation of the EM field to get these results and to treat even more larger surfaces. The difficulty lies in the existence of hot-spots at the resonance. The solutions we try to obtain, the magnetic field in the near field of the grooves, have very sharp variations which makes it harder to represent it with a few points and moreover to find it as the solution of a system of linear equations.

The surface integral equation method suited the needs for the modeling of the calculation of the steady-state EM solutions for an incident TM polarized plane wave impinging on a metallic surface of arbitrary shape. In order to study gratings, a periodic SIE was preferred. It prevents border effects and thus ensure to have an exact solution. The periodic SIE also enables to study smaller length of surface in order to study small features in a very detailed way. The changes that were performed concerns mostly the Green function. The calculation of the pseudo-periodic Green functions required the use of three different expressions as a sum of Hankel function, a sum of plane waves and a sum of Lattice sums. Each is used for specific conditions in order to optimize the number of operations needed to evaluate these pseudo-periodic Green function. All the specifics to calculate the fields in the whole space and the reflectivity were also examined.

In the SIE method, the values of the magnetic field and its derivative at N points of the discretized metallic surface are obtained numerically through the resolution of a linear set of 2N equations. The resolution is done by solving a dense matrix of size 2N by 2N with a LU decomposition. To solve the problem of a single groove grating of period d=30 nm, it may require 1000 points, so tens of thousands of points may be required to solve a system with a metallic surface length of 1 μ m. This is due to the high electric field enhancement which causes abrupt variations of the magnetic field and requires discretization steps of the metallic surface of the order of magnitude of $\lambda/1000$. The dense matrix is long to fill (N^2 operations) and to solve (N^3 operations) and occupies a lot of memory space (N^2). The SIE method is thus limited to small systems.

We aimed at improving the resolution performances and the expansion of the unknowns on the wavelet bases offers such a perspective. We showed that the projection of

the source functions on complementary wavelet bases of different resolutions enables to describe the solution with a sparse vector. The SIE matrices were also sparsified using a Discrete Wavelet Transform with a considerable gain in memory space. Indeed, the high localization of the hot-spots at the location of the grooves is responsible for an increased need of resolution, but only locally. Once the global shape of the solution is captured by a low resolution scalet subspace, only few wavelet basis functions are necessary to describe the sharp variations at the grooves. Based on that, we were also able to reduce the number of unknowns required to solve the system. Unfortunately, this method takes a long time to perform in exchange of a gain in the memory space. These results have nevertheless confirmed that a gain in the occupied memory space can be obtained by the application of the wavelets to the SIE in view of treating larger systems.

Outlook

The wavelet method using Coiflets directly as an expansion and test basis function appears as a very promising candidate to replace the wavelet transforms. The method makes use of the vanishing moments for both the scalet and the wavelet to obtain directly a matrix with a fully determined sparse structure. The benefits of this method in memory are acquired, the ones in time have yet to be assessed. The challenging terms in the matrix are the double integrals over a surface which includes the Green function singularity. Developments of the calculation of the double integrals will be needed to make the method functional. Applying a quadrature to the integral which takes into account the logarithmic divergence of the Green function near zero will most probably help the calculation.

The method may be developed further by adjusting the wavelet expansion as a function of the location over the surface. This approach proved to be useful for an example using the DWT for a surface with isolated grooves. A systematic process based on the evaluation of the hot-spots location based on the profile surface would reduce the needed number of unknowns and improve the time spent on the resolution.

Appendix A

Surface plasmon excitation Appendix

A.1 The approximation of surface impedance

The impedance of an EM field is defined as the ratio of the electric field, E, and the magnetic field, H, namely

$$Z = \frac{E}{H} \quad .$$

Considering two media (upper +, lower -) separated by a surface, one can also define the surface impedance $Z_s^{\pm}$ in the same way and for each side of the interface as the ratio of the electric field, $E^{\pm}$, and the magnetic field $H^{\pm}$ in the upper/lower media at the interface. The continuity equations at the boundary relates the surface impedances on each side. We consider the case of a TM polarized EM field surrounding an interface dielectric(+)/metal(-) (a plane x0y) for a problem invariant in the z direction. In the case of a metal/dielectric interface and for good conductors, we will show that the response of the metal to an EM wave incoming from the dielectric side depends weakly on the wavevector direction of the incoming wave and that the surface impedance of the metal side Z^- is thus constant. The continuity equations at the interface metal/dielectric may therefore be given as a relation between the magnetic field and its derivative at the surface in the dielectric side only. This new relation enables to find the solution of the EM problem in the dielectric without writing the EM field in the metal. We will now give further details of the demonstration.

To begin with, we investigate the behavior of the TM polarized EM wave in the metal. In a good conductor, the attenuation of EM waves is stronger in the perpendicular direction to the surface than in the direction parallel to the surface. As Jackson puts it p.237 in [48] "we make use of the fact that the spatial variation of the fields normal to the surface is much more rapid than the variations parallel to the surface". The spatial derivative in the x direction (parallel to the interface) can thus be neglected compared to the one in the y direction (perpendicular to the interface) and the Laplacian becomes $\Delta \approx \partial^2/\partial y^2$ (system invariant in

the z direction). The Helmholtz equation 1.3 becomes (for a TM polarized wave):

$$\frac{\partial^2 H_z}{\partial y^2} + \epsilon^- k_0^2 H_z \approx 0 \quad .$$

(A.1)

We deduce that the wavevector in the y direction for an EM wave in the metal $k_y^- \approx \sqrt{\epsilon^-} k_0$. Therefore the electric field E_x^- in the metal approximately verifies

$$E_x^- = -\frac{1}{i\epsilon^- \epsilon_0 \omega} \frac{\partial H_z^-}{\partial y} \approx -\frac{1}{i\epsilon^- \epsilon_0 \omega} \left(i k_0 \sqrt{\epsilon^-} H_z^- \right) \quad .$$

As the electric field is the result of the spatial variations of the magnetic field

$$\left| \frac{\partial H_z^-}{\partial x} \right|^2 + \left| \frac{\partial H_z^-}{\partial y} \right|^2 \approx \left| \frac{\partial H_z^-}{\partial y} \right|^2 \qquad \Rightarrow \qquad |E^-|^2 \approx |E_x^-|^2 \quad .$$

(A.2)

The impedance in the metal Z^- thus writes as

$$Z^- = \frac{E_x^-}{H_z^-} \approx -\sqrt{\frac{\mu_0}{\epsilon^- \epsilon_0}}$$

and becomes a constant. The impedance of the EM wave in the metal is also valid at the interface $Z_s^- = Z^-$ and the continuity of the fields tangent to the surface gives

$$\frac{E_x^+}{H_z^+} = \frac{E_x^-}{H_z^-} = Z_s^-$$

(A.3)

where the fields are taken on the surface. As Z_s^- depends only on the permittivity (and not on the angle of incidence of the EM field impinging on the metal for instance), the EM problem in the dielectric may be solved without looking for the EM field in the metal. At the interface, the derivative of H_z^+ is thus proportional to H_z^+ via E_x^+. Substituting the electric field E_x^+ with $Z_s^- H_z^+$ (equation A.3) in the equation 1.4 yields

$$\frac{\partial H_z^+}{\partial y} = -i k_0 \epsilon^+ \sqrt{\frac{\epsilon_0}{\mu_0}} \left(Z^- H_z^+ \right)$$

$$= i k^+ \sqrt{\frac{\epsilon^+}{\epsilon^-}} H_z^+$$

with $k^+ = \sqrt{\epsilon^+} k_0$.

The approximation of surface impedance may finally be written as a condition of continuity at the boundaries for the fields in the dielectric, valid only at the interface

$$\forall \vec{r} \in S \qquad \frac{\partial H_z^+}{\partial \vec{n}}(\vec{r}) - i k^+ \xi H_z^+(\vec{r}) = 0 \quad \text{with} \quad \xi = \sqrt{\frac{\epsilon^+}{\epsilon^-}}$$

212

A.2   The approximated modal method matrix system

In this section, we will present the method used to obtain numerically the amplitudes A_l and R_m of the function basis describing the magnetic field. We start again from the expression of $H_z^{(I)}$, equation 1.18, and $H_z^{(II)}$, equation 1.23 which are related by the continuity equations at the boundary between the media (I) and (II), equations 1.24, 1.25 and 1.26.

The function basis of the n$^{\text{th}}$ eigenmodes, of the field in the region (I) are $e^{ik_0\gamma_n x}$ and the l$^{\text{th}}$ ones of the region (II) are $\cos\left(\left(\frac{w}{2}+x\right)\frac{l\pi}{w}\right)$. The first continuity condition, equation 1.24, valid only in the region $x \in \left[-\frac{w}{2}, \frac{w}{2}\right]$, is projected on the function basis $\cos\left(\left(\frac{w}{2}+x\right)\frac{l\pi}{w}\right)$ with the scalar product $\frac{1}{d}\int_{-\frac{w}{2}}^{\frac{w}{2}} dx$

$$\frac{1}{d}\int_{-\frac{w}{2}}^{\frac{w}{2}} H_z^{(I)}(x,0)\cos\left(\left(\frac{w}{2}+x\right)\frac{l\pi}{w}\right)dx = \frac{1}{d}\int_{-\frac{w}{2}}^{\frac{w}{2}} H_z^{(II)}(x,0)\cos\left(\left(\frac{w}{2}+x\right)\frac{l\pi}{w}\right)dx$$

where $l \in \mathbb{N}$ and $n \in \mathbb{Z}$. The second continuity condition which can be written for the whole period, equations 1.25 and 1.26, is projected on the exponential function $e^{-ik_0\gamma_n x}$ with $\frac{1}{d}\int_{-\frac{d}{2}}^{\frac{d}{2}} dx$ so

$$\frac{1}{d}\int_{-\frac{d}{2}}^{\frac{d}{2}}\left[\frac{\partial H_z^{(I)}}{\partial y}(x,0) - ik^+\xi H_z^{(I)}(x,0)\right]e^{-ik_0\gamma_n x}dx = \frac{1}{d}\int_{-\frac{w}{2}}^{\frac{w}{2}}\left[\frac{\partial H_z^{(II)}}{\partial y}(x,0) - ik^+\xi H_z^{(II)}(x,0)\right]e^{-ik_0\gamma_n x}dx \quad .$$

Before going further, it is helpful to give the specific scalar products involving between the cosines and between the exponential functions

$$\frac{1}{w}\int_{-\frac{w}{2}}^{\frac{w}{2}}\cos\left(\left(\frac{w}{2}+x\right)\frac{l\pi}{w}\right)\cos\left(\left(\frac{w}{2}+x\right)\frac{k\pi}{w}\right)dx = \frac{\delta_{l,k}}{2} \quad ,$$

$$\frac{1}{d}\int_{-\frac{d}{2}}^{\frac{d}{2}} e^{-ik_0\gamma_n x}e^{ik_0\gamma_m x}dx = \delta_{n,m} \quad .$$

The scalar product mixing the cosine and the exponential function is

$$S_{n,l}^{\pm} = \frac{1}{w}\int_{-\frac{w}{2}}^{\frac{w}{2}} e^{\pm ik_0\gamma_n x}\cos\left(\left(\frac{w}{2}+x\right)\frac{l\pi}{w}\right)dx \quad .$$

Substituting the expanded form of the fields $H_z^{(I)}$ and $H_z^{(II)}$, one obtains a set of equations on R_n the amplitudes of the plane waves in the dielectric above the grating (function basis $f_n^{(I)}$) and on A_l the amplitudes of the eigenmodes in the groove (function basis $f_l^{(II)}$).

$$A_l = \frac{2}{\left(e^{2i\Lambda_l h}+r_l\right)(1+\delta_{0,n})}\left(S_{0,l}^+ + \sum_{n=-\infty}^{+\infty} S_{n,l}^+ R_n\right) \quad , \tag{A.4}$$

$$R_n = \frac{\beta_0+\xi}{\beta_0-\xi}\delta_{0,n} + \frac{w}{d}\frac{1}{\beta_m+\xi}\sum_{l=0}^{\infty} A_l\left(\frac{\Lambda_l}{k_0\sqrt{\epsilon^+}}+\xi\right)\left(e^{2i\Lambda_l y}-1\right)S_{n,l}^- \tag{A.5}$$

213

Substituting the expression of R_n, equation A.5, in the one of A_m, equation A.4, yields the matrix system

$$
\begin{bmatrix}
& \cdots & \\
\frac{w}{d}\left(\frac{\Lambda_l}{k_0\sqrt{\epsilon^+}}+\xi\right)\frac{e^{2i\Lambda_l h}-1}{e^{2i\Lambda_m h}+r_m}\sum_{n=0}^{N}\frac{S_{n,l}^-S_{n,m}^+}{\beta_n+\xi} \\
& \cdots &
\end{bmatrix}
\begin{bmatrix}
\cdots \\
A_{l\in[0,L-1]} \\
\cdots
\end{bmatrix}
=
\begin{bmatrix}
& \cdots & \\
\frac{1}{e^{2i\Lambda_m h}+r_m}\frac{2\beta_0}{\beta_0+\xi}S_{0,m}^+ \\
& \cdots &
\end{bmatrix}
$$

where L and N are the number of the unknowns A_l and respectively R_n (equivalently the number of the modes in the cavity and above the grating). Usually L is of the order of several tens and N of the order of several hundreds in order to achieve convergence. The resolution of the matrix system permits to calculate the A_l terms. The calculation of the R_n terms is directly deduced from the A_l terms with the equation A.5. The magnetic and electric fields are then calculated in the cavity with the amplitudes A_l and above the grating with the terms R_n. The reflectivity of the nth order of diffraction is $|R_n|^2\frac{\beta_n}{\beta_0}$ for real β_n. The problem is then solved.

Appendix B

Surface Integral Method Appendix

The demonstrations presented here are only intended as an insight for the reader into the different properties of pseudoperiodicity of functions and distributions. In particular, distributions will often be bound up to their associated functions if the physicists' notations are sufficient not to lead to wrong results. The interested reader may refer to the appendix of Petit in [82].

B.1   Warning on the handle of distribution

A distribution is an application of the space of locally integrable functions on $\mathbb{C}$. In this thesis, we consider regular distributions G and their associated functions {G} which are defined such that, for any locally integrable function f,

$$\langle G|f\rangle = \int_{\mathbb{R}} \{G\}(x)f(x)dx \quad .$$

For instance, the dirac distribution defined by

$$\langle \delta|f\rangle = f(0) \quad ,$$

is written improperly as

$$\langle \delta|f\rangle = \int_{\mathbb{R}} \delta(x)f(x)dx \quad .$$

Some operations differ from function to distribution, the derivation for instance. In that case, a distinction between the distribution G and its associated function {G} will be made. In this thesis, we deal with Green functions $G(\vec{r}) = G(x, y)$ which are discontinuous at the plane y=0. As it will be needed latter, we then give, in the particular case of distributions

whose associated function $\{G\}(x)$ is discontinuous at the point x=0, the derivative of the second order [82]

$$\langle G''|f\rangle = \int_{\mathbb{R}} \{G''_n(x)\}dx + \left(\{G\}(0^+) - \{G\}(0^-)\right)\langle \delta'|f\rangle + \left(\{G'\}(0^+) - \{G'\}(0^-)\right)\langle \delta|f\rangle$$

with δ' defined by $\langle \delta'|f\rangle = -f'(0)$. This may be improperly written as

$$G''(y) = \{G''_n(y)\} + (\{G\}(0+) - \{G\}(0-))\,\delta'(y) + \left(\{G'\}(0+) - \{G'\}(0-)\right)\delta(y) \quad . \tag{B.1}$$

B.2 The Green Function in a non-periodic infinite media expressed as a sum of plane waves

We are looking for the Green Function which follows the conditions of the section 2.2.2.1. When dealing with distributions, one has to be careful and the simplest way is to express the problem in term of functions corresponding with the distributions. We will differentiate the distribution denoted G from the corresponding function denoted $\{G\}$.

This resolution is based on the one done in 1D in [146]. Choosing Cartesian coordinates, the distribution must obey the equations

$$\forall (x, x', y, y') \in (\mathbb{R})^4 \qquad \Delta G(x, x', y, y') + k_0^2 G(x, x', y, y') = -\delta(x - x')\delta(y - y') \quad .$$

The solution is going to be looked for in the form

$$\forall (x, x', y, y') \in (\mathbb{R})^4 \qquad G(x, x', y, y') = \int dq \quad e^{iq(x-x')} \quad g(y, y', q)$$

with

$$\Delta_y g(y, y', q) + (k_0^2 - q^2)g(y, y', q) = -\frac{1}{2\pi}\delta(y - y') \quad .$$

We seek the solution in the form of a function $\{g\}$ using the equation B.1

$$\forall (y, y') \in (\mathbb{R})^2 \qquad \forall q \in \mathbb{R}$$
$$\begin{cases} \Delta_y\{g\}(y, y', q) + (k_0^2 - q^2)\{g\}(y, y', q) = 0 \\ \frac{\partial\{g\}}{\partial y}(y'^+, y', q) - \frac{\partial\{g\}}{\partial y}(y'^-, y', q) = -\frac{1}{2\pi} \\ \{g\}(y'^+, y', q) - \{g\}(y'^-, y', q) = 0 \end{cases}$$

and

$$\lim_{y \to \pm\infty} \frac{\partial\{g\}}{\partial y} \mp i k_y\{g\} = 0 \quad .$$

We are now going to solve the equation for $\{g\}$. The general solution of the equation on $\{g\}$ is $Ae^{iQy} + Be^{-iQy}$. Because of the radiation condition $\{g\}$ is:

$$\forall (y, y') \in (\mathbb{R})^2 \qquad \forall q \in \mathbb{R}$$

$$\exists (A, B) \in (\mathbb{C})^2 \qquad \begin{cases} y > y' & \{g\}(y, y', q) = Ae^{iQy} \\ y < y' & \{g\}(y, y', q) = Be^{-iQy} \end{cases}$$

with $q^2 + Q^2 = k_0^2$. The continuity of $\{g\}$ implies

$$\exists C \in \mathbb{C} \qquad Ae^{iQy'} = Be^{-iQy'} = C$$

and the discontinuity of $\frac{\partial \{g\}}{\partial y}$ implies

$$CiQe^{i0} - C(-iQ)e^{-i0} = -\frac{1}{2\pi} \quad,$$

$$C = -\frac{1}{2\pi}\frac{1}{2iQ} \quad.$$

Finally obtaining the solution for $\{g\}$:

$$\forall (y, y') \in (\mathbb{R})^2 \qquad \forall q \in \mathbb{R}$$

$$\begin{cases} y > y' & \{g\}(y, y', q) = Ce^{iQ(y-y')} = -\frac{1}{2\pi}\frac{1}{2iQ}e^{iQ(y-y')} \\ y < y' & \{g\}(y, y', q) = Ce^{-iQ(y-y')} = -\frac{1}{2\pi}\frac{1}{2iQ}e^{-iQ(y-y')} \end{cases}$$

with $q^2 + Q^2 = k_0^2$.

The solution for G is deduced from g

$$\forall (x, x', y, y') \in (\mathbb{R})^4$$

$$G(x, x', y, y') = -\frac{1}{2\pi}\int dq e^{iq(x-x')}\frac{e^{iQ|y-y'|}}{2iQ} \tag{B.2}$$

with $q^2 + Q^2 = k_0^2$/ The relation (2.11) in [120] which expresses the Hankel function as an integral of plane waves gives the equality with $\frac{i}{4}H_0^{(1)}(k_0 r)$.

B.3 Appendix to the SIE method with a periodic profile

B.3.1 Pseudo-periodicity of the problem

B.3.1.1 Pseudo-periodicity of a function associated to a pseudo-periodic problem

We want to demonstrate
If a function f follows $\Delta f + k^2 f = g$ and g is pseudo-periodic then f is pseudo-periodic.

The hypothesis are with $\alpha \in \mathbb{C}$

$$\forall n \in \mathbb{Z} \qquad g(x+nd) = g(x)e^{ni\alpha_0 d} \quad,$$
$$\Delta f + k^2 f = g \quad.$$

We define the function f_n and g_n as

$$\forall n \in \mathbb{Z} \qquad f_n : x \in \mathbf{R} \to f_n(x) = f(x+nd) \quad,$$
$$g_n : x \in \mathbf{R} \to g_n(x) = g(x+nd) = g(x)e^{ni\alpha_0 d} \quad.$$

We thus have

$$\forall n \in \mathbb{Z} \qquad \Delta f + k^2 f = g$$
$$\Delta f_n + k^2 f_n = g_n$$
$$\Delta f_n + k^2 f_n = e^{ni\alpha_0 d} g$$
$$\Delta f_n + k^2 f_n = e^{ni\alpha_0 d}[\Delta f + k^2 f]$$
$$\Delta[f_n - e^{ni\alpha_0 d} f] + k^2[f_n - e^{ni\alpha_0 d} f] = 0 \quad.$$

The uniqueness of the solution yields

$$\forall n \in \mathbb{Z} \qquad f_n - e^{ni\alpha_0 d} f = 0$$
$$f_n = e^{ni\alpha_0 d} f \quad.$$

The function f is pseudo-periodic.

B.3.1.2   Pseudo-periodicity of the magnetic field

The incident field H_i is pseudo-periodic of phase-shift $\alpha_0 d$, property 2.38. Splitting the total field in an incident field and a diffracted field $H_d^+ = H_z^+ - H_i$, the Helmholtz equation

$$\Delta H_z^+(x,y) + k^{+2} H_z^+(x,y) = 0$$

gives

$$\Delta H_d^+(x,y) + k^{+2} H_d^+(x,y) = -\Delta H_i(x,y) - k^{+2} H_i(x,y) \quad.$$

$g(x) = \Delta H_i(x,y) + k^{+2} H_i(x,y)$ is pseudo-periodic because H_i is. Using the above property for the diffracted field H_d^+ which follows $\Delta H_d^+(x,y) + k^{+2} H_d^+(x,y) = g(x)$; the pseudo-periodicity of H_d^+ is given as well as the one of H_z^+ because the pseudo-periodicity is preserved under the addition.

As the field H_z^- in the lower media is directly linked to the field in the upper media on the surface, it is possible to demonstrate its pseudo-periodicity on the boundary where

$$H_z^-(x+d,D(x)) = H_z^+(x+d,D(x))$$
$$= H_z^+(x,D(x))e^{i\alpha_0 d}$$
$$= H_z^-(x,D(x))e^{i\alpha_0 d}$$

The field H_z^- in the lower media being generated by the one on the boundary, it is pseudoperiodic everywhere.

B.3.1.3 Pseudo-periodicity of a distribution associated to a pseudo-periodic problem

We want to demonstrate
The distribution associated to a space of pseudo-periodic functions $H_{\bar{z}}^{\pm}(x+d,y) = H_{\bar{z}}^{\pm}(x,y)e^{i\alpha_0 d}$
is also pseudo-periodic i.e. the Green function $G\left(x' + d - x, y\right) = G\left(x' + d - x, y\right)e^{i\alpha_0 d}$.

It is easy to demonstrate in the case of the Dirac distribution $\delta\left(\vec{r}' - \vec{r}\right)$ in a physicists'
way. Be aware that it is not mathematically rigorous as previously explained. Taking the
particular case of the Dirac function $\delta(x' - x)$ applied on a pseudo-periodic function u(x)
such that $u(x+d) = u(x)e^{i\alpha_0 d}$ then

$$\int_{\mathbb{R}} \delta(x' - x)u(x)dx = u(x')$$
$$= u(x' + d)e^{-i\alpha_0 d}$$
$$= \int_{\mathbb{R}} \delta(x' + d - x)e^{-i\alpha_0 d}u(x)dx \quad .$$

The property of the Dirac function associated with the distribution is then

$$\delta(x + d) = \delta(x)e^{i\alpha_0 d} \quad . \tag{B.3}$$

So the distribution δ is pseudo-periodic of phase shift $\alpha_0 d$.

Going further, in the same manner as for functions, if a distribution f fulfills:

$$\Delta f + k^2 f = \delta$$

and the distribution δ is pseudo-periodic then f is pseudo-periodic.

We note that, as a consequence of the property B.3, the distribution δ is equivalent to

$$\delta(x) = \sum_{n=-\infty}^{\infty} \delta(x + nd)e^{i\alpha_0 nd} \quad . \tag{B.4}$$

B.3.1.4 Fourier Series of a pseudo-periodic function

We want to demonstrate
A function or distribution which is pseudo-periodic of phase shift $\alpha_0 d$ *and periodic of period*
d may be expressed as a Fourier series

$$u(x,y) = \sum_{n=-\infty}^{\infty} u_n(y)e^{i\alpha_n x}$$

with $\alpha_n = \alpha_0 + \frac{2\pi}{d}n$.

If u is pseudo-periodic of phase shift $\alpha_0 d$ and periodic of period d, $u(x)e^{-i\alpha_0 x}$ is periodic

$$\forall n \in \mathbb{Z} \qquad u(x + nd)e^{-i\alpha_0 x - i\alpha_0 nd} = u(x)e^{-i\alpha_0 x} \quad .$$

That is why $u(x, y)e^{-i\alpha_0 x}$ can be expressed as a Fourier series

$$u(x, y)e^{-i\alpha_0 x} = \sum_{n=-\infty}^{\infty} u_n(y)e^{i\frac{2\pi}{d}nx}$$

and so u can be expressed as a Fourier series

$$u(x, y) = \sum_{n=-\infty}^{\infty} u_n(y)e^{i\alpha_n x}$$

with $\alpha_n = \alpha_0 + \frac{2\pi}{d}n$. As the distribution has the same phase shift, the demonstration is identical.

Finally, we look for the expansion of the Dirac distribution as a Fourier series Again, be aware that it is not mathematically rigorous as previously explained. Starting from the sum of Dirac and remembering $a\delta(ax) = \delta(x)$

$$\delta(x) = e^{i\alpha_0 x} \sum_{n=-\infty}^{\infty} \delta(x + nd)$$

$$= e^{i\alpha_0 x} \sum_{n=-\infty}^{\infty} \frac{2\pi}{d}\delta\left(\frac{2\pi}{d}(x + nd)\right) \quad .$$

Substituting the Poisson sum

$$\sum_{m=-\infty}^{\infty} \delta(x - 2\pi m) = \frac{1}{2\pi} \sum_{m=-\infty}^{\infty} e^{imx}$$

gives

$$\delta(x) = e^{i\alpha_0 x}\frac{2\pi}{d}\frac{1}{2\pi} \sum_{n=-\infty}^{\infty} e^{-in\frac{2\pi}{d}x}$$

$$= \frac{1}{d} \sum_{n=-\infty}^{\infty} e^{i(\alpha_0 + n\frac{2\pi}{d})x} \quad .$$

Hence the Dirac distribution can be written as a Fourier series

$$\delta(\vec{r}) = \delta(x)\delta(y) = \frac{1}{d} \sum_{n=-\infty}^{\infty} \delta(y)e^{-i\alpha_n x}$$

with$\alpha_n = \alpha_0 + \frac{2\pi}{d}n$.

B.3.2 The pseudo-periodic Green Function expressed as a sum of plane waves demonstration

We look for the pseudo-periodic distribution which satisfies the Helmholtz, equation 2.41, as well as the radiation conditions, equation 2.42, in the form of a Fourier series as shown in section B.3.1.4 substituting δ with its own Fourier series ie solving

$$\tilde{G}^{\pm}(x, y) = \sum_{n=-\infty}^{\infty} g^{\pm}{}_n(y)e^{i\alpha_n x}$$

$$\Delta g^{\pm}{}_n(y) + (k^{\pm 2} - \alpha_n^2)g^{\pm}{}_n(y) = -\frac{1}{d}\delta(y) \quad .$$

The resolution can be found p.22 of [82]. $\tilde{G}^{\pm}$ is a distribution and $g_n^{\pm}(y)$ as well. Substituting the Laplacian of a distribution $g_n^{\pm}(y)$ in terms of function $\{g_n^{\pm}\}(y)$, the equation B.1, into the Helmholtz equation on $g_n(y)$ gives

$$\frac{1}{d}\delta(y) = \left\{g^{\pm\,''}_{n}(y)\right\} + (\left\{g^{\pm\,'}_{n}\right\}(0+) - \left\{g^{\pm\,'}_{n}\right\}(0-))\delta(y)$$
$$+ (\{g_n^{\pm}\}(0+) - \{g_n^{\pm}\}(0-))\delta(y)' + (k^{\pm 2} - \alpha_n^2)\{g_n^{\pm}\}(y) \quad .$$

The equality of the distributions gives in the sense of functions

$$\{g_n^{\pm}\}(0+) - \{g_n^{\pm}\}(0-) = 0$$
$$\left\{g^{\pm\,'}_{n}\right\}(0+) - \left\{g^{\pm\,'}_{n}\right\}(0-) = -\frac{1}{d}$$
$$\begin{cases} \forall y > 0 & \{g_n^{\pm}\}(y) = A_n e^{i\beta_n^{\pm}y} + B_n e^{-i\beta_n^{\pm}y} \\ \forall y < 0 & \{g_n^{\pm}\}(y) = C_n e^{i\beta_n^{\pm}y} + D_n e^{-i\beta_n^{\pm}y} \end{cases}$$

with $\beta_n^{\pm} = \sqrt{k^{\pm 2} - \alpha_n^2}$ and $\Re(\beta_n^{\pm}) > 0$. The Sommerfeld radiation condition, equation 2.39, tells

$$\begin{cases} \forall y > 0 & \{g_n^{\pm}\}(y) = A_n e^{i\beta_n^{\pm}y} \\ \forall y < 0 & \{g_n^{\pm}\}(y) = C_n e^{-i\beta_n^{\pm}y} \end{cases}$$

and the continuity of $\{g_n^{\pm}\}$

$$\forall y < 0 \qquad \{g_n^{\pm}\}(y) = A_n e^{-i\beta_n^{\pm}y} \quad .$$

For all y, we have $\{g_n^{\pm}\}(y) = A_n e^{i\beta_n^{\pm}|y|}$. The coefficient A_n comes from the gap of $\left\{g^{\pm\,'}_{n}\right\}$ at the boundary y=0

$$i\beta_n^{\pm}A_n - \left(-i\beta_n^{\pm}\right)A_n = -\frac{1}{d} \quad ,$$
$$A_n = -\frac{1}{2i\beta_n^{\pm}d} \quad .$$

To sum up, as the distribution $g_n^{\pm}$ is bounded up with its associated function $\{g_n^{\pm}\}(y)$

$$\tilde{G}^{\pm}(x, y) = -\frac{1}{2id}\sum_{n=-\infty}^{\infty}\frac{1}{\beta_n^{\pm}}e^{i\beta_n^{\pm}|y|}e^{i\alpha_n x} \tag{B.5}$$

with $\beta_n^{\pm} = \sqrt{k^{\pm 2} - \alpha_n^2}$.

This pseudo-periodic Green function is similar to the one of the Green function expressed as a sum of plane waves, equation B.2,

$$\frac{1}{d}\sum_n \quad \Leftrightarrow \quad \frac{1}{2\pi}\int dq$$
$$\beta_n^{\pm} = \sqrt{k^{\pm 2} - \alpha_n^2} \quad \Leftrightarrow \quad Q = \sqrt{\epsilon^{\pm}k_0^2 - q^2}$$

B.3.3 Graf's theorem for the Green function $\tilde{G}_{LS}$GLS expressed as a lattice sum

The Graf theorem, formula (9.1.79) p. 363 of [115], expresses a Bessel family function as a sum of the Bessel function but with a change of coordinates. We first define a triangle with the two vectors $\vec{v}$ and $\vec{w}$. The third vector, which completes the triangle, is $\vec{u} = \vec{w} - \vec{u}$. The angle between $\vec{v}$ and $\vec{u}$ is α and the angle between $\vec{w}$ and $\vec{u}$ is χ. The triangle is represented in the figure B.1. The length of the vector $\vec{i}$ is $i = |\vec{i}|$.
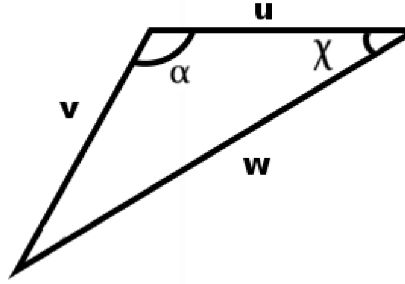
Figure B.1: *Sketch of a triangle with three sides of length u,v,w and with α and χ two angles.*

The Graf theorem gives

$$C_v(w)e^{iv\chi} = \sum_{n=-\infty}^{+\infty} C_{v+n}(u)J_n(v)e^{in\alpha}$$

where C_v denotes J_v, Y_v, $H_v^{(1)}$ and $H_v^{(2)}$.

The theorem is applied to $\tilde{G}_{HS}$ for each Hankel function $H_0^{(1)}(k^{\pm}r_m)$. The main idea is to transform the Hankel function which is applied to a point $\vec{r}_m = (x + md, y)$ into a sum of Bessel functions J_n applied to $\vec{r}_0$ so that the Bessel function are calculated once and for all at the point $\vec{r}_0$. The vector $\vec{w}$ is chosen to be $k^{\pm}\vec{r}_m$ and the vector $\vec{v}$ is chosen to be $k^{\pm}\vec{r}_0$ which leaves $\vec{u} = k^{\pm}md\vec{e}_x$.

B.3.4 the second order derivatives of the Pseudo-periodic Green function

The second order derivatives of the Green function presented in the section 2.4.1 are given here with the same conventions.

222

B.3.4.1 Green's function $\tilde{G}_{HS}$GHS expressed as a Hankel function Sum

The second order derivatives of $\tilde{G}_{HS}$ are

$$
\frac{\partial}{\partial x}\frac{\partial \tilde{G}_{HS}^{\pm}}{\partial \vec{n}_0}(x,y) =
$$
$$
\frac{-ik_+^2}{8}\sum_{m=-\infty}^{\infty}\left[n_x\mathrm{H}_0^{(1)}(k^{\pm}r_m) - \frac{2(x-md)yn_y+(x-md)^2-y^2)n_x}{r_m^2}\mathrm{H}_2^{(1)}(k^{\pm}r_m)\right]e^{im\alpha_0 d}\quad,
$$
$$
\frac{\partial}{\partial y}\frac{\partial \tilde{G}_{HS}^{\pm}}{\partial \vec{n}_0}(x,y) =
$$
$$
\frac{-ik_+^2}{8}\sum_{m=-\infty}^{\infty}\left[n_y\mathrm{H}_0^{(1)}(k^{\pm}r_m) + \frac{((x-md)^2-y^2)n_y-2(x-md)yn_x}{r_m^2}\mathrm{H}_2^{(1)}(k^{\pm}r_m)\right]e^{im\alpha_0 d}
$$

with $r_m = \sqrt{(x-md)^2+y^2}$.

B.3.4.2 Green's function $\tilde{G}_{WS}$GWS expressed as a plane Wave Sum

The second order derivatives of $\tilde{G}_{WS}$ are

$$
\frac{\partial}{\partial x}\frac{\partial \tilde{G}_{WS}^{\pm}}{\partial \vec{n}_0}(x,y) = -\frac{1}{2d}\sum_{m=-\infty}^{\infty}\alpha_m(i\alpha_m n_x + \mathrm{sign}(y)i\beta_m^{\pm}n_y)\frac{e^{i\alpha_m x}e^{i\beta_m^{\pm}|y|}}{\beta_m^{\pm}}\quad,
$$
$$
\frac{\partial}{\partial y}\frac{\partial \tilde{G}_{WS}^{\pm}}{\partial \vec{n}_0}(x,y) = -\frac{1}{2d}\mathrm{sign}(y)\sum_{m=-\infty}^{\infty}(i\alpha_m n_x + \mathrm{sign}(y)i\beta_m^{\pm}n_y)e^{i\alpha_m x}e^{i\beta_m^{\pm}|y|}
$$

with $\beta_m^{\pm} = \sqrt{\epsilon^{\pm}k_0^2 - \alpha_m^2}$.

B.3.4.3 Green's function $\tilde{G}_{LS}$GLS expressed with Lattice Sums

The second order derivatives of $\tilde{G}_{LS}$ are

$$
\frac{\partial}{\partial x}\frac{\partial \tilde{G}_{LS}}{\partial \vec{n}_0}(x,y) = -k^{\pm 2}\frac{i}{8}\Big\{n_x\mathrm{H}_0^{(1)}(k^{\pm}r) - (n_y\sin 2\theta + \cos 2\theta n_x)\mathrm{H}_2^{(1)}(k^{\pm}r) + 2\mathrm{S}_1^{\pm}\cos\theta n_x\mathrm{J}_1(k^{\pm}r)
$$
$$
+ \sum_{l=1}^{L-1}\big(\mathrm{S}_{l+1}^{\pm}\mathrm{C}_{l-1} - \mathrm{S}_{l-1}^{\pm}\mathrm{C}_{-(l-1)}\big)\mathrm{J}_{l-1}(k^{\pm}r) + \big(-\mathrm{S}_{l+1}^{\pm}\mathrm{C}_{l+1} + \mathrm{S}_{l-1}^{\pm}\mathrm{C}_{-(l+1)}\big)\mathrm{J}_{l+1}(k^{\pm}r)\Big\}
$$
$$
\frac{\partial}{\partial y}\frac{\partial \tilde{G}_{LS}}{\partial \vec{n}_0}(x,y) = -k^{\pm 2}\frac{i}{8}\Big\{n_y\mathrm{H}_0^{(1)}(k^{\pm}r) + (n_y\cos 2\theta - \sin 2\theta n_x)\mathrm{H}_2^{(1)}(k^{\pm}r) + 2\mathrm{S}_1^{\pm}\sin\theta n_x\mathrm{J}_1(k^{\pm}r)
$$
$$
+ \sum_{l=1}^{L-1}\big(\mathrm{S}_{l+1}^{\pm}\mathrm{D}_{l-1} + \mathrm{S}_{l-1}^{\pm}\mathrm{D}_{-(l-1)}\big)\mathrm{J}_{l-1}(k^{\pm}r) + \big(\mathrm{S}_{l+1}^{\pm}\mathrm{D}_{l+1} + \mathrm{S}_{l-1}^{\pm}\mathrm{D}_{-(l+1)}\big)\mathrm{J}_{l+1}(k^{\pm}r)\Big\}
$$

with $\mathrm{C}_l = \sin\theta l n_y - \cos\theta l n_x$ and $\mathrm{D}_l = \cos\theta l n_y + \sin\theta l n_x$.

Appendix C

Wavelets Appendix

C.1   Theory of wavelets

C.1.1   Classification of wavelet families

Even if it is not the case in this thesis, the wavelets may be defined and used without a mother scaling function. In the general sense, a group of functions $\{\psi_{a,b}\}$ are called wavelets if they are the result of a dilatation and translation from a mother wavelet ψ such that

$$\psi_{a,b} : x \rightarrow \frac{1}{\sqrt{a}} \psi \left(\frac{x-b}{a} \right)$$ (C.1)

with $a > 0$ the scale and b the shift. In most cases a is a power of a half. The wavelets are split in two main groups, the wavelets with filters which may be used within the Multi-Resolution Analysis (MRA) and the wavelets without filters which are used with a continuous wavelet transform. Some wavelets of the two groups are indicated in table C.1. Only the first group, the wavelets with filter, are discussed within this thesis.

wavelet with filter				wavelet without filter	
compact support			infinite support	real	complex
orth.	biorth.	not orth.	orth.		
Haar	Biorthogonal	BSpline	Meyer	Gaussian	CGaussian
Daubechies	Cohen		D Meyer	mexican hat	Shannon
Symmlet			Battle-Lemarié	Morlet	C freq. B spline
Coiflet			Strömberg		C Morlet

Table C.1: *classification of wavelet families adapted from [147]*

C.1.2 The MRA

A Multi-Resolution Approximation or the Multi-Resolution Analysis (MRA) by Mallat [133] is an infinite sequence of subspaces $\{V_j\}_{j\in\mathbb{Z}}$ that tend to $L^2(\mathbb{R})$ as j increases. If the subspaces $\{V_j\}_{j\in\mathbb{Z}}$ fulfill the following properties

$$(i) \qquad \forall j,k \in \mathbb{Z}^2 \qquad f(x) \in V_j \Leftrightarrow f\left(x - \frac{k}{2^j}\right) \in V_j$$

$$(ii) \qquad \forall j \in \mathbb{Z} \qquad f(x) \in V_j \Leftrightarrow f(2x) \in V_{j+1}$$

$$(iii) \qquad \forall j \in \mathbb{Z} \qquad V_{j-1} \subset V_j$$

$$(iv) \qquad \bigcup_{j=-\infty}^{\infty} V_j = L^2(\mathbb{R})$$

$$(v) \qquad \bigcap_{j=-\infty}^{\infty} V_j = \{0\}$$

there exists a function θ such that $\{\theta(x-k)\}_{k\in\mathbb{Z}}$ is a basis of V_0.

The properties of the subspaces can be understood in terms of the resolution of the projected function details. The resolution of the projection of a function in the subspace V_j is 2^{-j}. The first property (i) assures that the subspaces are invariant with any translation k proportional to the resolution and the second one (ii) that the resolution is increased by a factor two for the subspaces of increasing scale parameter. The property (iii) states that a projected function with details of resolution $2^{-(j-1)}$ can be described by a basis with a finer resolution of 2^j. The property (iv) states that by increasing j and so the resolution, it is possible to describe all functions of $L^2(\mathbb{R})$. The property (v) states on the contrary that by decreasing j and so the resolution, the only function that it is possible to describe is the null one. Equivalently,

$$(iv) \qquad \forall f \in L^2(\mathbb{R}) \quad j \to +\infty \quad ||P_j f - f|| \to 0 \quad,$$

$$(v) \qquad \forall f \in L^2(\mathbb{R}) \quad j \to -\infty \quad ||P_j f|| \to 0 \quad.$$

The mother scaling function ϕ is a function such that $\{\phi(x-k)\}_{k\in\mathbb{Z}}$ is an orthonormal basis of V_0. The MRA with (ii) requires that ϕ is a refinable function. Similarly, the MRA requires from W_j

$$(i) \qquad \forall j \in \mathbb{Z} \qquad f(x) \in W_j \Leftrightarrow f(2x) \in W_{j+1}$$

$$(ii) \qquad \forall j,k \in \mathbb{Z}^2 \qquad f(x) \in W_j \Leftrightarrow f\left(x - \frac{k}{2^j}\right) \in W_j$$

$$(iii) \qquad \bigoplus_{j=-\infty}^{\infty} W_j = L^2(\mathbb{R})$$

$$(iv) \qquad W_j \perp W_{j'} \qquad j \neq j'$$

and assure that

$$(v) \qquad \exists \psi \in L^2(\mathbb{R}) \qquad \{\psi(x-k)\}_{k\in\mathbb{Z}} \text{ is an orthonormal basis of } W_0 \quad.$$

The properties (i) and (ii) are the same as for the scaling function subspaces. The projected function in the subspace W_j has details whose size goes from 2^{-j} to $2^{-(j+1)}$. The property (iii) assures that by adding details of any size, one can describe any function f of $L^2(\mathbb{R})$. The property (iv) states that a detail whose size goes from 2^{-j} to $2^{-(j+1)}$ is different from a detail whose size goes from $2^{-j'}$ to $2^{-(j'+1)}$ if j is different from j'.

All the stated properties assure the existence of a mother scaling function ϕ and a mother wavelet ψ that are able to build basis functions and generate subspaces which constitutes a multi-resolution approximation of $L^2(\mathbb{R})$.

C.1.3   The construction of the wavelets

The wavelets were designed to fit some particular needs and therefore it is insightful to know how they were built. In this subsection, we briefly present how the filter coefficients are calculated. All the coefficients in this thesis were however retrieved from literature.

The wavelets are used to decompose and recompose a function or a signal, in a sense they are sampling functions. In order to build the wavelets, one may consider their behavior in the Fourier space. Applying the Fourier transform (equation 4.7 with $\omega = 2\pi k$ and d=1) to the dilatation equation 4.10

$$\int e^{-j\omega x}\phi(x)dx = \sqrt{2}\sum_{k=k_0}^{k_0+\text{D}-1} a_k \int e^{-j\omega x}\phi(2x-k)dx \quad .$$

Changing $u = 2x - k$ in the right integral enables us to express it as a function of the Fourier Transform of ϕ namely $\hat{\phi}$

$$\hat{\phi}(\omega) = \text{P}(\omega)\,\hat{\phi}\left(\frac{\omega}{2}\right) \qquad \text{with} \qquad \text{P}(\omega) = \frac{1}{\sqrt{2}}\sum_{k=k_0}^{k_0+\text{D}-1} a_k \left(e^{-j\frac{\omega}{2}}\right)^k \quad . \qquad (\text{C.2})$$

The filter coefficients of the scaling function may be defined either by choosing a polynomial P which defines how the dilatation is done in the frequency domain, ie choosing the $\{a_k\}_{k\in[k_0,k_0+\text{D}-1]}$, or by solving a set of equations for the $\{a_k\}_{k\in\mathbb{Z}}$. The equations on $\{a_k\}_{k\in[k_0,k_0+\text{D}-1]}$ come from the fulfillment of some properties. The adequate choice of several properties leads to a unique solution for the filter coefficients $\{a_k\}_{k\in[k_0,k_0+\text{D}-1]}$ and thus define a new wavelet. The orthogonality is a mandatory requirement whereas having N vanishing moments is an optional one. The mother wavelet ψ is built in a similar way by looking for another polynomial Q of coefficients equal to the filter coefficients $\{b_k\}_{k\in[k_0,k_0+\text{D}-1]}$.

The first equations are obtained from the condition upon which the scalets form a normed basis. One may show by using a decomposition of a known function and its Fourier transform (p.51 in [132]) that $\hat{\phi}(2k\pi) = \delta_{k,0}$ and as a consequence

$$\text{P}(0) = 1 \quad , \qquad\qquad\qquad\qquad\qquad\qquad (\text{C.3})$$

$$\text{P}(2\pi) = 0 \qquad\qquad\qquad\qquad\qquad\qquad\qquad (\text{C.4})$$

The equations due to the orthogonality of the scaling function and the wavelet are obtained by substituting the dilatation equation of both of them, equation 4.10 and 4.11, into the relation of orthogonality, equation 4.1, and gives

$$\langle \psi | \phi \rangle = \sum_{k=k_0}^{k_0+D-1} b_k \sum_{l=k_0}^{k_0+D-1} a_l \langle \phi_1^k | \phi_1^l \rangle$$

$$0 = \sum_{k=k_0}^{k_0+D-1} b_k a_k \quad . \tag{C.5}$$

More over, the orthogonality of the scaling function basis gives, by substituting the dilation equation into the orthogonality relation of two scaling function children,

$$\langle \phi^0 | \phi^m \rangle = \sum_{k=k_0}^{k_0+D-1} a_k \sum_{l=k_0}^{k_0+D-1} a_l \langle \phi_1^k | \phi_1^{l+2m} \rangle$$

$$\delta_{0,m} = \sum_{k=k_0+2m}^{k_0+D-1} a_k a_{k-2m} \tag{C.6}$$

with m a positive integer. For instance, the additional equations due to have N vanishing moments for ψ which is equivalent to $\hat{\psi}(\omega)$ and its N-1 derivatives being null at $\omega = 0$ is (p. 20 in [134])

$$\forall p \in [0, N-1] \qquad \sum_{l=k_0}^{k_0+D-1} (-1)^l a_l l^p = 0 \quad .$$

To illustrate with one example, we will look for the solution of genus D=2 which two unknowns a_0 and a_1 are non-null. The equations C.2, C.3 and C.4 become

$$\frac{1}{\sqrt{2}} (a_0 + a_1) = 1$$

$$\frac{1}{\sqrt{2}} (a_0 - a_1) = 0$$

The solution is $a_0 = 1/\sqrt{2}$ and $a_1 = 1/\sqrt{2}$. This is our initial example (chapter 4): the Haar scalet. The relation C.6 is also verified such that the Haar scalet is orthogonal. The Haar wavelet filter coefficients have to fulfill the equation C.5 to build a basis orthogonal to the scalet one

$$0 = a_0 b_0 + a_1 b_1$$

$$b_0 = -b_1$$

The basis being normalized, it imposes furthermore that $b_0 = -b_1 = 1/\sqrt{2}$.

The main consequence of defining wavelets in this particular way, is that there exists no analytical formula for ϕ and ψ which are only described by the set of coefficients $\{a_k\}_{k \in [k_0, k_1]}$ and $\{b_k\}_{k \in [k_0, k_1]}$. The filter coefficients are a definition of the wavelet. They contain all their properties and they define the support of the function.

C.1.4 Construction of some wavelet families

The wavelets are constructed by finding a particular polynomial P of $e^{j\frac{\omega}{2}}$ for the equation C.2. The coefficients of P are the filter coefficients of the scalet and the wavelet. The number of coefficients is thus equal to the polynomial degree and the wavelet genus $D = k_1 - k_0 + 1$. A new wavelet is generated by choosing several properties and creating a set of equations. The members of a same wavelet family are generated by solving a set of equations that comes from the same properties but for polynomials of increasing degree [131].

C.1.4.1 From Haar to the Cardinal Spline

In order to have a wavelet which is designed to sample, the mother scaling function is chosen to be the band pass filter

$$\phi(x) = \Pi_{[0,1]}(x) \Longrightarrow \hat{\phi}(\omega) = \frac{1 - e^{-j\omega}}{j\omega} = e^{-j\frac{\omega}{2}} sinc\left(\frac{\omega}{2}\right) \quad .$$

The Fourier transform as a solution for C.2

$$\hat{\phi}(\omega) = \left(\frac{1 + e^{-j\frac{\omega}{2}}}{2}\right)\hat{\phi}\left(\frac{\omega}{2}\right) \quad .$$

This the starting point of the family of the Cardinal Spline. The higher order Cardinal Spline functions are then designed to optimize the repartition of localization in time-frequency domains. The gaussian function is such a filter, however it cannot be a scaling function. The aim is to tend to the same property concerning the time-frequency window:

$$\lim_{m \to \infty} \Delta x_m \Delta \omega_m = \frac{1}{2} \quad .$$

The goal is achieved by taking the mth power on the dilatation equation of the Haar equation

$$\hat{\phi}(\omega)^m = \left(\frac{1 + e^{-j\frac{\omega}{2}}}{2}\right)^m \hat{\phi}\left(\frac{\omega}{2}\right)^m \quad .$$

Defining by recurrence the mth order spline scaling function $\phi_m = \phi_1 * \phi_{m-1}$, one obtains a relation between ϕ_1 and ϕ_m which ensure that C.2 as a solution.

$$\hat{\phi}_m = \hat{\phi}_1^m \Rightarrow \hat{\phi}_m(\omega) = \left(\frac{1 + e^{-j\frac{\omega}{2}}}{2}\right)^m \hat{\phi}_m\left(\frac{\omega}{2}\right) \quad .$$

From the fact that we know the Fourier transform of the Haar function, the Fourier Transform from the mth order cardinal spline function is found. From the analytical expression of the Fourier transform, one can see that the transform is more localized for increasing m. On the contrary the scaling function is more delocalized.

$$\hat{\phi}_m = \hat{\phi}_1^m = \left(\frac{1 - e^{-j\omega}}{j\omega}\right)^m \quad .$$

229

This Cardinal Spline family is a compactly supported function of support [0 , m[hence it is appropriated for numerical implementation. However the obtained wavelets are not directly orthogonal. A complementary treatment must be applied in order to finally obtain an orthogonal family, the Battle-Lemarié family and the Strömberg family are good examples (they are no longer compactly supported though).

C.1.4.2   From the Cardinal Spline to the Daubechies

Starting once again from the Fourier Transform of another family, the B spline here, an additional polynomial S will be inserted. The additional degrees of liberty of this polynomial will allow to impose orthogonality to the wavelet

$$\hat{\phi}_m(\omega) = \left(\frac{1 + e^{j\frac{\omega}{2}}}{2}\right)^m S\left(e^{-j\frac{\omega}{2}}\right) \hat{\phi}_m\left(\frac{\omega}{2}\right) \quad .$$

There is a unique solution for a polynomial of degree inferior or equal to m-1 having all the roots in the polar circle. The corresponding wavelet is the Daubechies of order D=2m which has a support of [0, D-1[. The Coiflet or Symmlet are other families constructed in the same way. In the Symmlet case the polynomial is chosen in order for the wavelet to be symmetric and not have all his root in the polar circle. The Coiflet are chosen to have vanishing moment for ϕ as well as ψ for the regular Daubechies. They were constructed by Daubechies on the demand of Coifman.

C.2   The filter coefficients of some wavelet families

The filter coefficients of the 6th and 12th order of the Daubechies and the Coifman scalet and wavelet are given as an example in the tables C.2 and C.3.

C.3   Fast Wavelet Transformation (FWT)

The Fast Wavelet Transformation (FWT) is an efficient way to decompose a function on the wavelet subspaces starting from the decomposition on a scaling function space. The decomposition of f on the scaling function subspace $\tilde{V}_J$ may be transformed, using J-J_0 wavelet subspaces (J-J_0 is called the depth), into a decomposition in $\tilde{V}_{J_0} \bigoplus_{n=J_0}^{J-1} \tilde{W}_n = \tilde{V}_J$.

$$\sum_{k=0}^{2^J-1} C_J^k(f)\tilde{\phi}_J^k = \sum_{k=0}^{2^J_0-1} C_{J_0}^k(f)\tilde{\phi}_{J_0}^k + \sum_{j=J_0}^{J-1} \sum_{k=0}^{2^j-1} D_j^k(f)\tilde{\psi}_j^k \tag{C.7}$$

Because of the minimum scale J_{min} ($J_0 > J_{min}$), the depth is smaller than $J - J_{min}$. The FWT therefore consists in going from the scalet coefficients of the scale J, $\left\{C_J^k(f)\right\}_{k=[0,2^J]}$, to

Daubechies			
$\phi_6 : \{a_k\}_{k\in[0,5]}$	$\psi_6 : \{b_k\}_{k\in[0,5]}$	$\phi_{12} : \{a_k\}_{k\in[0,11]}$	$\psi_{12} : \{b_k\}_{k\in[0,11]}$
$3.326705\ 10^{-1}$	$3.522629\ 10^{-2}$	$1.115407\ 10^{-1}$	$-1.077301\ 10^{-3}$
$8.068915\ 10^{-1}$	$8.544127\ 10^{-2}$	$4.946238\ 10^{-1}$	$-4.777257\ 10^{-3}$
$4.598775\ 10^{-1}$	$-1.350110\ 10^{-1}$	$7.511339\ 10^{-1}$	$5.538422\ 10^{-4}$
$-1.350110\ 10^{-1}$	$-4.598775\ 10^{-1}$	$3.152503\ 10^{-1}$	$3.158203\ 10^{-2}$
$-8.544127\ 10^{-2}$	$8.068915\ 10^{-1}$	$-2.262646\ 10^{-1}$	$2.752286\ 10^{-2}$
$3.522629\ 10^{-2}$	$-3.326705\ 10^{-1}$	$-1.297668\ 10^{-1}$	$-9.750160\ 10^{-2}$
		$9.750160\ 10^{-2}$	$-1.297668\ 10^{-1}$
		$2.752286\ 10^{-2}$	$2.262646\ 10^{-1}$
		$-3.158203\ 10^{-2}$	$3.152503\ 10^{-1}$
		$5.538422\ 10^{-4}$	$-7.511339\ 10^{-1}$
		$4.777257\ 10^{-3}$	$4.946238\ 10^{-1}$
		$-1.077301\ 10^{-3}$	$-1.115407\ 10^{-1}$

Table C.2: *The filter coefficients of the 6th and 12th order of the Daubechies scalet ϕ and wavelet ψ (p.63 of [132]).*

Coifman			
$\phi_6 : \{a_k\}_{k\in[-2,3]}$	$\psi_6 : \{b_k\}_{k\in[-2,3]}$	$\phi_{12} : \{a_k\}_{k\in[-4,7]}$	$\psi_{12} : \{b_k\}_{k\in[-4,7]}$
$-7.273261\ 10^{-2}$	$-1.565572\ 10^{-2}$	$1.638733\ 10^{-2}$	$-7.205494\ 10^{-4}$
$3.378976\ 10^{-1}$	$7.273261\ 10^{-2}$	$-4.146493\ 10^{-2}$	$1.823208\ 10^{-3}$
$8.525720\ 10^{-1}$	$3.848648\ 10^{-1}$	$-6.737255\ 10^{-2}$	$5.611434\ 10^{-3}$
$3.848648\ 10^{-1}$	$-8.525720\ 10^{-1}$	$3.861100\ 10^{-1}$	$-2.368017\ 10^{-2}$
$-7.273261\ 10^{-2}$	$3.378976\ 10^{-1}$	$8.127236\ 10^{-1}$	$-5.943441\ 10^{-2}$
$-1.565572\ 10^{-2}$	$7.273261\ 10^{-2}$	$4.170051\ 10^{-1}$	$7.648859\ 10^{-2}$
		$-7.648859\ 10^{-2}$	$4.170051\ 10^{-1}$
		$-5.94344\ 110^{-2}$	$-8.127236\ 10^{-1}$
		$2.368017\ 10^{-2}$	$3.861100\ 10^{-1}$
		$5.611434\ 10^{-3}$	$6.737255\ 10^{-2}$
		$-1.823208\ 10^{-3}$	$-4.146493\ 10^{-2}$
		$-7.205494\ 10^{-4}$	$-1.638733\ 10^{-2}$

Table C.3: *The filter coefficients of the 6th and 12th order of the Coifman scalet ϕ and wavelet ψ (p.67 of [132]).*

the scalet coefficients of scale J_0 and the coefficients on all the wavelet subspace

$$\left\{\left\{C_{J_0}^k(f)\right\}_{k=[0,2^{J_0}-1]}\left\{D_j^k(f)\right\}_{k=[0,2^j-1]}\right\}_{j=[J_0,J-1]}\quad.$$

The matrix of the FWT with a depth $J - J_0$ is

$$\begin{bmatrix} C_{J_0}^l(f) \\ D_{J_0}^l(f) \\ \vdots \\ D_{J-1}^l(f) \end{bmatrix} = T(J_0,J) \begin{bmatrix} \vdots \\ C_J^l(f) \\ \vdots \\ \vdots \end{bmatrix}$$

To calculate the FWT, it is easier to use the recurrence relation that comes from the dilatation equation between the $C_j^k(f)$ coefficients and the $C_{j-1}^k(f)$ and $D_{j-1}^k(f)$ ones and to repeat $\tilde{V}_j = \tilde{V}_{j-1} \oplus \tilde{W}_{j-1}$ until the desired depth is reached.

The operation corresponds to transform the filtering coefficients as

$$C_{j-1}^l(f) = \sum_{k=k_0}^{k_1} a_k C_j^{2l+k}(f)$$

$$D_{j-1}^l(f) = \sum_{k=k_0}^{k_1} b_k C_j^{2l+k}(f)$$

Figure C.1: *Representation of the matrix* A_j. *In the sketch* $k_0 = 0$.

A_j and B_j are the matrices that transform $\{C_{j-1}\}_{k\in[0,2^j-1]}$ into $\{C_j\}_{k\in[0,2^{j-1}-1]}$ and $\{D_{j-1}\}_{k\in[0,2^{j-1}-1]}$ respectively. A_j is shown in figure C.1. B_j assumes the same form exchanging a_k with b_k.

The basic step, $\tilde{V}_i = \tilde{V}_{i-1} \oplus \tilde{W}_{i-1}$, is then

$$\begin{bmatrix} C_{i-1}^k \\ D_{i-1}^k \end{bmatrix} = \begin{bmatrix} A_i \\ B_i \end{bmatrix} \begin{bmatrix} C_i^k(f) \\ C_i^k(f) \end{bmatrix} \tag{C.8}$$

$$
\begin{pmatrix} C_{j-1}^k \\[4pt] D_{j-1}^k \\[4pt] D_j^k \\ \vdots \\ D_{J-1}^k \end{pmatrix} = \begin{pmatrix} A_j & 0 \\[4pt] B_j & 0 \\[4pt] 0 & I_{2^J-2^j} \\ 0 & \end{pmatrix} \begin{pmatrix} C_j^k \\[4pt] D_j^k \\ \vdots \\ D_{J-1}^k \end{pmatrix}
$$
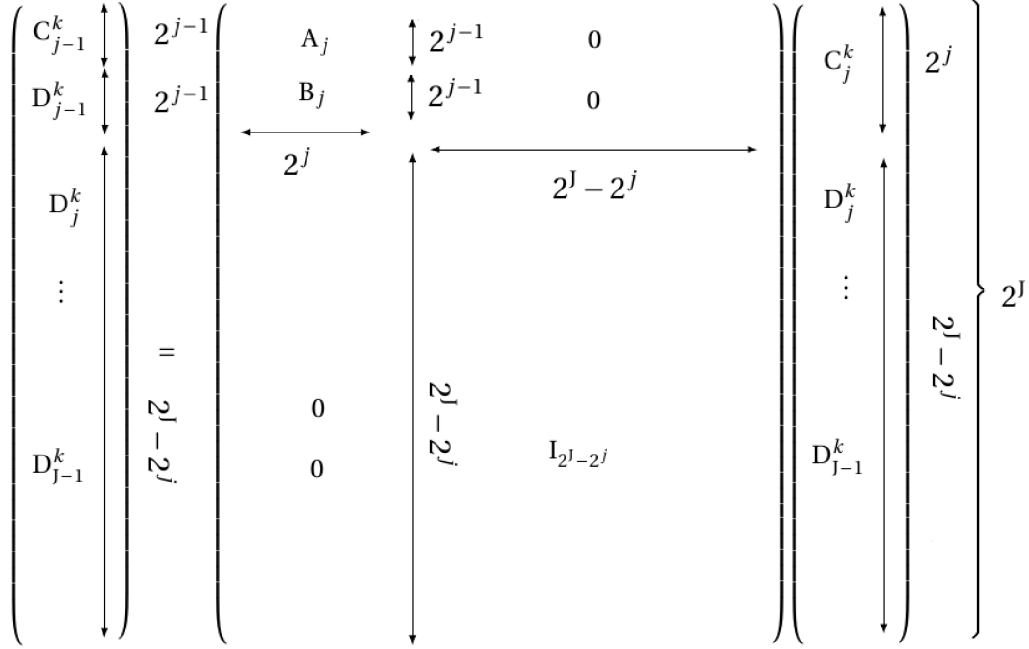
Figure C.2: *Definition of the matrix $Q^J(j-1,j)$ and dimension of involved subspaces $\tilde{V}_j$ and $\tilde{W}_j$ corresponding respectivlely to the coefficients C_j^k and D_j^k.*

If the decomposition has been done for the levels J to j ie a FWT with a depth $J-j$ has been done, we consider the transform to the level $j-1 < J$. This step corresponds to

$$
\tilde{V}_j \bigoplus_{n=j}^{J-1} \tilde{W}_n = V_{j-1} \oplus \tilde{W}_{j-1} \bigoplus_{n=j}^{J-1} \tilde{W}_n = V_{j-1} \bigoplus_{n=j-1}^{J-1} \tilde{W}_n
$$

The associated matrix is called $Q^J(j-1,j)$ and builds the matrix of the FWT with a depth $J-j+1$, $T(j-1,J)$, by recurrence from the matrix of the FWT with a depth $J-j$ as

$$
T(j-1,J) = Q^J(j-1,j)T(j,J)
$$

To obtain $Q^J(j-1,j)$, the basic step C.8 is applied with $i=j$ to C_j^k (size 2^j). The already transformed wavelet coefficients D_{j-1}^k however do not change hence the identity matrix $I_{2^J-2^j}$ is simply applied (size 2^J-2^j). The resulting matrix $Q^J(j-1,j)$ (size 2^J) is shown in figure C.2 and the dimension of subspaces are added for a better understanding. Finally the FWT with a depth $J-J_0$ is

$$
T(J_0,J) = \prod_{j=J_0}^{J-1} Q^J(j,j+1)
$$

233

Résumé de la thèse en français

Introduction générale

La Plasmonique, domaine émergent en physique, offre de nouvelles façons de concentrer et de manipuler la lumière. Le confinement du champ électromagnétique dans un volume sub-longueur d'onde par les polaritons plasmons de surface est à l'origine de propriétés optiques uniques des surfaces métalliques.

Les surfaces métalliques sont de très bonnes surfaces réfléchissantes dans le visible et l'infrarouge. Un creux dans la réflectivité, dont la valeur est normalement proche de un pour les bons conducteurs, peut indiquer l'existence d'une résonance électromagnétique à la surface. Au début du 20$^{\text{ème}}$ siècle, Wood ne s'attendait pas à trouver des bandes étroites brillantes et sombres dans le spectre de réflexion de réseaux métalliques [1]. Ces bandes apparaissaient à des fréquences et des angles spécifiques, et certaines dépendaient aussi de la polarisation. Non comprises à cette époque, elles furent nommées anomalies de Wood. En 1907, Rayleigh montra que certaines de ces anomalies, apparaissant à des fréquences équidistantes, coïncidaient avec l'émergence d'un ordre de diffraction [2]. Toutefois, aucune explication rigoureuse ne fut donnée pour les anomalies restantes.

Fano fut le premier à introduire une partie imaginaire pour la permittivité dans sa modélisation d'un réseau métallique excité par une onde plane, permettant ainsi l'existence d'ondes quasi-stationnaires polarisées Transverse-Magnétique (TM) à l'interface d'un métal et d'un diélectrique [3]. Ces ondes sont une superposition d'ondes électromagnétiques polarisées TM localisées à l'interface et se propageant le long de la surface qui seront plus tard appelées polariton plasmon de surface. Comme Fano le fit remarquer, Sommerfeld avait déjà mathématiquement décrit ces ondes électromagnétiques se propageant en incidence rasante sur une surface diélectrique pour décrire la propagation d'ondes radio à la surface de la mer. La réflexion ayant lieu à la surface d' un diélectrique, Sommerfeld n'avait pas pu prévoir la physique riche associée aux surfaces métalliques. Fano fit donc un parallèle entre les ondes quasi-stationnaires existant sur les réseaux métalliques et les ondes de Sommerfeld se réfléchissant sur une surface conductrice (c'est à dire, quand il y a une réflexion totale de l'onde à la surface).

Cependant, la description électromagnétique des plasmons de surface n'était pas faite en tant que telle puisque le plasmon n'avait pas encore été décrit et que la nature électro-

nique de l'onde n'avait pas été identifiée. Quelques années plus tard, Pines expliqua l'observation expérimentale des pertes d'énergie des électrons rapides passant à travers les métaux par l'excitation d'un mouvement collectif des électrons libres dans ce métal [4, 5]. Il nomma le quantum d'une excitation élémentaire, un plasmon, dont l'énergie est de $\hbar\omega_p$ et dont la fréquence ω_p est la fréquence de plasma des électrons dans le métal. Quelques années plus tard, Ritchies montra que les plasmons de surface pouvaient être excités par des électrons accélérés à une plus petite fréquence ω que la fréquence de plasma ω_p d'oscillation des plasmons de surface [6]. Les anomalies de Wood ont finalement été interprétées par Ritchies comme le couplage entre un plasmon de surface et des photons, un polariton plasmon de surface, le couplage étant rendu possible par le réseau [7].

Excités correctement, les électrons libres d'un conducteur peuvent osciller collectivement à la surface. Ce phénomène peut également être décrit comme une onde électromagnétique qui se propage le long de l'interface entre un diélectrique et un métal et qui est évanescente dans la direction perpendiculaire à la surface métallique. L'excitation collective des électrons et la propagation des photons sont deux aspects d'un même phénomène : le polariton plasmon de surface (ou plus simplement le plasmon de surface). Le champ électromagnétique du plasmon de surface est ainsi piégé à la surface sans être diffracté. Ce confinement des plasmons de surface à la surface est une propriété remarquable qui conduit à des applications sans précédent, allant de la biologie à l'optronique.

Pour exciter un plasmon de surface optiquement, le vecteur d'onde de l'onde électromagnétique incidente doit correspondre à celui du plasmon de surface. Or, les plasmons de surface ne sont pas radiatifs car la composante de leur vecteur d'onde parallèle à la surface, est supérieure à celle de la lumière. En 1968, Otto, Kretschmann et Raether ont proposé deux techniques expérimentales [8, 9] pour exciter les plasmons de surface, utilisant un prisme pour faire correspondre les moments du plasmon de surface et de la lumière, ouvrant la voie à la plasmonique. Aujourd'hui, le nombre de techniques expérimentales disponibles a été élargi et une description des principales techniques peut être trouvés dans [10]. Parallèlement à l'étude expérimentale des plasmons de surface, il y a un besoin de modélisation et de simulation. Cette thèse est une contribution à la simulation numérique des problèmes électromagnétiques visant à la compréhension de la physique des surfaces métalliques.

Les propriétés optiques des surfaces métalliques peuvent changer radicalement lorsque la rugosité de la surface passe de faibles variations de quelques nanomètres, à des variations très brusques d'amplitudes de l'ordre de 10 à 20 nanomètres. Une surface correspondant à ces dernières caractéristiques sera appelée une surface à rugosité nanométrique. Ces surfaces peuvent absorber fortement la lumière dans le domaine du visible. Cette observation est surprenante car des défauts dont les dimensions sont beaucoup plus petites que la longueur d'onde incidente n'interagissent généralement pas avec une onde plane.

Parmi les phénomènes optiques les plus déroutants découverts autour des surfaces métalliques à rugosité nanométrique au 20ème siècle, on trouve aussi la diffusion Raman exaltée par la surface (SERS) : l'augmentation de la diffusion Raman de molécules proches de ces surfaces. Les phénomènes qui sous-tendent ces deux changements de comporte-

ment optique d'une surface métallique est l'existence à la surface de forts champs électriques, très localisés, appelés points chauds. L'existence de points chauds sur ces surfaces particulières est censé être déclenché par les plasmons de surface. Des propriétés optiques similaires ont été observées sur des surfaces nano-structurées, c'est à dire sur des surfaces avec une rugosité nanométrique, habituellement périodiques, fabriquées par les techniques de nanofabrication standard.

Dans cette thèse, nous abordons la question de l'origine et des conditions d'existence de ces points chauds. Pour ce faire, nous étudions l'excitation par une onde plane des surfaces métalliques avec des défauts, des crêtes ou des rainures dont les tailles sont beaucoup plus petites que la longueur de la surface et aussi beaucoup plus petites que la longueur d'onde de l'onde plane incidente. Dans ce cadre, l'étude du champ proche électromagnétique, qui est le champ électromagnétique dans la région où la distance à la surface métallique est inférieure à la longueur d'onde, ainsi que la réflectivité, peuvent offrir un moyen de comprendre les processus impliqués dans la création de points chauds.

L'étude des propriétés optiques des réseaux métalliques d'échelle nanométrique est un sujet de recherche important dans notre groupe. Un modèle simple pour les surfaces rugueuses sont les réseaux métalliques à rainure rectangulaire. C'est un choix pertinent pour trois raisons. La première est que les réseaux à rainure rectangulaire peuvent être modélisés efficacement par la méthode modale qui donne une compréhension directe des mécanismes physiques sous-jacents à leurs propriétés optiques. La seconde est que les réseaux peuvent être fabriqués et permettent la confrontation des propriétés optiques calculées et expérimentales. Enfin, leur étude montre qu'ils peuvent reproduire quelques-unes des observations faites pour les surfaces rugueuses.

Hessel et Oliner décrivent pour la première fois des modes guidés existant dans les cavités sub-longueur d'onde rectangulaires profondes de réseaux métalliques [11]. Ces modes, formés par le couplage de deux plasmons de surface, que nous appelons *mode de cavité*, peuvent entrer en résonance forcée à des longueurs d'onde spécifiques, parfois appelées *résonance de forme* dans la littérature. Ces résonances jouent un rôle important dans la localisation du champ électromagnétique à la surface des réseaux à cavité rectangulaire. Les effets de localisation ont été largement étudiés théoriquement et expérimentalement sein de notre équipe [12, 13, 14, 15, 16, 17].

Afin d'étudier les surfaces à rugosité nanométrique de façon réaliste, le système modèle d'un réseau métallique de rainures rectangulaires, de taille correspondante à celle des films évaporés à froid, a été choisi. Il a été montré que des modes de cavité existent pour les rainures très petites d'une largeur w = 5 nm et de profondeur h = 15 nm dans le visible, c'est à dire pour une longueur d'onde $\lambda \sim 500$ nm très supérieure à la hauteur $h \sim 10$ nm. La résonance du champ électromagnétique dans ces rainures donne naissance à une exaltation du champ électrique suffisamment élevée pour provoquer l'effet SERS et est associée à un creux dans la réflectivité qui tombe alors presque à zéro [18, 17]. Ces résultats novateurs pour la compréhension des propriétés optiques des surfaces rugueuses ont été rendus possibles par le développement de la méthode modale exacte. La méthode modale est, ce-

pendant, limitée à des rainures ayant un profil rectangulaire.

Afin de continuer l'étude de ces phénomènes optiques, l'objectif principal de cette thèse est d'être capable de calculer avec précision le champ électromagnétique autour de défauts très petits, dont la taille caractéristique h est de quelques nanomètres, sur de très grandes surfaces métalliques dans le domaine visible. La principale difficulté pour ce faire est la disparité des dimensions du problème : la longueur d'onde du champ incident λ et la longueur d de la surface sont beaucoup plus grandes que la hauteur h de la rainure (λ >> h et d >> h).

Pour étendre certains de ces résultats à d'autres profils et en vue d'une étude future des effets de localisation du champ électromagnétique sur des surfaces rugueuses, nous avons décidé d'utiliser la méthode des équations intégrales de surface, méthode dans laquelle le profil de la surface peut être de forme arbitraire. La méthode des équations intégrales de surface est particulièrement appropriée pour la plasmonique car le problème électromagnétique en polarisation TM qu'il faut résoudre (les équations de Maxwell et les conditions limites) est réduit à deux équations pour le champ magnétique à la surface seulement.

La résolution numérique des intégrales nécessite la résolution d'un ensemble d'équations linéaires pour les valeurs du champ magnétique à des points régulièrement espacés à la surface. En dépit de la réduction du problème à un problème unidimensionnel, le pas doit être petit, parfois de l'ordre de grandeur de l'angström, et le nombre d'inconnues augmente donc rapidement avec la longueur du profil. Cela est dû au fait qu'il co-existe à la surface, simultanément, des ondes électromagnétiques dont la longueur d'onde est de l'ordre de grandeur de celle de l'onde incidente et des ondes électromagnétiques localisées similaires aux points chauds. Afin de résoudre la matrice dense qui résulte de ce système, la demande en temps et en espace mémoire de la méthode doit être satisfaite. A moins de réduire ces besoins, il est impossible d'étudier des surfaces dont la longueur est supérieure à quelques centaines de nanomètres.

Pour améliorer les performances de la méthode originale, nous avons cherché un moyen de traiter séparément les différentes échelles du problème et de le décrire de manière efficace afin que le nombre d'inconnues, et donc l'espace mémoire, soient réduits. Les ondelettes ont attiré notre attention car elles sont un outil mathématique dédié à l'étude des fonctions en fonction de leur niveau de détails. En effet, une base d'ondelettes divise l'espace des fonctions en sous-espaces de résolutions différentes. Les ondes électromagnétiques à la surface dont la modulation est faible sont décrites avec précision dans un sous-espace dont la résolution est faible, à l'aide de quelques points répartis sur toute la surface. Au contraire, les points chauds doivent être décrits dans un sous-espace dont la résolution est élevée, mais seulement localement, avec quelques points rapprochés à cet endroit précis. Cette propriété peut être utilisée à notre avantage pour adapter la description du champ magnétique en fonction de sa position à la surface et ainsi augmenter la précision de la description là où elle est nécessaire, dans les cavités profondes à la surface. En agissant ainsi, le nombre de termes nécessaires pour représenter le champ magnétique à la surface dans la base d'ondelettes est réduit par rapport au nombre de points de discrétisation de la surface

dans la méthode des équations intégrales de surface. C'est pourquoi les ondelettes semblent appropriées pour nous aider à résoudre ce problème dont les dimensions ont des échelles différentes.

De plus, la transformation de la matrice initiale dense dans une base d'ondelettes donne une matrice creuse à résoudre. On peut alors tirer avantage du gain en espace mémoire afin de traiter un système plus grand. Toutefois, l'application des ondelettes n'est pas directe et la bonne méthode doit être choisie de façon à réellement améliorer les performances de la méthode des équations intégrales de surface. Deux applications différentes, l'une utilisant la transformée d'ondelettes et l'autre en utilisant une ondelette spécifique (Coiflets) en tant que base pour la projection du champ magnétique, ont été considérées, la dernière seulement théoriquement. Le potentiel de l'utilisation des ondelettes avec les équations intégrales de surface est illustré dans cette thèse.

Le travail présenté dans ce manuscrit est la modélisation et la simulation numérique des phénomènes électromagnétiques existant sur les surfaces rugueuses par la résolution des équations intégrales de surface. Une nouvelle approche de la résolution, tirant profit de la théorie des ondelettes, est étudiée dans le but de traiter des systèmes plus complexes de surfaces rugueuses à l'échelle nanométrique. Le premier chapitre donne les fondamentaux de la physique des surfaces rugueuses. Le second chapitre décrit la méthode des équations intégrales de surface. Le troisième chapitre présente un exemple d'application de cette méthode pour des réseaux ayant une ou plusieurs cavités de forme Gaussienne. Le quatrième chapitre présente la théorie des ondelettes et finalement le cinquième et dernier chapitre expose deux façons d'appliquer les ondelettes à la méthode intégrale.

Chapitre 1 : Excitations des plasmons de surface

Dans ce chapitre, nous avons tout d'abord décrit nos motivations pour l'étude des surfaces rugueuses, parmi lesquelles on trouve les films évaporés à froid. La surface des films évaporés à froid, quoique difficile à caractériser expérimentalement, comporte des crevasses profondes dont la hauteur est supérieure à 5 nm, dont la largeur est inférieure à 5 nm et qui sont séparées de 5 à 30 nm. Deux phénomènes optiques intéressants observés pour les films évaporés à froids éclairés par une onde plane dans le domaine du visible ont été présentés : la diffusion Raman exaltée par la surface (SERS), et l'absorption optique anormale (AOA). Il a été souligné que les deux phénomènes sont liés à l'existence de la rugosité, car le SERS, l'AOA et la rugosité des films évaporés à froid disparaissent simultanément lorsque les films sont réchauffés à température ambiante.

Pour comprendre les mécanismes à l'origine des propriétés optiques de ces surfaces métalliques qui ont des défauts de taille beaucoup plus petite que la longueur d'onde, ce chapitre décrit, dans un deuxième temps, les fondamentaux de la plasmonique. La courbe de dispersion et les conditions d'excitation des plasmons de surface sur des réseaux métalliques ont été donnés. L'établissement d'une onde stationnaire, qui est une somme de

plasmons de surface, à la surface des réseaux métalliques excités par une onde plane est appelé *mode de surface*. Il est également possible d'exciter un mode guidé de plasmons de surface, se propageant le long des parois de part et d'autre d'une cavité sub-longueur d'onde et couplés en opposition de phase. La cavité joue pour ce mode guidé le rôle d'un résonateur de Fabry-Perot. La résonance de ce mode guidé dans la cavité résulte en une onde stationnaire qui localise le champ électromagnétique dans un volume sub-longueur d'onde nommé *mode de cavité*.

Ce chapitre a finalement introduit la méthode modale. La méthode modale qui considère les parois verticales de la cavité comme un métal parfait et les surfaces horizontales avec une approximation d'impédance de surface a été implémentée au cours de cette thèse à partir des travaux développés antérieurement dans notre groupe [16]. Une méthode modale exacte était nécessaire pour traiter les réseaux avec des cavités rectangulaires dont les dimensions sont de quelques nanomètres et avait donc été développée par le précédent doctorant J. Le Perchec [18, 17]. Grâce à cette méthode, il avait été montré qu'il existe deux régimes pour les modes de cavité en fonction de l'intensité du couplage des plasmons de surface se faisant face et formant le mode guidé. Lorsque la cavité est large (mais de taille sub-longueur d'onde), le couplage est faible et le mode de cavité est dans un régime dit *optique*. Le comportement de l'onde stationnaire dans la cavité est alors similaire à celui de la lumière et la résonance de Fabry-Perot a lieu pour une profondeur h de la cavité égale au quart de la longueur d'onde d'excitation λ. Au contraire lorsque la cavité est étroite, de largeur inférieure à 10 nm pour les réseaux en argent, le couplage est fort et le mode entre dans un régime dit *électrostatique*. Le vecteur d'onde du mode guidé est alors bien plus grand que celui de la lumière et la résonance de ce mode a lieu dans le visible pour des hauteurs h de cavité bien plus petites que la longueur d'onde du champ incident. Dans ce cas, le champ électrique est fortement exalté et les cavités sont de potentiels sites actifs, ou points chauds, pour l'effet SERS.

Dans cette thèse, nous nous sommes donc concentrés sur l'étude de surfaces ayant des cavités de très petites tailles (de largeurs inférieures à 10 nm pour l'argent, par exemple), similaires aux surfaces des films évaporés à froid qui ont de profondes crevasses. Afin de pouvoir estimer quantitativement le facteur d'exaltation de l'effet SERS et de comprendre qualitativement les mécanismes à l'origine de l'effet SERS, nous voudrions pouvoir étudier des surfaces de forme plus complexe que des réseaux à cavités rectangulaires afin de modéliser de façon plus réaliste la topographie des surfaces rugueuses. La méthode des équations intégrales qui a la flexibilité nécessaire pour de telles études a donc été choisie pour cette tache et a été présentée dans le chapitre suivant.

Chapitre 2 : Méthode des équations intégrales de surface

La méthode des équations intégrales a été décrite dans ce chapitre. Après un court état de l'art sur la simulation de surfaces métalliques rugueuses, la méthode d'équation intégrale de

surface pour une surface infinie développée par Maradudin [91] a été exposée. Le problème électromagnétique qui est résolu est celui d'une onde plane en polarisation Transverse-Magnétique excitant une surface métallique invariante par translation dans la direction du champ magnétique (direction $\vec{e}_z$ par convention). Le problème peut alors être résolu pour le champ magnétique uniquement dans le plan xOy où y est la direction normale au plan moyen xOz par rapport auquel la surface métallique est définie.

En appliquant le théorème de Green pour la fonction de Green associée au diélectrique et le champ magnétique, on obtient l'expression du champ magnétique en un point d'observation de l'espace en fonction de la somme des champs propagés à partir de la surface, dans notre cas une courbe uni-dimensionnelle, l'intersection du plan xOy avec la surface métallique. Cette somme prend la forme d'une intégrale curviligne, sommant en tous les points sources de la surface, le champ magnétique au point source et la fonction de Green allant du point source au point d'observation. Une deuxième équation est obtenue en utilisant la fonction de Green associée au métal. Deux équations intégrales auto-cohérentes sont obtenues en faisant tendre le point d'observation vers la surface. Les deux inconnues de ce système d'équations sont le champ magnétique et sa dérivée à la surface nommées les *fonctions sources* H et L. Nous avons choisi de périodiser le problème dans la direction x. Cela nous assure que la solution est exacte et qu'il n'y a pas d'effet de bord. La méthode d'équations intégrales de surface périodique permet également d'étudier des surfaces sur une longueur plus petite, ce qui permet d'étudier de très petits défauts d'une manière très détaillée. Dans ce cas, le problème devient pseudo-périodique et est réduit à l'obtention du champ sur une seule période du réseau. La fonction de Green est alors remplacée par la fonction de Green pseudo-périodique. L'expression de la réflectivité ainsi que celle du champ électrique ont également été exposées.

Après la description de la modélisation du système, vient celui de sa simulation numérique. Le calcul numérique de la fonction de Green pseudo-périodique nécessite d'utiliser trois expressions différentes de la fonction de Green : une somme de fonctions de Hankel, une somme d'ondes planes et une somme de fonctions de Bessel [120]. Chacune est utilisée dans des conditions spécifiques afin d'optimiser le nombre d'opérations nécessaires pour évaluer ces fonctions de Green pseudo-périodiques. Pour calculer numériquement la solution des équations intégrales, une formule de quadrature est appliquée aux intégrales et un système de 2N équations est obtenu pour la valeur des fonctions sources H et L en N points sources à la surface. Le système d'équations peut alors être écrit sous forme matricielle et la matrice associée est dense de taille 2N par 2N. Ce système est résolu numériquement par une décomposition LU. Les besoins en temps et en espace mémoire de la méthode ont été étudiés. Toutes les quantités physiques du problème peuvent ensuite être calculées à partir des valeurs des fonctions sources.

Finalement, la vérification du programme a été exposée. La bonne convergence des solutions de la méthode intégrale a d'abord été montrée puis les solutions obtenues avec la méthode intégrale ont été comparées avec celles de la méthode modale. Le chapitre suivant

a exposé les résultats obtenus par l'utilisation de cette méthode intégrale.

Chapitre 3 : Application de la méthode des équations intégrales de surface aux surfaces rugueuses à l'échelle nanométrique

Nous avons développé la méthode des équations intégrales de surface et l'avons implémentée afin d'étudier des réseaux de cavités de forme Gaussienne qui soient plus proches de la surface des films déposés à froid que les réseaux de cavités rectangulaires. En procédant par analogie, nous avons montré que les résonances électrostatiques ne sont pas limitées aux très petites cavités rectangulaires, mais que des cavités en forme de Gaussienne de hauteurs de 10 à 30 nm résonnent de la même manière dans le visible. Ces cavités de forme Gaussienne possèdent elles aussi un ou plusieurs modes de cavité dans le régime électrostatique. Celui-ci se manifeste par un creux dans la réflectivité à la fréquence de résonance et par une localisation du champ électromagnétique dans la cavité observée sur les cartes de champ. Le phénomène de résonance a été mis en évidence par l'existence d'un extremum dans le spectre du champ magnétique et du champ électrique E_x en différents points à l'intérieur de la cavité.

Le premier mode de cavité, celui dont l'énergie à la résonance est la plus basse, a été l'objet d'une étude plus approfondie dans le but de démontrer que ce mode appartient à un régime électrostatique. Premièrement, la résonance de Fabry-Perot a lieu pour de très faibles profondeurs h, de 15 et de 30 nm, très inférieures à la longueur d'onde de l'onde plane incidente $\lambda \simeq 500$ nm. De plus, la fréquence de résonance est identique pour les cavités ayant un rapport de taille identique entre la largeur et la hauteur. Cela indique que la dispersion du mode guidé dans la cavité n'est plus gouvernée par la longueur d'onde excitatrice comme dans le cas optique mais par la largeur de la cavité influant sur le couplage fort des plasmons de surface se propageant sur les parois de la cavité comme dans le cas électrostatique. Le champ électrique devient également très grand comparé au champ magnétique $|E_x/H_z| >> 10^2$. Enfin le fort champ électrique à la résonance est accompagné d'une réflectivité proche de zéro pour la cavité de hauteur h=15 nm. Tous ces arguments concordent pour caractériser la résonance comme étant dans le régime électrostatique. Finalement, une estimation de la courbe de dispersion du premier mode de cavité et la variation de la valeur maximum du facteur d'exaltation du champ électrique $|E_x/E_x^i|$ en fonction de la hauteur h de la cavité ont été discutés.

La dernière partie de ce chapitre commente la simulation d'une onde plane excitant 5 sillons de forme Gaussienne de 1-2 nm de large et d'environ 10 nm de profondeur répartis aléatoirement sur une période d'un réseau métallique. L'absorption spectralement large de la réflectivité observée pour les films évaporés à froid est reproduite par cette simulation. De plus, dans la même gamme spectrale que celle de l'absorption anormale, un fort champ

électrique au fond des cavités peut jouer le rôle de sites actifs dans l'effet SERS. Une telle valeur du champ électrique est capable de créer un effet SERS avec un facteur d'exaltation dont l'ordre de grandeur est de $|E_x/E_x^i|^4 \simeq 10^7$.

Il serait souhaitable de poursuivre cette étude par celle de surfaces de période supérieure à 1 μm, et ayant une forme plus complexe. La méthode des équations intégrales de surface requière, en l'état, un nombre trop important d'inconnues. Ainsi la simulation de la dernière section impose de discrétiser la surface avec 1000 points pour une période de 50 nm. Les simulations de réseaux à grande période sont donc hors de portée des capacités d'un ordinateur portable et même impossibles pour la plupart des grappes de serveurs. Par ailleurs, le temps demandé par la simulation serait déraisonnable. C'est pourquoi cette thèse s'est orientée vers l'amélioration des performances de la méthode intégrale. Les ondelettes ont été choisies pour réaliser cette tâche.

Chapitre 4 : Les ondelettes orthogonales à support compact

Les ondelettes sont un sujet très large, tout comme leur domaine d'application. Seules quelques familles d'ondelettes ont été considérées dans cette thèse, et nous sommes restés dans le cadre de l'analyse multi-résolution développée par Mallat. Ce chapitre avait pour but d'exposer les bases de la théorie des ondelettes utilisées dans le chapitre suivant, en particulier comment générer une base d'ondelettes, quelles sont les principales familles d'ondelettes et les transformées en ondelettes. Le point commun de toute base d'ondelettes est de construire les fonctions de base par la dilatation et la translation d'une fonction d'échelle mère unique ϕ

$$\forall\, j \in \mathbb{Z} \qquad V_j : \left\{ \phi_j^k : x \to \sqrt{2^j}\phi(2^j x - k) \right\}_{k \in \mathbb{Z}}$$

où j est le paramètre d'échelle , k le paramètre de décalage et V_j est le sous-espace de fonctions d'échelle 2^j. De façon identique l'ondelette mère ψ engendre un sous-espace d'ondelettes W_j de même résolution. Dans le cadre de l'analyse multi-résolution, les sous-espaces de fonctions d'échelle et d'ondelettes sont orthogonaux et leur somme $W_j \oplus V_j$ est égale au sous-espace de fonctions d'échelle V_{j+1}. La projection P_{W_j} d'une fonction f dans un sous-espace d'ondelettes W_j est ainsi égale à la différence entre les projections d'une fonction dans deux sous-espaces de fonctions d'échelles successives V_j et V_{j+1}

$$P_{W_j} f = f_{W_j} = f_{V_{j+1}} - f_{V_j} \quad .$$

Dans un premier temps, la décomposition sur une base d'ondelettes a été introduite à travers un exemple décomposant une fonction comportant une marche grâce à une ondelette particulière : la fonction de Haar. Il a été montré que la transformée d'ondelettes est appropriée à la description d'une marche par comparaison avec la transformée de Fourier. En effet, les fonctions de la base d'ondelettes diffèrent par leur localisation dans l'espace

et permettent de décrire les changements d'une fonction avec une résolution 2^{-j} où j est le paramètre d'échelle. Au contraire, les fonctions sinusoïdales diffèrent par leur fréquence d'oscillation et le développement d'une marche en série de Fourier tronquée entraîne l'apparition du phénomène de Gibbs.

Dans un deuxième temps, la décomposition sur une base d'ondelettes est généralisée pour des bases orthonormales d'ondelettes à supports compacts périodiques. Les bases d'ondelettes périodiques, notées par un tilde, sont obtenues en périodisant les fonctions de base d'une période égale à un. Le sous-espace périodisé de paramètre d'échelle j a alors une dimension finie 2^j. L'espace des fonctions périodiques $L^2([0,1])$ peut être décrit par un sous-espace d'échelle de résolution infiniment petite. De façon équivalente, il est possible de le décrire par un sous-espace $\tilde{V}_{J_0}$ d'échelle 2^{J_0} et de compléter par des sous-espaces d'ondelettes $\tilde{W}_j$ complémentaires de paramètre d'échelle j allant de J_0 à l'infini c'est à dire :

$$L^2([0,1]) = \tilde{V}_{+\infty} = \tilde{V}_{J_0} \bigoplus_{j=J_0}^{+\infty} \tilde{W}_j \quad .$$

Différentes familles d'ondelettes ont ensuite été introduites. Les ondelettes d'une même famille partagent les mêmes propriétés mais ont des supports de tailles différentes. On parle alors d'ondelette mère d'ordre D ayant un support de taille D-1. Deux familles particulières ont attiré notre attention et ont été utilisées dans le chapitre suivant : l'ondelette de Daubechies et l'ondelette de Coifman.

La fin du chapitre a présenté deux transformées en ondelettes en commençant par la transformée en fonctions d'échelle discrète. Celle-ci permet de calculer les coefficients de la décomposition d'une fonction f dans la base de fonctions d'échelle du sous-espace $\tilde{V}_J$ à partir des valeurs de f aux points d'abscisse $k/2^J$ où k∈ $[0,2^J[$. Ensuite, la transformée en ondelettes discrète a été décrite. La décomposition est dans ce cas faite dans l'espace $\tilde{V}_J = \tilde{V}_{J_0} \bigoplus_{j=J_0}^{J-1} \tilde{W}_j$ où le nombre de sous-espaces d'ondelettes $\tilde{W}_j$ utilisé, $J - J_0$, est appelé la profondeur de la décomposition.

Dans le chapitre suivant, nous avons développé comment utiliser les ondelettes pour améliorer la résolution des équations intégrales de surface .

Chapitre 5 : Application des ondelettes aux équations intégrales de surface

Dans ce chapitre, nous avons tout d'abord exposé pour quelles raisons les ondelettes sont adaptées à la description des fonctions sources H et L. La décomposition en ondelettes de ces fonctions sources dans des espaces de résolutions différentes permet de traiter les différents niveaux de détails de la fonction source séparément. La forme globale de la fonction source est tout d'abord décrite dans un sous-espace de fonctions d'échelles de résolution 2^{-J_0}. Les détails de la fonction de taille 2^{-j} de plus en plus petits sont ensuite ajoutés en

sommant à cette forme globale la projection de la fonction source dans des sous-espaces d'ondelettes complémentaires W_j, afin de recomposer la fonction totale. Pour une échelle 2^j assez élevée, les détails des fonctions sources n'existent qu'en des points fortement irréguliers de la surface, ceux pour lesquels des points chauds apparaissent. Très peu de coefficients sont nécessaires au développement de la fonction source dans des sous-espaces d'ondelettes d'échelles élevées. Les fonctions sources H et L peuvent donc être développées sur un nombre restreint de fonctions d'ondelettes et sont représentées dans cette base par un vecteur creux. Deux méthodes qui utilisent les ondelettes en vue de réduire les besoins en temps et espace mémoire du programme ont ensuite été présentées : la première repose sur la transformée en ondelettes discrète, et la seconde sur l'utilisation d'ondelettes de Coifman comme une base de fonctions de développement des inconnues et de projection des équations intégrales.

La mise en œuvre de la première méthode a été décrite, implémentée et testée durant cette thèse. Brièvement, cette méthode consiste à transposer le système matriciel obtenu par la méthode intégrale dans l'espace d'ondelettes en le multipliant adéquatement par les matrices associées à la transformée en ondelettes discrète et la transformée inverse. Il a été montré que le problème peut être résolu dans la base d'ondelettes sans compromettre la précision de la solution et que la densité de la matrice dans la base d'ondelettes est alors faible, avec environ 95 % de termes nuls. Cette méthode nécessitant cependant le calcul initial de la matrice dense de la méthode intégrale, l'espace mémoire gagné n'est pas grand. Afin de réduire l'espace mémoire occupé, il a été proposé de stocker temporairement certaines matrices sur le disque dur tandis que seule la matrice creuse dans la base d'ondelettes est stockée entièrement dans la RAM. Ce gain en espace mémoire est alors responsable d'un allongement du temps d'évaluation de la matrice à résoudre.

Une autre piste pour réduire l'espace mémoire occupé et le temps de résolution du problème est la réduction du nombre d'inconnues. Ceci a été réalisé en optimisant le nombre de coefficients nécessaires dans la décomposition des fonctions sources dans la base d'ondelettes. Les fonctions sources n'ont été développées sur les sous-espaces d'ondelettes W_j d'échelles élevées qu'aux points de la surface à proximité d'une cavité. Cela a permis de réduire le nombre initial d'inconnues de 4096 dans la méthode intégrale à 736 inconnues dans la méthode utilisant la transformée en ondelette. La pertinence du choix de la décomposition des fonctions sources sur une base d'ondelettes a ainsi été confirmé. Cette méthode, s'est cependant avérée être très coûteuse en temps, dû aux opérations supplémentaires imposées par les transformées en ondelettes, afin d'avoir un gain en espace mémoire occupé.

Finalement, la méthode de Pan qui utilise les moments nuls de l'ondelette de Coifman (aussi appelée Coiflet), a attiré notre attention [140]. Les principes de cette méthode ont été présentés et une brève étude de ses besoins en temps et en espace mémoire a été faite. Celle-ci n'a pas cependant pas été implémentée au cours de cette thèse, faute de temps. La particularité de l'ondelette de Coifman est que son ondelette mère et sa fonction d'échelle mère possèdent des moments nuls. Les coefficients dans la base de fonction

d'échelles d'une fonction sans heurt, c'est à dire une fonction pouvant être approximée par un polynôme de faible degré, peuvent alors être évalués simplement tandis que les coefficients dans les bases de sous-espaces d'ondelettes sont nuls. Cette propriété est exploitée pour la résolution d'équations intégrales en développant les fonctions sources H et L sur une base d'ondelette puis en projetant ces équations sur cette même base. Un système matriciel est alors obtenu pour les coefficients de H et L directement dans la base d'ondelette. Les termes de la matrice sont alors la projection des fonctions de Green $\tilde{G}$ sur les ondelettes $\tilde{\psi}_i^l$ et $\tilde{\psi}_j^k$ similaires à

$$\langle \tilde{\psi}_i^l | \tilde{G} | \tilde{\psi}_j^k \rangle = \int_0^1 du' \int_0^1 du \quad \tilde{\psi}_i^l(u') \tilde{G}(u', u) \tilde{\psi}_j^k(u)$$

où u' est l'abscisse du point d'observation et u celle du point source.

La structure creuse de la matrice correspondant aux équations intégrales dans la base d'ondelettes du sous-espace $\tilde{V}_J$ de l'ondelette de Coifman d'ordre D est connue avant son remplissage et contient environ $2^J JD$ termes. En effet, les fonctions de Green présentes dans les équations sont alors des fonctions sans heurts, excepté à la singularité et dans la grande majorité des cas, cette intégrale est soit nulle, soit elle est exprimée analytiquement à partir de la valeur de la fonction de Green. Le calcul des intégrales doubles de la fonction de Green sur un domaine qui contient sa singularité de la matrice requière cependant qu'elles soient évaluées numériquement. Le grand avantage de cette méthode est qu'elle ne nécessite pas de calculer toute la matrice pour sélectionner par la suite les termes non nuls comme cela est fait avec la méthode de la transformée en ondelettes.

Pan a appliqué cette méthode aux surfaces métalliques ayant de faibles modulations, comparables à la longueur d'onde [141] et une formule de quadrature de 5 points seulement lui a été nécessaire pour calculer ces intégrales. Comme nous souhaitons traiter des surfaces ayant des rugosités de taille très petite devant la longueur d'onde contrairement à Pan, ce calcul numérique pourrait être plus délicat. Le nombre total d'inconnues dans cette méthode utilisant les Coiflets peut également être réduit en optimisant la répartition des coefficients dans la base d'ondelette en fonction de la position des points irréguliers de la surface, réduisant encore la mémoire occupée, mais aussi le temps passé à résoudre la matrice. Ces arguments nous ont amené à croire que cette méthode pourrait traiter des problèmes EM de surfaces métalliques de longueur de 1-2 microns ayant une rugosité d'échelle nanométrique.

Conclusion générale et perspectives

Dans cette thèse, les propriétés optiques des surfaces métalliques avec une rugosité de taille nanométrique ont été étudiées à partir des résultats antérieurs de notre groupe. A basse température, ces films évaporés à froid présentent simultanément une absorption optique anormale et un effet de diffusion Raman exalté par la surface dans le visible. Il a été mon-

tré que de telles observations sont cohérentes avec celles obtenues par la simulation numérique de l'excitation par une onde plane incidente d'un réseau métallique comportant cinq cavités de forme Gaussienne et de taille nanométrique, reproduisant des crevasses de quelques nanomètres de large et de quelques nanomètres de hauteur. Notamment, l'existence de points chauds situés au fond des cavités pouvant jouer le rôle de sites actifs pour l'effet SERS a été observé sur les cartes de champ.

Le premier objectif de cette thèse a été de calculer exactement le champ électromagnétique pour obtenir ces résultats. Nous avons ensuite cherché à traiter des surfaces encore plus grandes. La difficulté réside dans l'existence de points chauds à la résonance. Les solutions recherchées, le champ magnétique et sa dérivée à la surface, ont de très fortes variations, ce qui les rend difficiles à représenter avec quelques points et à trouver comme la solution d'un système d'équations linéaires. La méthode des équations intégrales de surface périodique est adaptée à la modélisation de la solution stationnaire du champ électromagnétique créé par une onde plane incidente en polarisation TM excitant un réseau métallique dont le profil est de forme arbitraire. Les méthodes numériques permettant de calculer les champs dans l'espace ainsi que la réflectivité grâce à cette méthode ont été exposés.

Dans la méthode d'équations intégrales de surface, les valeurs du champ magnétique et de sa dérivé à N points de la surface métallique sont obtenues numériquement grâce à la résolution d'un ensemble de 2N équations linéaires. La résolution d'une matrice dense de taille 2N par 2N est faite grâce à une décomposition LU. Résoudre le problème de l'excitation d'un réseau avec une cavité de taille nanométrique et de période d = 30 nm, peut exiger d'utiliser 1 000 points. Des dizaines de milliers de points peuvent alors être nécessaires pour résoudre le même problème avec cette fois une période de 1 μm. Cela est dû à la forte exaltation du champ électrique qui provoque de brusques variations du champ magnétique et nécessite un pas de discrétisation de la surface métallique de l'ordre de grandeur de $\lambda/1000$. La matrice dense qui en résulte est longue à remplir (N^2 opérations) et à résoudre (N^3 opérations) et occupe beaucoup d'espace mémoire (N^2 termes). Pour ces raisons, la méthode d'équations intégrales de surface est limitée à de petits systèmes.

Développer les inconnues sur une base d'ondelettes offre de nouvelles perspectives pour améliorer les performances de la résolution du problème. Nous avons montré que la projection des fonctions source sur des bases d'ondelettes complémentaires de résolutions différentes permet de décrire la solution avec un vecteur creux. L'utilisation d'une transformée en ondelettes discrète transforme les matrices denses de la méthode des équations intégrales de surface en matrices creuses avec un gain considérable en espace mémoire. En effet, les points chauds localisés au dessus des cavités sont responsables d'un besoin accru de résolution, mais seulement localement. Une fois que la forme globale de la solution est capturée par un espace de fonctions d'échelle de basse résolution, seules quelques fonctions de base d'ondelettes sont nécessaires pour décrire les variations brutales au dessus des cavités. Nous avons ainsi pu réduire le nombre d'inconnues nécessaires pour résoudre le système. Malheureusement, en échange d'un gain d'espace mémoire, cette méthode de-

mande beaucoup de temps. Ces résultats ont néanmoins confirmé qu'un gain d'occupation de l'espace mémoire peut être obtenu par l'application des ondelettes à la méthode des équations intégrales de surface en vue de traiter de plus grands systèmes.

La méthode d'ondelette qui décompose directement les inconnues et les fonctions de Green contenues dans la matrice sur une base de Coiflets apparaît comme un candidat très prometteur pour remplacer celle utilisant la transformée en ondelettes. Cette méthode tire profit des moments nuls de la fonction d'échelle et de l'ondelette pour obtenir la structure creuse de la matrice avant même de la remplir. Ainsi, l'espace mémoire utilisé est réduit à son minimum car l'occupation de l'espace mémoire est uniquement celui de la matrice creuse. Les avantages en temps de cette méthode restent encore à évaluer. Le point technique de cette méthode réside dans l'évaluation d'intégrales doubles de la fonction de Green sur une surface qui comprend sa singularité. L'optimisation du calcul des intégrales doubles sera nécessaire pour rendre la méthode fonctionnelle. Appliquer une quadrature à l'intégrale qui prend en compte la divergence logarithmique de la fonction de Green proche de zéro aidera probablement à calculer l'intégrale plus rapidement.

La méthode pourra être développée davantage en ajustant la décomposition sur base d'ondelettes en fonction de la résolution voulue à chaque point de la surface. Cette approche s'est avérée utile dans le cas d'une surface avec des cavités isolées. Il serait souhaitable de mettre en place un processus systématique évaluant les points nécessitants une résolution accrue, ce qui permettrait de réduire le nombre nécessaire d'inconnues et d'améliorer le temps consacré à la résolution.

Bibliography

[1] R. W Wood. On a remarquable case of uneven distribution of light in a diffraction grating spectrum. *Phil. Mag.*, 4:396, 1902.

[2] Lord Rayleigh. On the dynamical theory of gratings. *Proc. R. Soc. London Ser. A,* 79(532):399–416, Aug 1907.

[3] U. Fano. The theory of anomalous diffraction gratings and of Quasi-Stationary waves on metallic surfaces (Sommerfeld?s waves). *Journal of the Optical Society of America,* 31(3):213–222, March 1941.

[4] David Pines and David Bohm. A collective description of electron interactions: Ii. collective vs individual particle aspects of the interactions. *Phys. Rev.*, 85:338–353, Jan 1952.

[5] David Pines. Collective energy losses in solids. *Rev. Mod. Phys.*, 28(3):184–198, Jul 1956.

[6] R. H. Ritchie. Plasma losses by fast electrons in thin films. *Phys. Rev.*, 106(5):874–881, Jun 1957.

[7] R. H Ritchie, E. T Arakawa, J. J Cowan, and R. N Hamm. Surface-Plasmon resonance effect in grating diffraction. *Phys. Rev. Letters*, 21:1530, November 1968.

[8] Andreas Otto. Excitation of nonradiative surface plasma waves in silver by the method of frustrated total reflection. *Zeitschrift für Physik A Hadrons and Nuclei*, 216:398–410, 1968. 10.1007/BF01391532.

[9] E. Kretschmann and H. Raether. Radiative decay of nonradiative surface plasmons excited by light. *Z. Naturforsch. A*, 23:2135, 1968.

[10] A. V Zayats and I. I Smolyaninov. Near-field photonics: surface plasmon polaritons and localized surface plasmons. *J. Opt. A: Pure Appl. Opt.*, 5:S16, July 2003.

[11] A. Hessel and A. A. Oliner. A new theory of wood's anomalies on optical gratings. *Appl. Opt.*, 4:1275, October 1965.

[12] A. Barbara, P. Quémerais, E. Bustarret, and T. Lopez-Rios. Optical transmission through subwavelength metallic gratings. *Physical Review B (Condensed Matter and Materials Physics)*, 66(16):161403, 2002.

[13] A. Barbara, P. Quémerais, E. Bustarret, T. López-Rios, and T. Fournier. Electromagnetic resonances of sub-wavelength rectangular metallic gratings. *Eur. Phys. Jour. D*, 23:143, 2003.

[14] A. Barbara, J. Le Perchec, P. Quemerais, T. Lopez-Rios, and N. Rochat. Experimental evidence of efficient cavity modes excitation in metallic gratings by attenuated total reflection. *Journal of Applied Physics*, 98(3):033705–5, 2005.

[15] P. Quémerais, A. Barbara, J. Le Perchec, and T. Lopez-Rios. Efficient excitation of cavity resonances of subwavelength metallic gratings. *Journal of Applied Physics*, 97(5):053507–4, March 2005.

[16] A. Barbara, J. Le Perchec, S. Collin, C. Sauvan, J-L. Pelouard, T. López-Ríos, and P. Quémerais. Generation and control of hot spots on commensurate metallic gratings. *Opt. Express*, 16(23):19127–19135, 2008.

[17] J. Le Perchec, P. Quemerais, A. Barbara, and T. Lopez-Rios. Why metallic surfaces with grooves a few nanometers deep and wide may strongly absorb visible light. *Physical Review Letters*, 100(6):066408–4, February 2008.

[18] J. Le Perchec. *Localisations et Exaltations de la Lumière dans des Structures Métalliques Sub-Longueur d'Onde*. PhD thesis, Université Joseph Fourier, 2007.

[19] M. Fleischmann, P.J. Hendra, and A.J. McQuillan. Raman spectra of pyridine adsorbed at a silver electrode. *Chemical Physics Letters*, 26(2):163–166, 1974.

[20] David L. Jeanmaire and Richard P. Van Duyne. Surface raman spectroelectrochemistry: Part i. heterocyclic, aromatic, and aliphatic amines adsorbed on the anodized silver electrode. *Journal of Electroanalytical Chemistry and Interfacial Electrochemistry*, 84(1):1–20, 1977.

[21] M. Grant Albrecht and J. Alan Creighton. Anomalously intense raman spectra of pyridine at a silver electrode. *Journal of the American Chemical Society*, 99(15):5215–5217, 1977.

[22] Michael R. Philpott. Effect of surface plasmons on transitions in molecules. *The Journal of Chemical Physics*, 62(5):1812–1817, 1975.

[23] K. Kneipp, Y. Wang, H. Kneipp, L. T Perelman, I. Itzkan, R. R Dasari, and M. S Feld. Single molecule detection using Surface-Enhanced raman scattering (SERS). *Phys. Rev. Letters*, 78:1667, March 1997.

[24] S. Nie and S. R Emory. Probing single molecules and single nanoparticles by Surface-Enhanced raman scattering. *Science*, 275:1102, 1997.

[25] Martin Moskovits. Surface-enhanced raman spectroscopy: a brief perspective. In Katrin Kneipp, Martin Moskovits, and Harald Kneipp, editors, *Surface-Enhanced Raman Scattering*, volume 103 of *Topics in Applied Physics*, pages 1–17. Springer Berlin / Heidelberg, 2006. 10.1007/3-540-33567-6_1.

[26] Stefan A. Maier. Enhancement of emissive processes and nonlinearities. In *Plasmonics: Fundamentals and Applications*, pages 159–176. Springer US, 2007. 10.1007/0-387-37825-1_9.

[27] Katrin Kneipp, Harald Kneipp, Irving Itzkan, Ramachandra R Dasari, and Michael S Feld. Surface-enhanced raman scattering and biophysics. *Journal of Physics: Condensed Matter*, 14(18):R597, 2002.

[28] D. A. Weitz, S. Garoff, and T. J. Gramila. Excitation spectra of surface-enhanced raman scattering on silver-island films. *Opt. Lett.*, 7(4):168–170, Apr 1982.

[29] Mark Stockman. Electromagnetic theory of sers. In Katrin Kneipp, Martin Moskovits, and Harald Kneipp, editors, *Surface-Enhanced Raman Scattering*, volume 103 of *Topics in Applied Physics*, pages 47–65. Springer Berlin / Heidelberg, 2006. 10.1007/3-540-33567-6_3.

[30] H. Seki and T.J. Chuang. The role of cavity sites in surface-enhanced raman scattering. *Chemical Physics Letters*, 100(5):393–396, 1983.

[31] J. K. Gimzewski, A. Humbert, J. G. Bednorz, and B. Reihl. Silver films condensed at 300 and 90 k: Scanning tunneling microscopy of their surface topography. *Phys. Rev. Lett.*, 55:951–954, Aug 1985.

[32] Constantine Douketis, Zhouhang Wang, Tom L. Haslett, and Martin Moskovits. Fractal character of cold-deposited silver films determined by low-temperature scanning tunneling microscopy. *Phys. Rev. B*, 51(16):11022–11031, Apr 1995.

[33] C. Douketis, T. L. Haslett, Z. Wang, M. Moskovits, and S. Iannotta. Rough silver films studied by surface enhanced raman spectroscopy and low temperature scanning tunnelling microscopy. *Progress in Surface Science*, 50(1-4):187–195, 1995.

[34] Robert L. Burwell. Chemisorption and reactions on metallic films in two volumes. vol. 1, xii, 556 pp., illus. vol. 2, xii, 324 pp., illus. *Science*, 176(4039):1116–1117, 1972.

[35] O Hunderi and H P Myers. The optical absorption in partially disordered silver films. *Journal of Physics F: Metal Physics*, 3(4):683, 1973.

[36] P. H. McBreen and M. Moskovits. Optical properties of silver films deposited at low temperatures. 54(1):329–335, 1983.

[37] T. Lopez-Rios, G. Vuye, and Y. Borensztein. Abnormal optical absorption of quenched ag films due to surface roughness. *Surface Science*, 131(1):L367–L372, 1983.

[38] E. V Albano, S. Daiser, G. Ertl, R. Miranda, K. Wandelt, and N. Garcia. Nature of Surface-Enhanced-Raman-Scattering active sites on coldly condensed ag films. *Phys. Rev. Lett.*, 51(25):2314–2317, December 1983.

[39] A. Wirgin and T. López-Ríos. Can surface-enhanced raman scattering be caused by waveguide resonances? *Optics Communications*, 48(6):416–420, 1984.

[40] Joel Gersten and Abraham Nitzan. Electromagnetic theory of enhanced raman scattering by molecules adsorbed on rough surfaces. 73(7):3023–3037, 1980.

[41] S.L. McCall, P.M. Platzman, and P.A. Wolff. Surface enhanced raman scattering. *Physics Letters A*, 77(5):381–383, 1980.

[42] I. Pockrand and A. Otto. Surface enhanced raman scattering (sers): Annealing the silver substrate. *Solid State Communications*, 38(12):1159–1163, 1981.

[43] Naomi Liver, Abraham Nitzan, and J. I. Gersten. Local fields in cavity sites of rough dielectric surfaces. *Chemical Physics Letters*, 111(4-5):449–454, 1984.

[44] T. Lopez-Rios and A. Wirgin. Role of waveguide and surface plasmon resonances in surface-enhanced raman scattering at coldly evaporated metallic films. *Solid State Communications*, 52(2):197–201, 1984.

[45] Xuegong Deng, Gary B. Braun, Sheng Liu, Paul F. Sciortino, Bob Koefer, Thomas Tombler, and Martin Moskovits. Single-order, subwavelength resonant nanograting as a uniformly hot substrate for surface-enhanced raman spectroscopy. *Nano Letters*, 10(5):1780–1786, 2010.

[46] A. Polyakov, S. Cabrini, S. Dhuey, B. Harteneck, P. J. Schuck, and H. A. Padmore. Plasmonic light trapping in nanostructured metal surfaces. *Applied Physics Letters*, 98(20):203104, 2011.

[47] Stefan A. Maier. Surface plasmon polaritons at metal / insulator interfaces. In *Plasmonics: Fundamentals and Applications*, pages 21–37. Springer US, 2007. 10.1007/0-387-37825-1_2.

[48] John David Jackson. *Classical Electrodynamics*. John Wiley & Sons, Inc., 1962.

[49] Charles Kittel. *Introduction to Solid State Physics*, volume 2011. 1995.

[50] H. Raether. *Surface Plasmons on smooth and Rough Surfaces and on Gratings*, volume 111. Springer-Verlag Berlin Heidelberg, 1988.

[51] William L. Barnes, Alain Dereux, and Thomas W. Ebbesen. Surface plasmon subwavelength optics. *Nature*, 424(6950):824–830, 2003.

[52] Lukas Novotny and Bert Hecht. *Principles of nano-optics*. Cambridge University Press, 2006.

[53] T. López-Rios, D. Mendoza, F. J García-Vidal, J. Sánchez-Dehesa, and B. Pannetier. Surface shape resonances in lamellar metallic gratings. *Phys. Rev. Lett.*, 81(3):665–668, July 1998.

[54] Aude Barbara, Stéphane Collin, Christophe Sauvan, Jérôme Le Perchec, Camille Maxime, Jean-Luc Pelouard, and Pascal Quémerais. Plasmon dispersion diagram andlocalization effects in a three-cavity commensurate grating. *Opt. Express*, 18(14):14913–14925, Jul 2010.

[55] J. Le Perchec, P. Quémerais, A. Barbara, and T. López-Ríos. Controlling strong electromagnetic fields at subwavelength scales. *Phys. Rev. Lett.*, 97:036405, Jul 2006.

[56] Neil W. Ashcroft and David N. Mermin. *Solid state physics.* Thomson Learning, Toronto, 1 edition, jan 1976.

[57] Ping Sheng, R. S. Stepleman, and P. N. Sanda. Exact eigenfunctions for square-wave gratings: Application to diffraction and surface-plasmon calculations. *Phys. Rev. B*, 26:2907–2916, Sep 1982.

[58] I. C. Botten, M. S. Craig, R. C. McPhedran, J. L. Adams, and J. R. Andrewartha. The dielectric lamellar diffraction grating. *Optica Acta*, 28:413–428, mar 1981.

[59] Botten L.C., Craig M.S., McPhedran R.C., Adams J.L., and Andrewartha J.R. The finitely conducting lamellar diffraction grating. *Journal of Modern Optics*, 28(8):1087–1102, 1981.

[60] Botten L.C., Craig M.S., and McPhedran R.C. Highly conducting lamellar diffraction gratings. *Journal of Modern Optics*, 28(8):1103–1106, 1981.

[61] L.C.Botten, M.S.Craig, and R.C.McPhedran. *Computer Phys. Commun.*, 29, 1983.

[62] L. C. Botten and R. C. McPhedran. Completeness and modal expansion methods in diffraction theory. *Optica Acta*, 32:1479–1488, dec 1985.

[63] Andrewartha J.R., Derrick G.H., and McPhedran R.C. A modal theory solution to diffraction from a grating with semi-circular grooves. *Journal of Modern Optics*, 28(9):1177–1193, 1981.

[64] J. R. Andrewartha, G. H. Derrick, and R. C. McPhedran. A general modal theory for reflection gratings. *Optica Acta*, 28:1501–1516, nov 1981.

[65] J Y Suratteau, M Cadilhac, and R Petit. On the numerical study of deep dielectric lamellar gratings. *Journal of Optics*, 14(6):273, 1983.

[66] G. Tayeb and R. Petit. On the numerical study of deep conducting lamellar diffraction gratings. *Optica Acta*, 31:1361–1365, dec 1984.

[67] Georgios Veronis and Shanhui Fan. Overview of simulation techniques for plasmonic devices. In Mark Brongersma and Pieter Kik, editors, *Surface Plasmon Nanophotonics*,

volume 131 of *Springer Series in Optical Sciences*, pages 169–182. Springer Berlin / Heidelberg, 2007. 10.1007/978-1-4020-4333-8_12.

[68] Weng Cho Chew, Jian-Ming Jin, Cai-Cheng Lu, E. Michielssen, and J.M. Song. Fast solution methods in electromagnetics. *Antennas and Propagation, IEEE Transactions on*, 45(3):533–543, March 1997.

[69] Andreas M. Kern and Olivier J. F. Martin. Surface integral formulation for 3D simulations of plasmonic and high permittivity nanostructures. *J. Opt. Soc. Am. A*, 26(4):732–740, 2009.

[70] M.A. Yurkin and A.G. Hoekstra. The discrete dipole approximation: An overview and recent developments. *Journal of Quantitative Spectroscopy and Radiative Transfer*, 106(1-3):558–589, 2007. IX Conference on Electromagnetic and Light Scattering by Non-Spherical Particles.

[71] B. Stout, A. Devilez, B. Rolly, and N. Bonod. Multipole methods for nanoantennas design: applications to yagi-uda configurations. *J. Opt. Soc. Am. B*, 28(5):1213–1223, May 2011.

[72] Andreas Hille, Rene Kullock, Stefan Grafstrom, and Lukas M. Eng. Improving nano-optical simulations through curved elements implemented within the discontinuous galerkin method computational. *Journal of Computational and Theoretical Nanoscience*, 7(8):1581–1586, 2010.

[73] H. Giovannini, M. Saillard, and A. Sentenac. Numerical study of scattering from rough inhomogeneous films. *J. Opt. Soc. Am. A*, 15(5):1182–1191, May 1998.

[74] Evgeni Popov and Michel Nevière. Grating theory: new equations in fourier space leading to fast converging results for tm polarization. *J. Opt. Soc. Am. A*, 17(10):1773–1784, Oct 2000.

[75] G. Granet and B. Guizal. Efficient implementation of the coupled-wave method for metallic lamellar gratings in tm polarization. *J. Opt. Soc. Am. A*, 13(5):1019–1023, May 1996.

[76] Brahim Guizal, Dominique Barchiesi, and Didier Felbacq. Electromagnetic beam diffraction by a finite lamellar structure: an aperiodic coupled-wave method. *J. Opt. Soc. Am. A*, 20(12):2274–2280, Dec 2003.

[77] K. Edee, B. Guizal, G. Granet, and A. Moreau. Beam implementation in a nonorthogonal coordinate system: Application to the scattering from random rough surfaces. *J. Opt. Soc. Am. A*, 25(3):796–804, Mar 2008.

[78] Alexander H.-D. Cheng and Daisy T. Cheng. Heritage and early history of the boundary element method. *Engineering Analysis with Boundary Elements*, 29(3):268–302, 2005.

[79] Alexander G. Voronovich. Rayleigh hypothesis. In David J. Lockwood and Alexei A. Maradudin, editors, *Light Scattering and Nanoscale Surface Roughness*, Nanostructure Science and Technology, pages 93–105. Springer US, 2007. 10.1007/978-0-387-35659-4_4.

[80] B. A. Lippmann. Note on the theory of gratings. *J. Opt. Soc. Am.*, 43(5):408–408, 1953.

[81] R. Petit and M. Cadilhac. Sur la diffraction d'une onde plane par un réseau infiniment conducteur. *C. R. Acad. Sci. B*, 262:468–471, 1966.

[82] R. Petit. *Electromagnetic theory of gratings*, volume 22. Springer-verlag Berlin Heidelberg N.Y., 1980.

[83] R. F. Millar. On the rayleigh assumption in scattering by a periodic surface. *Mathematical Proceedings of the Cambridge Philosophical Society*, 65(03):773–791, 1969.

[84] R. F. Millar. The rayleigh hypothesis and a related least-squares solution to scattering problems for periodic surfaces and other scatterers. *Radio Sci.*, 8(8,9):785–796, 1973.

[85] Jochen Wauer and Tom Rother. Considerations to rayleigh's hypothesis. *Optics Communications*, 282(3):339 – 350, 2009.

[86] Alexandre V. Tishchenko. Numerical demonstration of the validity of the rayleigh hypothesis. *Opt. Express*, 17(19):17102–17117, Sep 2009.

[87] Armand Wirgin and Roger Deleuil. Theoretical and experimental investigation of a new type of blazed grating. *J. Opt. Soc. Am.*, 59(10):1348–1357, Oct 1969.

[88] James Pavageau and Mlle Jacqueline Bousquet. Diffraction par un réseau conducteur nouvelle méthode de résolution. *Optica Acta: International Journal of Optics*, 17(6):469–478, 1970.

[89] F. Toigo, A. Marvin, V. Celli, and N. R Hill. Optical properties of rough surfaces: General theory and the small roughness limit. *Phys. Rev. B*, 15(12):5618–5626, 1977.

[90] John A. DeSanto. Exact spectral formalism for rough-surface scattering. *J. Opt. Soc. Am. A*, 2(12):2202–2206, Dec 1985.

[91] A. A. Maradudin, T. Michel, A. R. McGurn, and E. R. Méndez. Enhanced backscattering of light from a random grating. *Annals of physics(Print)*, 203(2):255–307, 1990.

[92] A. A. Maradudin, I. Simonsen, T. A. Leskova, and E. R. Mi¿½ndez. Localization of surface plasmon polaritons on a random surface. *Physica B: Condensed Matter*, 296(1-3):85 – 97, 2001.

[93] John A. DeSanto. Overview of rough surface scattering. In David J. Lockwood and Alexei A. Maradudin, editors, *Light Scattering and Nanoscale Surface Roughness*, Nanostructure Science and Technology, pages 211–235. Springer US, 2007. 10.1007/978-0-387-35659-4_8.

[94] Ingve Simonsen, Alexei A. Maradudin, and Tamara A. Leskova. The scattering of elec-tromagnetic waves from two-dimensional randomly rough perfectly conducting sur-faces: The full angular intensity distribution. *Phys. Rev. A*, 81:013806, Jan 2010.

[95] G. Kobidze, B. Shanker, and D. P. Nyquist. Efficient integral-equation-based method for accurate analysis of scattering from periodically arranged nanostructures. *Phys. Rev. E*, 72(5):056702, Nov 2005.

[96] Jonas Beermann, Sergey M. Novikov, Thomas Søndergaard, Jens Rafaelsen, Kjeld Ped-ersen, and Sergey I. Bozhevolnyi. Localized field enhancements in two-dimensional v-groove metal arrays. *J. Opt. Soc. Am. B*, 28(3):372–378, Mar 2011.

[97] Benjamin Gallinet, Andreas M. Kern, and Olivier J. F. Martin. Accurate and versatile modeling of electromagnetic scattering on periodic nanostructures with a surface in-tegral approach. *J. Opt. Soc. Am. A*, 27(10):2261–2271, Oct 2010.

[98] T. Søndergaard and Sergey I. Bozhevolnyi. Surface-plasmon polariton resonances in triangular-groove metal gratings. *Phys. Rev. B*, 80(19):195407, Nov 2009.

[99] Thomas Søndergaard, Sergey I. Bozhevolnyi, Jonas Beermann, Sergey M. Novikov, Eloïse Devaux, Thomas W. Ebbesen, and Jens Rafaelsen. Optical resonances and nanofocusing in triangular metal nano-grooves. 7757(1):77571R, 2010.

[100] Thomas Søndergaard, Jesper Gadegaard, Peter Kjær Kristensen, Thøger Kari Jensen, Thomas Garm Pedersen, and Kjeld Pedersen. Guidelines for 1d-periodic surface mi-crostructures for antireflective lenses. *Opt. Express*, 18(25):26245–26258, Dec 2010.

[101] Thomas Søndergaard, Sergey I. Bozhevolnyi, Jonas Beermann, Sergey M. Novikov, Eloïse Devaux, and Thomas W. Ebbesen. Resonant plasmon nanofocusing by closed tapered gaps. *Nano Letters*, 10(1):291–295, 2010. PMID: 20028028.

[102] Jonas Beermann, Thomas Søndergaard, Sergey M Novikov, Sergey I Bozhevolnyi, Eloïse Devaux, and Thomas W Ebbesen. Field enhancement and extraordinary op-tical transmission by tapered periodic slits in gold films. *New Journal of Physics*, 13(6):063029, 2011.

[103] I. Simonsen. Optics of surface disordered systems. *The European Physical Journal - Special Topics*, 181:1–103, 2010. 10.1140/epjst/e2010-01221-4.

[104] J. A. Sánchez-Gil and M. Nieto-Vesperinas. Resonance effects in multiple light scat-tering from statistically rough metallic surfaces. *Phys. Rev. B*, 45(15):8623–8633, Apr 1992.

[105] J. A. Sánchez-Gil and J. V. García-Ramos. Calculations of the direct electromagnetic enhancement in surface enhanced raman scattering on random self-affine fractal metal surfaces. 108(1):317–325, 1998.

[106] José A. Sánchez-Gil, José V. García-Ramos, and Eugenio R. Méndez. Near-field electromagnetic wave scattering from random self-affine fractal metal surfaces: Spectral dependence of local field enhancements and their statistics in connection with surface-enhanced raman scattering. *Phys. Rev. B*, 62(15):10515–10525, Oct 2000.

[107] Jose Sanchez-Gil, Jose Garcia-Ramos, and Eugenio Mendez. Electromagnetic mechanism in surface-enhanced raman scattering from gaussian-correlated randomly rough metal substrates. *Opt. Express*, 10(17):879–886, 2002.

[108] José A. Sánchez-Gil. Localized surface-plasmon polaritons in disordered nanostructured metal surfaces: Shape versus anderson-localized resonances. *Phys. Rev. B*, 68(11):113410, Sep 2003.

[109] José A. Sánchez-Gil, José V. García-Ramos, Vincenzo Giannini, and Eugenio R. Méndez. Scattering of electromagnetic waves from nanostructured, self-affine fractal surfaces: Near-field enhancements. In David J. Lockwood and Alexei A. Maradudin, editors, *Light Scattering and Nanoscale Surface Roughness*, Nanostructure Science and Technology, pages 285–304. Springer US, 2007. 10.1007/978-0-387-35659-4_11.

[110] José A. Sánchez-Gil, José V. García-Ramos, and Eugenio R. Méndez. Influence of nanoscale cutoff in random self-affine fractal silver surfaces on the excitation of localized optical modes. *Opt. Lett.*, 26(16):1286–1288, Aug 2001.

[111] Arnold Sommerfeld. *Partial differential equations in physics*, volume 6. Academic Press Inc, New York, 1949.

[112] Alexandre Munnier, Bruno Pinçon, and Karim Ramdani. Méthodes d'équations intégrales pour les edp. application à l'étude des opérateurs de laplace et de helmholtz en domaine extérieur. Cours de Master Recherche – Nancy-Université, february 2011.

[113] George C. Hsiao and Wolfgang L. Wendland. Boundary integral equations. In *Boundary Integral Equations*, volume 164 of *Applied Mathematical Sciences*, pages 25–94. Springer Berlin Heidelberg, 2008. 10.1007/978-3-540-68545-6_2.

[114] J. A. Sánchez-Gil and M. Nieto-Vesperinas. Light scattering from random rough dielectric surfaces. *J. Opt. Soc. Am. A*, 8(8):1270–1286, 1991.

[115] Milton Abramowitz and Irene A. Stegun. *Handbook of Mathematical Functions with Formulas, Graphs, and Mathematical Tables*. Dover, New York, tenth printing, december 1972, with corrections edition, 1964.

[116] C. M. Linton and P. Mciver. *Handbook of Mathematical Techniques for Wave/Structure Interactions*. Chapman & Hall/CRC, 2001.

[117] D. Maystre. *Rigorous vector theories of diffraction gratings*, volume 21. Elsevier Science Publishers B.V., 1984.

[118] Gregory Beylkin, Christopher Kurcz, and Lucas Monzón. Fast algorithms for helmholtz green's functions. *Proceedings of the Royal Society A: Mathematical, Physical and Engineering Science*, 464(2100):3301–3326, 2008.

[119] D. Van Orden and V. Lomakin. Rapidly convergent representations for 2d and 3d green's functions for a linear periodic array of dipole sources. *IEEE Transactions on Antennas and Propagation*, 57(7):1973–1984, July 2009.

[120] C.M. Linton. The green's function for the two-dimensional helmholtz equation in periodic domains. *Journal of Engineering Mathematics*, 33:377–401, 1998. 10.1023/A:1004377501747.

[121] D. E. Amos. Algorithm 644: A portable package for bessel functions of a complex argument and nonnegative order. *ACM Trans. Math. Softw.*, 12:265–273, September 1986.

[122] Gaël Guennebaud, Benoît Jacob, et al. Eigen v3. http://eigen.tuxfamily.org, 2010.

[123] Edward D. Palik. *Handbook of Optical Constants of Solids*. Academic Press, January 1997.

[124] Jun Q Lu and A. A Maradudin. Channel plasmons. *Phys. Rev. B*, 42(17):11159–11165, December 1990.

[125] I. V Novikov and A. A Maradudin. Channel polaritons. *Phys. Rev. B*, 66(3):035403, 2002.

[126] Sergey I. Bozhevolnyi, Valentyn S. Volkov, Eloïse Devaux, and Thomas W. Ebbesen. Channel plasmon-polariton guiding by subwavelength metal grooves. *Phys. Rev. Lett.*, 95:046802, Jul 2005.

[127] Sergey I. Bozhevolnyi. Effective-index modeling of channel plasmon polaritons. *Opt. Express*, 14(20):9467–9476, Oct 2006.

[128] Sergey I. Bozhevolnyi and Jesper Jung. Scaling for gap plasmon based waveguides. *Opt. Express*, 16(4):2676–2684, Feb 2008.

[129] Esteban Moreno, Sergio G. Rodrigo, Sergey I. Bozhevolnyi, L. Martín-Moreno, and F. J. García-Vidal. Guiding and focusing of electromagnetic fields with wedge plasmon polaritons. *Phys. Rev. Lett.*, 100:023901, Jan 2008.

[130] Ingrid Daubechies. *Ten Lectures on Wavelets*. CBMS-NSF Regional Conference Series in Applied Mathematics. SIAM: Society for Industrial and Applied Mathematics, 1 edition, jun 1992.

[131] C. K. Chui. *a mathematical tool for signal processing*. SIAM, 1997.

[132] George W. Pan. *Wavelets in Electromagnetics and Device Modeling*. John Wiley & Sons, Inc., 2003.

[133] S.G. Mallat. A theory for multiresolution signal decomposition: The wavelet representation. *IEEE Transactions on Pattern Analysis and Machine Intelligence*, 11:674–693, 1989.

[134] O. M. Nielsen. *Wavelets in scientific computing*. PhD thesis, Informatics and Mathematical Modelling, Technical University of Denmark, DTU, Richard Petersens Plads, Building 321, DK-2800 Kgs. Lyngby, 1998. Vejleder: Per Christian Hansen.

[135] Ingrid Daubechies. Orthonormal bases of compactly supported wavelets. *Communications on Pure and Applied Mathematics*, 41(7):909–996, 1988.

[136] B.Z. Steinberg and Y. Leviatan. On the use of wavelet expansions in the method of moments [em scattering]. *Antennas and Propagation, IEEE Transactions on*, 41(5):610–619, May 1993.

[137] Gaofeng Wang. Application of wavelets on the interval to numerical analysis of integral equations in electromagnetic scattering problems. *International Journal for Numerical Methods in Engineering*, 40(1):1–13, 1997.

[138] D. Zahn, K. Sarabandi, K.F. Sabet, and J.F Harvey. Orthogonal wavelets with applications in electromagnetics. *Antennas and Propagation, IEEE Transactions on*, 48(2):246–253, February 2000.

[139] M.Y. Xia, C.H. Chan, Shu-Qing Li, Jin-Lin Hu, and Leung Tsang. Wavelet-based simulations of electromagnetic scattering from large-scale two-dimensional perfectly conducting random rough surfaces. *Geoscience and Remote Sensing, IEEE Transactions on*, 39(4):718–725, April 2001.

[140] Guangwen Pan and M.V Toupikov .and B.K. Gilbert. On the use of coifman intervallic wavelets in the method of moments for fast construction of wavelet sparsified matrices. *Antennas and Propagation, IEEE Transactions on*, 47(7):1189–1200, July 1999.

[141] G. W. Pan, Wang Ke, and D. Cochran. Coifman wavelets in 3-d scattering from very rough random surfaces. *Antennas and Propagation, IEEE Transactions on*, 52(11):246–253, 2004.

[142] R.L. Wagner and Weng Cho Chew. A study of wavelets for the solution of electromagnetic integral equations. *Antennas and Propagation, IEEE Transactions on*, 43(8):802–810, August 1995.

[143] N. Guan, K. Yashiro, and S. Ohkawa. On a choice of wavelet bases in the wavelet transform approach. *Antennas and Propagation, IEEE Transactions on*, 48(8):1186–1191, August 2000.

[144] H. A. van der Vorst. Bi-cgstab: A fast and smoothly converging variant of bi-cg for the solution of nonsymmetric linear systems. 13(2):631–644, 1992.

[145] J. Ma, V. Rokhlin, and S. Wandzura. Generalized gaussian quadrature rules for systems of arbitrary functions. 33(3):971–996, 1996.

[146] Michio Masujima. *Applied Mathematical Methods in Theoretical Physics*. Wiley-VCH, 2009.

[147] Michel Misiti and Yves Misiti. *Wavelets and their applications*. John Wiley and Sons, 2007.

Abstract

   The framework of this thesis is the numerical simulation of the interaction of light with rough metallic surfaces which can be the origin of giant enhancements of the electromagnetic field due to plasmonic resonances. The abrupt profile of these surfaces have characteristic sizes of a few nanometers of width and a few tens of nanometers of height. The main difficulty in the simulation of such phenomena is in the scale difference of the wavelength of the incident wave and the size of the roughness as well as the abrupt variations of the magnetic field at the surface. A suited method of simulation is the numerical resolution of surface integral equations for periodic profile of the surface. This method was implemented in C++ and the numerical calculation of the pseudo-periodic Green function was optimized. The intensity of the refracted beam and that of the electromagnetic field maps are rigorously calculated from the obtained solution. We showed by applying this method that plasmonic resonances situated in the cavity of gratings with Gaussian shaped grooves of nanometric sizes have an electrostatic behavior similar to that of the rectangular grooves, in particular, a very low specular reflectivity at the resonance. The current performances of computers limit the studies to gratings with a small period. In order to overcome these limitations, we considered a function basis enabling to decompose a functions into its components of different resolutions: the wavelets. This work ends with a discussion on the potential of two different applications of the wavelets to the resolution of integral equations.

Résumé

Le cadre de cette thèse est la simulation numérique de l'interaction de la lumière avec des surfaces métalliques rugueuses pouvant être à l'origine de fortes localisation du champ électromagnétique dû à des résonances plasmoniques. Les profils accidentés de ces surfaces ont des tailles caractéristiques de quelques nanomètres de largeur et de quelques dizaines de nanomètres de hauteur. La principale difficulté dans la simulation de tels phénomènes réside dans la différence d'échelle entre la longueur d'onde de l'onde incidente et la taille des rugosités ainsi que les variations brutales du champ magnétique à la surface. Une méthode de simulation adaptée est la résolution numérique d'équations intégrales de surface ayant un profil périodique. Cette méthode a été implémentée en C++ et le calcul numérique de la fonction de Green pseudo-périodique a été optimisé. L'intensité du faisceau réfracté ainsi que les cartes de champ proche peuvent être calculées rigoureusement à partir de la solution obtenue. A l'aide de cette méthode, on a montré que des résonances plasmoniques situées dans les cavités d'un réseaux ayant des rainures de forme Gaussienne de taille nanométrique ont un comportement électrostatique similaire à celles des cavités rectangulaires, notamment une réflectivité spéculaire très faible en condition de résonance. Les performances actuelles des ordinateurs limitent cependant les études à des réseaux de petite période. Afin de dépasser ces limitations, on a fait appel à des bases de fonctions permettant de décomposer une fonction en ses parties de résolutions différentes : les ondelettes. Ce travail se conclue par une discussion sur le potentiel de deux utilisations différentes des ondelettes pour la résolution d'équation intégrales.